Universiteit Leiden
The Netherlands

Radio emission from merging galaxy clusters : characterizing shocks, magnetic fields and particle acceleration

Weeren, R.J. van

Citation

Weeren, R. J. van. (2011, December 20). *Radio emission from merging galaxy clusters : characterizing shocks, magnetic fields and particle acceleration*. Retrieved from https://hdl.handle.net/1887/18259

Version:	Corrected Publisher's Version
License:	Licence agreement concerning inclusion of doctoral thesis in the Institutional Repository of the University of Leiden
Downloaded from:	https://hdl.handle.net/1887/18259

Note: To cite this publication please use the final published version (if applicable).

Radio emission from merging galaxy clusters

characterizing shocks, magnetic fields and particle acceleration

Radio emission from merging galaxy clusters

characterizing shocks, magnetic fields and particle acceleration

Proefschrift

ter verkrijging van
de graad van Doctor aan de Universiteit Leiden,
op gezag van Rector Magnificus prof. mr. P. F. van der Heijden,
volgens besluit van het College voor Promoties
te verdedigen op dinsdag 20 december 2011
klokke 15:00 uur

door

Reinout Johannes van Weeren

geboren te De Bilt
in 1980

Promotiecommissie

Promotores:	Prof. dr. H. J. A. Röttgering	
	Prof. dr. G. K. Miley	
Overige leden:	Prof. dr. M. Brüggen	(Jacobs University Bremen, Germany)
	Prof. dr. A. G. de Bruyn	(Stichting ASTRON, Dwingeloo; Rijksuniversiteit Groningen)
	Prof. dr. H. Falcke	(Radboud Universiteit Nijmegen)
	Prof. dr. M. A. Garrett	(Stichting ASTRON, Dwingeloo; Universiteit Leiden)
	Prof. dr. W. Jaffe	
	Prof. dr. K. H. Kuijken	

The cover shows a GMRT 150 MHz radio image of the field around the galaxy cluster CIZA J2242.8+5301. LOFAR antennas are visible at the bottom.

GMRT image by Huib Intema.

Cover design by Brigitta van Weeren.

ISBN: 978-94-6191-099-8

Contents

1 Introduction **1**
1.1 Cosmology & large-scale structure formation . . . 1
1.2 Galaxy clusters . . . 2
1.3 Radio emission from galaxy clusters . . . 2
1.3.1 Radio halos . . . 3
1.3.1.1 Origin of radio halos . . . 3
1.3.2 Radio relics . . . 4
1.4 This thesis . . . 5
1.5 Future prospects . . . 8

2 A search for steep spectrum radio relics and halos with the GMRT **11**
2.1 Introduction . . . 12
2.2 Sample selection . . . 14
2.3 Observations & data reduction . . . 14
2.4 Results . . . 16
2.4.1 Individual sources . . . 16
2.4.1.1 VLSS J1133.7+2324 . . . 16
2.4.1.2 VLSS J1431.8+1331 . . . 18
2.4.1.3 VLSS J2217.5+5943, 24P73 . . . 19
2.4.1.4 VLSS J0004.9−3457 . . . 21
2.4.1.5 VLSS J0717.5+3745, MACS J0717.5+3745 . . . 21
2.4.1.6 VLSS J0915.7+2511 . . . 23
2.4.1.7 VLSS J1515.1+0424, Abell 2048 . . . 24
2.5 Spectral index modeling . . . 24
2.6 Discussion . . . 27
2.7 Conclusions . . . 32
2.8 Appendix: Other sources in the sample . . . 35

3 Diffuse steep-spectrum sources from the 74 MHz VLSS survey 41
3.1 Introduction . . . 42
3.2 Observations & data reduction . . . 43
3.2.1 GMRT 325 MHz observations . . . 43
3.2.2 VLA 1.4 GHz observations . . . 44
3.2.3 WSRT 1.3 – 1.7 GHz observations of 24P73 . . . 46
3.2.4 Optical WHT & INT imaging . . . 47
3.3 Results . . . 47
3.3.1 VLSS J1133.7+2324, 7C 1131+2341 . . . 48
3.3.2 VLSS J1431.8+1331, MaxBCG J217.95869+13.53470 . . . 50
3.3.3 VLSS J2217.5+5943, 24P73 . . . 52
3.3.4 VLSS J0004.9−3457 . . . 53
3.3.5 VLSS J0915.7+2511, MaxBCG J138.91895+25.19876 . . . 55
3.3.6 VLSS J1515.1+0424, Abell 2048 . . . 55
3.4 Optical imaging around five compact steep-spectrum sources . . . 59
3.4.1 VLSS J2043.9−1118 . . . 59
3.4.2 VLSS J1117.1+7003 . . . 61
3.4.3 VLSS J2209.5+1546 . . . 61
3.4.4 VLSS J0516.2+0103 . . . 61
3.4.5 VLSS J2241.3−1626 . . . 62
3.5 Discussion . . . 62
3.6 Conclusions . . . 64

4 Radio continuum observations of new radio halos and relics from the NVSS and WENSS surveys: Relic orientations, cluster X-ray luminosity and redshift distributions 67
4.1 Introduction . . . 68
4.2 Observations & data reduction . . . 69
4.2.1 Radio observations . . . 69
4.2.2 Optical WHT & INT images . . . 71
4.3 Results . . . 71
4.3.1 Abell 1612 . . . 71
4.3.2 Abell 746 . . . 76
4.3.3 Abell 523 . . . 76
4.3.4 Abell 697 . . . 79
4.3.5 Abell 2061 . . . 80
4.3.6 Abell 3365 . . . 84
4.3.7 CIZA J0649.3+1801 . . . 86
4.3.8 CIZA J0107.7+5408 . . . 89
4.3.9 Abell 2034 . . . 89
4.3.10 RXC J1053.7+5452 . . . 90
4.4 Discussion . . . 90
4.4.1 Comparison with the REFLEX and NORAS X-ray clusters . . . 94
4.4.2 X-ray peak and galaxy distribution separation . . . 96
4.5 Conclusions . . . 99

5 Diffuse radio emission in the merging cluster MACS J0717.5+3745: the discovery of the most powerful radio halo 101
5.1 Introduction . . . 102
5.2 Observations & data reduction . . . 103
5.3 Results: images, equipartition magnetic field & spectral index maps . . . 104
5.3.1 Equipartition magnetic field strength . . . 106
5.3.2 Spectral index . . . 107
5.4 Discussion . . . 109
5.4.1 Alternative explanations for the elongated radio structures . . . 109
5.4.2 Origin of the radio relic . . . 110
5.5 Conclusions . . . 111

6 Radio observations of ZwCl 2341.1+0000: a double radio relic cluster 113
6.1 Introduction . . . 114
6.2 Observations & data reduction . . . 116
6.3 Results . . . 121
6.4 Radio, X-ray, and galaxy distribution comparison . . . 123
6.5 Spectral index & equipartition magnetic field strength . . . 125
6.5.1 Spectral index . . . 125
6.5.2 Equipartition magnetic field . . . 126
6.6 Discussion . . . 127
6.6.1 Alternative explanations . . . 127
6.6.2 Comparison of spectral indices and magnetic field strengths with other double relics . . . 128
6.6.3 Origin of the double relic . . . 129
6.7 Conclusions . . . 130
6.8 Appendix: Compact sources at 610 MHz and optical counterparts . . . 132

7 A double radio relic in the merging galaxy cluster ZwCl 0008.8+5215 135
7.1 Introduction . . . 136
7.2 Observations & data reduction . . . 137
7.2.1 GMRT observations . . . 137
7.2.2 WSRT 1.3–1.7 GHz observations . . . 138
7.2.3 Optical images & spectroscopy . . . 139
7.3 Results . . . 140
7.3.1 Redshift of ZwCl 0008.8+5215 . . . 140
7.3.2 Thermal ICM and galaxy distribution . . . 140
7.3.3 Radio continuum maps . . . 141
7.3.4 Spectral index and polarization maps . . . 144
7.3.5 Radio galaxies in the cluster . . . 145
7.4 Discussion . . . 147
7.4.1 Origin of the double radio relic . . . 147
7.4.2 Radio luminosity profile for the eastern relic . . . 151
7.4.3 Simulated radio luminosity and spectral index profiles . . . 152
7.4.4 Equipartition magnetic field strength . . . 153
7.5 Conclusions . . . 154

8 Particle acceleration on megaparsec scales in a merging galaxy cluster 157
8.1 Appendix: Data reduction . . . 165

9 The "toothbrush-relic": evidence for a coherent linear 2-Mpc scale shock wave in a massive merging galaxy cluster? 169
9.1 Introduction . . . 170
9.2 Observations & data reduction . . . 173
9.2.1 GMRT observations . . . 173
9.2.2 WSRT observations . . . 174
9.2.3 WHT spectroscopy & imaging . . . 174
9.3 Results: redshift, X-rays, and radio continuum maps . . . 174
9.3.1 Redshift of 1RXS J0603.3+4214 . . . 174
9.3.2 X-ray emission from the ICM . . . 175
9.3.3 Radio continuum maps . . . 175
9.4 Radio spectra . . . 178
9.4.1 Spectral index maps . . . 178
9.4.2 Integrated radio spectra . . . 182
9.5 Radio color-color diagrams . . . 182
9.5.1 Spectral models . . . 185
9.5.2 Effect of resolution on surface brightness . . . 186
9.5.3 Color-color diagrams . . . 187
9.5.3.1 Color-color diagrams for B1 and B2+B3 . . . 187
9.5.3.2 The effect of resolution and mixing . . . 188
9.5.4 Global spectrum . . . 188
9.5.4.1 Shift diagrams . . . 188
9.6 RM-synthesis & polarization maps . . . 189
9.6.1 Polarization maps . . . 189
9.6.2 RM-synthesis . . . 189
9.6.2.1 Application to the L-band WSRT data . . . 195
9.6.3 The depolarization properties of the radio relic . . . 195
9.7 Discussion . . . 197
9.7.1 Relic spectra . . . 198
9.7.2 Alternative models to explain the relativistic electrons from the radio relic 199
9.7.3 Magnetic field . . . 200
9.8 Conclusions . . . 200

10 Using double radio relics to constrain galaxy cluster mergers: A model of double radio relics in CIZA J2242.8+5301 203
10.1 Introduction . . . 204
10.2 Overview: Simulations of galaxy cluster mergers . . . 205
10.3 Numerical method . . . 207
10.3.1 Radio emission from shocks . . . 207
10.3.2 Initial conditions . . . 209
10.4 Results . . . 210
10.4.1 Radio maps . . . 211
10.4.1.1 Mass ratio . . . 211

10.4.1.2 Impact parameter . . . 216
10.4.1.3 Viewing angle . . . 216
10.4.1.4 β-model . . . 219
10.4.1.5 Cool core . . . 219
10.4.2 Spectral index . . . 219
10.5 Substructure & clumping . . . 221
10.6 Discussion . . . 223
10.6.1 Effect of dark matter dynamics . . . 223
10.6.2 Relic width and brightness profiles . . . 223
10.6.3 Origin of single radio relics . . . 224
10.6.4 A quantitative metric for the goodness of fit . . . 224
10.7 Summary . . . 225

11 The discovery of diffuse steep spectrum sources in Abell 2256 227
11.1 Introduction . . . 228
11.2 Observations & data reduction . . . 228
11.3 Results . . . 230
11.3.1 Spectral indices . . . 231
11.4 Discussion . . . 232
11.5 Conclusions . . . 233

12 LOFAR Abell 2256 observations between 18 and 67 MHz 235
12.1 Introduction . . . 236
12.2 Observations & data reduction . . . 237
12.2.1 Primary beam correction, absolute flux-scale and self-calibration . . . 240
12.2.2 Radio images . . . 242
12.2.3 Spectral index map and integrated fluxes . . . 243
12.3 Discussion . . . 245
12.3.1 Source F . . . 245
12.3.2 Source AG+AH . . . 246
12.3.3 Radio relic and halo . . . 247
12.4 Conclusions . . . 249

Bibliography 251

Nederlandse samenvatting 265

Curriculum vitae 271

Nawoord / Acknowledgements 273

CHAPTER 1

Introduction

1.1 Cosmology & large-scale structure formation

Observations reveal that the Universe has an age of 13.75 ± 0.11 billion years (Komatsu et al. 2011). The current standard model of cosmology is the ΛCDM model which consists of dark energy, cold dark matter and baryonic matter. These contribute about 73%, 22%, and 5%, to the energy density, respectively. This model has successfully explained some of the key properties of our Universe. These include the large-scale distribution of galaxies (e.g., Abazajian et al. 2009), the primordial abundances of the elements hydrogen, helium and lithium, the existence and properties of the Cosmic Microwave Background (CMB) radiation (e.g., Mather et al. 1990; Smoot et al. 1992; Mather et al. 1994; Kovac et al. 2002), and the observed large-scale flat geometry and isotropy. In addition, the ΛCDM model also includes the observed accelerated expansion of the Universe (Riess et al. 1998).

A key ingredient of the ΛCDM model is cosmic inflation, where just after the Big Bang the Universe underwent a short period of rapid exponential expansion. Quantum physics implies that temperature fluctuations should have existed immediately after the Big Bang, while the temperature of the CMB has precisely the same value all over the sky (within one part to 10^{-5} – 10^{-6}). Inflation has been invoked to smooth out the quantum fluctuations which also results in a flat space geometry. This assures isotropy and homogeneity on the largest scales. Furthermore, it explains why different regions of the Universe, that are not casually connected because of the large distances between them, have the same physical properties, the so-called horizon problem. This could also explain the lack of observed magnetic-monopoles, which should have otherwise been produced just after the Big Bang.

Observations of the CMB reveal the matter distribution in the Universe to be extremely homogenous 3.8×10^5 yrs after the Big Bang, but in 1992 tiny variations variations in the CMB temperature were discovered (Smoot et al. 1992). These temperature anisotropies correspond to small-scale density variations. In the ΛCDM model, these tiny fluctuations grow hierar-

chically under the influence of gravity. These form halos of cold dark matter that merge and subsequently acquire more mass (e.g., Springel et al. 2006). The baryonic matters follows the dark matter halos, but its physics is much more complicated as other interactions besides gravity have to be taken into account. These include gas heating, cooling, ionization and recombination. Dark matter only interacts with baryonic matter through gravity. The nature of this dark matter remains one of the biggest mysteries in astronomy. Eventually the baryonic matter cools and collapses, forming stars, galaxies, and clusters of galaxies. On the largest scales the distribution of baryonic matter forms sheets and filaments of galaxies. At nodes, where filaments meet, galaxy clusters are located. Clusters and filaments are surrounded by voids, large empty regions devoid of visible matter (e.g., Peacock et al. 2001).

1.2 Galaxy clusters

Galaxy clusters play a very special role, as they are the largest gravitationally bound structures that formed out of the CMB fluctuations. They also formed relatively late in the process, at a time when the Universe had roughly half of its present age. As of today galaxy cluster are still acquiring more mass and new clusters are being formed. Galaxy clusters consist of dark matter ($\sim$ 75% in total by mass), hot ionized gas (20% by mass) that emits at X-ray wavelengths (Byram et al. 1966; Gursky et al. 1971), called the intracluster medium (ICM), and stars, cold gas, and dust, which are mostly found in galaxies (5% by mass). The ICM has temperatures in the range of about 0.1 keV to $\sim$ 40 keV. The global X-ray luminosity and temperature of clusters scale with the cluster mass, but significant spatial temperature variations within clusters exist (e.g., Markevitch et al. 2002; Fabian et al. 2006; Ma et al. 2009). Typical masses for galaxy clusters are in the range of 10^{14} –10^{15} $M_{\odot}$, and clusters span about 5 Mpc in the present day Universe.

As predicted by the hierarchical model of structure formation galaxy cluster grow by mergers with other clusters and galaxy groups, as well as through the continuous accretion of gas from the intergalactic medium (IGM, or the warm-hot intergalactic medium, WHIM). In fact, about 50% of the total baryon mass is thought to reside in the IGM (Cen & Ostriker 1999). Both galaxy cluster mergers and the accretion of gas create shocks in and around galaxy clusters, heating the ICM. Cluster merger events are the most energetic events in the present day Universe, releasing energies of 10^{63} – 10^{64} erg. They therefore play an important role in the energy budget of the ICM and dynamical state of clusters.

Magnetic fields are another important component of galaxy clusters. Magnetic fields reveal themselves by the synchrotron radiation (e.g., Willson 1970; Jaffe et al. 1976) from charged relativistic particles (also called cosmic rays, CR) spiraling around the field lines. In addition, magnetic fields can be studied through Inverse Compton (IC) X-ray emission (e.g., Finoguenov et al. 2010) and polarized radio emission, e.g., by Faraday rotation of polarized radio sources located behind or within the ICM (e.g., Clarke et al. 2001; de Bruyn & Brentjens 2005).

1.3 Radio emission from galaxy clusters

Radio observations show that some clusters host diffuse radio sources that are not associated with any of the individual galaxies in clusters. This emission generally has a low surface bright-

ness, $\sim 1\mu$Jy arcsec^{-2} at 1.4 GHz, and relatively steep radio spectrum with $\alpha < -0.5$[1], but more typically $\alpha \lesssim -1$. With the improved capabilities of radio interferometers the number of these diffuse sources known has increased considerably over the past 15 years. Currently, more than 50 of these diffuse sources are known. The classification of these sources has been driven by the observed properties of the radio sources, these include the location with respect to the ICM, morphology, polarization properties, size, and radio spectrum.

Three main classes of diffuse sources in clusters have been identified. These are radio halos, mini-halos, and relics. In addition, claims have been made of radio emission originating from the space between galaxy clusters (e.g., Bagchi et al. 2002; Kronberg et al. 2007), these sources have been called *radio filaments*. Radio mini-halos are found in relaxed cool-cores clusters (e.g., Fabian et al. 1991; Peterson & Fabian 2006). They surround the central radio-loud active galactic nuclei (AGN) and have sizes of $\lesssim 500$ kpc. We focus here on the halos and relics that are found in merging galaxy clusters.

1.3.1 Radio halos

Radio halos are large (~ 1 Mpc) diffuse sources that have a steep radio spectrum ($\alpha \leq -1$). Halos are centrally located and have a regular smooth morphology. They are all found in clusters with a disturbed dynamical state (e.g., Cassano et al. 2010b). For a number of halos a point-to-point spatial correlation is observed between the radio and X-ray brightness, indicating an interaction between non-thermal and thermal components (e.g., Govoni et al. 2004). A spatial correlation between the radio spectral index and X-ray temperature of the gas is also observed, in the sense that regions/clusters with a higher temperature tend to have flatter radio spectra (Feretti et al. 2004; Orrú et al. 2007; Giovannini et al. 2009). Usually no polarized emission is detected from radio halos.

Unlike the thermal X-ray emission from clusters, radio halos are not a common phenomena. From a complete X-ray sample ($0.2 < z \leq 0.4$, $L_{\mathrm{X,0.1-2.4\ keV}} > 5 \times 10^{44}$ erg s^{-1}) Venturi et al. (2008, 2007) found the fraction of clusters hosting radio halos to be 0.29 ± 0.09. This fraction seems to increase for the more luminous/massive clusters. For cluster with $L_{\mathrm{X,0.1-2.4\ keV}} > 8 \times 10^{44}$ erg s^{-1} the fraction is 0.38 ± 0.13.

The 1.4 GHz radio power of halos ($P_{1.4\mathrm{GHz}}$) correlates with the X-ray luminosity. This L_{X}–$P_{1.4\mathrm{GHz}}$ correlation for giant radio halos (e.g., Liang et al. 2000; Cassano et al. 2006) could reflect a dependence of the radio halo power on the cluster mass. Observations from Venturi et al. (2008, 2007) separate the radio halo clusters from clusters without radio halos, showing a bimodal distribution of clusters in the $P_{1.4\ \mathrm{GHz}}$–L_X diagram, i.e., a fraction of clusters hosts giant radio halos, while the majority of clusters does not show evidence of diffuse cluster-scale radio emission (Brunetti et al. 2007, 2009). The upper limits on the radio power of clusters without radio halos lie about one order of magnitude below the L_{X}–$P_{1.4\mathrm{GHz}}$ correlation. Therefore, the bimodal distribution does not arise from observational biases.

1.3.1.1 Origin of radio halos

The radiative lifetime of the synchrotron emitting electrons is about 10^8 yr at ~ 1 GHz. Within this time the CR electrons can only diffuse over about 1–10 kpc (in the Bohm approximation, e.g., Drury 1983). However, radio halos have Mpc sizes. This implies that the electrons must

[1] $F_\nu \propto \nu^\alpha$, where α is the spectral index

be accelerated in-situ (Jaffe 1977). The clear connection with cluster mergers strongly suggests that some fraction of the gravitational energy released during merger events is channelled into the production of the non-thermal particles in ICM.

Two main classes of models have been proposed for the origin of radio halos:

- Primary models: primary CR electrons are re-accelerated by the turbulence generated during cluster merger events (Brunetti et al. 2001; Petrosian 2001). These primary electrons are injected into the ICM by for example radio galaxies, supernovae, or galactic winds.

- Secondary models: electrons are secondary products which originate from hadronic collisions between long-lived relativistic protons and thermal ions in the ICM (Dennison 1980; Blasi & Colafrancesco 1999). Since the energy losses for protons are very small this allows them to diffuse over the large distances required to from Mpc-size radio halos. The relativistic protons accumulate over the entire formation history of a cluster and could for example originate from accretion shocks or radio galaxies. A consequence of the secondary models is that gamma ray emission is expected, through the decay of neutral pions generated by the hadronic collisions.

Observations mostly support the primary re-acceleration models. These observations include (i) the connection with cluster mergers (e.g., Cassano et al. 2010b), (ii) the existence of the radio halo bi-modality (Venturi et al. 2007) which suggests that the radio emission is suppressed and amplified on a time-scale significantly shorter than 1 Gyr. This is difficult to reconcile with the hypothesis that the radio emission is suppressed due to dissipation of magnetic fields in galaxy clusters, as is required for the secondary models (Brunetti et al. 2009). (iii) The lack of Gamma rays from the ICM (e.g., Jeltema & Profumo 2011), (iv) the radial radio brightness profiles (e.g., Donnert et al. 2010a; Brown & Rudnick 2011), i.e., the brightness profiles of the synchrotron emission from secondary models are much steeper than what is seen in observations, (v) the existence of radio halos with $\alpha < -1.5$ (Brunetti et al. 2008) which in the case of secondary models requires an unrealistic amount of energy in the relativistic protons, and (vi) the similar magnetic field properties between clusters with and without halos (Bonafede et al. 2011). This poses problems for the secondary models since they require a difference in the magnetic field strength between clusters with and without radio halos (e.g., Dolag & Enßlin 2000; Pfrommer & Enßlin 2004). Although, it should be noted that all these results are still actively being debated (e.g., Enßlin et al. 2011).

1.3.2 Radio relics

Radio relics are elongated, filamentary, sometimes arc-like sources unrelated to individual galaxies. Their sizes range from 50 kpc to 2 Mpc. They can be highly polarized with fractional polarization levels of 20 – 40% (e.g., Andernach et al. 1984; Clarke & Ensslin 2006). Their integrated radio spectra range from $\alpha \approx -1$ for large relics to $\alpha < -2$ for smaller relics. Relics have been divided into three groups (Kempner et al. 2004).

(1) *Radio gischt* are large elongated, often Mpc-sized, radio sources located at the periphery of merging clusters. Among these are rare *double-relics*. In this case two relics are located on opposite sides of the cluster center (e.g., Bonafede et al. 2009b; van Weeren et al. 2009b; Venturi et al. 2007; Bagchi et al. 2006; Röttgering et al. 1997; van Weeren et al. 2010; Brown et al. 2011; Bagchi et al. 2011). It has been proposed (Ensslin et al. 1998; Miniati et al. 2000)

that gischt relics trace shock fronts in which particles are accelerated via the diffusive shock acceleration mechanism (DSA; Krymskii 1977; Axford et al. 1977; Bell 1978a,b; Blandford & Ostriker 1978; Drury 1983; Blandford & Eichler 1987; Jones & Ellison 1991; Malkov & O'C Drury 2001). According to DSA theory, the injection radio spectral index is related to the Mach number of the shock. However, the efficiency with which collisionless shocks can accelerate particles is unknown and may not be enough to produce the observed radio brightness of relics. A closely linked scenario is that of shock re-acceleration of pre-accelerated electrons in the ICM, which is a more efficient mechanism for weak shocks (e.g., Markevitch et al. 2005; Giacintucci et al. 2008; Kang & Ryu 2011).

An alternative scenario for gischt has been proposed by Keshet (2010). This model is based on a secondary cosmic ray electron model, where the amplification and time evolution of magnetic fields and the cosmic ray distribution are taken into account to explain both halos and giant relics.

Very recently, X-ray brightness discontinuities have been found at the location of a few relics, most likely these discontinuities are shocks with Mach numbers of ~ 2 (Finoguenov et al. 2010; Macario et al. 2011). By comparing the limit on the IC X-ray emission with the measured radio flux, a lower limit of 3 μG on the magnetic field strength has been obtained for the bright relic in the cluster Abell 3667 by Finoguenov et al. (2010).

The class of double radio relics is particular interesting as, based on current models of electron acceleration for this class of radio sources, it enables us to explore the connection between clusters mergers and shock waves (e.g., Roettiger et al. 1999a). These relics are thought to trace diametrically outward traveling shocks emanating from the cluster center, and created during a binary cluster merger event. In this case, steepening of the spectral index in the direction towards the cluster is expected due to the radiation losses of the electrons in the shock downstream region.

An alternative shockwave-inducing mechanism is that of external "accretion" shocks, where filaments of galaxies from the cosmic web funnel into the clusters (Miniati et al. 2000; Miniati 2003; Keshet et al. 2003). Merger shocks are weaker than the external accretion shocks, as the gas has already been heated by these external shocks. The external accretion shocks occur farther out than the merger shocks, up to a few times the virial radius of the cluster. The gas density is very low at these distances from the cluster center and so are the energy densities in the CR electrons and magnetic fields. Therefore, the radio emission from external accretion shocks is likely too faint to be detected with the current radio telescopes (e.g., Hoeft et al. 2008).

Besides the above discussed radio gischt there are (2) *AGN relics* and (3) *Radio phoenices*. AGN relics are associated with extinct or dying radio galaxies. The radio plasma has a steep curved spectrum due to synchrotron and IC losses. AGN relics can be compressed adiabatically by merger shock waves producing so-called radio phoenices (Enßlin & Gopal-Krishna 2001; Enßlin & Brüggen 2002). Phoenices again have steep and curved radio spectra due to radiation losses. Proposed examples of phoenices are the relics found by Slee et al. (2001).

1.4 This thesis

Because radio halos and relics are diffuse, have low luminosities and steep radio spectra, they are difficult to observe with radio telescopes that mostly operate above 1 GHz. Therefore studies of non-thermal processes in the ICM, as traced by the diffuse radio sources, are mainly limited

to the brightest and most nearby clusters. It is expected though that there are still a significant number of radio halos and relics to be found in the NVSS (Condon et al. 1998), WENSS (Rengelink et al. 1997) and VLSS (Cohen et al. 2007) surveys, but a problem is how to recognize these sources in the survey data. As a result there are only a few dozen radio halos and relics known. The origin of the radiating electrons is currently still being debated, and for many radio halos and relics spectral and polarization studies are missing which could distinguish between the different acceleration models. Some of the main questions that need to be answered are:

- How are the particles accelerated that form the radio halos and relics?
- How common are diffuse cluster radio sources? What is the occurrence of these sources as function of cluster properties, such as mass, temperature and substructure.
- What are the properties of merging clusters (mass ratios, impact parameters) and how do these properties evolve over cosmic time?
- What is the contribution of cosmic rays and magnetic fields to the energy budget of the ICM?
- What are the properties of the magnetic fields (topology and strength) in the ICM? How do they relate to models for the origin of these fields in clusters?

To start answering these questions (i) larger samples of diffuse cluster radio sources have to be compiled, (ii) multi-frequency and polarization observations are needed, (iii) halos and relics should be observed at very low frequencies, and (iv) radio observations of merging clusters need to be compared with simulations and observations at other wavelengths.

In this thesis an interferometric study of diffuse radio sources in and around galaxy clusters is performed to address some of the above mentioned points. Multi-frequency observations from the Giant Metrewave Radio Telescope (GMRT), Westerbork Synthesis Radio Telescope (WSRT), and Very Large Array (VLA) radio telescopes are analyzed to measure the spectral and polarimetric properties of diffuse cluster sources. A search for new relics and halos is carried out based on existing radio surveys. As a theoretical part of this thesis numerical simulations of cluster mergers, with the aim of constraining the cluster mergers parameters from observations of double radio relics, are carried out. In addition, one of the first LOFAR observations of cluster-scale diffuse radio emission is presented. LOFAR is a new pan-European radio telescope that operates at the lowest radio frequencies accessible from the surface of the Earth. These observations are very challenging due the large fields of view, radio frequency interference (RFI), ionospheric phase distortions, differential Faraday rotation, spatially and time varying stations beams, direction dependent calibration, and enormous data-rates. In spite of these challenges, the LOFAR images are the deepest ever obtained at frequencies below 100 MHz.

In **Chapters 2** and **3** GMRT, VLA, and WSRT observations of a sample of 26 diffuse (angular size $\gtrsim 15''$) ultra-steep spectrum radio sources selected from the 74 MHz VLSS survey are presented. Most of these sources have a spectral index of $\alpha \leq -1.35$, between 74 and 1400 MHz. The aim of these observations was to search for steep-spectrum radio halos and relics, either associated with clusters or the cosmic web. It turns out that the majority of the sources in the sample are associated with galaxies in clusters or groups. Most likely these sources trace old (possibly compressed) radio plasma from AGN activity. One large radio halo and relic in a distant massive galaxy cluster is found (see also **Chapter 5**). By complementing the observations

with measurements from the literature, correlations between the physical size and spectral index of relics are found, in the sense that smaller relics have steeper spectra. Furthermore, larger relics are mostly located in the outskirts of clusters while smaller relics are located closer to the cluster center.

In **Chapter 4** a search for radio halos and relics in the NVSS and WENSS surveys is described. Candidate halos and relics were followed up with GMRT, WSRT, and VLA observations. These observations revealed 6 new radio relics and 2 radio halos. In addition, the presence of diffuse radio emission in four galaxy clusters is confirmed. With a sample of 35 radio relics, it is found that relics are mostly located along the major axis of the X-ray emission from the ICM, while their orientation is perpendicular to this axis. The location and orientation of radio relics with respect to the ICM elongation is consistent with the scenario that relics trace merger shock waves. The X-ray luminosity and redshift distributions of clusters with relics are compared to an X-ray selected cluster sample from the NORAS and REFLEX surveys. There is evidence for an increase in the relic fraction with X-ray luminosity and redshift.

In **Chapter 5** the diffuse radio emission in the cluster MACS J0717.5+3745 ($z = 0.5548$) is discussed. This cluster hosts the most luminous and distant radio halo. MACS J0717.5+3745 is also one of the hottest ($\sim$ 11.6 keV) and most X-ray luminous clusters known and display signs of undergoing a triple merger event. Furthermore, the cluster hosts a giant relic, which location roughly coincides with regions of the ICM that have a significant enhancement in temperature as shown by Chandra. This could mean that the relic traces a merger-related shock wave, where particles are accelerated via the diffusive shock acceleration mechanism. Alternatively, the relic traces an accretion shock of a large-scale galaxy filament extending to the southeast.

Chapters 6 and **7** deal with the discovery of double radio relics in the galaxy clusters ZwCl 2341.1+0000 and ZwCl 0008.8+5215. Both clusters show an elongated ICM and the galaxy distributions are also either elongated or bimodal. The relics are located on opposite sides of the cluster center, along the major axis of the X-ray emission, at the location where outwards traveling merger shock waves are expected. For ZwCl 0008.8+5215 there is steepening of the spectral index across the relics in the direction towards the cluster center. It is concluded that the double relics in ZwCl 2341.1+0000 and ZwCl 0008.8+5215 are best explained by two outward moving shock waves in which particles are (re)accelerated through the diffusive shock acceleration mechanism.

In **Chapter 8** GMRT, WSRT and VLA observations of a new radio relic in the cluster CIZA J2242.8+5301 are presented. This relic has a large $\sim$ 2 Mpc extent, but its width measures only 55 kpc. For the relic, highly aligned magnetic fields and a strong spectral index gradient, in the direction towards the cluster center, are observed. The power-law integrated spectral index, clear spectral index gradient and aligned magnetic fields are evidence for particle acceleration in an outward moving shock wave. The very small width of the relic makes it possible to derive the magnetic field strength at the location of the relic, without resorting to equipartition arguments. A magnetic field strength of 5–7 μG is found.

In **Chapter 9** multi-frequency and polarization observations of a new massive galaxy cluster ($z = 0.225$) are analyzed. The cluster hosts a large bright 1.9 Mpc radio relic, an elongated $\sim$ 2 Mpc radio halo, and two fainter relics. Part of the bright radio relic has a very peculiar linear morphology. For the bright relic, a clear spectral index gradient is observed, with spectral steepening in the direction towards the cluster center. The results from Rotation Measure (RM) Synthesis suggest that some of the observed Faraday rotation is caused by the ICM and is not due to galactic foregrounds. Color-color radio diagrams for the bright relic are constructed,

which allow for a detailed spectral analysis. This points towards (i) an injection spectral index of -0.6 to -0.7, (ii) increasing spectral index and curvature in the post-shock region, and (iii) an overall power-law spectrum between 74 MHz and 4.9 GHz with $\alpha = -1.10 \pm 0.02$. From the analysis, it is found that mixing of emission in the beam and spectral ageing are probably the dominant factors that determine the shape of the radio spectra. Changes in the magnetic field, total electron content, or adiabatic gains/losses do not seem to play a major role.

In **Chapter 10** simulations of binary cluster merger events are carried out. A method is developed to use these simulations in combination with the observations to derive cluster merger parameters. This method is applied to the double radio relics in the cluster CIZA J2242.8+5301 (see also **Chapter 8**). It is found that CIZA J2242.8+5301 is undergoing a merger in the plane of the sky (less then 10° from edge-on) with a mass ratio of about 2 : 1, and an impact parameter $\lesssim$ 400 kpc. The core passage of the clusters happened about 1 Gyr ago. From these simulations it is also concluded that the morphology of radio relics constrains the degree of clumping in the outskirts of the ICM. Determining the ICM clumping is important to properly measure the baryon fraction, density and entropy profiles, around the virial radius and beyond.

GMRT 325 MHz and WSRT 115–165 MHz radio continuum observations of Abell 2256 are presented in **Chapter 11**. Three new steep-spectrum ($\alpha \lesssim -1.5$) sources are revealed in the cluster, located about 1 Mpc from the cluster center. Two are located to the west of the cluster center, and one to the southeast. The extremely steep spectral index suggests these sources are most likely the result of adiabatic compression of fossil radio plasma due to merger shocks. We did not find any optical counterparts to the radio sources in the WHT images. The discovery of the steep spectrum sources implies the existence of a population of faint diffuse radio sources in (merging) clusters with such steep spectra that they have gone unnoticed in higher frequency ($\gtrsim$ 1 GHz) observations. Considering the timescales related to AGN activity, synchrotron losses, and the presence of shocks, we find that most massive clusters should possess similar sources.

LOFAR observations of Abell 2256 are discussed in **Chapter 12**. The observations were taken at 18 to 67 MHz with 25 stations. The longest baseline for these observations was about 80 km. The 63 MHz image clearly reveals the radio halo and relic. In addition, the presence of an ultra-steep spectrum source, earlier reported in deep GMRT and WSRT observations, is confirmed (see **Chapter 11**). Images made around 20 and 30 MHz also reveal the diffuse cluster emission, but they are affected by direction dependent ionospheric phase distortions. Removing these effects will be crucial to fully exploit the high-spatial resolution LOFAR offers at low frequencies.

1.5 Future prospects

During the last decade considerable progress has been made in our understanding of diffuse radio emission in galaxy clusters. In addition, new radio telescope are becoming operative (e.g., LOFAR, ASKAP, MWA) and older telescopes are being upgraded (VLA, WSRT, GMRT).

These new and upgraded facilities will greatly improve our knowledge about the non-thermal component in clusters. Extending the wavelength coverage towards much lower frequencies is a crucial aspect. In particular, the turbulent re-acceleration model predicts the existence of large population of ultra-steep spectrum radio halos that can only be uncovered through sensitive low-frequency observations (e.g., Cassano et al. 2010a). Also, it is expected that there should be many fossil radio sources, dying radio galaxies or AGN relics, that have such steep radio spectra

that they are missed by current higher frequency ($\gtrsim$ 100 MHz) observations.

Extending the wavelength coverage to frequencies $\gtrsim$ 5 GHz is also important. The high-frequency spectral shapes can be used to distinguish between various models for the origin of the synchrotron emitting electrons. Polarization measurements are another area where progress can be made. This will allow to study the magnetic field strength and topology in more detail (e.g., Govoni et al. 2006; Vacca et al. 2010; Pizzo et al. 2011; Bonafede et al. 2011).

Models for the formation of relics and halos can be tested through statistical studies of correlations between the non-thermal and thermal components of the ICM (Liang et al. 2000; Feretti et al. 2006; Cassano et al. 2006, 2007, 2008, 2010a). With large unbiased samples it is possible to study the redshift evolution of halos and relics. LOFAR will play a crucial role here because of its (i) good sensitivity, (ii) large field of view, and (iii) multi-beaming capability. At higher frequencies, the ASKAP and upgraded WSRT will complement the LOFAR surveys. Extremely deep observations of selected clusters, with LOFAR and the extended VLA, might also reveal new and unexpected phenomena.

Finally, combining the radio data with observations at other wavelengths is important, in particular with sensitive X-ray, gamma ray, and Sunyaev-Zel'dovich effect (Zeldovich & Sunyaev 1969) measurements. This will allow a much better understanding of shocks, particle acceleration mechanisms, magnetic fields, and the interplay between the non-thermal and thermal components of the ICM.

CHAPTER 2

A search for steep spectrum radio relics and halos with the GMRT

Abstract. Diffuse radio emission, in the form of radio halos and relics, traces regions in clusters with shocks or turbulence, probably produced by cluster mergers. The shocks and turbulence are important for the total energetics and detailed temperature distribution within the intracluster medium (ICM). Only a small fraction of clusters exhibit diffuse radio emission, whereas a large majority of well-studied clusters shows clear substructure in the ICM. Some models of diffuse radio emission in clusters indicate that virtually all clusters should contain diffuse radio sources with a steep spectrum. External accretion shocks associated with filamentary structures of galaxies could also accelerate electrons to relativistic energies and hence produce diffuse synchrotron emitting regions. The detection of radio emission from such filaments is important for our understanding of the origin of the Warm-Hot Intergalactic Medium (WHIM), and relativistic electrons and magnetic fields in the cosmic web. Here we report on Giant Metrewave Radio Telescope (GMRT) observations of a sample of steep spectrum sources from the 74 MHz VLSS survey. These sources are diffuse on scales $\gtrsim$ 15″, and not clearly associated with nearby ($z \lesssim 0.1$) galaxies. The main aim of the observations is to search for diffuse radio emission associated with galaxy clusters or the cosmic web. We have carried out GMRT 610 MHz continuum observations of unidentified diffuse steep spectrum sources. We have constructed a sample of diffuse steep spectrum sources, selected from the 74 MHz VLSS survey. We identified eight diffuse radio sources probably all located in clusters. We found five radio relics, one cluster with a giant radio halo and a radio relic, and one radio mini-halo. The giant radio halo has the highest radio power ($P_{1.4}$) known to date. By complementing our observations with measurements from the literature we find correlations between the physical size of relics and the spectral index, in the sense that smaller relics have steeper spectra. Furthermore, larger relics are mostly located in the outskirts of clusters while smaller relics are located closer to the cluster center.

R. J. van Weeren, H. J. A. Röttgering, M. Brüggen, and A. Cohen
Astronomy & Astrophysics, **508**, 75, 2009

2.1 Introduction

Studies of large-scale structure (LSS) formation have made significant advances during the last decade. It has been found that nearly all massive clusters have undergone at least several mergers in their history and that presently clusters are still in the process of accreting matter. A significant fraction of the accreting mass is in the form of (smaller) clusters and galaxy groups. Cluster mergers are the most energetic events in the present day Universe, with kinetic energies of the order of $10^{63} - 10^{64}$ erg, which are dissipated in giant shock waves and turbulence. An important aspect is the total energy budget and the detailed temperature distribution within the ICM, both of them are affected by the merger history of a cluster (e.g., Dolag et al. 2008).

Diffuse steep spectrum radio emission is observed in about 50 massive merging and post-merging galaxy clusters (see the review by Ferrari et al. 2008, and references therein). This diffuse emission is difficult to detect due to its low surface brightness and steep spectral index[1], so the fraction of clusters hosting diffuse radio emission is probably larger than we currently know. The diffuse emission in clusters is commonly divided into three main classes (Feretti & Giovannini 1996). *Radio Halos* are extended ($\gtrsim$ 1 Mpc) diffuse unpolarized ($\lesssim$ 5%) sources, located in the center of clusters. They have a regular smooth appearance, and follow the thermal X-ray emission. *Radio Relics* are elongated structures with an irregular morphology, mostly located in the periphery of clusters. Relics can be highly polarized (10 – 50%). Several different subclasses have been identified (Kempner et al. 2004). Most known radio relics and halos are found in clusters which show signs of a current or recent merger. This supports the scenario in which the relativistic electrons are accelerated by merger-induced shocks or turbulence. However, *Radio Mini-halos* are not associated with merging clusters. They are found in the centers of cool core clusters (e.g., Fabian et al. 1991; Peterson & Fabian 2006) and are associated with the central cluster galaxy and typically have sizes $\lesssim$ 500 kpc, with the diffuse emission surrounding the central cluster galaxy (e.g., Govoni et al. 2009).

Two different mechanisms for in-situ acceleration of particles have been proposed to explain relics in clusters: (i) adiabatic compression of fossil radio plasma by a passing shock wave producing a so called radio "phoenix" (Enßlin & Gopal-Krishna 2001; Enßlin & Brüggen 2002), or (ii) diffusive shock acceleration (DSA) by the Fermi-I process (e.g., Drury 1983; Blandford & Eichler 1987; Jones & Ellison 1991; Ensslin et al. 1998; Malkov & O'C Drury 2001). In the first scenario, radio relics should have toroidal and complex filamentary morphologies. These relics are capable of producing very steep, curved radio spectra due to inverse Compton (IC) and synchrotron losses. In the DSA scenario the electrons are accelerated by multiple crossings of the shock front (in a first order Fermi process). These relics have large sizes (Mpc) and are direct tracers of shock fronts in clusters. The spectral index is determined by the balance between the continuous acceleration at the shock front and energy losses in the post-shock region.

The diffuse emission within clusters reveals the presence of relativistic electrons and magnetic fields on scales $\sim$ 1 Mpc. Spectral aging, due to synchrotron and IC losses of the emitting electrons may explain the steep spectra. If the electrons are injected via Fermi acceleration (DSA), their energy follows a power-law distribution. The power-law index of the injected electrons is related to the Mach number of the shocks (e.g., Hoeft & Brüggen 2007): shocks with a low Mach number have steeper radio spectra. Clearly, low-frequency surveys are needed to locate and study these sources (Cassano et al. 2006, 2007, 2008). Interestingly, Brunetti et al. (2008) discovered a radio halo in the cluster Abell 521, which was previously known to host a

[1] $F_\nu \propto \nu^\alpha$, with α the spectral index

radio relic, with a spectral index of ~ -2.1, suggesting the existence of a population of diffuse source in clusters with spectral indices < -1.5.

Numerical simulations show the development of various types of shocks during structure formation (Miniati et al. 2000). These shocks differ in their location with respect to the cluster center and Mach numbers (Miniati et al. 2000; Miniati 2002; Ryu et al. 2003; Pfrommer et al. 2006; Vazza et al. 2009). External accretion shocks have $\mathcal{M} \gg 1$ and process the low-density, unshocked intergalactic medium (IGM). This results in relatively flat spectral indices of about -0.5 at the location of the shock front. Further away from the shock front the spectral index steepens due to synchrotron and IC losses. Internal shocks, (i.e., merger and flow shocks) occur within the cluster. The Mach numbers of these shocks are lower resulting in steeper spectral indices. Binary merger shocks are the result of a cluster merging with a another cluster or a large sub-structure. In this case a double radio relic is expected (e.g., Roettiger et al. 1999a; Hoeft et al. 2008; van Weeren et al. 2009b).

As pointed out by Cen & Ostriker (1999), hydrodynamic models indicate that up to half of the baryons at present time should have temperatures in the range of $10^5 - 10^7$ K. Unfortunately, studying the abundance and distribution of this WHIM is very challenging, since its main tracers are highly excited Oxygen lines which are difficult to observe (e.g., Nicastro et al. 2005). A fraction of the accretion shocks will be supersonic and can accelerate energetic electrons up to energies of $10^{18} - 10^{19}$ eV (e.g., Norman et al. 1995; Kang et al. 1996; Inoue et al. 2008). In the presence of magnetic fields, such electrons will emit faint diffuse synchrotron radiation. The detection of these radio filaments is very important as this would provide a probe of the WHIM. Recent magnetohydrodynamical modeling indicates that detecting radio emission from the filamentary cosmic web should be possible (e.g., Keshet et al. 2004; Hoeft & Brüggen 2007). Hoeft et al. (2008); Pfrommer (2008); Pfrommer et al. (2008) however find that in the outskirts of clusters (at a few times the virial radius) or filaments, external accretion shocks cause little radio emission, owing to the low density of both magnetic field energy and cosmic ray (CR) particles there (Miniati et al. 2001). They are therefore difficult to detect even with the sensitivity of upcoming radio telescopes such as LOFAR. Relic emission from internal accretion shocks occur in a higher density environment so that they should be detected with current radio facilities.

When searching for radio halos, relics and filaments in low-frequency radio surveys, various other steep spectrum sources are also present. These include ultra-steep (angular size $\lesssim 15''$) spectrum sources (USS, see Miley & De Breuck 2008, for a review) associated with high-z radio galaxies (HzRG), "fossil" or "dying" FR-I (Fanaroff & Riley 1974) radio sources, and "head-tail" sources, the last two having a steep spectrum due to spectral aging of the radio emission. In high-resolution ($\lesssim 5''$) observations, for example at 1.4 GHz with the Very Large Array (VLA), diffuse objects will be resolved out due to missing short baselines. This provides a method for selecting diffuse radio sources associated with galaxy clusters or the cosmic web. FR-I sources can be partly excluded by removing sources that are clearly associated with individual galaxies.

The 74 MHz VLA low-frequency Sky Survey (VLSS), Cohen et al. (2007), covers about 3π steradians of sky north of $\delta = -30°$. The resolution of the survey is $80''$ (FWHM) and the rms noise level is about 0.1 Jy beam^{-1}. The source catalog contains roughly 70, 000 sources with a point source detection limit of 0.7 Jy beam^{-1}. A new calibration algorithm (Cotton et al. 2004) was used to remove the ionospheric distortions, which can be severe at this low-frequency. The 1.4 GHz NRAO VLA Sky Survey (NVSS), Condon et al. (1998), covers the entire sky above $\delta = -40°$. The NVSS images have a rms noise of about 0.45 mJy beam^{-1}, and a resolution of $45''$(FWHM). The catalog contains about 2×10^6 sources above a flux of ~ 2.5 mJy.

In this paper we present radio continuum observations of 26 diffuse (angular size $\gtrsim 15''$) steep spectrum sources selected from the VLSS survey with the GMRT at 610 MHz. The main aim of this project is to determine the morphology of the sources and search for diffuse structures which could be associated with shock fronts or turbulence in clusters, and accretion shocks onto filaments of galaxies.

The layout of this paper is as follows. In Sect. 2.2 we discuss the sample selection, this is followed by an overview of the observations and data reduction in Sect. 2.3. In Sect. 2.4 we present the radio maps of the most interesting sources and discuss these sources individually. By combining our radio observations with data from the literature (X-ray and optical observations) we have tried to classify the sources. In Sect. 2.5, spectral indices are modeled using our flux measurements combined with literature values. We end with a discussion and conclusions in Sects. 2.6 and 2.7.

Throughout this paper we assume a ΛCDM cosmology with $H_0 = 71$ km s^{-1} Mpc^{-1}, $\Omega_m = 0.3$, and $\Omega_\Lambda = 0.7$.

2.2 Sample selection

Spectral indices (between 1400 and 74 MHz) were calculated for all sources in the VLSS survey. We selected sources with $\alpha \leq -1.35$ which resulted in a total of 176 sources. This cutoff is somewhat arbitrary, but a significant lower cutoff resulted in a very small number of sources selected while a higher cutoff would select too many sources for follow-up observations. VLA B-array 1.4 GHz $\sim$ 5 min snapshot observations were carried out on March 25–29 and May 10, 2005 of a subsample of 68 from the 176 sources. Two intermediate frequencies (IFs) with a bandwidth of 50 MHz each were used, centered at 1385 and 1465 MHz. From this 68 sources, 36 were found to be resolved out. This showed that these sources had extended emission on scales $\gtrsim 15''$. From the 36 sources 13 were identified with known nearby galaxies. The remaining 23 sources were included in the sample. We have also searched for additional sources with $\alpha \leq -1.15$, by making use of the 1.4 GHz FIRST survey ($5''$ FWHM, Becker et al. 1995). Sources with a FIRST flux at least 8 times lower than the 1.4 GHz NVSS flux were initially selected and visually inspected to remove obvious double lobe sources. The spectral index cutoff of -1.15 was chosen because higher values resulted in too many double lobes to be selected for visual inspection. Furthermore, most known radio halos and relics have spectral indices steeper than this value. The amount of flux resolved out in the selection criterium was a tradeoff as lower values also resulted in too many sources to be selected for visual inspection. After visual inspection we found three additional sources which showed the presence of diffuse emission. None of these sources were clearly associated with nearby individual galaxies in the POSS-II or SDSS surveys (Abazajian et al. 2009). The final list of sources and their coordinates are given in Table 2.1.

2.3 Observations & data reduction

High-sensitivity radio observations at 610 MHz were carried out with the GMRT in February and November 2008 of a sample of 26 diffuse steep spectrum radio sources. We divided a total 102 hours of observation time evenly between the 26 sources. A total of 32 MHz bandwidth was recorded, using both the upper (USB) and lower sidebands (LSB) which included both RR and

LL polarizations. The data were collected in spectral line mode with 128 channels per sideband (IF), resulting in a spectral resolution of 125 kHz per channel. To increase UV-coverage we cycled between various sources, typically spending 40 min on a sources before moving to the next source. However, due to scheduling constraints it was only possible to do this for about half of our sources. The observations resulted in a net on-source time of $\sim$ 3 hours, after flagging certain time-ranges which were affected by radio frequency interference (RFI) or had other problems.

The data were reduced and analyzed with the NRAO Astronomical Image Processing System (AIPS) package. Bandpass calibration was carried out using the standard flux calibrators: 3C48, 3C147, and 3C286. Fluxes of 29.43 Jy (3C48), 38.26 Jy (3C147), and 21.07 Jy (3C286) at 610 MHz were assigned to these sources using the Perley & Taylor (1999) extension to the Baars et al. (1977) scale. A set of 6 channels free of RFI was taken to normalize the bandpass (channel 15 – 20) for each antenna. Strong RFI was removed automatically (with the AIPS task 'FLGIT'). The data was then visually inspected for remaining low-level RFI using the AIPS tasks 'SPFLG' and 'TVFLG'. After that an initial phase and amplitude calibration was carried out using the bandpass and secondary calibrators, where we also transferred the flux densities from the primary calibrators to the secondary calibrators. The found solutions were then transferred to the target sources. We have not chosen to average any channels in order to minimize the effects of bandwidth smearing and to aid further removal of RFI. The first and last few channels of the data were discarded as they were noisy.

For making images we used the polyhedron method (Perley 1989; Cornwell & Perley 1992) to minimize the effects of non-coplanar baselines. Both USB and LSB were simultaneously gridded, imaged and cleaned. We used a total of 199 facets to cover $\sim$ 2 times the full primary beam. This made the removal of sidelobes from strong sources far away from the field center possible. After a first round of imaging, in some cases "ripples" were seen in the maps which were subsequently removed after identifying the corresponding baseline(s). Several rounds of phase self-calibration were carried out before doing a final amplitude and phase selfcalibration. Images were made using robust weighting (robust = 0.5, Briggs 1995) and corrected for the primary beam attenuation. Images were cleaned to 3 times the rms noise level to minimize clean bias effects.

The thermal noise in each map is expected[2] to be

$$\sigma_{\rm thermal} = \frac{\sqrt{2}T_s}{G\sqrt{n(n-1)N_{IF}\Delta\nu t_{\rm int}}}\,, \tag{2.1}$$

with $T_s = 92$ K the system temperature, $G = 0.32$ K Jy^{-1} the antenna gain, $n \approx 28$ the number of working antennas, $N_{IF} = 2$ the number of sidebands used (both recording RR and LL polarizations), $\Delta\nu = 13.5$ MHz the bandwidth per sideband, and $t_{\rm int}$ the net integration time. The expected thermal noise for 3 hrs integration time is about 32 μJy beam^{-1}, where we have taken into account that typically 20% of the data is flagged due to RFI. The noise levels in our maps range from 40 to 202 μJy beam^{-1}. The noise levels dependent on the UV-coverage and the presence of strong confusing sources in the field of view limiting the dynamic range. The lowest noise level of 40 μJy beam^{-1} is quite close to the thermal noise level. The uncertainty in the calibration of the absolute flux-scale is between 5 – 10%, see Chandra et al. (2004).

[2] http://www.gmrt.ncra.tifr.res.in/gmrt_hpage/Users/doc/manual/UsersManual/node13.html

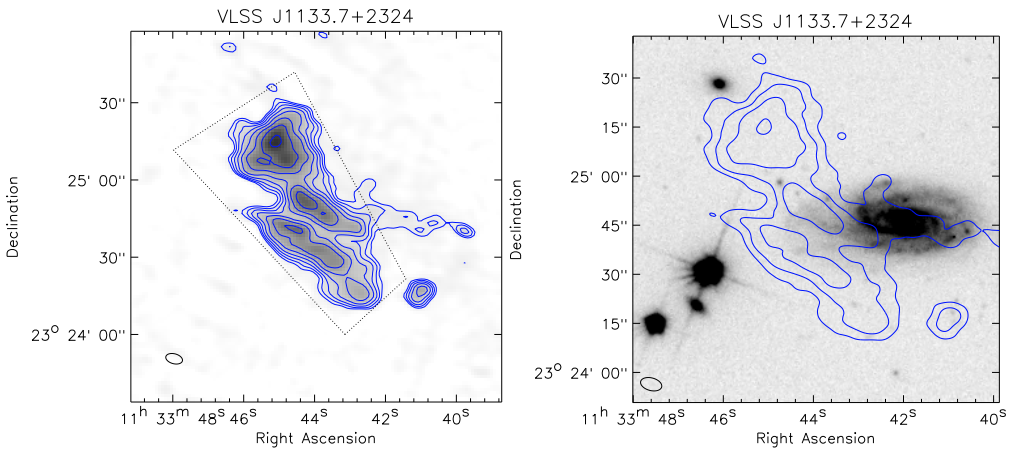

Figure 2.1: Left: GMRT 610 MHz radio map. The Gaussian beam size is shown at the bottom left corner. Contour levels are drawn at $\sqrt{[1,2,4,6,8,16,32,...]} \times 4\sigma_{\rm rms}$, see Table 2.1. The dotted lines indicate the region where the 610 MHz flux (S_{610}), reported in Table 2.1, has been extracted. Right: SDSS r band image overlaid with GMRT 610 MHz contours. Contour levels are drawn at $\sqrt{[1,8,32,128,512,...]} \times 4\sigma_{\rm rms}$.

2.4 Results

All sources, except VLSS J2229.1−0136, were detected in the GMRT images. The NVSS counterpart of VLSS J2229.1−0136 has a position offset of about 40″, the flux density in the NVSS and VLSS surveys of these sources is also close to the detection threshold. We therefore conclude that VLSS J2229.1−0136 is most likely a noise peak as the GMRT observations should have easily detected the source. From here on we have left out VLSS J2229.1−0136 in the further discussions. A summary of the beam parameters and noise levels for the maps is given in Table 2.1. To identify optical counterparts overlays were made using SDSS and POSS-II images. Spectroscopic redshifts were included from the literature. For sources without a spectroscopic redshift, but having SDSS DR7 coverage we took the SDSS photometric redshift. For other sources we used that *K* and *R* magnitudes of massive elliptical galaxies correlate with redshift (*K*-*z* and *R*-*z* relations, e.g., Willott et al. 2003; de Vries et al. 2007).

We have also checked for any X-ray counterparts to the radio sources. In the next subsection we describe the most interesting sources that appear to be related to shocks or turbulence in clusters or filaments. The other sources are discussed in Appendix 2.8.

2.4.1 Individual sources

2.4.1.1 VLSS J1133.7+2324

The radio emission shows two parallel filamentary structures and a northern patch of diffuse emission connected with the western filamentary component. Some faint radio emission is extending towards the west. This extension coincides with the galaxy UGC 6544 (MCG+04-27-065; PGC 35694) located a z=0.02385 (Haynes et al. 1997). This galaxy was classified as a Sbc

Table 2.1: Source properties and results

Source Name	RA (J2000)	DEC (J2000)	Beam size arcsec	$\sigma_{\rm rms}$ μJy	$S_{610}^{j,k}$ mJy	$\alpha_{74\rm MHz}^{1400\rm MHz}$	LAS[h] arcsec	Redshift z
VLSS J0004.9−3457	00 04 53.63	−34 56 34.1	11.4 × 6.6	73	158 ± 16	−1.40 ± 0.04	116	0.29 ± 0.08[a]
VLSS J0227.4−1642	02 27 26.74	−16 42 47.2	5.3 × 4.0	94	37.0 ± 6.2	−1.50 ± 0.06	89	$\gtrsim$ 0.7
VLSS J0250.5−1247	02 50 30.83	−12 47 30.3	9.4 × 3.7	118	33.2 ± 3.3	−1.94 ± 0.07	21	$\gtrsim$ 0.7
VLSS J0511.6+0254	05 11 37.79	+02 54 19.4	8.7 × 6.1	139	98.0 ± 10.3	−1.42 ± 0.05	45	0.20 ± 0.05[a]
VLSS J0516.2+0103	05 16 17.89	+01 03 40.1	8.1 × 6.5	79	17.4 ± 4.4	−1.73 ± 0.06	35	$\gtrsim$ 0.7
VLSS J0646.8−0722	06 46 52.10	−07 22 37.9	5.7 × 4.8	63	120 ± 13	−1.70 ± 0.05	59	0.23 ± 0.06[a]
VLSS J0717.5+3745[i]	07 17 30.92	+37 45 29.7	8.2 × 6.0	78	501 ± 50	−1.15 ± 0.04	171	0.5548[f]
VLSS J0915.7+2511[i]	09 15 41.51	+25 11 48.2	8.6 ×5.9	134	194 ± 21	−1.52 ± 0.04	63	0.324[c]
VLSS J1117.1+7003	11 17 06.46	+70 03 57.1	7.8 × 4.3	52	9.1 ± 0.9	−1.87 ± 0.07	18	$\gtrsim$ 0.7
VLSS J1133.7+2324	11 33 44.73	+23 24 50.6	6.6 × 3.9	51	80.6 ± 10.1	−1.69 ± 0.06	84	0.61 ± 0.16[d]
VLSS J1431.8+1331	14 31 49.90	+13 31 54.1	5.3 × 4.8	51	120 ± 13	−2.03 ± 0.05	101	0.159936[c]
VLSS J1515.1+0424[i]	15 15 09.18	+04 24 41.1	7.6 × 5.4	79	192 ± 33	−1.50 ± 0.05	169	0.0972[g]
VLSS J1636.5+3326	16 36 34.93	+33 26 33.9	5.2 × 4.7	40	16.1 ± 1.9	−1.84 ± 0.14	28	0.65 ± 0.19[d]
VLSS J1710.5+6844	17 10 35.03	+68 44 58.4	8.9 × 4.7	63	23.3 ± 2.8	−1.75 ± 0.06	45	0.28 ± 0.08[a]
VLSS J1930.4+1048	19 30 27.19	+10 48 02.5	5.3 × 4.8	56	67.4 ± 7.0	−1.90 ± 0.06	101	...
VLSS J2043.9−1118	20 43 58.46	−11 18 45.6	5.8 × 4.2	77	53.9 ± 6.3	−1.74 ± 0.05	41	0.43 ± 0.15[b]
VLSS J2044.7+0447	20 44 43.64	+04 47 24.5	10.5 × 7.5	202	57.7 ± 5.8	−1.55 ± 0.06	71	0.46 ± 0.15[b]
VLSS J2122.9+0012	21 22 54.14	+00 12 03.4	5.8 × 3.8	81	24.0 ± 2.4	−2.00 ± 0.08	12	$\gtrsim$ 1.4
VLSS J2209.5+1546	22 09 32.91	+15 46 29.9	6.9 × 6.2	64	36.4 ± 3.8	−1.56 ± 0.07	61	$\gtrsim$ 0.7
VLSS J2213.2+3411	22 13 12.45	+34 11 51.6	5.5 × 4.6	94	127 ± 13	−1.55 ± 0.04	62	1.6 ± 0.5[a,e]
VLSS J2217.5+5943	22 17 30.39	+59 43 05.3	6.3 × 4.3	47	79.9 ± 8.0	−2.20 ± 0.06	99	...
VLSS J2229.1−0136	22 29 11.95	−01 36 58.8	8.6 × 4.2	101	...	...	...	...
VLSS J2241.3−1626	22 41 22.57	−16 25 35.7	6.1 × 5.8	129	69.7 ± 7.3	−1.44 ± 0.06	47	$\gtrsim$ 0.7
VLSS J2341.1+1231	23 41 06.91	+12 31 36.9	5.5 × 4.4	50	117 ± 14	−1.70 ± 0.04	115	0.62 ± 0.15[b]
VLSS J2345.2+2157	23 45 15.47	+21 57 55.1	4.8 × 4.2	63	79.3 ± 8.4	−2.14 ± 0.05	70	0.23 ± 0.06[a]
VLSS J2357.0+0441	23 57 05.54	+04 41 14.7	7.8 × 4.9	82	...	...	...	...

[a] redshift estimated using the fitted Hubble-K relation from Willott et al. (2003)
[b] redshift estimated using the fitted Hubble-R relation from de Vries et al. (2007)
[c] spectroscopic redshift from SDSS DR7
[d] median photometric redshift from SDSS DR7
[e] using the K_s band magnitude from De Breuck et al. (2002b)
[f] Edge et al. (2003)
[g] Struble & Rood (1999)
[h] LAS = largest angular size
[i] resolved out in the 1.4 GHz FIRST survey
[j] fluxes are extracted from the regions indicated in the figures by dotted lines.
[k] for the compact sources (LAS < 45″) the fluxes were measured by fitting single Gaussians to the sources after convolving the maps to the 45″NVSS resolution

spiral by Nilson (1973) and Paturel et al. (2003). The source is also listed in the IRAS Faint Source Catalog (F11311+2341) and detected at 60 and 100 μm (Moshir & et al. 1990). The galaxy has been included in 21 cm hydrogen emission line surveys. Springob et al. (2005) give a self-absorption corrected line flux of 2.97 ± 0.32 Jy km s^{-1} and a line-width of 372 ± 3 km s^{-1}.The galaxy also has a small UV-excess (Miyauchi-Isobe & Maehara 2002).

Using the IRAS fluxes we can estimate the star forming rate (SFR) in this galaxy (Solomon et al. 1997) by calculating the Far Infrared Luminosity ($L_{\rm FIR}$)

$$L_{\rm FIR} = 3.94 \times 10^5 (2.58 S_{60\mu\rm m} + S_{100\mu\rm m}) r(S_{60\mu\rm m}/S_{100\mu\rm m}) D_L^2 \,, \tag{2.2}$$

with $L_{\rm FIR}$ in $L_\odot$, the flux S in Jy, D_L the luminosity distance in Mpc, and $r(S_{60}/S_{100})$ a color correction factor (Lonsdale & Helou 1985) which is of the order of one. This gives a SFR of $\sim 3 M_\odot {\rm yr}^{-1}$, using SFR ($M_\odot {\rm yr}^{-1}$) = $L_{\rm FIR}/(5.8 \times 10^9 L_\odot)$, Kennicutt (1998). The radio flux of the galaxy is difficult to measure as part of the radio emission from the galaxy overlaps with the emission from the filamentary source. For the part which does not overlap with the steep spectrum source we measure a flux of about 6 mJy. We adopt a total flux for the galaxy of 10 mJy, assuming we missed about 40% of the previously reported flux. The luminosity at 1.49 GHz ($L_{1.49\,\rm GHz}$) is $L = 4\pi D_L^2 S_\nu (1+z)^{-\alpha-1}$, with S_ν the observed flux at the rest frequency, and $\alpha \sim -0.5$. This results in $L_{1.49\,\rm GHz} = 8.2 \times 10^{21}$ W Hz^{-1}. Using the FIR radio correlation (Condon et al. 1991) we find a luminosity of $\sim 10^{22}$ W Hz^{-1}, in good agreement.

The galaxy is unlikely to be associated with the filamentary radio structure to the east, given the above calculation, the steep spectral index, morphology, and spatial offset. In the background (partly behind the spiral galaxy) there is an overdensity of faint red galaxies. These have a median photometric redshift of about 0.6 (SDSS DR7) and follow roughly the filamentary radio source. This is probably a cluster or a galaxy filament, with the foreground galaxy hiding part of the cluster/filament. Based on the morphology, the radio source is then classified as a relic. If the steep spectrum radio source is located at a distance of $z = 0.6$, the LAS of 84″corresponds to a physical size of of 660 kpc.

2.4.1.2 VLSS J1431.8+1331

The radio emission shows two distinct components, the brightest one located to the east. This source has an optical counterpart, the cD galaxy of the cluster MaxBCG J217.95869+13.53470 (Koester et al. 2007). The cluster is also detected in X-rays by ROSAT (Voges et al. 1999, 2000) as source 1RXS J143150.6+133256. A SDSS DR7 spectrum puts the cD galaxy at a distance of $z = 0.160$. Three other sources in the cluster have a measured redshifts of 0.15962, 0.159153, and 0.164794. At this redshift the radio emission corresponds to a physical size of 170 kpc for the eastern and 125 kpc for the western component. The eastern component is an irregular curved structure with several bright knots. One of these corresponds with the nucleus of the cD galaxy. The morphology suggests that we are either seeing the interaction of radio plasma from the central AGN with the surrounding ICM or a small central radio source with a bright relic tracing a shock front (seen in projection).

The western fainter component does not seem to be associated with any galaxy. The source could either be remnant radio emission from a previous AGN episode or the signature of a shock wave. In the former case, the spectral index should be steeper then eastern component because of spectral aging.

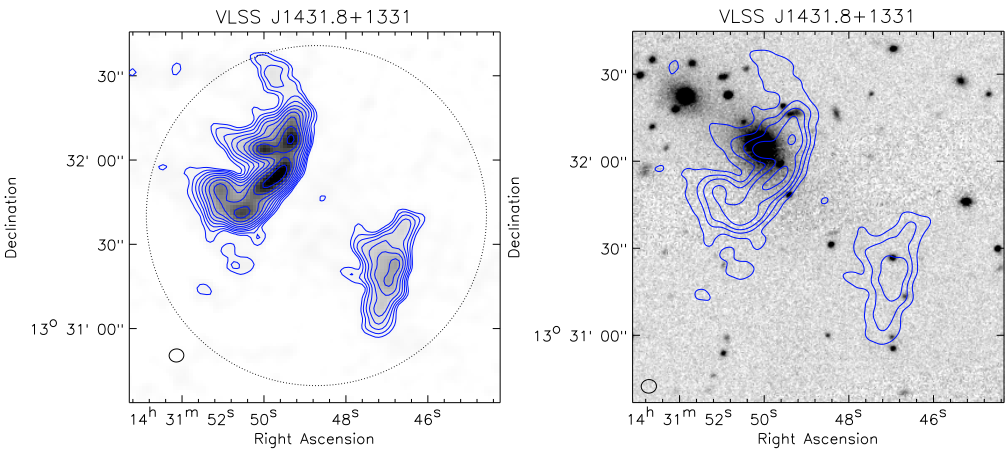

Figure 2.2: Left: GMRT 610 MHz radio map. Contour levels are drawn as in Fig. 2.1 (left panel). Right: SDSS r band image overlaid with GMRT 610 MHz contours. Contour levels are drawn as in Fig. 2.1 (right panel).

2.4.1.3 VLSS J2217.5+5943, 24P73

This source was found to have an ultra-steep spectrum ($\alpha = -2.58 \pm 0.14$) by the Synthesis Telescope of the Dominion Radio Observatory (DRAO) Galactic plane survey at 408 MHz and 1.42 GHz (Higgs 1989; Joncas & Higgs 1990). Since this source was located in the galactic plane, Joncas & Higgs (1990) suggested the sources might be a pulsar. However, they noted that the source seemed to be slightly extended at 408 MHz. At 1.42 GHz the source was resolved into two distinct components. Both of these components were also listed as a single source 25P23. The source was also detected in the 38 MHz 8C survey (Rees 1990; Hales et al. 1995). Subsequent L-band (1.4 GHz) and X-band (8.4 GHz) observations with the VLA by Green & Joncas (1994), separated the source clearly into two components. A compact northern component and a southern diffuse component. The X-band observations only detected the northern component. By comparing the fluxes of the VLA and DRAO observations they concluded that the southern diffuse component had an ultra-steep spectrum and provided the bulk of the emission at low frequencies. Since the source was resolved this ruled out a pulsar identification. In fact it was suggested that this source might be a radio halo or relic located in a galaxy cluster behind the galactic plane.

GMRT observations of 24P73 show a complex filamentary source. The source has some similarities with the relic sources in Abell 85 and Abell 133 (Slee et al. 2001). POSS-II and 2MASS images covering the area do not show the presence of any cluster. However this is not unexpected given the extinction of $A_B = 6.7$ (Schlegel et al. 1998). Given the steep spectral index and morphology we conclude that the sources is a radio relic. Deep NIR imaging will be necessary to identify the galaxy cluster associated with the relic.

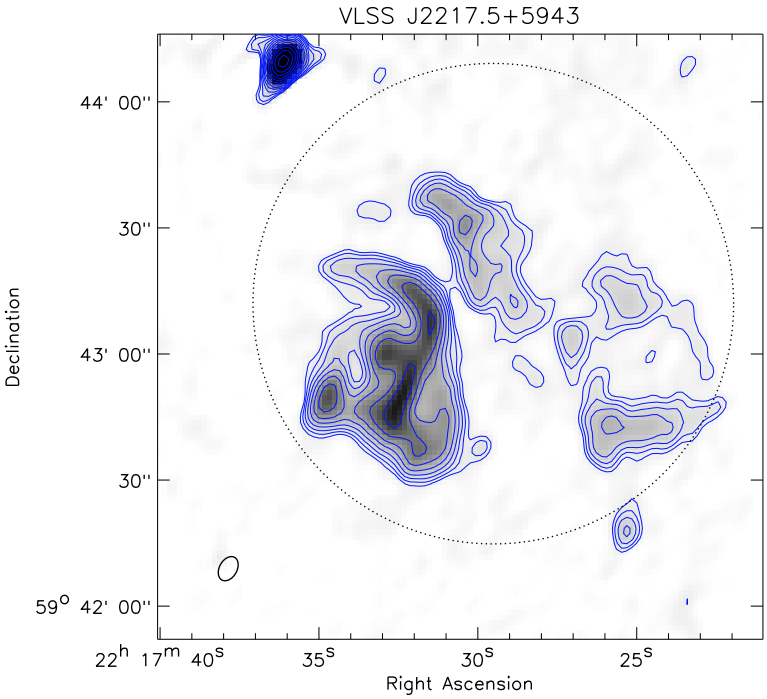

Figure 2.3: GMRT 610 MHz radio map. Contour levels are drawn as in Fig. 2.1 (left panel).

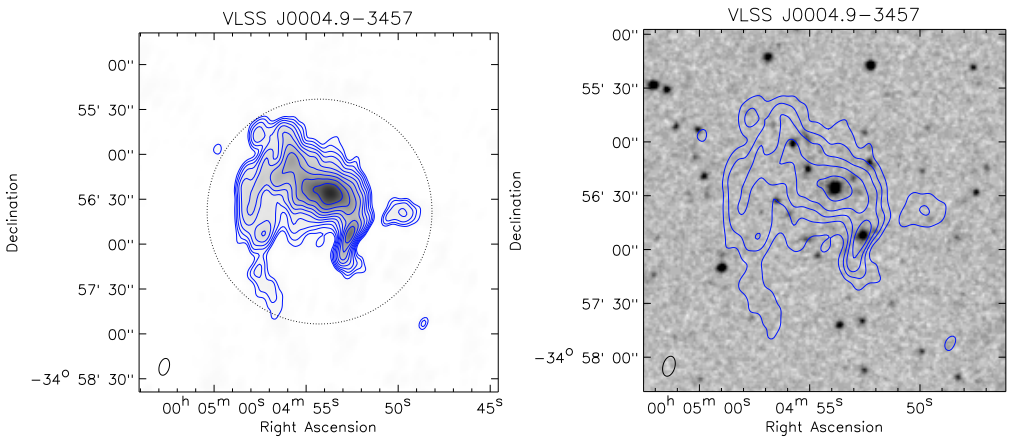

Figure 2.4: Left: GMRT 610 MHz radio map. Contour levels are drawn as in Fig. 2.1 (left panel). Right: POSS-II red image overlaid with GMRT 610 MHz contours. Contour levels are drawn as in Fig. 2.1 (right panel).

2.4.1.4 VLSS J0004.9−3457

The central component of the radio source is associated with a K=14.86 mag elliptical galaxy. An overdensity of galaxies indicates the presence of a cluster, candidate B02291 (Zanichelli et al. 2001) from radio-optically selected clusters of galaxies. We estimate a redshift for the cluster of 0.29 ± 0.08 (using the K-band magnitude and the K-z relation). The cluster may be linked to a larger cluster about 3′ towards the southwest at a redshift of 0.33 ± 0.09. The X-ray source 2E 0002.2-3515 (Harris et al. 1996) is probably associated with this cluster of galaxies visible in POSS-II images. The diffuse radio emission surrounding the central elliptical galaxy resembles a mini-halo. No X-ray emission from the ICM of the cluster is detected in the ROSAT All Sky Survey. This implies that the cluster is not very massive. The object is similar to the mini-halo in the cluster MRC 0116+111 located at $z = 0.131$ (Gopal-Krishna et al. 2002; Bagchi et al. 2009), which was also not detected in the ROSAT All Sky Survey. The size of the mini-halo is about 200 kpc, similar to other mini-halos (e.g., Govoni et al. 2009). The radio image shows a bright knot at RA $00^{\rm h}\ 04^{\rm m}\ 52.5^{\rm s}$ DEC $-34^\circ\ 56'\ 55''$, to the south of the main component. This knot has an optical counterpart. To the east an arc-like structure extends from the central component and bends towards the south. The arc is not associated with an optical counterpart. The origin of the arc is unclear, it could be part of a disturbed FR-I source, or a relic-like structure of fossil radio plasma.

2.4.1.5 VLSS J0717.5+3745, MACS J0717.5+3745

The radio source is associated with the massive X-ray luminous cluster MACS J0717.5+3745 at z=0.5548, with an overall ICM temperature of 11.6 keV (Ebeling et al. 2001; Edge et al. 2003; Ebeling et al. 2007). The cluster shows a pronounced substructure in optical images. Ebeling et al. (2004) reported the discovery of a large-scale filamentary structure of galaxies connected to the cluster. NVSS, WENSS and VLSS images reveal the presence of a steep-spectrum radio source ($\alpha = -1.15$). The radio source was classified as a radio relic by Edge et al. (2003). Ma et al. (2009) presented X-ray (Chandra) and optical observations (Hubble Space Telescope, ACS; Keck-II, DEIMOS) of the cluster. They found the cluster to be an active triple merger. Temperatures in the cluster exceeding 20 keV were found in some regions. Regions with a lower temperature of ~ 5 keV were found at the position of two subclusters, probably remnants of cool cores.

Here we shortly describe our results for this cluster, a more detailed analysis in combination with additional archival VLA observations has been presented in a separate paper (van Weeren et al. 2009d), see also Bonafede et al. (2009a). Our radio maps reveal a complex source, consisting of different components. The main component is a twisted structure, with enhanced regions of radio emission in the north and southwest of the cluster. These regions are connected by two bridges of emission to a bright central elongated source. The structure has a linear size of 700 kpc. No obvious counterparts are visible for both the north and south-west components. The presence of the two radio bridges suggest a relation with the central component. Although, no obvious counterpart was found for the central component by Edge et al. (2003), we identify an elliptical galaxy at RA $07^{\rm h}\ 17^{\rm m}\ 35^{\rm s}.5$, DEC $+37^\circ\ 45'\ 05''.5$ as a possible counterpart. If this is indeed the case then the source could be a wide-angle tail (WAT) source with the two bridges being the tails of the central source and the north and south-west components the hotspots. The eastern boundary of the structure is sharp, while on the other side some faint emission is seen extending further westwards. Diffuse radio emission is also seen to the south of the main structure.

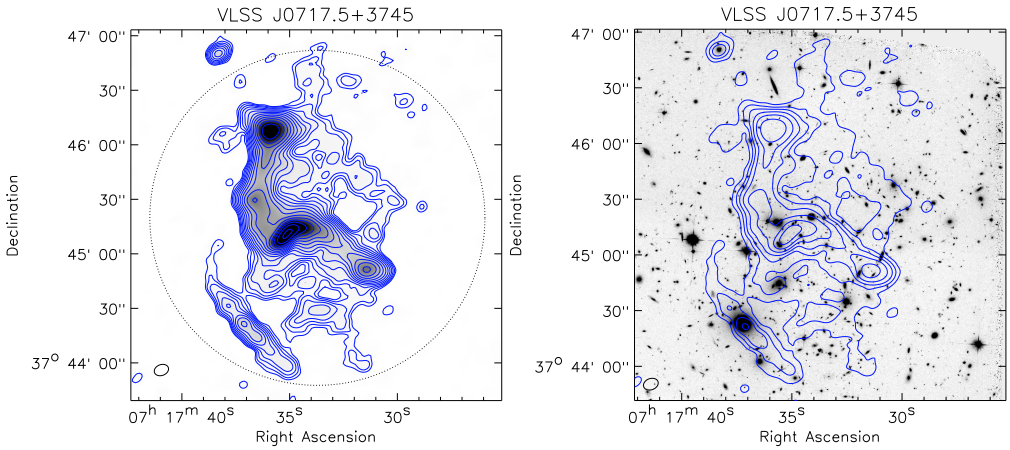

Figure 2.5: Left: GMRT 610 MHz radio map. Contour levels are drawn as in Fig. 2.1 (left panel). Right: HST F814W ACS image overlaid with GMRT 610 MHz contours. Contour levels are drawn as in Fig. 2.1 (right panel).

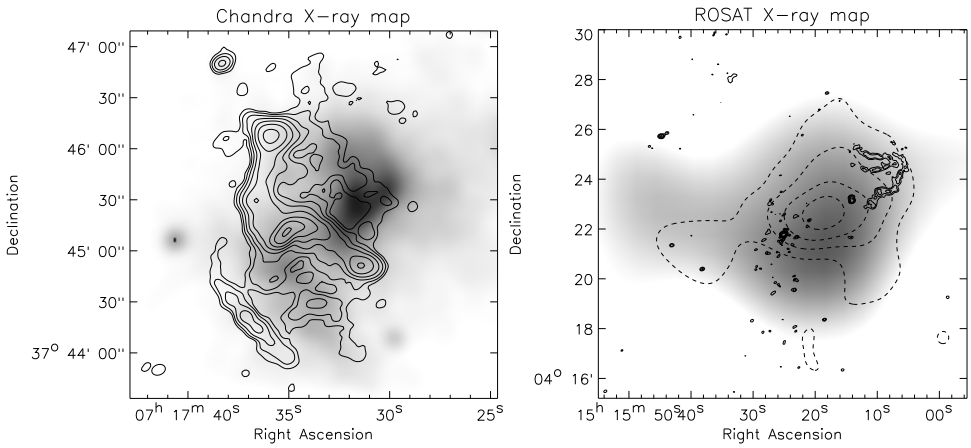

Figure 2.6: Left: Chandra X-ray map overlaid with radio contours at 610 MHz from the GMRT. The color scale represents the X-ray emission from 0.5 − 7.0 keV. The image has been adaptively smoothed using the TARA[a] package using a minimal significance of 5. Contour levels are drawn at $[1, 2, 4, 8, 16, 32, ...] \times 0.312$ mJy beam^{-1}. Right: X-ray emission from ROSAT in the 0.1 − 2.0 keV energy band. The image has been convolved with a circular Gaussian of 225″. The solid contours represent the radio emission at 610 MHz from the GMRT. The radio contours are drawn at $[1, 2, 4, 8, 16, 32, ...] \times 7\sigma_{\rm rms}$. Dashed contours show the galaxy distribution from SDSS DR7. Only galaxies with a photometric redshift between $0.06 + z_{\rm err} < z < 0.15 - z_{\rm err}$ were selected from the catalogs, with $z_{\rm err}$ the error in the photometric redshift and $z = 0.0972$ The galaxy isodensity contours are drawn at $[6, 9, 12, 15, ...]$ galaxies arcmin^{-2}.
[a] http://www.astro.psu.edu/xray/docs/TARA

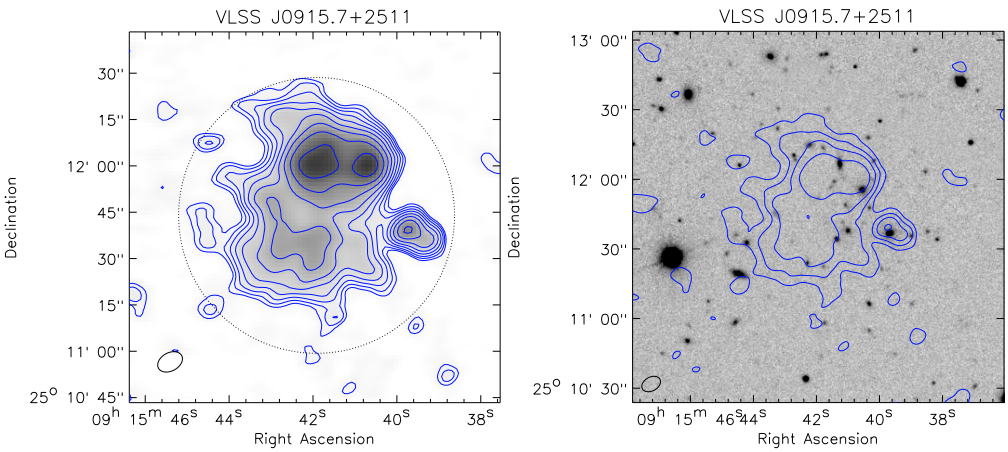

Figure 2.7: Left: GMRT 610 MHz radio map. Contour levels are drawn as in Fig. 2.1 (left panel). Right: SDSS r band image overlaid with GMRT 610 MHz contours. Contour levels are drawn as in Fig. 2.1 (right panel).

The diffuse emission within the cluster has a total size of about 1.2 Mpc and given that it roughly follows the X-ray emission we classify it as a radio halo. Clearly, the emission is not associated with individual sources. Using a spectral index of −1.2, typical for radio halos, we estimate the radio power ($P_{1.4}$) to be 5×10^{25} W Hz^{-1}. This makes it the most powerful radio known to date, in agreement with the X-ray luminosity-radio power ($L_X - P_{1.4}$) and temperature-radio power ($T - P_{1.4}$) correlations (Liang et al. 2000; Enßlin & Röttgering 2002; Cassano et al. 2006).

Towards the south a fainter linear structure is seen. A compact core, located halfway the linear structure is associated with a bright elliptical foreground galaxy (RA $07^h\ 17^m\ 37^s.2$, DEC +37° 44′ 23″). The source is probably a FR-I source associated with the compact core.

Interestingly, the main twisted radio structure is located in between the brightest X-ray emission of the cluster. The main cool core visible in the X-ray image has no radio emission associated with it. The central radio structure also coincides with regions having a significantly higher X-ray temperature $\gtrsim$ 15 keV. The ICM temperature and X-ray morphology of the cluster favor of a relic-like interpretation. We therefore conclude that the twisted radio structure is a giant relic tracing a shock front linked to the merger activity of the system.

2.4.1.6 VLSS J0915.7+2511

The radio map shows a diffuse region of emission associated with a cluster of galaxies (MaxBCG J138.91895+25.19876) at a redshift of 0.324. The radio source consists of a northern component and a fainter southern one. To the west a source is associated with an elliptical galaxy (RA $09^h\ 15^m\ 39^s.7$, DEC +25° 11′ 37″). A few possible counterparts are visible in SDSS DR7 images for the northern diffuse component. The southern diffuse component has no obvious optical counterpart. This could be a radio relic with a projected size of about 190 kpc. High-resolution observations will be needed to confirm this interpretation.

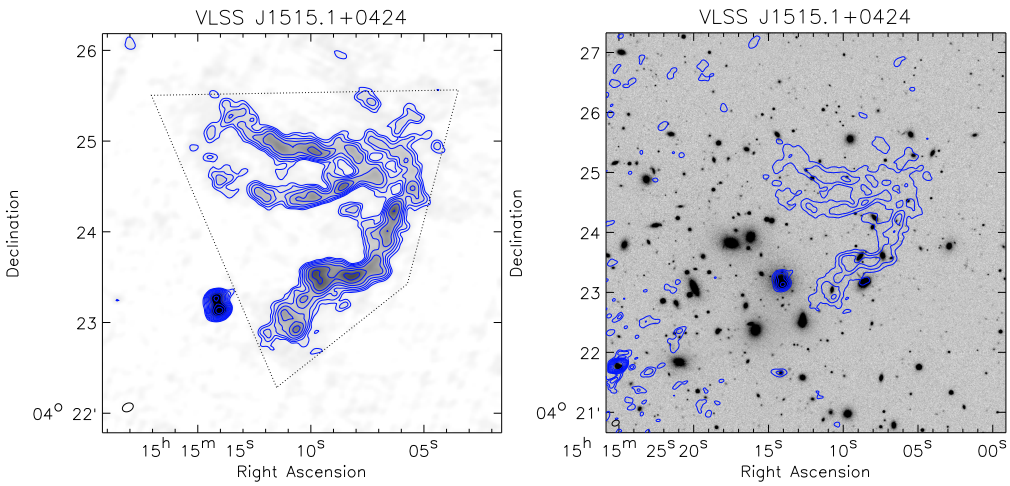

Figure 2.8: Left: GMRT 610 MHz radio map. Contour levels are drawn as in Fig. 2.1 (left panel). Right: SDSS r band image overlaid with GMRT 610 MHz contours. Contour levels are drawn as in Fig. 2.1 (right panel).

2.4.1.7 VLSS J1515.1+0424, Abell 2048

The radio image shows a filamentary radio source in the periphery of the cluster Abell 2048 at a redshift of 0.0972. The source consists of three elongated structures orientated roughly east-west. The three structures connect to the east. The source could be a complex double WAT source. However, the radio structure itself does not seem to be connected to any particular galaxy. The source has a projected size of 310 kpc, if located in the cluster. In the southeast a compact double-lobe source is associated with a large elliptical galaxy (RA $15^h\ 15^m\ 14^s.1$, DEC $+04°\ 23'\ 10''$) located in the cluster. On the other side of the cluster a 0.19 Jy source (PMN J1515+0421) limits the dynamic range. The cluster is also detected in X-rays as RX J1515.2+0421 (Bade et al. 1998). A substructure on the east-side of the main cluster is visible, hinting at a possible cluster merger, see Fig. 2.6 (right panel). Given the location of the radio source at the edge of the cluster, the lack of a connection with a single optical counterpart, the steep radio spectrum, and the morphology, we classify the source as a peripheral radio relic.

2.5 Spectral index modeling

Radio spectra can be an important tool to understand the origin of the relativistic electrons and to determine the age of the radio emitting plasma. We have combined our flux measurements at 610 MHz with literature values to determine the radio spectra for the sources in our sample. We have included flux measurements from the following surveys: 38 MHz 8C (Rees 1990; Hales et al. 1995), 74 MHz VLSS, 151 MHz 7C (Waldram et al. 1996; Hales et al. 2007), 232 MHz Miyun (Zhang et al. 1997), 325 MHz WENSS (Rengelink et al. 1997), 352 MHz WISH (De Breuck et al. 2002a), 365 MHz TEXAS (Douglas et al. 1996) and 1400 MHz NVSS.

Table 2.2: JP model fits with $\alpha_{\rm inj} = -0.75$

Source Name	$t_{\rm CI}$ 10^8 yr	$t_{\rm RE}$ 10^8 yr	$B'_{\rm eq}$ μGauss
VLSS J0646.8−0722	0.227 ± 0.0775	0.0869 ± 0.00624	24.5
VLSS J1133.7+2324	0.121 ± 0.034	0.0870 ± 0.00634	23.3
VLSS J1710.5+6844	0.421 ± 0.259	0.0946 ± 0.00812	23.1
24P73 (VLSS J2217.5+5943), $z = 0.05$	0.156 ± 0.0464	0.120 ± 0.00406	29.1
24P73 (VLSS J2217.5+5943), $z = 0.10$	0.173 ± 0.0534	0.131 ± 0.00503	27.0
24P73 (VLSS J2217.5+5943), $z = 0.15$	0.176 ± 0.0557	0.131 ± 0.00443	26.4
24P73 (VLSS J2217.5+5943), $z = 0.20$	0.169 ± 0.0500	0.129 ± 0.00497	26.3

We model the integrated radio spectra using the Jaffe-Perola (JP) model (Jaffe & Perola 1973) described by Komissarov & Gubanov (1994), see also Slee et al. (2001). We assume that (i) synchrotron self-absorption is negligible as this only occurs in compact sources, (ii) radiative energy losses dominate over other losses such as adiabatic ones, (iii) the magnetic field is spatially uniform and constant in time, (iv) radiative electrons do not escape from the region, (v) the emission in the region is uniform, (iv) relativistic electrons were injected at a single point with a power-law distribution of energy, and (vii) the pitch angles of the synchrotron emitting electrons are assumed to be continuously isotropized on a timescale shorter than the radiative timescale. Relativistic electrons lose their energy by synchrotron emission and IC scattering off the cosmic microwave background (CMB).

In the Kardashev-Pacholczyk (KP) model (Kardashev 1962; Pacholczyk 1970), also used by Komissarov & Gubanov (1994), the pitch angle of the electrons remains in its original orientation with respect to the magnetic field. This introduces one more free parameter in the spectral index modeling (the ratio between the source magnetic field (B) and the effective magnetic field for IC losses ($B_{\rm IC}$). We have chosen not to fit this model to limit the number of free parameters. Furthermore, the JP model is more realistic from a physical point of view, as an anisotropic pitch angle distribution will become more isotropic due to changes in the magnetic field strength between different regions and scattering by self-induced Alfvén waves (e.g., Carilli et al. 1991; Slee et al. 2001).

Our adopted scenario is as follows: When the source starts, we assume that it is fueled at a constant rate for a certain time $t_{\rm CI}$ (the time of the continuous injection (CI) of relativistic electrons, with an injection spectral index $\alpha_{\rm inj}$). This is followed by a relic phase (RE) where the injection of electrons is switched off ($t_{\rm RE}$). During both of these phases the electrons lose energy by synchrotron and IC losses. The total source age is $t_{\rm age} = t_{\rm RE} + t_{\rm CI}$.

In the spectrum two break frequencies occur both related to spectral aging. The first is the break frequency $\nu_{\rm b}$ of the first injected electron population (at the beginning of the CI phase)

$$\nu_{\rm b} \propto \frac{B}{\left([B^2 + B_{\rm IC}^2]t\right)^2} \,. \tag{2.3}$$

A second higher frequency break $\nu\prime_{\rm b}$ is caused by the last electron population injected, at the

end of the CI phase

$$\nu\prime_{\rm b} = \nu_{\rm b}\left(1 + \frac{t_{\rm CI}}{t_{\rm RE}}\right)^2 . \tag{2.4}$$

The injection spectral index ($\alpha_{\rm inj}$) is determined by the AGN in the case of (relic) radio lobes or radio phoenices. For relics where the particles are accelerated by DSA the injection spectral index is related to the Mach number ($\mathcal{M}$) of the shock. In linear theory the relevant expression is

$$\alpha_{\rm inj} = -\frac{3\mathcal{M}^{-2} + 1}{2 - 2\mathcal{M}^{-2}} , \tag{2.5}$$

see van Weeren et al. (2009b). The injection time must be comparable with the crossing time of the relic region by the shock front. Since "DSA-relics" are mostly located in the cluster periphery, where the pressure of the ICM gas is lower, adiabatic energy losses may become important. These adiabatic energy losses affect the radio spectrum, depending on the expansion rate of the relic and evolution of the magnetic field strength ($B(t)$) with time (Kardashev 1962; Goldshmidt & Rephaeli 1994; Murgia et al. 2002). However, we only have a limited number of flux measurements for our sources and only one proposed DSA-relic with enough flux measurements to model the spectrum. Furthermore, the location of this relic in the cluster as well as the identification of the cluster itself are uncertain. We therefore chose to ignore the effects adiabatic expansion losses.

The JP model is thus characterized by four free parameters: (1) the injection spectral index $\alpha_{\rm inj}$, (2) the length of the CI phase $t_{\rm CI}$, (3) the length of the RE phase $t_{\rm RE}$, and (4) a flux normalization constant. To reduce the number of free parameters we have chosen to keep $\alpha_{\rm inj}$ fixed to a value of -0.75 (Parma et al. 2007).

The spectra are fitted by minimizing the χ-squared value of the fit in a two-step process. We first determine the shape of the spectrum for different values of $t_{\rm RE}$ and $t_{\rm CI}$, both ranging from 0 to 10^9 yrs in 25 equal logarithmically spaced steps. Then an overall flux scaling (normalization) constant is determined by multiplying the spectrum with a constant until the χ-squared value is minimized. In this way, a 2-dimensional (25×25) array of χ-squared values is created. We continue the fitting using the same process but now centering the $t_{\rm RE}$ and $t_{\rm CI}$ values around the minimum χ-squared value in the array and increasing the time resolution by a factor of 1.5. The process is repeated until both $t_{\rm RE}$ and $t_{\rm CI}$ converge to a constant value, i.e., do not change by more than 1% between subsequent iterations. The formal errors in the fitted parameters are determined by the corresponding distribution of the χ-squared values. For the sources where we successfully fitted the JP-model we should take in mind that some of the simplifying assumptions we made may not be valid and could have affected our results.

For the magnetic field strength we use the revised equipartition magnetic field strength $B'_{\rm eq}$ (Brunetti et al. 1997; Beck & Krause 2005). We use the same procedure as in van Weeren et al. (2009b) and take for the depth of the source (d) the average of the major and minor axis. The ratio of energy in relativistic protons to that in electrons (k) is set to 100. For the low-energy cutoff ($\gamma_{\rm min}$, the energy boundary indicated by the Lorentz factor) we take 100. For other values of k and $\gamma_{\rm min}$, $B'_{\rm eq}$ scales with $\gamma_{\rm min}^{(1+2\alpha)/(3-\alpha)}(1 + k)^{1/(3-\alpha)}$, with α the spectral index.

We have only fitted the radio spectra for sources with a redshift (because the energy loss rate due to IC scattering is proportional to $(1 + z)^4$) and at least four flux measurements available. An exception is 24P73 (or VLSS J2217.5+5943) for which we have no redshift. If 24P73 has a similar size as the relic in A85 (150 kpc, Slee et al. 2001), then its redshift would be around

0.1. Since this is a very rough estimate we have also fitted the radio spectrum using redshifts of 0.05, 0.15, and 0.2.

The fluxes for the sources could be contaminated by the presence of field sources within the beam of the low-resolution surveys. In the case of 24P73, there is a 5.0 mJy NVSS source (NVSS J221736+594403) nearby which is blended with the diffuse source in the 8C, VLSS, and WENSS surveys. We fitted a second order polynomial in log-log space to the 610 MHz GMRT, NVSS, and the 1.4 and 8.4 GHz fluxes from Green & Joncas (1994) for this source. We then extrapolated the flux to 325, 74, and 38 MHz and subtracted off this flux to recover the uncontaminated flux for the diffuse source. For the three other diffuse sources no unrelated sources were found that could have significantly contributed to the flux.

The fitted radio spectra are show in Fig. 2.9. The values for $t_{\rm CI}$, $t_{\rm RE}$, and $B'_{\rm eq}$ are reported in Table 2.2. The fitting process for the sources VLSS J1636.5+3326, VLSS J2213.2+3411, VLSS J0004.9−3457 did not converge. For VLSS J1636.5+3326 the 1.4 GHz flux measurement is relatively high, in this case the source may have restarted its activity causing the high 1.4 GHz flux value. This is also seen for several radio sources by Parma et al. (2007). For the other sources the flux measurements are too closely spaced in frequency to provide enough constraints for the fitting process.

For the sources where we successfully modeled the synchrotron spectrum $t_{\rm CI} > t_{\rm RE}$. All of these sources show steepening of the radio spectrum at higher frequencies which is expected in case of spectral aging. For 24P73 the spectral index modeling is consistent with the source being a radio phoenix with a total source age of 3×10^7 yrs. We find that the derived synchrotron age does not critically depend on the adopted redshift of 0.1 for this source (see Table 2.2).

2.6 Discussion

Based on their toroidal or filamentary morphologies and curved radio spectra two of our relics could be classified as radio phoenices: VLSS J1515.1+0424 and VLSS J2217.5+5943. Contrary, VLSS J1133.7+2324 and the twisted structure in MACS J0717.5+3745 are probably the result of DSA from structure formation shocks. In the case of VLSS J0717.5+3745, the distorted morphology and high temperature of the ICM are clear evidence for a cluster undergoing a merger. For the other relics more observations are needed to determine their origin.

Most of the sources in our sample are associated with galaxies in clusters and show irregular morphologies. This can be caused by the interaction of the radio plasma with the ICM. The steep spectrum of the sources is caused by spectral aging, e.g., in some cases the central AGN activity may have stopped, producing a so called “dying” radio source. Confinement of the radio plasma by the ICM could also have contributed to the steep radio spectra, as in this case the radio plasma has “the time” to display the effects of spectral aging.

We have calculated the physical size (largest extent), projected distance from the cluster center ($R_{\rm projected}$), and 1.4 GHz radio power ($P_{1.4}$) for the radio relics in our sample. We have complemented this with values from the literature for radio relics with measured spectral indices: A13, A85, A133, and A4038 (Slee et al. 2001), A1240 and A2345 (Bonafede et al. 2009b), A3667 (Röttgering et al. 1997), A548b (Feretti et al. 2006), A2256 (Clarke & Ensslin 2006), A521 (Giacintucci et al. 2008), 1253+275 (Giovannini et al. 1991), A2163 (Feretti et al. 2004), A2744 (Orrú et al. 2007), AS753 (Subrahmanyan et al. 2003), A115 (Govoni et al. 2001) A610 (Giovannini & Feretti 2000) and RXC J1314.4-2515 (Venturi et al. 2007). The spectral indices

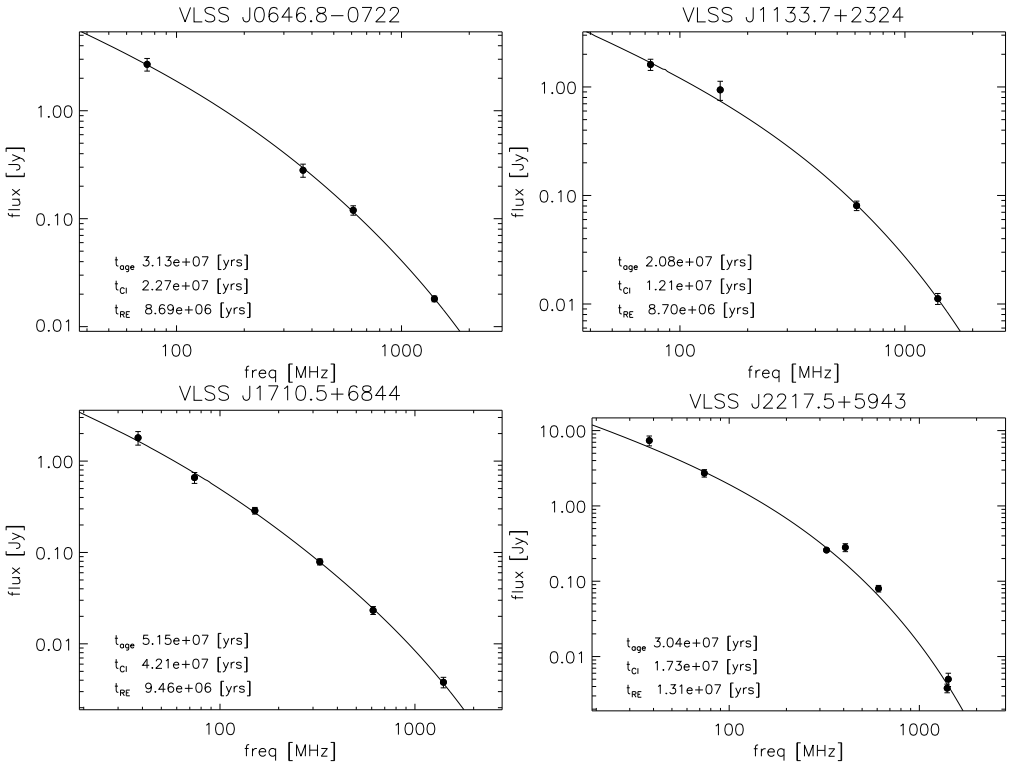

Figure 2.9: Jaffe-Perola fit to the flux measurements. The duration of the CI and RE phases are indicated in the figure. Top left: VLSS J0646.8−0722; Top right: VLSS J1133.7+2324; Bottom left: VLSS J1710.5+6844; Bottom right: VLSS J2217.5+5943 (24P73 and using $z = 0.1$).

Table 2.3: Radio relic properties

Source Name	$\alpha_{74\mathrm{MHz}}^{1400\mathrm{MHz}}$	spectral curvature $\alpha_{74\mathrm{MHz}}^{610\mathrm{MHz}} - \alpha_{610\mathrm{MHz}}^{1400\mathrm{MHz}}$	$P_{1.4}$ 10^{24} W Hz^{-1}	size[a] kpc	$R_{\mathrm{projected}}$ kpc
VLSS J1133.7+2324	−1.69	0.96	24.1	570	
VLSS J1431.8+1331[d]	...	...	...	125	175
24P73 (VLSS J2217.5+5943)	−2.20	2.0	...	...	...
MACS J0717.5+3745	−1.09[b]	−0.02	138[b]	700	320
Abell 2048 (VLSS J1515.1+0424)	−1.50	1.60	0.566	310	310
Abell 2256	−1.2	...	3.95	1100	300
Abell 1240-N	−1.2	...	0.427	650	700
Abell 1240-S	−1.3	...	0.730	1250	1100
Abell 2345-E	−1.3	...	2.62	1500	890
Abell 2345-W	−1.5	...	2.83	1150	1000
Abell 13	−1.79	0.65	0.853	260	170
Abell 85	−2.30	1.36	0.322	150	430
Abell 133	−1.70	1.39	1.07	55	40
Abell 4038	−1.88	1.03	0.0983	55	35
Abell 3667	−1.1	...	17.4	1920	1950
Abell 548b A	~ -2	...	0.260	310	500
Abell 548b B	< -2.0	...	0.250	370	430
Abell 521	−1.48	...	2.90	1000	930
Coma cluster[c]	−1.18	...	0.284	850	1940
Abell 2163	−1.02	...	2.23	450	1550
Abell 2744	−1.1	...	6.20	1620	1560
Abell S753	−2.0	...	0.205	350	410
Abell 115	−1.1	...	16.7	1960	1510
Abell 610	−1.4	...	0.444	330	310
RXCJ1314.4-2515-E	−1.41	...	2.08	920	685
RXCJ1314.4-2515-W	−1.40	...	4.81	920	685

[a] largest linear scale
[b] excluding the flux of the halo and central head-tail source (see also van Weeren et al. 2009d; Bonafede et al. 2009a)
[c] 1253+275
[d] blended with a nearby AGN (except in the GMRT 610 MHz image), therefore no spectral index or spectral curvature could be calculated

for our newly found relics were calculated between 74 and 1400 MHz. The spectral indices for the relics taken from the literature were usually measured between 325 and 1400 MHz, but for some relics the frequency range is somewhat different (for more details the reader is referred the references given above).

The spectral index of the radio relics, versus the physical size is shown in Fig. 2.10 (left panel). The projected distance from the cluster center is color coded. We find that on average the smaller relics have steeper spectra. There are two different explanations for this correlation. The found correlation between physical size and spectral index may (partly) be the result of the proposed radio phoenices occupying the lower left region in Fig. 2.10. Ignoring the proposed radio phoenices the trend remains, although the scatter is large so this result is less significant. Such a trend though, is in line with predictions from shock statistics derived from cosmological simulations (Hoeft et al. 2008; Skillman et al. 2008; Battaglia et al. 2009). They find that larger shock waves occur mainly in lower-density regions and have larger Mach numbers, and consequently shallower spectra. Conversely, smaller shock waves are more likely to be found in cluster centers and have lower Mach numbers and steeper spectra. We note that more spectral index measurements of high quality are needed to confirm the correlation between physical size and spectral index (leaving out the proposed radio phoenices).

The size of the relics versus $R_{\text{projected}}$ is shown in Fig. 2.10 (right panel). The projected distance from the cluster center for the shallow spectra relics is indeed on average larger than for the steep spectrum relics, indicating that they are mostly located in the periphery of clusters where the Mach numbers of the shock are higher. We contribute this to the fact that in the periphery the shock surfaces are larger and the density/pressure of the ICM is lower. Therefore large radio relics are mainly located in the cluster periphery. Because we are using the projected distance from the cluster center, and not the (unknown) de-projected distance, some additional scatter is introduced in the plot. Furthermore, the spectral indices for the various radio relics are calculated using data from radio telescopes with different array configurations, sensitivities, and/or frequencies ranges, adding to the scatter.

Giant Mpc-scale radio relics are probably caused by DSA in an outwards traveling shock front. It is unlikely that they are the result of compression and reignition of fossil radio plasma as the time to compress such a large radio "ghost" would remove most of the electrons responsible for the radio emission by radiative energy losses (Clarke & Ensslin 2006). In the case of giant peripheral relics shock-acceleration is ongoing resulting in relatively flat spectral indices of about -1, i.e., a balance between electron cooling in the post-shock regions and continuous acceleration at the shock front. Behind the shock front, the spectral index is indeed observed to steepen for some giant relics (e.g., Röttgering et al. 1997). After a few times 10^8 yrs the electrons behind the shock front have lost most of their energy and cause little synchrotron emission. It takes of the order of 1 Gyr for a shock wave to travel from the center of the cluster to about the virial radius.

As has been mentioned, an alternative explanation for the found size-spectral index correlation could be a possible different origin of the smaller radio relics. With the smaller radio relics originating from the adiabatic compression of fossil radio plasma. In fossil radio plasma, the high-frequency synchrotron emitting electrons have lost most of their energy. Due to compression and the increase in magnetic field strength the radio plasma becomes visible again. Therefore these sources are characterized by (very) steep and curved spectra. Proposed examples of such sources are 24P73 and those found by Slee et al. (2001). If spectral aging occurs, the steeper radio spectra should be more curved.

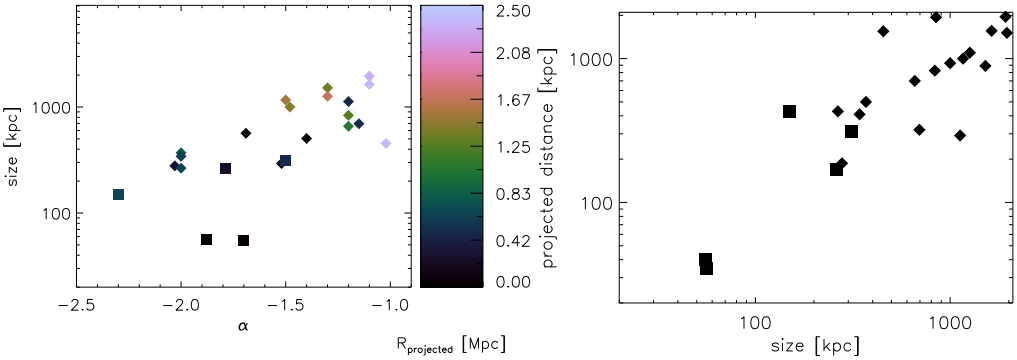

Figure 2.10: Left: Spectral index of radio relics versus their size. Squares are the proposed radio phoenices, i.e., the sources from Slee et al. (2001), 24P73 and the relic in Abell 2048. Diamonds represent the radio relics tracing merger shocks where particles are being accelerated by the DSA mechanism. The brightness coding is according to the projected distance from the cluster center. For the relics represented by black symbols we could not obtain a reliable projected distance to the cluster center. Right: Projected distance from the cluster center of radio relics versus their size.

It would be interesting to determine the injection spectral indices ($\alpha_{\rm inj}$) for the radio relics. This requires reliable flux measurements over a wide range of frequencies, especially below the break frequency $\nu_{\rm b}$. With enough flux measurements it should be possible to separate the effect of spectral aging and a steep $\alpha_{\rm inj}$. In particular, if the correlation is explained by the different Mach numbers of shocks the injection spectral indices for smaller relics located close to the cluster center should be steeper than that of larger relics. If this is indeed the case this is evidence for DSA. For radio phoenices the injection spectral index should be around −0.5 to −0.75 because the fossil radio plasma originated from AGN. Their steep spectral indices should then solely be the result of spectral aging and not a steep injection spectral index. Currently, with a limited number of flux measurements, mainly at frequencies where electrons have already lost some of their energy, there is a degeneracy between the injection spectral index and the amount of spectral aging. New low-frequency radio facilities, such as LOFAR, will be needed to determine $\alpha_{\rm inj}$ for radio relics.

The spectral index versus the 1.4 GHz radio power for the relics is shown in Fig. 2.11 (left panel). From the figure we can see that there is a lack of high power sources with steep radio spectra. This is not surprising since relics with less steep spectra are larger (Fig. 2.10) and therefore should have a higher radio power.

We have plotted the amount of spectral curvature for our sources versus their spectral index, between 74 and 1400 MHz, in Fig. 2.11 (right panel). The curvature is defined as $\alpha_{74-610} - \alpha_{610-1400}$. A higher positive value for the curvature implies that the spectra are steeper at higher frequencies. We have only added the four sources from Slee et al. (2001) for which flux measurements at both 1.4 GHz and 74 MHz (VLSS) are available. We calculated the 610 MHz fluxes by interpolating the fluxes (linearly in log-log space) between 408 and 834 MHz. For other radio relics, flux measurements are less reliable or not available at 74 and/or 610 MHz. As shown in Fig. 2.11 there is an indication that the curvature is higher for the sources with a steeper spectral index, although the number of sources in the plot is rather low. If the spectral index of

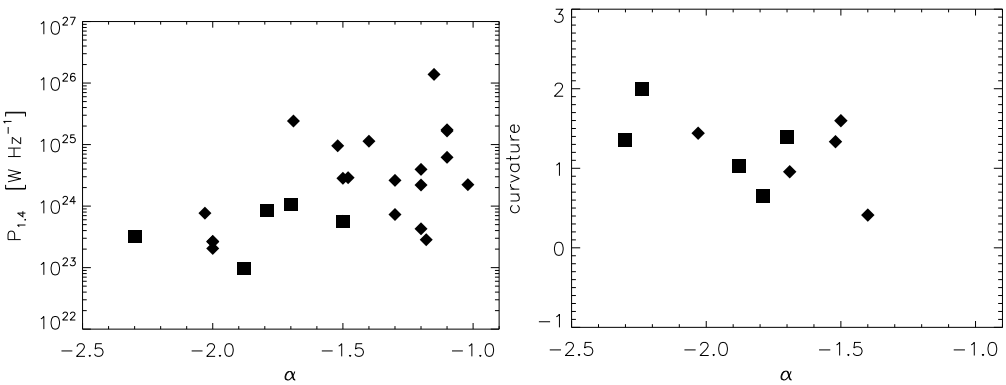

Figure 2.11: Left: Radio power at 1.4 GHz of radio relics versus their spectral index. Symbols are defined in Fig. 2.10. Right: Curvature of the radio spectra versus their spectral index between 74 and 1400 MHz. The curvature is defined as $\alpha_{74-610} - \alpha_{610-1400}$.

relics steepens by spectral aging such a trend is expected, but more measurements of spectral curvature will be needed to show that this correlation with the spectral index really exists.

2.7 Conclusions

We carried out 610 MHz radio continuum observations with the GMRT of 26 diffuse steep spectrum sources. All of these sources were resolved out by 1.4 GHz VLA B-array snapshot observations or in the 1.4 GHz FIRST survey. Of these 26 sources 25 were detected with the GMRT. The radio observations show a wide range of sources: radio relics, a giant radio halo, a mini-halo, FR-I, head-tail, and USS sources. Here we shortly summarize the properties of the relics and halos in our sample.

-The radio relic 24P73 (VLSS J2217.5+5943) is located close to the galactic plane. This source was previously known to have a steep spectrum but remained unclassified due to the limited sensitivity and resolution of previous observations. Due to the crowed Milky Way field and high extinction no cluster is found in POSS-II images. Deep NIR imaging will be needed to reveal the presence of a cluster. The sources has an extremely steep curved spectrum, likely the result of adiabatic compression of fossil radio plasma and spectral aging.

-VLSS J1133.7+2324 is a filamentary relic located next to a nearby spiral galaxy. The radio source breaks up into two parallel filamentary structures. This relic source is probably associated with a structure of galaxies located at a distance of $z \sim 0.6$. The nearby spiral galaxy itself is also detected in the radio images, the flux density consistent with that predicated by the FIR-radio correlation (using IRAS fluxes for this galaxy). The galaxy is partly blocking our view of the distant structure of galaxies, making follow-up observations more difficult.

-VLSS J1431.8+1331 consists of two components. The eastern part is probably associated with a cD galaxy in the center of the cluster MaxBCG J217.95869+13.53470 at $z = 0.16$. The radio morphology suggests we are seeing signs of interaction between the radio plasma and the ICM. The other part is probably a relic source. These sources makes an interesting target for

follow-up X-ray observations.

-VLSS J0004.9−3457 is associated with an elliptical galaxy in a small cluster at $z \sim 0.3$. The diffuse radio emission surrounds the galaxy in the form of a mini-halo. The source has an arc-like extension to the east.

- VLSS J0717.5+3745 is located in the cluster MACS J0717.5+3745, a massive merging system at a redshift of 0.5548. The radio emission is complex, consisting of a large elongated radio relic and a giant 1.2 Mpc radio halo. The halo has a radio power ($P_{1.4}$) of 5×10^{25} W Hz^{-1}, the highest one known to date. The relic might trace a giant shock wave related to the cluster merger. This is consistent with the very hot ICM and relatively flat spectral index.

-VLSS J1515.1+0424 is a radio relic consisting of three filamentary structures in the periphery of the cluster Abell 2048. Adiabatic compression of fossil radio plasma probably resulted in the complex morphology.

We find that larger relics are mostly located in the cluster periphery, while smaller relics are found closer to the cluster center. We also discovered a correlation between the spectral index and the physical size of the relics. A likely explanation for this correlation is that the larger shock waves occur mainly in lower-density regions and have larger Mach numbers. As a consequence they have shallower spectra. However, the correlation can also (partly) be explained by invoking different origins for relics. Relics formed by diffusive shock acceleration are direct tracers of large shock fronts in clusters, while the compression of fossil radio plasma is thought to produce relatively small relics with steep curved spectra.

If the correlation is explained by the fact that the larger shock waves occur mainly in lower-density regions and have larger Mach numbers then the injection spectral indices should flatten away from the cluster center for the various relics. To measure this requires a sufficient number of flux measurements, especially below the break frequency in the spectrum. With upcoming new radio facilities operating at lower frequencies it should therefore be possible to break the degeneracy between the injection spectral index and spectral aging.

Follow-up observations to measure the polarization properties are currently underway. We also plan to create spectral index maps for our sources which should give more information on the life-times of the various synchrotron emitting regions. Optical observations have been taken to characterize the large-scale environment around the radio sources. For two of our diffuse sources these observations should confirm the presence of a cluster. X-ray observations will be needed to study the dynamical state of the clusters and reveal the presence of shock fronts in the ICM.

Acknowledgements. We thank the staff of the GMRT who have made these observations possible. The GMRT is run by the National Centre for Radio Astrophysics of the Tata Institute of Fundamental Research. RJvW would like to thank J.B.R. Oonk and A. Omar for helping with the observations, D. A. Green for the discussion about source 24P73, and F. Govoni for pointing out the correct flux of A115. We have used the "cubehelix" color scheme from Green (2011). RJvW acknowledges funding from the Royal Netherlands Academy of Arts and Sciences.

This publication makes use of data products from the Two Micron All Sky Survey, which is a joint project of the University of Massachusetts and the Infrared Processing and Analysis Center/California Institute of Technology, funded by the National Aeronautics and Space Administration and the National Science Foundation. This research has made use of the VizieR catalogue access tool, CDS, Strasbourg, France. The Digitized Sky Surveys were produced at the Space Telescope Science Institute under U.S. Government grant NAG W-2166. The images of these surveys are based on photographic data obtained

using the Oschin Schmidt Telescope on Palomar Mountain and the UK Schmidt Telescope. The plates were processed into the present compressed digital form with the permission of these institutions. The Second Palomar Observatory Sky Survey (POSS-II) was made by the California Institute of Technology with funds from the National Science Foundation, the National Geographic Society, the Sloan Foundation, the Samuel Oschin Foundation, and the Eastman Kodak Corporation.

2.8 Appendix: Other sources in the sample

VLSS J0227.4−1642

The radio map shows two resolved elongated patches of emission. The brighter eastern component has a flux of 25.8 mJy and the weaker western component 11.2 mJy. Both components are resolved, 28.3″ by 10.3″ (eastern component) and 22.3″ by 9.0″ (western component), and show structure at the limit of the ∼ 5″ beam. The position angles of the longest axes are roughly the same, which suggests a link between the two components. No optical counterpart is detected at the limit of the POSS-II survey. The steep spectral index of about −1.5 could be explained if this source is a FR-I type AGN, where the central engine has stopped and the synchrotron emission in the two lobes has steepened by spectral aging. In this case both components should roughly have the same spectral index.

VLSS J0250.5−1247

The radio observations show a double source. The two components are slightly resolved, have a similar flux and seem to be connected by a faint bridge. The separation between the two radio components is 15″. No optical counterpart is detected.

VLSS J0646.8−0722

The radio map shows a source with an angular size of 1.0′ by 0.5′. An optical counterpart (PCG 76039, mag_R=18.4) is detected in both the POSS-II and 2MASS surveys. This galaxy was also listed in the catalog of Galaxies Behind the Milky Way (CGMW 1-0379, Saito et al. 1990) and in the catalog Galaxies in the "zone of avoidance" (ZOAG G218.99-04.37, Weinberger et al. 1995) and was in both cases classified as an elliptical galaxy. The amount of extinction in this region is A_B = 2.2 mag. The radio map shows a one-sided tail originating from the optical counterpart. This might indicate that the source is located in a cluster and we see the effects of the interaction between radio plasma and the surrounding ICM.

VLSS J1117.1+7003

This source has a remarkable steep and straight radio spectrum without any indication of a flux turnover at lower frequencies. The source is resolved into a smooth featureless roughly spherical blob (26″ by 23″). No optical counterpart is detected. Given the steep straight radio spectrum it could be a radio halo, however the small size of the source argues against such an identification. The source could be a mini-radio halo surrounding a central cD galaxy of a distant (proto) cluster.

VLSS J1636.5+3326

The radio map shows two compact components, with the northern component extending to the west. SDSS images show several faint mostly red galaxies around the radio source. Photometric redshifts (SDSS DR7) indicate the presence of a cluster at $z = 0.65 \pm 0.19$. Several galaxies can be identified as possible optical counterparts.

VLSS J1710.5+6844

This "head-tail" radio source has a length of 0.73′ and a width of 0.27′. An optical counterpart is detected, a galaxy with a K-magnitude of 14.75. An optical *i*-band image from the 2.5m Isaac Newton Telescope (INT) shows that this source is located within a cluster at a redshift of $z \sim 0.3$. An east-west elongated X-ray source 1RXS J171034.0+684403 follows roughly the galaxy distribution confirming the presence of a cluster.

VLSS J1930.4+1048

The radio map shows an elongated source with a LAS of 101″. The radio morphology is consistent with a FR-I radio source. No optical counterpart is detected at the position of the core, but this is not surprising given the amount of extinction ($A_B = 3.759$) at this galactic latitude of −3.6 degrees and the high star density in the POSS-II images. A 69.6 mJy (probably unrelated) radio source is located 70″to the north.

VLSS J2043.9−1118

An optical counterpart for this source is detected in POSS-II images. The faint optical source is located on the peak of the radio emission. The radio emission surrounds the galaxy and there is a hint of a faint extension to the east.

VLSS J2044.7+0447

The source is elongated in the east-west direction and has a LAS of 101″. A R-magnitude 19.56 galaxy corresponds to a peak in the radio emission, consistent with this being a FR-I radio source. The high rms noise is the radio map is caused by dynamic range limitations from 4C 04.71, a 1.24 Jy source (610 MHz), located 3.3′ to the south.

VLSS 2122.9+0012

The radio source is compact, 11.6″ by 10.7″. This is probably a USS source associated with a HzRG. The lack of an optical counterpart in SDSS images in consistent with this explanation, and implies the source is located at $z \gtrsim 1.4$.

VLSS J2213.2+3411

This source was also included in the USS sample of De Breuck et al. (2000), WN J2213+3411. A K_s band image from De Breuck et al. (2002b) showed a possible counterpart. However, because no high-resolution ($\lesssim 10''$) VLA images were available the identification was uncertain on the basis of position alone. Our high-resolution 5″ image shows a distorted double-lobe source. The central radio core is not detected. The NIR counterpart is located in between the two lobes, confirming that this is indeed the host galaxy. The K-band magnitude of 18.3 implies a redshift of 1.6 ± 0.5 for this source using the K-z relation.

VLSS J2341.1+1231

The radio map shows a FR-I type radio source. The northwestern and southeastern lobes are listed as NVSS J234104+123203 and NVSS J234107+123126, respectively. An optical counterpart is detected on POSS-II images at roughly the expected position based on the location of the lobes. This source may be a so called “dying” radio source.

VLSS J2345.2+2157

The radio source shows an S-shape symmetry. An optical counterpart is detected in 2MASS and POSS-II images being the central cD galaxy of a cluster. This is confirmed by the presence of the X-ray source 1RXS J234518.4+215753.

VLSS J0511.6+0254

The radio map shows a FR-I type radio source. Two possible optical counterparts are detected which are the central elliptical galaxies in a cluster at a redshift of about 0.2.

VLSS J0516.2+0103

VLSS J0516.2+0103 is a relatively compact source, without a double lobe structure. The source does not have an optical counterpart in POSS-II images. This implies the source is probably located at $z \gtrsim 0.7$.

VLSS J2209.5+1546

The radio map shows an elongated source. No optical counterpart is detected at the limit of the POSS-II images. The source is probably a distant FR-I source. Optical imaging will be needed to confirm this classification.

VLSS J2241.3−1626

This source could be a disturbed FR-I source, no optical counterpart is detected. Optical imaging will be needed to confirm this classification.

VLSS J2357.0+0441

The source is found to be a blend of three compact sources, all without optical counterparts. By convolving the GMRT image to the NVSS resolution ($45''$) it seems that the two outer components are responsible for the steep spectrum. These are probably distant FR-II sources.

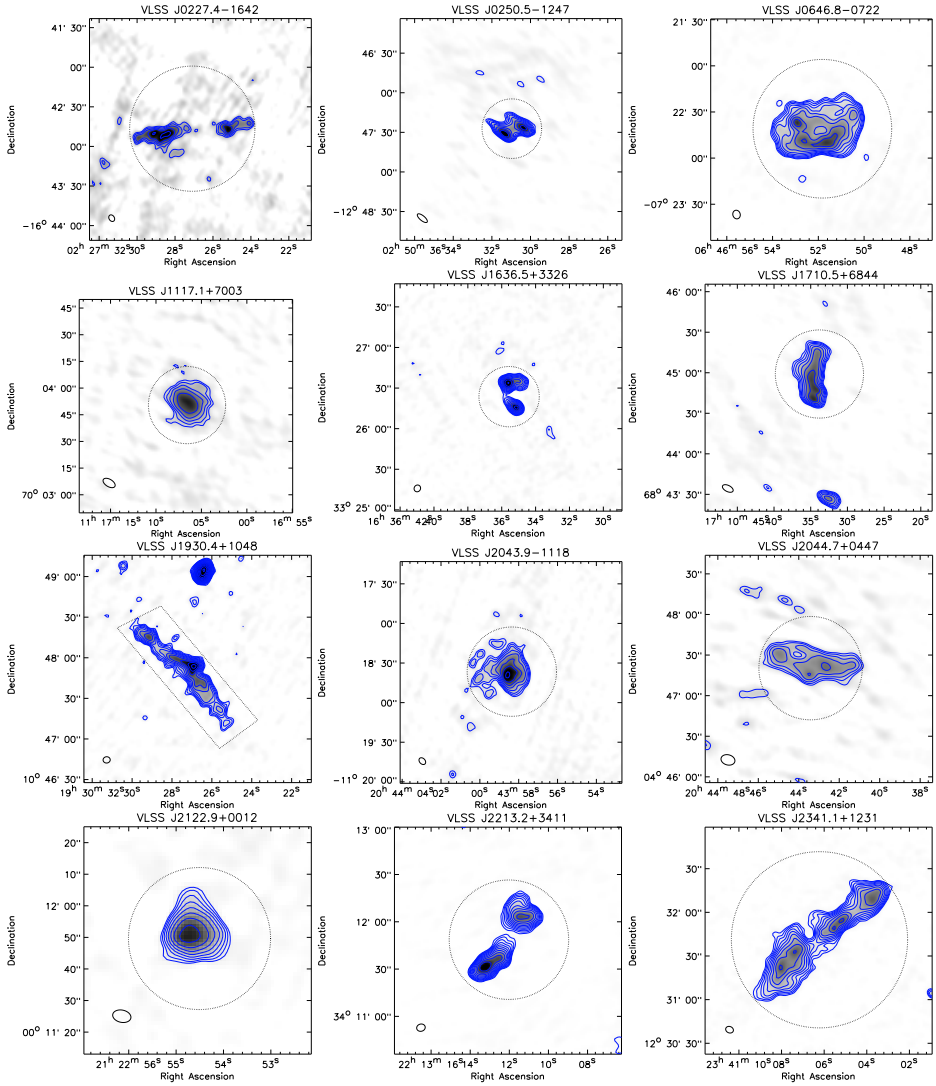

Figure 2.12: GMRT 610 MHz radio maps. Contour levels are drawn as in Fig. 2.1 (left panel).

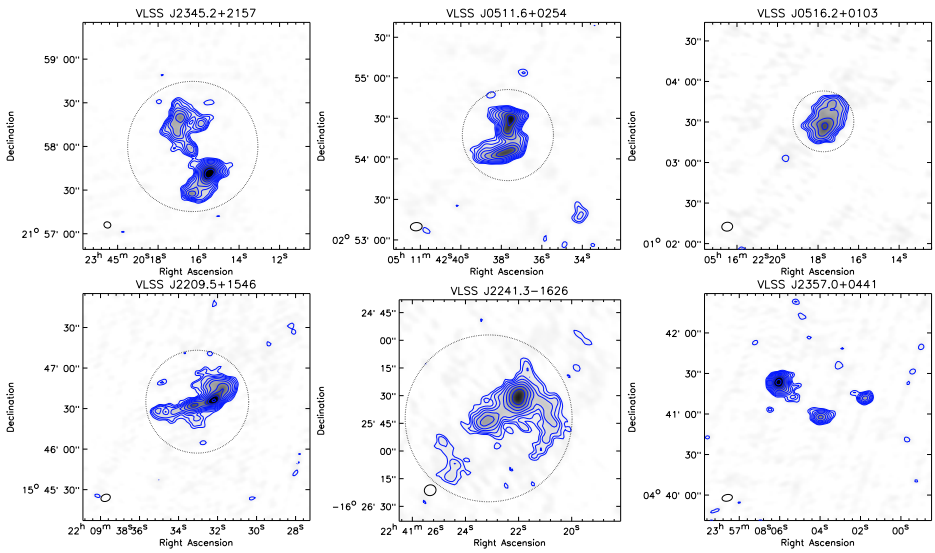

Figure 2.13: GMRT 610 MHz radio maps. Contour levels are drawn as in Fig. 2.1 (left panel).

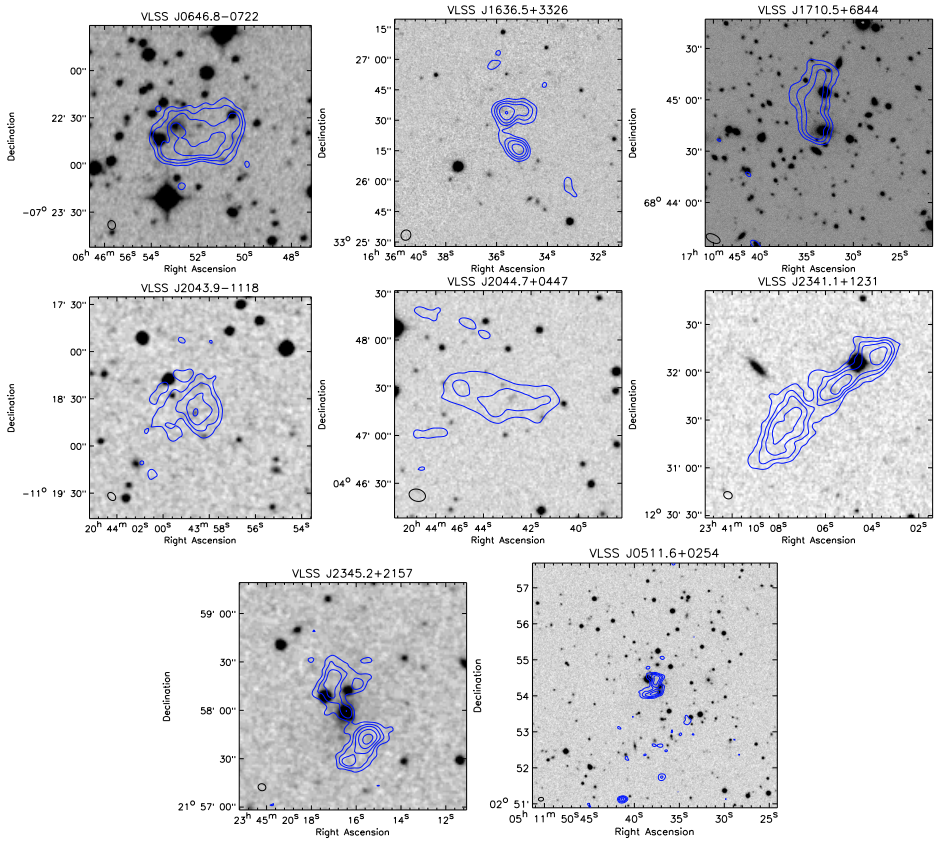

Figure 2.14: Optical images for radio sources with counterparts. Images are from SDSS or POSS-II (red), except for VLSS J1710.5+6844 for which we took seven *i*-band images from the INT Wide Field Camera with a total exposure time of 2520 sec. GMRT 610 MHz contour levels are drawn as in Fig. 2.1 (right panel).

CHAPTER 3

Diffuse steep-spectrum sources from the 74 MHz VLSS survey

Abstract. Galaxy clusters grow by a sequence of mergers with other clusters and galaxy groups. During these mergers, shocks and/or turbulence are created within the intracluster medium (ICM). In this process, particles could be accelerated to highly relativistic energies. The synchrotron radiation from these particles is observed in the form of radio relics and halos that are generally characterized by a steep radio spectral index. Shocks can also revive fossil radio plasma from a previous episode of AGN activity, creating a so-called radio "phoenix". Here we present multi-frequency radio observations of diffuse steep-spectrum radio sources selected from the 74 MHz VLSS survey. Previous Giant Metrewave Radio Telescope (GMRT) observations showed that some of these sources had filamentary and elongated morphologies, which are expected for radio relics. We attempt to understand the nature of diffuse steep-spectrum radio sources and characterize their spectral index and polarization properties. We carried out radio continuum observations at 325 MHz with the GMRT. Observations with the Very Large Array (VLA) and Westerbork Synthesis Radio Telescope (WSRT) were taken at 1.4 GHz in full polarization mode. Optical images around the radio sources were taken with the William Herschel and Isaac Newton Telescope (WHT, INT). Most of the sources in our sample consist of old radio plasma from AGNs located in small galaxy clusters. The sources can be classified as AGN relics or radio phoenices. The spectral indices across most of the radio sources display large variations. We conclude that diffuse steep-spectrum radio sources are not only found in massive X-ray luminous galaxy clusters but also in smaller systems. Future low-frequency surveys will uncover large numbers of steep-spectrum radio relics related to previous episodes of AGN activity.

R. J. van Weeren, H. J. A. Röttgering, and M. Brüggen
Astronomy & Astrophysics, **527**, 114, 2011

3.1 Introduction

Studies of large-scale structure formation show that galaxy clusters grow through mergers with other clusters and galaxy groups, as well as through the continuous accretion of gas from the intergalactic medium (IGM). The baryonic content of clusters is mostly in the form of hot thermal gas visible at X-ray wavelengths. Several clusters also have a non-thermal component within the ICM, which is observable at radio wavelengths (e.g., Ferrari et al. 2008; Giovannini et al. 2009; Giovannini & Feretti 2000; van Weeren et al. 2010). The idea is that shocks and/or turbulence generated during cluster merger events can accelerate particles to relativistic energies, and in the presence of a magnetic field, synchrotron radiation is emitted (e.g., Ensslin et al. 1998; Miniati et al. 2001; Hoeft & Brüggen 2007; Hoeft et al. 2008; Pfrommer 2008; Battaglia et al. 2009; Skillman et al. 2011). These radio sources, which trace the non-thermal component of the ICM, can be divided into several classes.

Radio *halos* are found at the center of merging galaxy clusters and have typical sizes of about a Mpc. They follow the X-ray emission from the thermal ICM and are mostly unpolarized, although there are some exceptions (see Govoni et al. 2005; Bonafede et al. 2009a). Radio halos have been explained by turbulence injected by recent merger events. This injected turbulence might be capable of re-accelerating relativistic particles (e.g., Brunetti et al. 2001; Petrosian 2001). Alternatively, the energetic electrons are secondary products of proton-proton collisions (e.g., Dennison 1980; Blasi & Colafrancesco 1999; Dolag & Enßlin 2000). The turbulent re-acceleration model currently seems to provide a better explanation of the occurrence of radio halos (e.g., Brunetti et al. 2008).

Mini-halos (also called core-halo systems) are diffuse radio sources with sizes $\lesssim$ 500 kpc located in relaxed galaxy clusters, in which diffuse emission surrounds the central cluster galaxy (Murgia et al. 2009; Govoni et al. 2009; Gitti et al. 2007, 2004; Bacchi et al. 2003; Gitti et al. 2002; Burns et al. 1992).

Radio *relics* are irregularly shaped radio sources with sizes ranging from 50 kpc to 2 Mpc, which can be divided into three groups (Kempner et al. 2004). *Radio gischt* are large elongated, often Mpc-sized, radio sources located at the periphery of merging clusters. They probably trace shock fronts in which particles are accelerated via the diffusive shock acceleration mechanism (DSA; Krymskii 1977; Axford et al. 1977; Bell 1978a,b; Blandford & Ostriker 1978; Drury 1983; Blandford & Eichler 1987; Jones & Ellison 1991; Malkov & O'C Drury 2001). Among these are rare double-relics that have two relics located on both sides of the cluster center (e.g., Bonafede et al. 2009b; van Weeren et al. 2009b; Venturi et al. 2007; Bagchi et al. 2006; Röttgering et al. 1997; van Weeren et al. 2010; Brown et al. 2011). According to DSA theory, the integrated radio spectrum should be a single power-law. *Radio phoenices* and *AGN relics* are both related to radio galaxies. AGN relics are associated with extinct or dying radio galaxies. The radio plasma has a steep curved spectrum due to synchrotron and inverse Compton (IC) losses. Fossil radio plasma from a previous episode of AGN activity can also be compressed by a merger shock wave producing a radio phoenix (Enßlin & Gopal-Krishna 2001; Enßlin & Brüggen 2002), these sources again having steeply curved radio spectra. Proposed examples of these are those found by Slee et al. (2001).

In van Weeren et al. (2009c), we presented observations of a sample of 26 diffuse steep-spectrum sources, with $\alpha \leq -1.15$, selected from the 1.4 GHz NVSS (Condon et al. 1998) and 74 MHz VLSS (Cohen et al. 2007) surveys. These sources were either resolved out in the VLA B-array 1.4 GHz snapshot observations or 1.4 GHz FIRST survey (Becker et al. 1995).

GMRT 610 MHz observations of these 26 sources detected one distant powerful radio halo with a radio relic (van Weeren et al. 2009d), five radio relics including two radio phoenices, and one possible mini-halo. The remaining sources were classified as radio sources directly related to AGN activity. The spectral indices of the radio relics in the sample are generally steeper than most previously known relics. By complementing our observations with results for other relics from the literature, we found that the larger relics generally have flatter spectra and are located farther away from the cluster center. This is in line with predictions from shock statistics derived from cosmological simulations (Hoeft et al. 2008; Skillman et al. 2008; Battaglia et al. 2009). In these simulations, it is found that larger shock waves occur mainly in lower-density regions and have larger Mach numbers, and consequently shallower spectra. On the other hand, smaller shock waves are more likely to be found in cluster centers and have lower Mach numbers, thus steeper spectra.

In this paper, we present follow-up radio observations of six sources (i.e., those most likely related to radio relics and halos) found in van Weeren et al. (2009c). GMRT 325 MHz as well as VLA and WSRT 1.4 GHz observations were obtained to create spectral index and polarization maps. Optical images were acquired with the 4.2m WHT and 2.5m INT telescopes at the position of the radio sources to search for optical counterparts and identify galaxy clusters associated with the radio sources.

The layout of this paper is as follows. In Sect. 3.2, we present an overview of the observations and data reduction. In Sect. 3.3, we present the radio and spectral maps as well as optical images around the radio sources. In Sect. 3.4, we show additional optical images around five slightly more compact radio sources (also from the sample of 26 sources) to search for optical counterparts. These sources are not located in nearby galaxy clusters and their nature remains unclear. We end with a discussion and conclusions in Sects. 3.5 and 3.6.

Throughout this paper, we assume a ΛCDM cosmology with $H_0 = 71$ km s^{-1} Mpc^{-1}, $\Omega_m = 0.3$, and $\Omega_\Lambda = 0.7$. All images are in the J2000 coordinate system.

3.2 Observations & data reduction

3.2.1 GMRT 325 MHz observations

Radio continuum observations with the GMRT at 325 MHz were carried out on 14, 15, and 17 May, 2009. Both upper (USB) and lower (LSB) sidebands (IFs, which included RR and LL polarizations) were recorded with a total bandwidth of 32 MHz. The observations were carried out in spectral line mode with 128 channels per IF to facilitate the removal of radio frequency interference (RFI) and reduce the effect of bandwidth smearing. The integration time per visibility was 8 sec. Each source was observed for about 4 hrs in total. The data were reduced with the NRAO Astronomical Image Processing System (AIPS) package.

The data was visually inspected for the presence of RFI, which was subsequently removed (i.e., “flagged”). We carried out an amplitude and phase calibration on the flux and bandpass calibrators 3C147 and 3C286 on a timescale of 8 sec. For this, we chose three neighboring frequency channels free of RFI. These gain solutions were applied before determining the bandpass response of the antennas. This assures that any amplitude and/or phase variations during the scans on the calibrators are corrected before determining the bandpass solutions. At higher frequencies (e.g., 1.4 GHz), both amplitude and phases are assumed to be constant during bandpass calibration. However, for the GMRT observing at low frequencies, this assumption is not

Table 3.1: GMRT 325 MHz observations

	rms noise μJy beam^{-1}	beam size arcsec
VLSS J1431.8+1331	178	$11.8'' \times 7.8''$
VLSS J1133.7+2324	132	$10.4'' \times 7.7''$
Abell 2048	248	$9.7'' \times 9.6''$
24P73	162	$13.6'' \times 9.0''$
VLSS J0004.9−3457	309	$13.5'' \times 11.0''$
VLSS J0915.7+2511	412	$14.7'' \times 8.1''$

always valid and can affect the quality of the bandpass solutions as well as the determination of the flux scale.

After correcting for the bandpass response, both the amplitude and phase solutions for both primary and secondary calibrators were determined but in this case using the full channel range. The fluxes of the primary calibrators were set according to the Perley & Taylor (1999) extension to the Baars et al. (1977) scale. The flux densities for the secondary calibrators were bootstrapped from the primary calibrators. The amplitude and phase solutions were interpolated and applied to the target sources. Some targets were observed over multiple days (observing runs), the resulting different data sets were combined with the AIPS task 'DBCON'.

For each of the target sources, we created a model of the surrounding field using the NVSS survey with a spectral index scaling of −0.7. We carried out a phase-only self-calibration against this model to improve the astrometric accuracy. This was followed by several rounds of phase self-calibration and two final rounds of amplitude and phase self-calibration. To produce the images, we used the polyhedron method (Perley 1989; Cornwell & Perley 1992) to minimize the effects of non-coplanar baselines. The model was then subtracted from the data, a step that facilitated the removal of additional RFI or baselines with problems. Final images were made using robust weighting (robust = 0.5, Briggs 1995). Images were cleaned using the automatic clean-box windowing algorithm in AIPS and cleaned down to 2 times the rms noise level ($2\sigma_{\rm rms}$) within the clean boxes. The final images were corrected for the primary beam response[1]. The uncertainty in the calibration of the absolute flux-scale is in the range 5 − 10%, see Chandra et al. (2004). The resulting noise levels and beam sizes are shown in Table 3.1.

Radio observations at 610 MHz were taken with the GMRT in February and November 2008 of the sources in Table 3.1. The reduction of these observations is similar to the GMRT 325 MHz data and is described in more detail in van Weeren et al. (2009c). We used these images to create the spectral index maps.

3.2.2 VLA 1.4 GHz observations

We carried out L-band observations of four sources with the VLA (see Table 3.2). The observations were taken in standard continuum mode with two IFs, each having a bandwidth of 50 MHz recording all polarization products (RR, LL, RL, and LR). Gain solutions were determined for the calibrator sources and transferred to the target sources. The fluxes for the primary calibrators

[1] http://gmrt.ncra.tifr.res.in/gmrt_hpage/Users/doc/manual/UsersManual/node27.html

Table 3.2: VLA 1.4 GHz observations

	VLSS J1133.7+2324	MaxBCG J217.95869+13.53470	VLSS J0004.9−3457	Abell 2048
Frequency bands (IFs)	1385, 1465 MHz	1385, 1465 MHz	1385, 1465 MHz	1385, 1465 MHz
Bandwidth	2×50 MHz	2×50 MHz	2×50 MHz	2×50 MHz
Polarization	RR, LL, RL, LR	RR, LL, RL, LR	RR, LL, RL, LR	RR, LL, RL, LR
Observation dates	4 Nov 2008, 17 Apr 2009, 10 Aug 2009	2 Nov 2008, 18 Apr 2009, 31 Jul 2009	11 Jun 2009	15 Jul 2009
Project code	AV305, AV312	AV305, AV312	AV312	AV312
Integration time	3.3 s	3.3 s	3.3 s	3.3 s
Total on-source time	5.0 hr, 6.8 hr, 3.9 hr	4.9 hr, 6.8 hr, 3.9 hr	4.0 hr	4.0 hr
VLA configuration	A+B+C	A+B+C	CnB	C
Beam size	$1.3'' \times 1.4''^{a}$, $6.7'' \times 6.7''^{b}$	$1.6'' \times 1.5''^{a}$, $6.4'' \times 5.3''^{b}$	$19.8'' \times 10.3''$	$13.0'' \times 12.4''$
Rms noise ($\sigma_{\rm rms}$)	14^{a}, 19^{b} μJy beam^{-1}	15^{a}, 17^{b} μJy beam^{-1}	49 μJy beam^{-1}	88 μJy beam^{-1}

[a] Briggs weighting (robust = −1.0)
[b] natural weighting

Table 3.3: WSRT observations

Frequency bands 21 cm (IFs)	1311, 1330, 1350, 1370, 1392, 1410, 1432, 1450 MHz
Frequency bands 18 cm (IFs)	1650, 1668, 1686, 1704, 1722, 1740, 1758, 1776 MHz
Bandwidth per IF	20 MHz
Number of channels per IF	64
Channel width	312.5 kHz
Polarization	XX, YY, XY, XY
Observation dates	11, 17, and 18 March, 2009
Integration time	30 s
Total on-source time	6.5 hr 21cm + 6.5 hr 18cm
Beam size	$19.0'' \times 16.5''$
Rms noise ($\sigma_{\rm rms}$)	37 μJy beam^{-1}

were set according to the Perley & Taylor (1999) extension to the Baars et al. (1977) scale. The effective feed polarization parameters (the leakage terms or D-terms) were found by observing the phase calibrator over a wide range of parallactic angles and simultaneously solving for the unknown polarization properties of the source. The polarization angles were set using the polarized sources 3C286 and 3C138. For the R-L phase difference, we assumed values of −66.0 and 15.0 deg for 3C286 and 3C138, respectively. Stokes Q and U images were compiled for each source. From the Stokes Q and U images, the polarization angles (Ψ) were determined ($\Psi = \frac{1}{2}\arctan(U/Q)$). Total polarized intensity (P) images were also made ($P = \sqrt{Q^2 + U^2}$). The polarization fraction were found by dividing the total polarized intensity by the total intensity (Stokes I) image ($\sqrt{Q^2 + U^2}$/I).

3.2.3 WSRT 1.3 – 1.7 GHz observations of 24P73

WSRT observations were taken of a single source (24P73) not included in the VLA observations. Every 5 min, the frequency setup was changed within the L-band, alternating between the 21cm and 18cm setups. Both of these frequency setups have 160 MHz bandwidth divided over 8 IFs, each having 20 MHz bandwidth. The data were recorded in spectral line mode with 64 spectral channels per IF in 4 polarizations. The observations were carried out in three runs on 11, 17, and 18 March, 2009 resulting in a more or less complete 12-hour synthesis run, see Table 3.3.

The data were partly calibrated using the CASA (formerly AIPS++)[2] package. The L-band receivers of the WSRT telescopes have linearly polarized feeds[3]. The leakage terms (D-terms) for the WSRT are frequency dependent (e.g., Brentjens 2008). As a first step, we flagged the autocorrelations, and removed any obvious RFI and corrupted data. Time ranges of antennas affected by shadowing were also taken out. Bandpass and gain solutions were determined using observations of two standard calibrators, both at the start and end of an observing run. The fluxes for the calibrators were set according to the Perley & Taylor (1999) extension to the Baars et al. (1977) scale. We used both polarized (3C138 or 3C286) and unpolarized (CTD93,

[2]http://casa.nrao.edu/

[3]The WSRT records XX = I − Q, YY = I − Q, XY = −U + iV, and XY = −U − iV, where I, Q, U, and V are the Stokes parameters.

3C48) calibrator sources. The bandpass and gain solutions were applied and the data were calibrated for the leakage terms using the unpolarized calibrator source. The polarization angles were set using the polarized calibrators sources, the angles being the same as in Sect. 3.2.2. The data was then exported into AIPS for two rounds of phase only and two rounds of amplitude and phase self-calibration (separately for each IF). The solutions for the amplitude and phase self-calibrations were determined by combing both XX and YY polarizations as Stokes Q is not necessarily zero.

The images for each IF were cleaned to about $2\sigma_{\rm rms}$ using clean boxes. The images for each IF were combined into a deep image by convolving the images of the individuals IFs to a common resolution and using a spectral index scaling of -1.

3.2.4 Optical WHT & INT imaging

Optical images around the radio sources were made using the PFIP camera on the 4.2m WHT telescope and the WFC camera on the INT. The observations were carried out between 15 and 19 April, 2009 (WHT) and 1 – 8 October, 2009 (INT). The field of view was $16' \times 16'$ for the PFIP and $34' \times 34'$ for the WFC camera. The seeing varied between $0.6''$ and $2.0''$, but was mostly between $1.0''$ and $1.5''$. Most nights were photometric. The total integration time per target was about 1500 s for both V, R, and I bands for the WHT observations and 4000 s for the INT observations. The data were reduced with IRAF (Tody 1986, 1993) and the *mscred* package (Valdes 1998). All images were flat-fielded and bias-corrected. The I and R band images were fringe corrected. The individual exposures were averaged, with pixels being rejected above $3.0\sigma_{\rm rms}$ to remove cosmic rays and other artifacts.

Zero-points were determined using various observations of standard stars taken during the nights. Images taken on non-photometric nights were scaled such that the flux of a few targets within the field of view agreed with that of the images taken on photometric nights.

3.3 Results

A list of the observed sources with their integrated fluxes and redshifts is given in Table 3.4. For sources without a spectroscopic redshift, we used the Hubble-K or Hubble-R relations to estimate the redshift (Willott et al. 2003; Snellen et al. 1996; de Vries et al. 2007). Spectral index maps were also made for the radio sources. Only common UV-ranges were used to minimize errors due to differences in the UV-coverage and the individual maps were convolved to the same resolution. For sources with high-resolution ($\lesssim 10''$) 1.4 GHz observations, we created a high-resolution spectral index map between 610 and 1425 MHz. A low-frequency spectral index map between 325 and 610 MHz was also made for most sources. Pixels below $4\sigma_{\rm rms}$ at either one of the two frequency maps were blanked. Low-resolution spectral index maps between 325, 610, and 1425 MHz were created to map the spectral index in low signal-to-noise ratio (SNR) regions. We fitted a single (power-law) spectral index through the three frequencies, pixels below $2.5\sigma_{\rm rms}$ being neglected.

For two sources, the SNR was high enough to create spectral curvature maps. The spectral curvature we defined as $\alpha_{325-610} - \alpha_{610-1425}$. Pixels with a spectral index error larger than 0.06 were blanked in the spectral curvature maps. The errors in the spectral index map are based on the noise levels (rms) of the individual images. In the following subsections, the radio and

spectral index maps are presented together with optical overlays.

3.3.1 VLSS J1133.7+2324, 7C 1131+2341

VLSS J1133.7+2324 is a filamentary radio source, possibly associated with a galaxy cluster at $z = 0.61$ (van Weeren et al. 2009c). To the west of the filamentary source, our 610 MHz image detected diffuse emission associated with the foreground galaxy UGC 6544 located at $z = 0.02385$ (Haynes et al. 1997).

The 325 MHz image (see Fig. 3.1 left panel), is similar to our previous 610 MHz image. In the 325 MHz image, the southern part of the filamentary source is significantly brighter than the northern part, while little emission from UGC 6544 is detected at 325 MHz. The VLA 1.4 GHz image made with natural weighting is shown in Fig. 3.1 (right panel) and reveals much more emission from UGC 6544. The southern part of the filamentary source is quite faint at 1.4 GHz, confirming that it has a steep spectrum. A high-resolution VLA image, also at 1.4 GHz, reveals only three faint compact radio sources, see Fig. 3.3 (left panel). This shows that the emission from the steep-spectrum source is truly diffuse, and cannot be attributed to the combined emission from compact sources. We do not detect any polarized emission from the source at 1425 MHz. We place a 5σ upper limit of 5% on the polarization fraction.

The spectral index map, between 325 and 610 MHz, is shown in Fig. 3.2 (left panel). The spectral index of the southern part of the filamentary source is -2.0, while for the rest of the diffuse emission it is $\alpha \sim -1.7$. Towards UGC 6544, the spectral index flattens. The spectral index map between 610 and 1425 MHz is shown in Fig. 3.2 (right panel). Here the spectral index steepens to $\alpha \leq -2.5$ for the southern part of the filamentary source. The spectral index of the foreground galaxy UGC 6544 is relatively flat with $\alpha \sim -0.5$.

VLSS J1133.7+2324 was also observed by Dwarakanath & Kale (2009) at 1287 MHz with the GMRT and at 330 MHz with the VLA. The reported integrated spectral indices were -1.6 ± 0.03 between 74 and 328 MHz and -1.9 ± 0.08 between 328 and 1278 MHz. The integrated flux density was 151 ± 12 mJy at 328 MHz. We measure a flux of 273 ± 28 mJy at 325 MHz, which is significantly higher than the reported value from Dwarakanath & Kale. This may be partly caused by the higher SNR of our image as we may pick up additional emission beyond what is visible in the Dwarakanath & Kale image. Although, this cannot completely explain the difference in fluxes.

The source could be old radio plasma from a previous episode of AGN activity, although UGC 6544 is a spiral galaxy which normally do not host AGN. If the radio emission were explained by relic lobes, they would be expected to be located symmetrically with respect to the nucleus of the galaxy, which is not the case. The flat spectrum radio emission we detect from the galaxy is fully consistent with that predicted by the far-infrared radio correlation (van Weeren et al. 2009c).

At the location of the filamentary radio source, we detected an overdensity of faint galaxies (see Fig. 3.3). These galaxies are partly hidden behind UGC 6544. The median SDSS photometric redshift is 0.61 for these galaxies. To confirm the presence of a cluster, X-ray observations and/or spectroscopic redshifts of several galaxies are needed.

If this is indeed a distant galaxy cluster, the radio emission is very likely to be associated with the cluster. The source may then trace a shock wave in the cluster where particles are accelerated by the DSA mechanism. In that case the integrated radio spectrum should be a single power-law. Our flux measurements however indicate a slightly curved spectrum. A redshift of 0.61

Table 3.4: Source list & properties

source/cluster	z	S_{325} Jy	S_{1425} mJy	$\alpha_{74-1400}$	curvature $\alpha_{74-610} - \alpha_{610-1425}$	LLS kpc	classification[h]
VLSS J1431.8+1331	0.1599	0.373 ± 0.040	14.6 ± 1.1	−2.03 ± 0.05	1.03[f]	125	AGN + AGNR or PHNX
VLSS J1133.7+2324	0.61 ± 0.16[g]	0.273 ± 0.028	12.3 ± 1.1	−1.69 ± 0.06	0.96	570[g]	AGNR or DSAR
Abell 2048	0.0972	0.559 ± 0.061	18.9 ± 4.3	−1.50 ± 0.05	1.6	310	PHNX
24P73	0.15 ± 0.1[b,g]	0.307 ± 0.033	12.0 ± 3.0	−2.20 ± 0.06	2.0	270	PHNX
VLSS J0004.9−3457	0.3 ± 0.1[e]	0.417 ± 0.046	32.2 ± 1.9	−1.40 ± 0.04	0.30[f]	200	AGN (or MH + DSAR?)
VLSS J0915.7+2511	0.324	0.417 ± 0.046	24.7 ± 1.5[a]	−1.52 ± 0.04	1.02	190	AGNR or PHNX
VLSS J1117.1+7003	0.8 ± 0.4[d]	0.030 ± 0.006[c]	2.9 ± 0.5[a]	−1.87 ± 0.07	0.0	130	AGN?
VLSS J2043.9−1118	0.5 ± 0.3[d]	...	7.7 ± 0.6[a]	−1.74 ± 0.05	0.84	250	AGN (MH? + DSAR?)
VLSS J0516.2+0103	1.2 ± 0.7[d]	...	4.3 ± 0.4[a]	−1.73 ± 0.06	0.0	290	AGN (or MH?)
VLSS J2209.5+1546	1.1 ± 0.7[d]	...	7.0 ± 0.9[a]	−1.56 ± 0.07	0.59	500	AGN?
VLSS J2241.3−1626	0.5 ± 0.3[d]	...	14.6 ± 1.1[a]	−1.44 ± 0.06	0.0	290	AGN?

[a] flux from NVSS (Condon et al. 1998)
[b] identification of the cD galaxy uncertain
[c] flux from WENSS (Rengelink et al. 1997)
[d] redshift estimated using the fitted Hubble-R relation from de Vries et al. (2007), since it is unclear whether there is a common underlying population of massive elliptical galaxies for extended steep-spectrum radio sources we have taken the 3C Hubble-R relation from Snellen et al. (1996) as an upper limit for the redshift (i.e., the 3C galaxies are about 1 mag brighter at the same redshift)
[e] redshift estimated using the fitted Hubble-K relation from Willott et al. (2003)
[f] varies across the source
[g] association with cluster uncertain
[h] PHNX = radio phoenix, AGNR = AGN relic, MH = radio mini-halo, DSAR = relic tracing shock wave with DSA

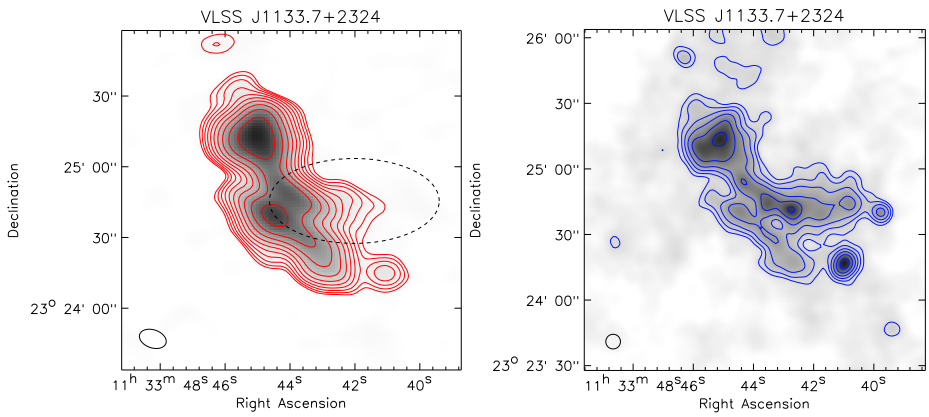

Figure 3.1: Left: GMRT 325 MHz map. Contour levels are drawn at $\sqrt{[1,2,4,8,\ldots]}\times 4\sigma_{\rm rms}$. The position of is UGC 6544 is indicated by the dashed ellipse. Right: VLA 1425 MHz map. Contour levels are drawn as in the left panel.

would correspond to a physical size of about 500 kpc. The very steep and somewhat curved radio spectrum then suggest the source to be an AGN relic, rather than a radio phoenix because the source is quite large and the time to compress such a large radio "ghost" would remove most of the electrons responsible for the radio emission by radiative energy losses (Clarke & Ensslin 2006). Additional flux measurements at lower and/or higher frequencies will be needed to confirm whether the radio spectrum is indeed curved.

3.3.2 VLSS J1431.8+1331, MaxBCG J217.95869+13.53470

VLSS J1431.8+1331 is located in the galaxy cluster MaxBCG J217.95869+13.53470 (z = 0.1599, Koester et al. 2007) and associated with the central cD galaxy of the cluster. The cluster has a moderate X-ray luminosity of $L_{\rm X,\ 0.1-2.4\ keV} \sim 1\times 10^{44}$ erg s^{-1} based on the ROSAT count rate (Voges et al. 1999). The GMRT 325 MHz image (see top left panel Fig. 3.4) shows a bright elongated source. To the west a somewhat fainter diffuse component can be seen. This component is not associated with any optical galaxy (see Fig. 3.3, right panel). A third fainter source is located further to the southwest. The first two components are connected by a faint radio "bridge". This bridge was not seen in our previous 610 MHz image. The bright source is a currently active radio galaxy with the radio core clearly being visible in our VLA 1.4 GHz images (see Fig. 3.4 top middle and right panels). Probably, radio plasma from the core flows westwards and then forms the north-south elongated structure.

The spectral index maps (see Fig. 3.4 bottom panels), are indicative of a relatively flat spectral index of −0.5 for the radio core between 325 and 610 MHz. Spectral steepening is observed to the north and south of the elongated structure. The spectral index for the southern part of the elongated structure steepens to −3.5 between 610 and 1425 MHz. The spectral index of the southwestern component is about −1.5 between 325 and 610 MHz, there being smaller spectral index variations across it than in the brighter western component. Between 610 and 1425 MHz, the spectral index steepens to about −2.5. The spectral curvature map ($\alpha_{325-610} - \alpha_{610-1425}$) (see

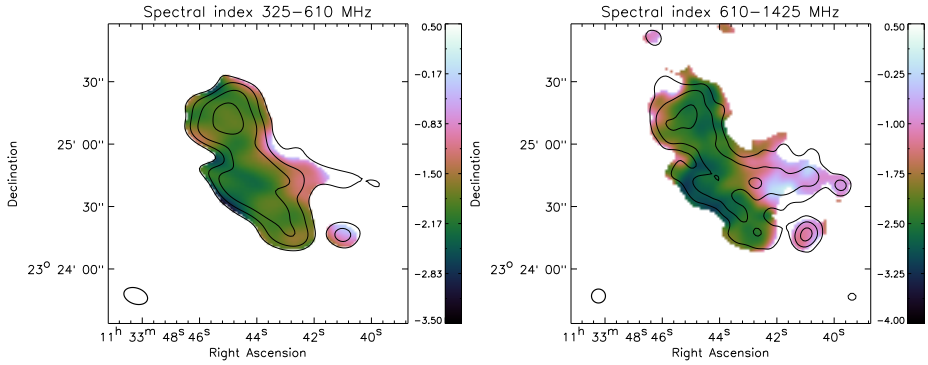

Figure 3.2: Left: Spectral index map between 325 and 610 MHz at a resolution of $11.75'' \times 7.65''$. Contour levels are from the 325 MHz GMRT image and drawn at levels of $[1, 2, 4, 8, \ldots] \times 6\sigma_{\rm rms}$. Right: Spectral index between 610 and 1425 MHz. Contour levels are from the 1425 MHz VLA image and drawn at levels of $[1, 2, 4, 8, \ldots] \times 5\sigma_{\rm rms}$. The beam size is $6.7'' \times 6.7''$.

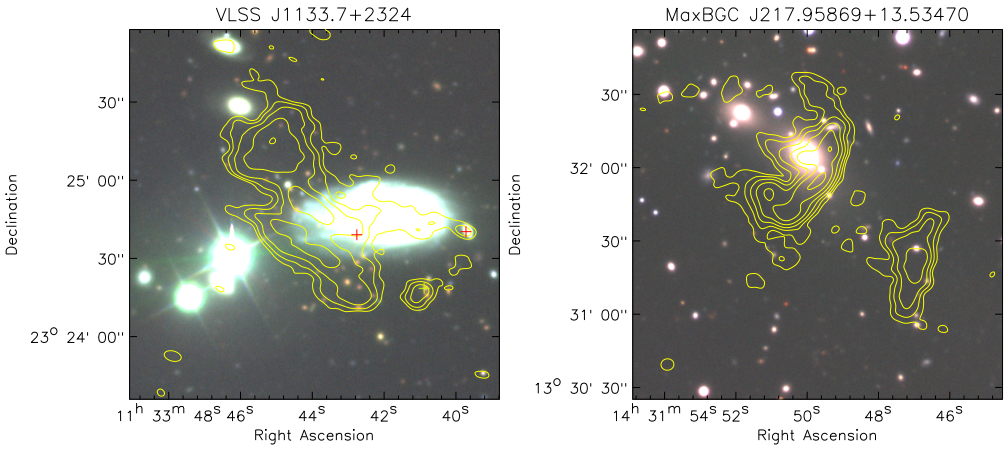

Figure 3.3: Left: Optical WHT color image for VLSS J1133.7+2324. GMRT 610 MHz contours are overlaid. The beam size is $6.6'' \times 3.9''$. Three compact sources detected in the VLA 1425 MHz high-resolution image are marked with crosses. Right: Optical WHT color image for MaxBCG J217.95869+13.53470. GMRT 610 MHz contours are overlaid. The beam size is $5.3'' \times 4.8''$. Contour levels are drawn as in the left panel.

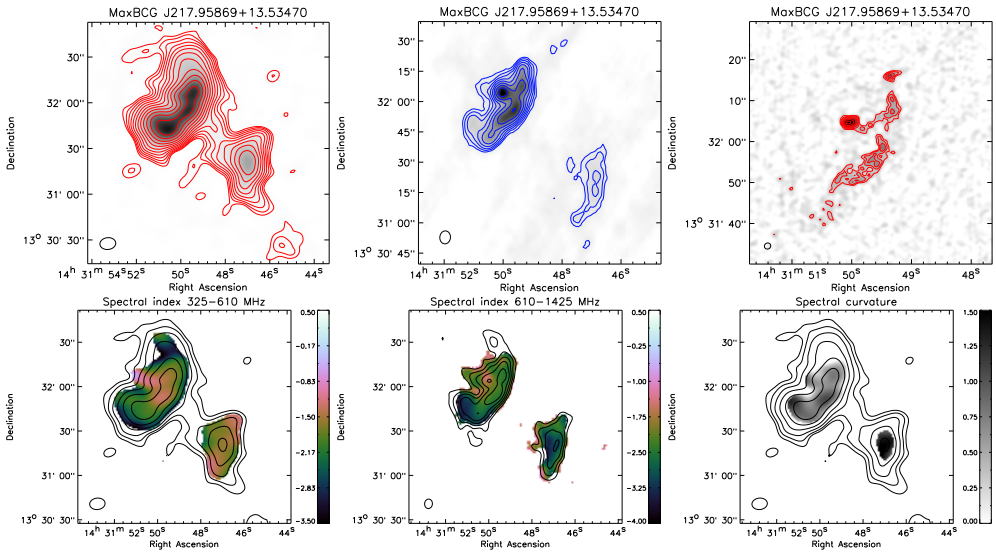

Figure 3.4: Top left: GMRT 325 MHz map. Contour levels are drawn as in Fig. 3.1. Top middle: VLA 1425 MHz map. Contour levels are drawn as in Fig. 3.1. Top right: VLA 1425 MHz high-resolution image. The image was made using Briggs weighting with robust set to −1. Contour levels are drawn at $\sqrt{[1,2,4,8,\ldots]} \times 4\sigma_{\rm rms}$. Bottom left: Spectral index map between 325 and 610 MHz at a resolution of $10.4'' \times 7.7''$. Contour levels are from the 325 MHz GMRT image and drawn at levels of $[1,2,4,8,\ldots] \times 6\sigma_{\rm rms}$. Bottom middle: Spectral index between 610 and 1425 MHz. Contour levels are from the 610 MHz GMRT image and drawn at levels of $[1,2,4,8,\ldots] \times 5\sigma_{\rm rms}$. The beam size is $6.41'' \times 5.26''$. Bottom right: Spectral curvature map. Contour levels are drawn as in the left panel and the resolution is $10.4'' \times 7.7''$.

Fig. 3.4 bottom right panel), shows that the southwestern source has a very curved radio spectrum. The southern end of the radio structure from the active AGN is also quite curved. The high spectral curvature is likely to be the result of spectral ageing, the gradient in the spectral index away from the core providing evidence of this. The two diffuse sources the southwest of the active AGN are probably old "bubbles" of radio plasma linked to this AGN, which is consistent with the curved radio spectrum. The presence of a faint radio bridge also suggests a relation between this southwestern component and the radio galaxy. The southwestern component can therefore be classified as a radio phoenix (if the radio plasma has been compressed) or an AGN relic. XMM-Newton observations of the cluster will be presented by Ogrean et al. (submitted).

3.3.3 VLSS J2217.5+5943, 24P73

This source was discovered during the Synthesis Telescope of the Dominion Radio Observatory (DRAO) Galactic plane survey at 408 MHz and 1.42 GHz (Higgs 1989; Joncas & Higgs 1990). Green & Joncas (1994) found the source to be diffuse and have an ultra-steep spectrum ($\alpha = -2.58 \pm 0.14$). Our GMRT 610 MHz observations (see Fig. 3.5 bottom right panel) detected a very complex filamentary source, resembling the relics found in Abell 13 and Abell 85 (Slee et al. 2001). Our GMRT 325 MHz image, Fig. 3.5 top left panel, is similar to the 610 MHz

image. In our combined WSRT 1.3 – 1.8 GHz image (top right panel), the fainter western part of the relic is only marginally detected, which is indicative of a steep spectral index in this region. We set an upper limit to the polarization fraction of 5% for the source at 1.4 GHz.

The spectral index map between 325 and 610 MHz is shown in the bottom left panel of Fig. 3.5. The spectral index varies between −1.4 and −2.9 over the source. The western part of the source has the steepest spectrum. Towards the southwest, the spectral index flattens to about −1.0. This part may be associated with a separate compact radio AGN.

Our optical WHT image (bottom right panel Fig. 3.5) is dominated by foreground stars as the source is located in the Galactic plane, at Galactic latitude of 2.44 degrees. However, there are also several faint red galaxies seen in the image that may belong to a galaxy cluster, and these are marked by circles. The brightest galaxy (located southwest) has an R-band magnitude of 20.69. Using the Hubble-R relation (de Vries et al. 2007), we estimate a redshift of 0.15 ± 0.1, including an extinction in the R-band of 4.173 mag (Schlegel et al. 1998). We note that this redshift estimate is based on the corrected identification of the cD galaxy in the cluster. If the source is indeed located at $z = 0.15$, then its largest physical extent is 270 kpc. We classify the source as a radio phoenix given the filamentary morphology and extreme spectral index. In fact, the relic is very similar to the proposed phoenix in Abell 13 (Slee et al. 2001). To confirm the presence of a cluster, deep near-infrared (NIR) imaging will be necessary.

3.3.4 VLSS J0004.9−3457

The radio source is located in a small galaxy cluster or group, B02291 (Zanichelli et al. 2001). The cluster/group is located at a redshift of 0.3 ± 0.1 (van Weeren et al. 2009c). No X-ray emission from the system is detected in the ROSAT All-Sky Survey (Voges et al. 1999, 2000), which implies that the system is not very massive. An optical POSS-II color composite is shown in Fig. 3.6 (bottom right panel). The various radio components are labeled alphabetically (see Fig. 3.6 top right panel).

Our GMRT 325 MHz image of VLSS J0004.9−3457 (top left panel) displays a diffuse source (A) centered on a K-mag=14.86 galaxy. The source extends somewhat further northwards than in the 610 MHz image (bottom right panel).

Source B is associated with another galaxy, C does not have an optical counterpart and seems to be related to source A. Source D is a fainter source (resolved in the 610 MHz image) located just east of VLSS J0004.9−3457 at RA $00^{\rm h}\ 04^{\rm m}\ 50^{\rm s}$, Dec $-34^\circ\ 56'\ 38''$. In the CnB-array VLA 1.4 GHz image, shown in Fig. 3.6 (top right), component C is less prominent than in the 325 MHz image, while source B is clearly visible.

The spectral index map between 325 and 610 MHz is shown in Fig. 3.7 (right panel). Source B has a flat spectral index of ~ -0.5. Source D has a steeper spectral index of −1.1. The spectral index of A steepens away from the center (defined as the peak flux and located at the position of the K-mag=14.86 galaxy). The central region has a spectral index of −1.2. Outwards, the spectral index steepens to < -2. Component C has a spectral index of about −1.5. A spectral index map, for the frequencies 325, 610, and 1425 MHz, is shown in Fig. 3.7 (middle panel). The spectral curvature map, in the right panel of Fig. 3.7, shows the least curvature (i.e., less than 0.5 units) for the western part of A and source B. Emission to the east of A shows more spectral steepening, with a curvature of about 1.0 units.

Polarized emission from source A, B, and component C is observed in the VLA images, Fig. 3.6 (bottom left panel). Source B is polarized at the 8% level. The polarization fraction at

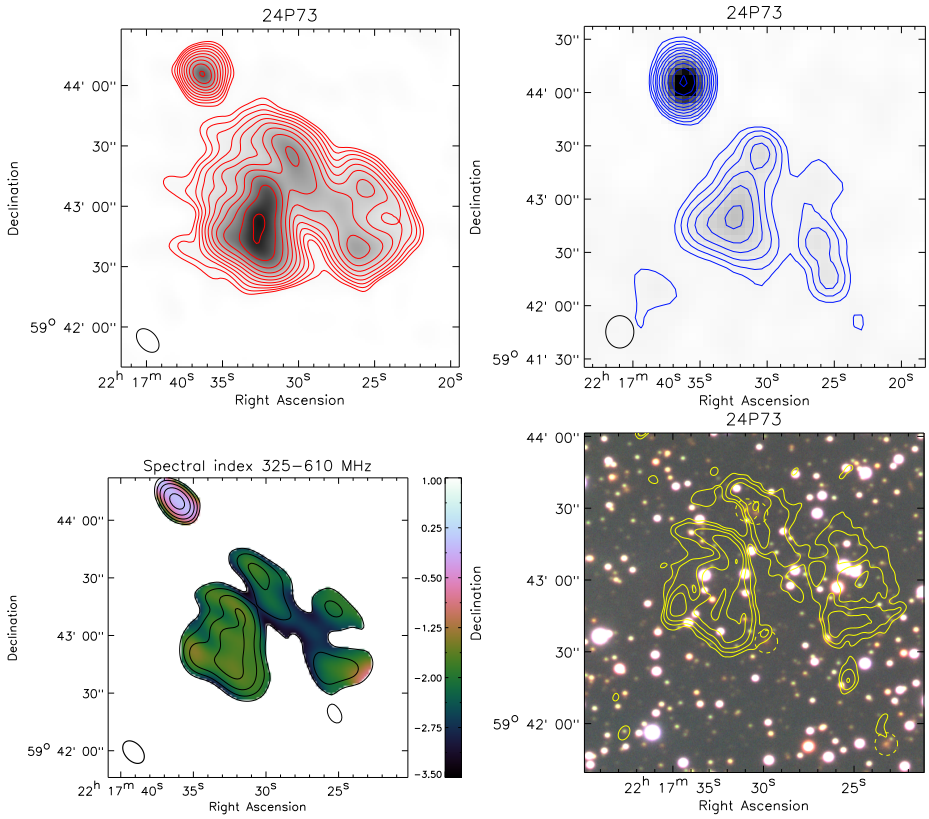

Figure 3.5: Top left: GMRT 325 MHz map. Contour levels are drawn as in Fig. 3.1. Top right: WSRT 1.3 – 1.8 GHz map. Contour levels are drawn as in Fig. 3.1. Bottom left: Spectral index map between 325 and 610 MHz at a resolution of $13.44'' \times 8.96''$. Contour levels are from the 325 MHz image and drawn as in Fig. 3.2. Bottom right: Optical WHT color image for 24P73. GMRT 610 MHz contours are overlaid. The beam size is $6.4'' \times 4.3''$. Contour levels are drawn as in Fig.3.3. Several faint galaxies in the image are marked by circles.

the center of A is roughly 6%. The arc-like southeast extension (C) is highly polarized, with a polarization fraction between 25 and 35%.

We tentatively classify the source as a 200 kpc "mini-halo" (or core-halo), because the radio emission of diffuse source A surrounds a central galaxy in a cluster or galaxy group. The spectral steepening away from the core is then the result of synchrotron and IC losses. The eastern arc-like extension could be a radio relic based on its elongated nature and high polarization fraction. The high polarization fraction is indicative of the presence of ordered magnetic fields. Therefore it is likely that this component traces a region in the ICM that has been compressed by a shock wave. Radio mini-halos usually occur in massive relaxed galaxy clusters. The possible presence of a radio relic indicates merger activity so it is possible that the "mini-halo" can also be linked to the merger activity of the system. Radio plasma from the central AGN might have been re-accelerated or compressed by this merger event. The source is somewhat similar to MRC 0116+111 studied by Gopal-Krishna et al. (2002) and Bagchi et al. (2009). We find that MRC 0116+111 exhibits two bubble-like radio lobes, whereas VLSS J0004.9−3457 seems to consist of a single component. The morphology of the source is more similar to the core-halo system in ZwCl 1454.8+2223 and candidate core-halo system in Abell 3444 (Venturi et al. 2008, 2007). The cluster/group would make an interesting target for future X-ray observations to study the relation between the radio sources and the surrounding ICM.

3.3.5 VLSS J0915.7+2511, MaxBCG J138.91895+25.19876

The radio source is located in the cluster MaxBCG J138.91895+25.19876. The source consists of a northern component (Fig. 3.8 left panel) and a slightly more extended fainter component to the south. A compact source to the west is associated with the galaxy J091539.68+251136.9. This source has a spectroscopic redshift (SDSS DR7, Abazajian et al. 2009) of 0.324. This cluster has a photometric redshift of 0.289 (Koester et al. 2007), but the galaxy seems to be part of the cluster, hence we adopt a redshift of 0.324 for the cluster. The compact source is resolved in our 610 MHz GMRT image and displays a double lobe structure (see Fig.3.8 right panel).

The spectral index map between 325 and 610 MHz is shown in Fig. 3.8 (middle panel). The spectral index map is noisy because of dynamic range limitations from the source 4C +25.24 (1.35 Jy at 325 MHz) located about 3′ to the southeast. The eastern part of the northern component has the steepest spectrum with an index of $\alpha \sim -2$, although the SNR is low in this region. The compact source to the west has a flat spectral index of about −0.2.

The classification of the source is unclear. The source might contain old radio plasma that originated in the AGN to the west. In this case, the source could be classified as a radio phoenix or AGN relic.

3.3.6 VLSS J1515.1+0424, Abell 2048

VLSS J1515.1+0424 is located in the cluster Abell 2048 ($z = 0.0972$; Struble & Rood 1999) to the east of the cluster center. The source has a largest extent of 310 kpc (see Fig. 3.9 top left panel), and has a complex morphology. Only the brighter parts of the source are seen in the VLA 1.4 GHz C-array image (Fig. 3.9 top right panel). No polarized flux is detected from the source. We set an an upper limit on the polarization fraction of 8% for the source, again requiring a SNR of 5 for a detection. An optical V, R, and I color image of the cluster with 610 MHz contours overlaid does not reveal an obvious optical counterpart for the source.

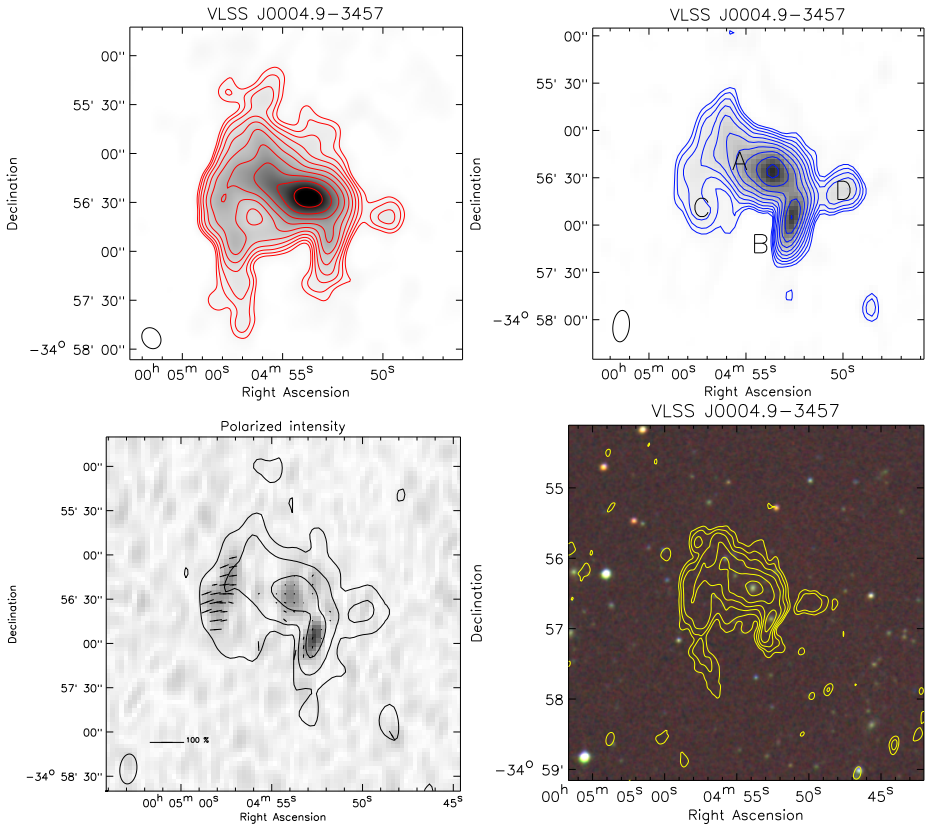

Figure 3.6: Top left: GMRT 325 MHz map. Contour levels are drawn as in Fig. 3.1. Top right: VLA 1425 MHz map. Contour levels are drawn as in Fig. 3.1. Bottom left: VLA 1425 MHz polarization map. Total polarized intensity is shown as grayscale image. Vectors refer to the polarization E-vectors, with their length representing the polarization fraction. A reference vector for a polarization fraction of 100% is shown in the bottom left corner. The polarization fractions were corrected for Ricean bias (Wardle & Kronberg 1974). No polarization E-vectors were drawn for pixels with a SNR less than 3 in the total polarized intensity map. Contours show the total intensity image (Stokes I) at 1425 MHz. Contour levels are drawn at $[1, 16, 256, 4096, \ldots] \times 0.147$ mJy beam^{-1}. Bottom right: Optical POSS-II color image for VLSS J0004.9−3457. GMRT 610 MHz contours are overlaid. The beam size is $6.4'' \times 4.3''$. Contour levels are drawn as in Fig.3.3.

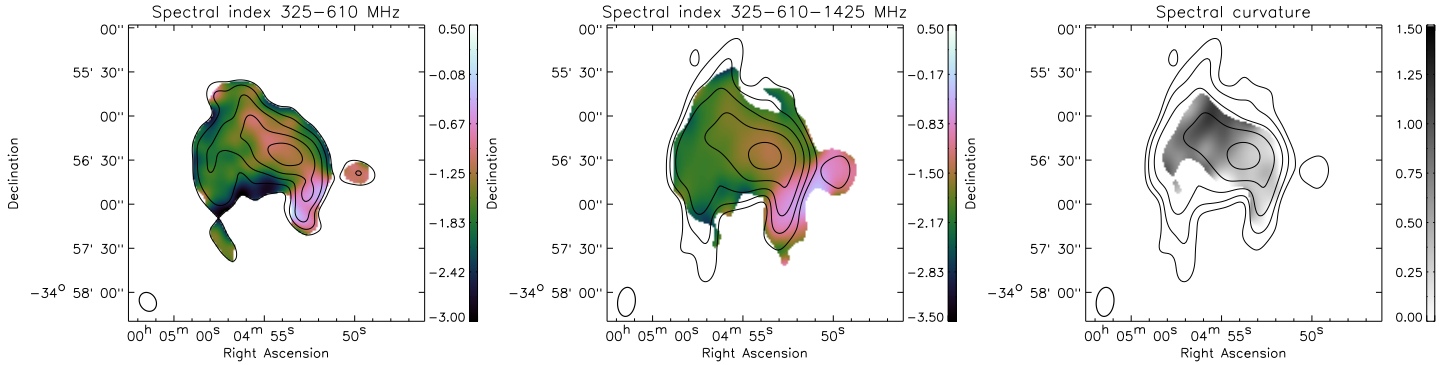

Figure 3.7: Left: Spectral index map between 325 and 610 MHz at a resolution of $13.5'' \times 11.0''$. Contour levels are from the 325 MHz image and drawn as in Fig. 3.2. Middle: Power-law spectral index fit between 325, 610, and 1425 MHz. Contours are from the 325 MHz image and drawn at levels of $[1, 2, 4, 8, \ldots] \times 4\sigma_{\mathrm{rms}}$. The beam size is $19.83'' \times 12.0''$. Right: Spectral curvature map. Contour are drawn as in the middle panel.

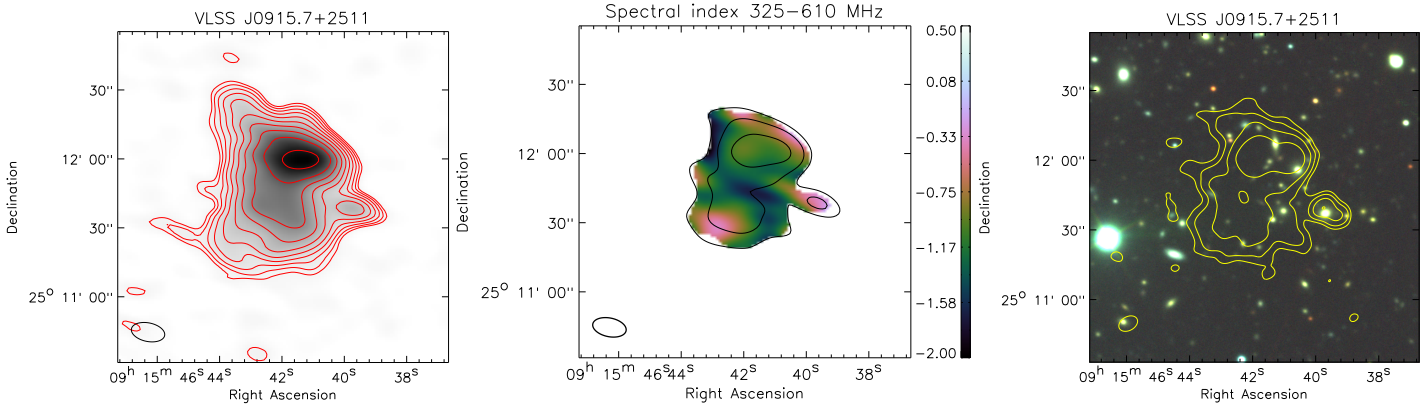

Figure 3.8: Left: GMRT 325 MHz map. Contour levels are drawn as in Fig. 3.1. Middle: Spectral index map between 325 and 610 MHz at a resolution of 14.7″ × 8.1″. Contour levels are from the 325 MHz image and drawn as in Fig. 3.2. Right: Optical WHT color image for VLSS J0915.7+2511. GMRT 610 MHz contours are overlaid. The beam size is 8.6″ × 5.9″. Contour levels are drawn as in Fig.3.3.

The spectral index map between 325, 610, and 1425 MHz, is shown in Fig. 3.9 (bottom left panel). No systematic spectral index gradients are seen across the source. A region with a flat spectral index ($\alpha > -0.5$) is located under the southern "arm" of the source at RA $15^{\rm h}\,15^{\rm m}\,08.6^{\rm s}$, Dec $+04^\circ\,23'\,08''$. This part is associated with the galaxy 2MASX J15150860+0423085 in front of the cluster ($z = 0.047856$ from SDSS DR7) (see Fig. 3.9 bottom right panel). The spectral index of the relic is steep with an average value of about -1.7 between 1425 and 325 MHz.

The complex morphology of the radio source suggests that the source can be classified as a radio phoenix. The steep curved radio spectrum is consistent with this interpretation. If the source is indeed a radio phoenix, the radio plasma should have originated in a galaxy that has gone through phases of AGN activity. A candidate is the elliptical galaxy MCG +01−39−011 ($z = 0.095032$; Slinglend et al. 1998). This galaxy is currently active and located close to the eastern end of the southern "arm". However, there are several other elliptical galaxies around, although at the moment they are not radio-loud. A ROSAT image (see van Weeren et al. 2009c) of the cluster shows a substructure to the east of the main cluster, which implies that the cluster is presently undergoing a merger. The velocity dispersion, σ, of the galaxies in the cluster is 857 km s^{-1} (Shen et al. 2008). The bolometric X-ray luminosity is 1.914×10^{44} erg s^{-1}. On the basis of the $L_{\rm X} - \sigma$ relation (X-ray luminosity versus velocity dispersion) from Shen et al.

$$\log\left(\frac{L_X}{10^{44}\ \mathrm{erg\ s^{-1}}}\right) = 4.39 \log\left(\frac{\sigma}{500\ \mathrm{km\ s^{-1}}}\right) - 0.530\,, \tag{3.1}$$

we predict a velocity dispersion of 765 ± 40 km s^{-1} given the X-ray luminosity. This is lower than the observed value, which is not inconsistent with the cluster having undergone a recent merger event. A shock wave generated by the proposed merger event might have compressed fossil radio plasma and produced the radio phoenix. Future X-ray observations will be needed to study the dynamical state of the cluster and the relation between the ICM and the radio phoenix.

3.4 Optical imaging around five compact steep-spectrum sources

We present optical images around five slightly more compact steep-spectrum radio sources, which nature was found to be unclear in van Weeren et al. (2009c).

3.4.1 VLSS J2043.9−1118

The radio source has a largest angular size of 41″. An optical counterpart (R band magnitude of 20.1) is visible in our WHT image (see Fig. 3.10). The radio emission surrounds the galaxy and there is a hint of a faint extension to the east. We estimate a redshift of 0.5 ± 0.3 for the optical counterpart, which implies a physical extent of 250 kpc for the radio source. The source could be a mini-halo or core-halo system given its steep spectral index of -1.74 ± 0.05 (between 74 and 1400 MHz). Alternatively, we are detecting radio plasma from an AGN that has undergone a significant amount of spectral ageing.

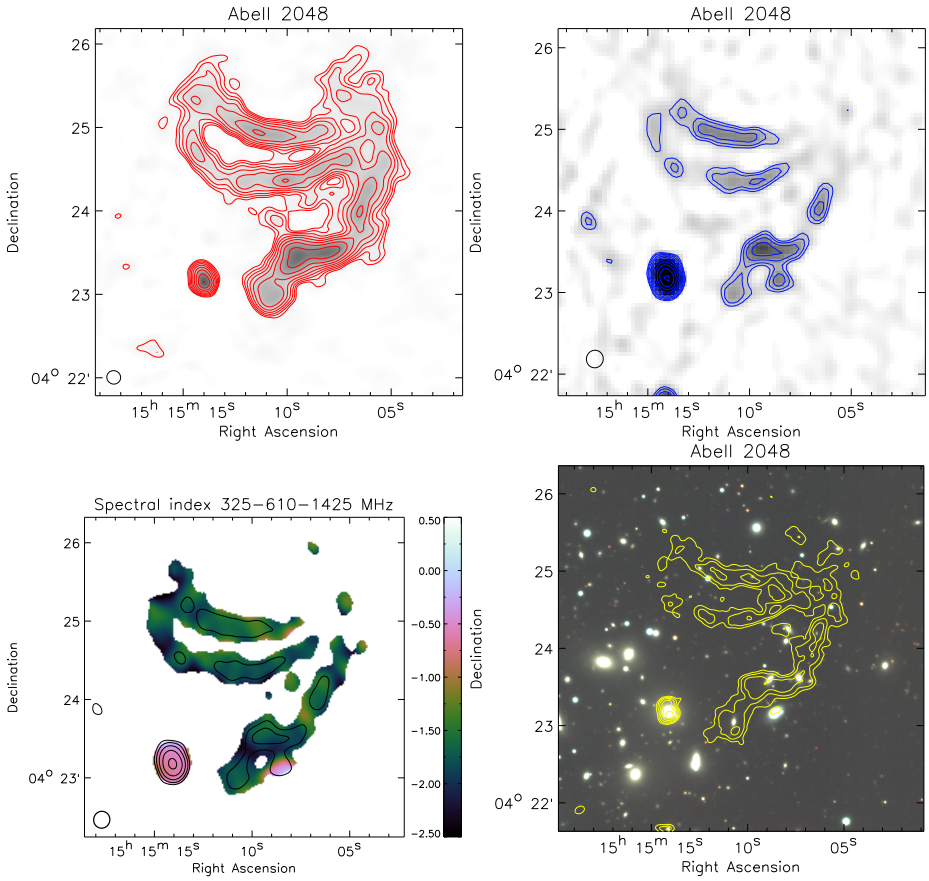

Figure 3.9: Tot left: GMRT 325 MHz map. Contour levels are drawn as in Fig. 3.1. Top right: VLA 1425 MHz map. Contour levels are drawn as in Fig. 3.1. Bottom left: Power-law spectral index fit between 325, 610, and 1425 MHz. Contours are from the 1.4 GHz VLA image and drawn as in Fig. 3.2 (left panel). The resolution is $13.0'' \times 12.4''$. Bottom right: Optical WHT color image for Abell 2048. GMRT 610 MHz contours are overlaid. The beam size is $7.6'' \times 5.4''$. Contour levels are drawn as in Fig.3.3.

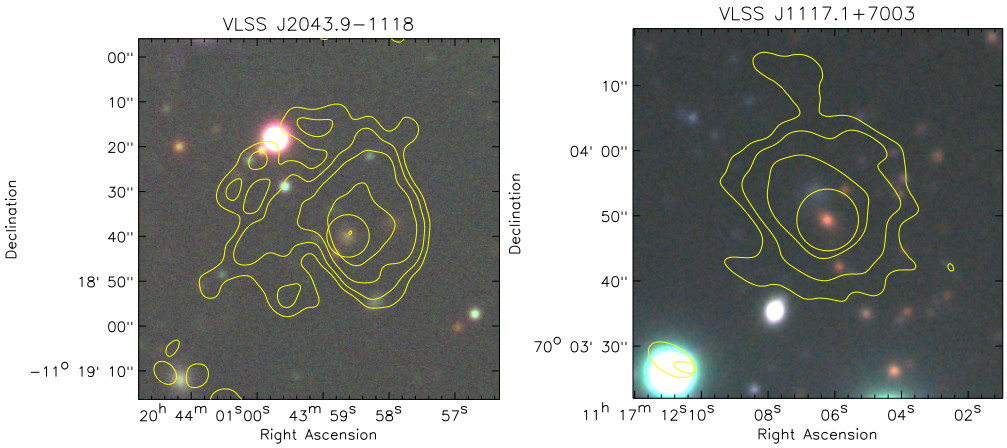

Figure 3.10: Left: Optical WHT color image for VLSS J2043.9−1118. GMRT 610 MHz contours are overlaid. The beam size is 5.8″ × 4.2″. Contour levels are drawn as in Fig.3.3. A circle indicates the proposed optical counterpart. Right: Optical WHT color image for VLSS J1117.1+7003. GMRT 610 MHz contours are overlaid. The beam size is 7.8″ × 4.3″. Contour levels are drawn as in Fig.3.3. A circle indicates the proposed optical counterpart.

3.4.2 VLSS J1117.1+7003

This source has a remarkably steep radio spectrum ($\alpha_{74-1400} = -1.87 \pm 0.07$) without any indication of a spectral turnover at low frequencies. The source is resolved into a smooth featureless roughly spherical blob (26″ by 23″). We identify a red galaxy, with an R magnitude of 21.2, as a possible counterpart, which would put the source at a redshift of 0.8 ± 0.4. A blue galaxy is located only 5″ north of the red galaxy. This might also be the counterpart of the radio source. The integrated R-band magnitude is about the same as the redder galaxy putting it at about the same redshift if it were the optical counterpart. At $z = 0.8$, the radio emission would have a physical extent of 130 kpc.

3.4.3 VLSS J2209.5+1546

The radio map shows an elongated source. We find a faint (R band magnitude of 22.4) counterpart halfway along the elongated source. We estimate a redshift of $z = 1.1 \pm 0.7$ (using the Hubble-R relation), giving a physical extent of 500 kpc.

3.4.4 VLSS J0516.2+0103

VLSS J0516.2+0103 is a slightly elongated source that does not have an optical counterpart in POSS-II images. In our INT image, we identify a possible faint red counterpart with an R magnitude of 22.9. This implies a redshift of 1.2 ± 0.7 (including an extinction of 0.367 in the R band), which gives a size of 290 kpc and makes it a candidate mini-halo or core-halo system.

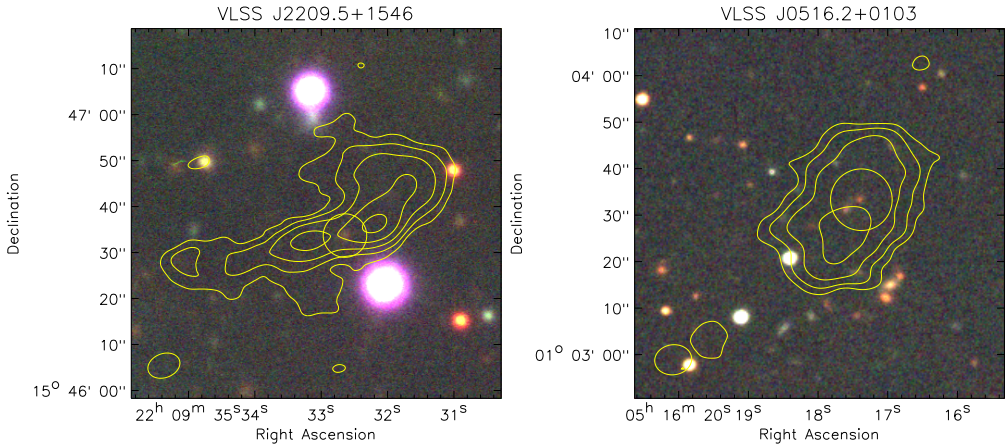

Figure 3.11: Left: Optical WHT color image for VLSS J2209.5+1546. GMRT 610 MHz contours are overlaid. The beam size is 6.9″ × 6.2″. Contour levels are drawn as in Fig.3.3. A circle indicates the proposed optical counterpart. Right: Optical INT color image for VLSS J0516.2+0103. GMRT 610 MHz contours are overlaid. The beam size is 8.1″ × 6.5″. Contour levels are drawn as in Fig.3.3. A circle indicates the proposed optical counterpart.

3.4.5 VLSS J2241.3−1626

The morphology of this source is complex. A potential optical counterpart has an R-band magnitude of 20.2 giving a redshift of 0.5 ± 0.3 and a physical extent of 290 kpc for the source. The optical counterpart is located roughly halfway along the extended source. The enhancements in the radio emission to the east and west of the proposed counterpart suggest that these are the lobes of an AGN. The fainter more-extended radio emission might be older radio plasma causing the steep radio spectrum.

3.5 Discussion

Most radio relics and halos known till date are located within massive X-ray luminous clusters. The majority of these sources were discovered in the NVSS and WENSS surveys by visual inspection of the radio maps in and around known galaxy clusters (mostly Abell clusters, Giovannini et al. 1999; Kempner & Sarazin 2001). Venturi et al. (2007, 2008) carried out a search in a complete sample of 50 massive X-ray selected ($L_{\mathrm{X,\ 0.1-2.4\ keV}} > 5 \times 10^{44}$ erg s^{-1}) clusters to determine the fraction of radio halos in these systems. The fraction of clusters hosting a giant radio halo was found to be 0.29 ± 0.09. The number of small galaxy clusters with low X-ray luminosity known to host a diffuse radio source is very small. An example is the radio halo in Abell 1213 identified by Giovannini et al. (2009) with $L_{\mathrm{X,\ 0.1-2.4\ keV}} = 0.1 \times 10^{44}$ erg s^{-1}.

We note that the sources presented in this paper were selected on the basis of their steep spectral index and diffuse nature. There was no requirement for the radio sources to be located in a galaxy cluster. The question arises of whether most radio relics and halos are indeed located in massive galaxy clusters or whether they also occur in poor clusters and galaxy groups.

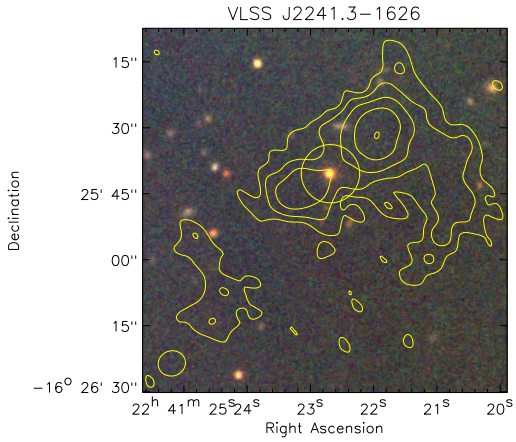

Figure 3.12: Optical INT color image for VLSS J2241.3−1626. GMRT 610 MHz contours are overlaid. The beam size is 6.1″×5.8″. Contour levels are drawn as in Fig.3.3. A circle indicates the proposed optical counterpart.

None of the sources in our sample, with $\alpha < -1.35$ (between 74 and 1400 MHz), are located in massive known galaxy clusters. Only VLSS J1515.1+0424 (in Abell 2048) and VLSS J1431.8+1331 (in MaxBCG J217.95869+13.53470) are found in clusters detected in the ROSAT All-Sky Survey. The X-ray luminosities of these clusters are moderate, with values between 1–2 $\times 10^{44}$ erg s^{-1}. Therefore, our observations indicate that diffuse steep-spectrum sources do also occur in less massive clusters and galaxy groups. Most of the sources seem to be radio relics related to previous episodes of AGN activity: either AGN relics or radio phoenices. Some other sources in our sample can be classified as core-halo or mini-halo candidates, where the radio emission surrounds a central galaxy of a poor cluster or galaxy group. In our case, they are not found in massive cool-core clusters.

Amongst the sources in our sample, there are also a number of more distant ($z \sim 1$) filamentary radio sources related to AGN activity. These could be relatively "nearby" ultra-steep spectrum (USS) sources (e.g., see Miley & De Breuck 2008, for a review). As they are relatively nearby, they are clearly extended in for example the 1.4 GHz FIRST survey images (5″ resolution) and therefore included in our sample.

We did not detect any ultra-steep spectrum radio halos (Brunetti et al. 2008) in our sample. This could be because the surface brightness of these objects is too low for them to be detected in the 74 MHz VLSS survey (Brunetti et al. 2008; Macario et al. 2010). The 74 MHz VLSS survey is relatively shallow with an average rms noise of 0.1 Jy beam^{-1}.

Since poor galaxy clusters and groups are more numerous, it is expected that the sources in our sample are only the tip of the iceberg and many more of them should turn up in low-frequency surveys, as will be carried out for example by LOFAR in the near future. In terms also of the timescales related to AGN activity and the ubiquity of shocks, these surveys will uncover large populations of AGN relics and radio phoenices. One of the difficulties will be to classify these sources on the basis of the radio morphology, polarization, and spectral index alone. The differences between radio phoenices, AGN relics, and relics tracing shock fronts with DSA are

often subtle. The AGN relics and phoenices should have very curved radio spectra, while relics caused by electrons accelerated at shocks should have straight radio spectra. Nevertheless, deep optical/NIR and X-ray surveys will play an important role in identifying the nature of these diffuse radio sources.

3.6 Conclusions

We have presented 325 MHz and 1.4 GHz radio observations of six diffuse steep-spectrum sources. The sources were selected from an initial sample of 26 diffuse steep-spectrum ($\alpha < -1.15$) sources (van Weeren et al. 2009c). Optical WHT and INT images were taken at the positions of 10 radio sources from the sample. We briefly summarize the results.
-The radio source VLSS J1431.8+1331 is located in the cluster MaxBCG J217.95869+13.53470 ($z = 0.16$) and associated with the central cD galaxy. A second radio source is located 175 kpc to the east. This source is connected by a faint radio bridge to the central radio source. This source probably traces an old bubble of radio plasma from a previous episode of AGN activity of the central source. The spectral curvature of this source is large, indicating the radio plasma is old, which is consistent with the above scenario.
-VLSS J1133.7+2324 is an elongated filamentary steep spectrum source, the nature of the source is unclear. It might be a radio relic located in a galaxy cluster at $z \sim 0.6$.
-The relic in Abell 2048 and the source 24P73 are both classified as radio phoenices, which consist of compressed fossil radio plasma from AGNs. We detect several galaxies close to 24P73, probably belonging to the cluster hosting the radio phoenix.
-VLSS J0004.9−3457 is a diffuse radio source with emission surrounding the central elliptical galaxy of a small cluster or galaxy group. The source could be a radio mini-halo (or core-halo system). An arc-like structure is located to the east of the source which has a high polarization fraction of about 30% at 1.4 GHz indicative of ordered magnetic fields. This is probably a relic, where either particles are accelerated by the DSA mechanism or radio plasma from the central AGN is compressed.
-The origin of VLSS J0915.7+2511, a diffuse radio source in MaxBCG J138.91895+25.19876, is somewhat unclear. The source is most likely an AGN relic or radio phoenix.
We also presented optical images around five other diffuse radio source from the sample. For these sources, we could not find optical counterparts in POSS-II and 2MASS images. We detected candidate counterparts for all of these sources with redshifts in the range $0.5 < z < 1.2$. Some of these sources are radio galaxies, some others may be classified as mini-halos as the radio emission surrounds the host galaxy.

From our observations, we conclude that radio relics are located not only in the most massive merging galaxy clusters. They can also be found in smaller galaxy clusters and groups. Most of these sources probably trace old radio plasma from previous episodes of AGN activity. Several other sources resemble mini-halos or core-halos that are also found in less massive systems. Future low-frequency surveys will probably uncover large numbers of these sources, which can then be used to constrain timescales related to AGN activity and study the interaction between radio plasma and the ICM in clusters and galaxy groups.

Acknowledgements. We thank the staff of the GMRT who have made these observations possible. The GMRT is run by the National Centre for Radio Astrophysics of the Tata Institute of Fundamental Research.

The Westerbork Synthesis Radio Telescope is operated by ASTRON (Netherlands Institute for Radio Astronomy) with support from the Netherlands Foundation for Scientific Research (NWO). The National Radio Astronomy Observatory is a facility of the National Science Foundation operated under cooperative agreement by Associated Universities, Inc. The William Herschel Telescope and Isaac Newton Telescope are operated on the island of La Palma by the Isaac Newton Group in the Spanish Observatorio del Roque de los Muchachos of the Instituto de Astrofísica de Canarias.

This publication makes use of data products from the Two Micron All Sky Survey, which is a joint project of the University of Massachusetts and the Infrared Processing and Analysis Center/California Institute of Technology, funded by the National Aeronautics and Space Administration and the National Science Foundation. This research has made use of the VizieR catalogue access tool, CDS, Strasbourg, France.

The Digitized Sky Surveys were produced at the Space Telescope Science Institute under U.S. Government grant NAG W-2166. The images of these surveys are based on photographic data obtained using the Oschin Schmidt Telescope on Palomar Mountain and the UK Schmidt Telescope. The plates were processed into the present compressed digital form with the permission of these institutions. The Second Palomar Observatory Sky Survey (POSS-II) was made by the California Institute of Technology with funds from the National Science Foundation, the National Geographic Society, the Sloan Foundation, the Samuel Oschin Foundation, and the Eastman Kodak Corporation.

RJvW would like to thank S. van der Tol for helping with the observations. RJvW acknowledges funding from the Royal Netherlands Academy of Arts and Sciences.

CHAPTER 4

Radio continuum observations of new radio halos and relics from the NVSS and WENSS surveys: Relic orientations, cluster X-ray luminosity and redshift distributions

Abstract. Radio halos and relics are diffuse radio sources found in galaxy clusters showing significant substructure at X-ray wavelengths . These sources provide important information about non-thermal processes taking place in the intracluster medium (ICM). Until now only a few dozen relics and halos are known, while models predict that a much larger number of these sources exist. In this paper we present the results of an extensive observing campaign to search for new diffuse radio sources in galaxy clusters. We carried out radio continuum observations with the Westerbork Synthese Radio Telescope (WSRT), Giant Metrewave Radio Telescope (GMRT) and Very Large Array (VLA) of clusters with diffuse radio emission visible in NVSS and WENSS survey images. Optical images were taken with the William Herschel and Isaac Newton Telescope (WHT, INT). We discovered 6 new radio relics, including a probable double relic system, and 2 radio halos. In addition, we confirm the presence of diffuse radio emission in four galaxy clusters. By constructing a sample of 35 radio relics we find that relics are mostly found along the major axis of the X-ray emission from the ICM, while their orientation is perpendicular to this axis. We also compared the X-ray luminosity and redshift distributions of clusters with relics to an X-ray selected sample from the NORAS and REFLEX surveys. We find tentative evidence for an increase of the cluster's relic fraction with X-ray luminosity and redshift. The major and minor axis ratio distribution of the ICM for clusters with relics is broader than that of the NORAS-REFLEX sample. The location and orientation of radio relics with respect to the ICM elongation is consistent with the scenario that relics trace merger shock waves.

R. J. van Weeren, M. Brüggen, H. J. A. Röttgering, M. Hoeft, S. E. Nuza, H. T. Intema
Astronomy & Astrophysics, **533**, 35, 2011

4.1 Introduction

Radio halos and relics are found in massive merging galaxy clusters. These radio sources indicate the presence of magnetic fields and in-situ particle acceleration within the ICM (e.g., Jaffe 1977; Govoni & Feretti 2004). Galaxy clusters form through mergers with other clusters and galaxy groups as well as through continuous accretion of gas from the intergalactic medium. Since giant radio halos and relics are found in merging clusters (e.g., Buote 2001; Govoni et al. 2004; Barrena et al. 2007; Brunetti et al. 2009; Cassano et al. 2010b), it has been proposed that a small fraction of the energy released during a cluster merger event is channeled into the (re)acceleration of particles.

One scenario for the origin of radio relics is that they trace merger shock waves within the ICM in which particles are accelerated by the diffusive shock acceleration (DSA) mechanism (Krymskii 1977; Axford et al. 1977; Bell 1978a,b; Blandford & Ostriker 1978; Drury 1983; Blandford & Eichler 1987; Jones & Ellison 1991; Malkov & O'C Drury 2001). In the presence of a magnetic field these particles emit synchrotron radiation at radio wavelengths (e.g., Ensslin et al. 1998; Miniati et al. 2000). The efficiency with which collisionless shocks can accelerate particles is unknown and may not be enough to produce the observed radio brightness of relics. A closely linked scenario is that of shock re-acceleration of pre-accelerated electrons in the ICM, which is a more efficient mechanism for weak shocks (e.g., Markevitch et al. 2005; Giacintucci et al. 2008; Kang & Ryu 2011).

An alternative scenario has been proposed by Keshet (2010) based on a secondary cosmic ray electron model, where the time evolution of magnetic fields and the cosmic ray distribution are taken into account to explain both halos and giant relics. Detailed spectral maps, at multiple frequencies, and measurements of the magnetic field via the polarization properties can test this model. For relics, strong magnetic fields ($B > B_{\rm cmb} = 3.25 \times (1+z)^2$) are predicted and the spectral index[1] at the outer edges of relics should be flat, with $\alpha \simeq -1$.

Unlike relics, radio halos are found in the center of merging galaxy clusters and follow the X-ray emission from the ICM. Radio halos have been explained by turbulence injected by recent merger events. The injected turbulence is thought to be capable of re-accelerating relativistic particles (e.g., Brunetti et al. 2001; Petrosian 2001; Cassano & Brunetti 2005). Alternatively, the energetic electrons are secondary products which originate from hadronic collisions between relativistic protons and thermal ions (e.g., Dennison 1980; Blasi & Colafrancesco 1999; Dolag & Enßlin 2000; Keshet & Loeb 2010; Enßlin et al. 2011). Recent observations put tension on the secondary models (e.g, Donnert et al. 2010a,b; Jeltema & Profumo 2011; Brown & Rudnick 2011; Bonafede et al. 2011). The existence of ultra-steep spectrum radio halos is also claimed not to be in agreement with these secondary models (Brunetti et al. 2008), but they can be explained by the turbulent re-acceleration model. However, currently only a few of these ultra-steep spectrum radio halos are known so more observations, such as presented in this paper, are needed to increase this number and provide better measurements of the radio spectra.

In the last decade a number of successful searches have been carried out to find new diffuse radio sources in galaxy clusters (e.g., Giovannini et al. 1999; Giovannini & Feretti 2000; Govoni et al. 2001; Kempner & Sarazin 2001; Bacchi et al. 2003; Venturi et al. 2007, 2008; Giovannini et al. 2009; van Weeren et al. 2009c; Rudnick & Lemmerman 2009). However, our understanding of the formation of these sources is still limited. Models for the formation of relics and halos can be tested through statistical studies of correlations between the non-thermal radio emission

[1] $F_\nu \propto \nu^\alpha$, where α is the spectral index

and global properties of the clusters, such as mass, temperature, and dynamical state (Liang et al. 2000; Feretti et al. 2006; Cassano et al. 2006, 2007, 2008, 2010a).

We recently discovered two large radio relics in the NVSS and WENSS surveys (van Weeren et al. 2010, 2011c). Interestingly, these relics remained unnoticed for about 15 years. This suggests that more diffuse radio sources could be discovered by inspection of the NVSS (Condon et al. 1998) and WENSS (Rengelink et al. 1997) survey images. We therefore carried out a visual inspection of the NVSS and WENSS images around known clusters detected by ROSAT (Voges et al. 1999, 2000; Ebeling et al. 1998; Böhringer et al. 2000; Kocevski et al. 2007; Ebeling et al. 2002; Böhringer et al. 2004).

Candidate clusters hosting diffuse radio emission were observed with the WSRT, GMRT and/or VLA. Clusters with existing published observations were not re-observed. In this paper we present the radio images and global properties of the clusters. In addition, we investigate the position and orientation of radio relics with respect the ICM, and compare the X-ray luminosity and redshift distributions of clusters with relics to an X-ray selected sample. In a follow-up paper we will present the polarization and detailed spectral properties of the radio emission in these clusters. The layout of this paper is as follows. In Sect. 4.2 we give an overview of the observations and the data reduction. In Sect. 4.3 we present the radio images and give an short overview of the cluster's properties. We end with discussions and conclusions in Sects. 4.4 and 4.5.

Throughout this paper we assume a ΛCDM cosmology with $H_0 = 71$ km s^{-1} Mpc^{-1}, $\Omega_m = 0.27$, and $\Omega_\Lambda = 0.73$. All images are in the J2000 coordinate system.

4.2 Observations & data reduction

4.2.1 Radio observations

Most of candidate clusters with diffuse radio emission were observed with the WSRT. GMRT or VLA observations were taken of a few clusters which were missed by the WSRT observations. A summary of the observations is given in Table 4.1. The WSRT observations were taken in frequency switching mode, alternating every 5 minutes between the 21 and 18 cm bands. In this paper we will only use the 21 cm data, except for the clusters Abell 697 and Abell 2061. The other data will be presented in a future paper which will focus on the polarization properties and rotation measure synthesis. The total integration time for the WSRT observations was 6 hr per cluster, except for Abell 3365 (see Table 4.1). VLA observations of Abell 523 were taken in D-array. We also included archival observations from project AB1180 (L-band D and C-array). Abell 3365 L-band VLA observations were taken in DnC and CnB array (project AR690).

GMRT 325 MHz observations (with the hardware correlator) were taken of Abell 1612 on May 13, 2009, recording both RR and LL polarizations with 32 MHz bandwidth. We observed Abell 1612 and CIZA J0649.3+1801 at 610/241 MHz with the GMRT. The 610/241 MHz observations were taken in dual-frequency mode, recording RR polarization at 610 MHz and LL polarization at 241 MHz. Total recorded bandwidth was 32 MHz at 610 MHz and 6 MHz at 241 MHz. The GMRT software backend (GSB; Roy et al. 2010) was used.

For the data reduction we used the NRAO Astronomical Image Processing System (AIPS) package. Standard gain calibration and RFI removal were performed. Bandpass calibration was carried out for observations done in spectral line mode. For the 241 MHz observations RFI was fitted and subtracted from the data using the technique described by Athreya (2009) which was

Table 4.1: Observations

Cluster	observation date	frequency MHz	bandwidth MHz	integration time hr	map resolution arcsec	rms noise μJy beam^{-1}
Abell 1612	GMRT, 13 May, 2009	325	32	4.0	$11.6'' \times 9.5''$	236
	GMRT, 22 Nov, 2009	610, 241	32, 6	2.5, 2.5	$7.7'' \times 4.7''$, $21'' \times 12''$	64, 777
Abell 523	VLA Aug, 25, 2005; Nov 28, 2005; Dec 28, 2009	1425	37.5	1.1[a1], 3.7[a2]	$21'' \times 20''$[d]	40
Abell 697[e]	WSRT, 24 Aug, 2009	1382, 1714	160, 160	6.0, 6.0	$34'' \times 21''$[b]	24, 32
Abell 3365[e]	WSRT, 22 Feb, 2009	1382	160	12.0	$108'' \times 13''$	29
Abell 3365	VLA, 30 Sep, 2009 30 May, 2009	1425	2×50	0.7[g1], 2.5[g2]	$43'' \times 35''$, $13.5'' \times 9.2''$	84, 27
Abell 746[e]	WSRT, 19 Sep, 2009	1382	160	6.0	$23'' \times 18''$	28
Abell 2034[f]	WSRT, 26 Jul, 2009	1382	160	6.0	$30'' \times 16''$	24
Abell 2061[f]	WSRT, 23 Jul, 2009	1382, 1714	160, 160	6.0, 6.0	$32'' \times 16''$[b]	22, 26
RXC J1053.7+5452[e]	WSRT, 14 Mar, 2009	1382	160	6.0	$24'' \times 18''$	30
CIZA J0649.3+1801	GMRT, 22 Nov, 2009	610, 241	32, 6	3.0, 3.0	$25'' \times 25''$[c], $17'' \times 14''$	515, 1800
RX J0107.8+5408[e]	WSRT, 29 Aug, 2009	1382	160	6.0	$21'' \times 17''$	29

[a1] D array
[a2] C array
[b] the WSRT 1714 MHz image was convolved to the same resolution as the 1382 MHz image
[c] convolved to a beam of $25'' \times 25''$
[d] D and C array data were combined
[e] The minimum baseline length is 36 m.
[f] The minimum baseline length is 54 m.
[g1] DnC array
[g2] CnB array

implemented in Obit (Cotton 2008). The fluxes of the primary calibrators were set according to the Perley & Taylor (1999) extension to the Baars et al. (1977) scale. Several rounds of phase self-calibration were performed before doing two final rounds of amplitude and phase self-calibration.

For GMRT data in the imaging step we used the polyhedron method (Perley 1989; Cornwell & Perley 1992) to minimize the effects of non-coplanar baselines. Images were made using "Briggs" weighting (with robust set to 0.5, Briggs 1995) and cleaned down to 2 times the rms noise level ($2\sigma_{\rm rms}$) using clean boxes. Finally, we corrected the image for the primary beam attenuation. For more details on the data reduction the reader is referred to van Weeren et al. (2011e).

4.2.2 Optical WHT & INT images

For the clusters Abell 1612, Abell 523, Abell 3365, Abell 2034, CIZA J0649.3+1801 and RX J0107.8+5408 we made use of optical V, R and I band images taken with the WHT (PFIP camera) and INT (WFC camera) telescopes between 15–19 April (WHT) and 1–8 October (INT), 2009 (for more details see van Weeren et al. 2011e).

4.3 Results

In this section we present the radio continuum images of the clusters. We briefly discuss the results of the radio observations for each cluster, a summary is given in Table 4.2. To compute the integrated fluxes for the diffuse radio sources we subtracted the flux contribution from the discrete sources. We alphabetically labeled these discrete sources for each cluster where applicable. The fluxes of the discrete sources are reported in Table 4.3 and they are measured from images made with uniform weighting. We included the uncertainties in the subtraction of the discrete sources in the uncertainty for the integrated flux measurements of the diffuse cluster emission in Table 4.2. We assume that the uncertainties for the discrete sources are uncorrelated. More details are given in the subsections of the individual clusters.

We also display overlays onto ROSAT images and galaxy iso-density contours (mostly derived from SDSS DR7 photometric redshifts, Abazajian et al. 2009). The iso-densities were computed by counting the number of galaxies per unit surface area within a certain photometric redshift range (for SDSS) or V–R and R–I color range (for INT images). For the INT images we created a catalog of objects using Sextractor (Bertin & Arnouts 1996). We then removed all point-like objects (i.e., stars) from the catalogs. To exclude galaxies not belonging to the cluster we selected only galaxies with R−I and V−R colors within 0.15 magnitude from the average color of a massive elliptical cD galaxy in the cluster. The range of 0.15 in the colors was taken to maximize the contrast of the cluster with respect to the fore and background galaxies in the field, but not being too restrictive so that a sufficient number of candidate cluster members was selected.

4.3.1 Abell 1612

Abell 1612 is a little studied cluster at $z = 0.179$ (Popesso et al. 2004) with a moderate X-ray luminosity of $L_{\rm X,\,0.1-2.4\,keV} = 2.41 \times 10^{44}$ erg s^{-1} (Böhringer et al. 2004). In the NVSS

Table 4.2: Cluster properties

Relic	z	$S_{1382\ \mathrm{MHz}}$ mJy	$P_{1.4\ \mathrm{GHz}}$ 10^{24} W Hz^{-1}	$L_{\mathrm{X},\ 0.1-2.4\ \mathrm{keV}}$[d] 10^{44} erg s^{-1}	LLS[a] kpc	classification[b]
Abell 1612	0.179	62.8 ± 2.6[e]	7.9	2.41	780	R
Abell 746 (center, periphery)	0.232	18 ± 4, 24.5 ± 2.0	3.8, 6.8	3.68	850, 1100	H, R
Abell 523	0.10	61 ± 7[f]	1.7	0.89	1350	H or R
Abell 697	0.282	5.2 ± 0.5, 4.0 ± 0.5[g]	2.2	19.42	750	H
Abell 2061	0.0784	27.6 ± 1.0, 21.2 ± 2.1[g]	0.45	3.95	675	R
Abell 3365	0.0926	42.4 ± 3.0[j], 5.4 ± 0.5[k] 42.6 ± 2.6[f,j], 5.3 ± 0.5[f,k]	1.1[j], 0.14[k]	0.859	560[j], 235[k]	DR
CIZA J0649.3+1801	0.064	321 ± 46[i]	1.2[h]	2.38	800	R
RX J0107.8+5408[c]	0.1066	55 ± 5	1.8	5.42	1100	H
Abell 2034 (center, periphery)	0.113	7.3 ± 2.0, 24 ± 2	0.28, 0.89,	3.56	600, 220	H or R, R
RXC J1053.7+5452	0.0704	15 ± 2	0.2	0.44	600	R

[a] largest linear size
[b] R = radio relic, H = radio halo, DR = double radio relic
[c] also known as CIZA J0107.7+5408 or ZwCl 0104.9+5350
[d] Abell 3365 and Abell 1612: Böhringer et al. (2004), CIZA J0649.3+1801 and RX J0107.8+5408: Ebeling et al. (2002), RXC J1053.7+5452: Popesso et al. (2004), Abell 697: (Popesso et al. 2004), Abell 2034 and Abell 2061: Ebeling et al. (1998), Abell 523: Böhringer et al. (2000), Abell 746: this work
[e] NVSS flux
[f] VLA flux at 1425 MHz
[g] WSRT flux at 1714 MHz
[h] using a typical relic spectral index of −1.3
[i] GMRT flux at 610 MHz
[j] eastern relic
[k] western relic

Table 4.3: Fluxes of compact sources embedded in the diffuse emission

	A	B	C	D	E	F	H	I	J	Figure
A746	1.52 ± 0.09	0.36 ± 0.06	0.24 ± 0.06	0.37 ± 0.06	0.45 ± 0.07	0.93 ± 0.06	0.51 ± 0.07	0.33 ± 0.06	0.34 ± 0.06	4.4
A523	10.9 ± 0.2	5.7 ± 0.1	2.9 ± 0.1							4.6
A697[a]	0.50 ± 0.07	0.29 ± 0.06	0.22 ± 0.06	0.25 ± 0.08	0.16 ± 0.06	0.19 ± 0.05				4.9
A697[b]	0.38 ± 0.08	0.24 ± 0.07	0.17 ± 0.05	0.12 ± 0.05[d]	0.15 ± 0.06[d]	0.07 ± 0.05[d]				4.9
A2061[a]	0.53 ± 0.08	0.41 ± 0.07	0.36 ± 0.07							4.12
A2061[b]	0.31 ± 0.08[d]	0.33 ± 0.08	0.20 ± 0.08[d]							4.12
A3365[c]	1.5 ± 0.1	0.53 ± 0.06	0.62 ± 0.06							4.14
CIZA J0649.3+1801	7.7 ± 0.8	1.2 ± 0.1	2.5 ± 0.3							4.16
RX J0107.8+5408	2.6 ± 0.2	1.1 ± 0.1	1.0 ± 0.1	0.7 ± 0.1						4.17
A2034	0.93 ± 0.06	0.59 ± 0.06	0.34 ± 0.05							4.18
RXC J1053.7+5452	1.2 ± 0.1	1.4 ± 0.1								4.20

Note: reported fluxes are in mJy
[a] 1382 MHz
[b] 1714 MHz
[c] from VLA CnB array image
[d] by measuring the flux at the 1382 MHz source position

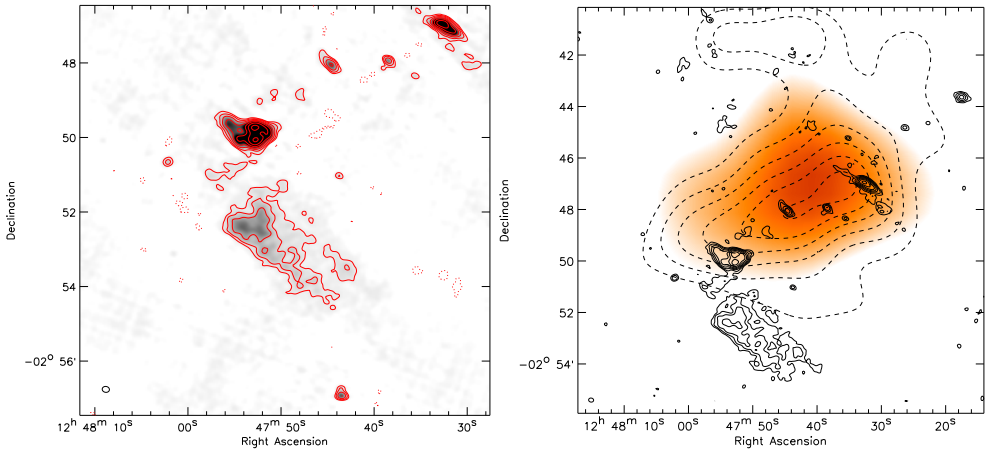

Figure 4.1: Left: GMRT 325 MHz image of Abell 1612. Radio contours are drawn at levels of $[1, 2, 4, \ldots]\times 4\sigma_{\rm rms}$. Dashed contours are drawn at $-3\sigma_{\rm rms}$. Right: A1612 X-ray emission from ROSAT, tracing the thermal ICM, is shown by the color image. The original image from the ROSAT All Sky Survey was convolved with a 270″FWHM Gaussian. Solid contours are from the GMRT 325 MHz image and drawn at levels of $[1, 2, 4, \ldots]\times 3\sigma_{\rm rms}$. Dashed contours show the galaxy iso-density distribution derived from the SDSS survey. Contours are drawn at $[1.0, 1.4, 1.8, \ldots]\times 1.1$ galaxies arcmin^{-2} selecting only galaxies with $0.16 < z_{\rm phot} < 0.20$.

survey we found an elongated radio source located about 5′ to the south of the cluster center. The source was completely resolved out in the 1.4 GHz 5″ FIRST survey (Becker et al. 1995) indicating diffuse emission on scales of about 4′. In our GMRT 325 MHz image (Fig. 4.1, left panel) the source has a total extent of 4.5′, which corresponds to a physical size of 780 kpc. We could not identify an optical counterpart for the source (Fig. 4.3, left panel). We therefore classify the source as a radio relic. In the 610 MHz image (Fig. 4.2, left panel) the source is connected to a tailed radio galaxy to the north. Combining flux measurements at 1.4 GHz (NVSS) and GMRT fluxes at 241, 325 and 610 MHz gives $\alpha \approx -1.4$. However, we note that the individual flux measurements give a large scatter (Fig. 4.3, right panel). We checked the absolute flux calibration between the different frequencies by measuring the integrated fluxes of several compact sources. This did not reveal any problems. Some of the short baselines in the 325 and 241 MHz observations were affected by RFI which could have affected the flux measurement since the source is quite extended. In addition, the declination is close to 0°which gives a non-optimal uv-coverage.

Probably the relic traces a shock in which particles are accelerated or re-accelerated by a merger-related shock wave. The large extent makes it unlikely that the source traces compressed fossil radio plasma (Clarke & Ensslin 2006). The connection with the tailed radio source to the north favors a re-acceleration scenario. In this case, the seed relativistic electrons could be supplied by the tailed-radio source. The elongated galaxy iso-density contours and ICM, see Fig. 4.1 (right panel), also hint at a merger event along a northwest-southeast axis.

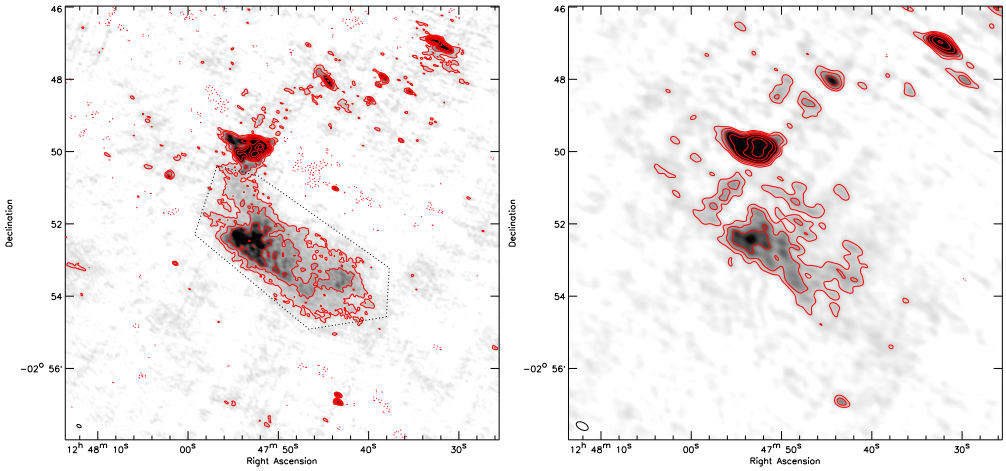

Figure 4.2: GMRT 610 (left) and 241 MHz (right) image of A1612. Contour levels are drawn as in Fig. 4.1. Black dotted lines in the 610 MHz image indicate the integration area for the flux measurements.

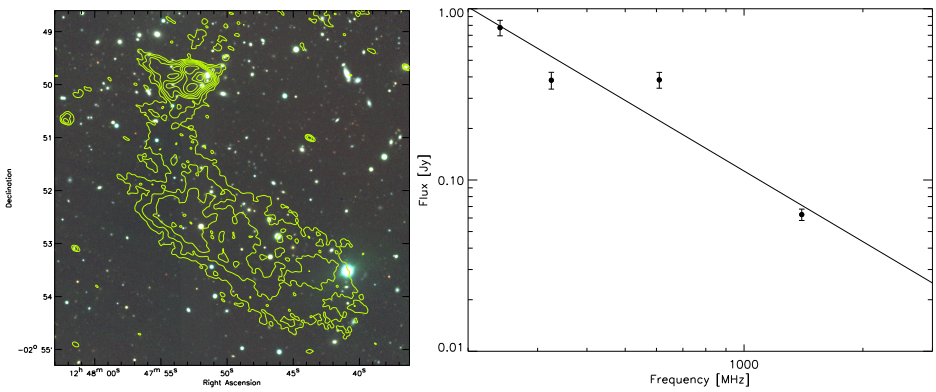

Figure 4.3: Left: WHT V, R, I color image of Abell 1612. Overlaid are the radio contours from Fig. 4.2 (left panel). Right: A1612 radio relic spectrum. Flux measurements at 241, 325, and 610 MHz are from the GMRT observations. The 1.4 GHz flux is from the NVSS survey image.

4.3.2 Abell 746

Abel 746 is a Bautz-Morgan (B/M) class III type cluster located at $z_{\rm phot} = 0.232 \pm 0.01$ (Koester et al. 2007). Based on the ROSAT flux from Böhringer et al. (2000) we calculate $L_{\rm X,\ 0.1-2.4\ keV} \sim 3.68 \times 10^{44}$ erg s^{-1}. We discovered an elongated radio source located northwest of the cluster center in the NVSS survey. The diffuse source is resolved out in the FIRST image, except for an unresolved source located at the southern tip of the diffuse source. In our WSRT image the elongated source is easily detected (Fig. 4.4, left panel) . The source has a largest angular extent of 5′, which corresponds to a physical size of 1.1 Mpc at the distance of Abell 746. The source has a width of 345 kpc and is located at a distance of 1.7 Mpc from the cluster center.

We do not find it very likely that the point source at the southern end of the elongated source is the hotspot of a radio galaxy because the second hotspot is missing. In addition, we do not detect any radio core. The compact source at the southern end of the diffuse source does not have an optical counterpart in SDSS images. The SDSS images are contaminated by the bright star f Uma ($V_{\rm mag} = 4.5$). We only conclude that a possible optical counterpart should be located farther away than A746. This limit on the redshift does not provide any useful constraints to rule it out as a giant radio galaxy on the basis of its physical size or radio luminosity. The morphology of the source is more typical for a radio relic. The size of the sources an its location would also agree with this interpretation. As an additional check, we analyzed the polarization data from the WSRT observation. Radio relics are often polarized at a level of $\sim$ 20% or more (e.g., Clarke & Ensslin 2006; Bonafede et al. 2009b; van Weeren et al. 2010). Indeed, we find that the elongated source is polarized up to the $\sim$ 50% level (Fig. 4.5), which provides additional support for the classification as radio relic.

Galaxy iso-density contours show the cluster to be somewhat elongated along a northwest-southeast axis, see Fig. 4.4 (right panel). The ROSAT image reveals little structure. However, the number of photons detected from the cluster is low.

The WSRT image reveals additional diffuse emission in the center of the cluster, albeit at a low SNR. The emission has an extent of at least 850 kpc which is typical for a giant radio halo. The flux of this radio halo is difficult to estimate due to the low SNR, but subtracting the contribution from the compact sources we find a flux of about 18 ± 4 mJy for the radio halo. To better image the diffuse emission we subtracted the clean components from the compact sources using an image made with uniform weighting. We then convolved the image (made with natural weighting) to a resolution of 1′. The contours from this image are overlaid in Fig. 4.4 (right panel). The halo is now better detected and the radio emission roughly follows the X-ray emission. The radio power of 3.8×10^{24} W Hz^{-1} is above the $L_{\rm X}$–$P_{\rm 1.4GHz}$ correlation for giant radio halos (e.g., Liang et al. 2000; Cassano et al. 2006). The fitted relation from Cassano et al. (2006) gives a power of 0.64×10^{24} W Hz^{-1}. We note that both the integrated radio flux and $L_{\rm X}$ (from ROSAT) are uncertain, and that the intrinsic scatter in the $L_{\rm X}$–$P_{\rm 1.4GHz}$ relation is quite large (Brunetti et al. 2009). The measured radio power is therefore still marginally consistent with being on the $L_{\rm X}$–$P_{\rm 1.4GHz}$ correlation.

4.3.3 Abell 523

Abel 523 is a little studied galaxy cluster located at $z = 0.10$ (Struble & Rood 1999), with $L_{\rm X,\ 0.1-2.4\ keV} = 0.89 \times 10^{44}$ erg s^{-1} (Böhringer et al. 2000). Galaxy iso-densities derived from INT images show a north-south elongated cluster consisting of two galaxy clumps. The VLA

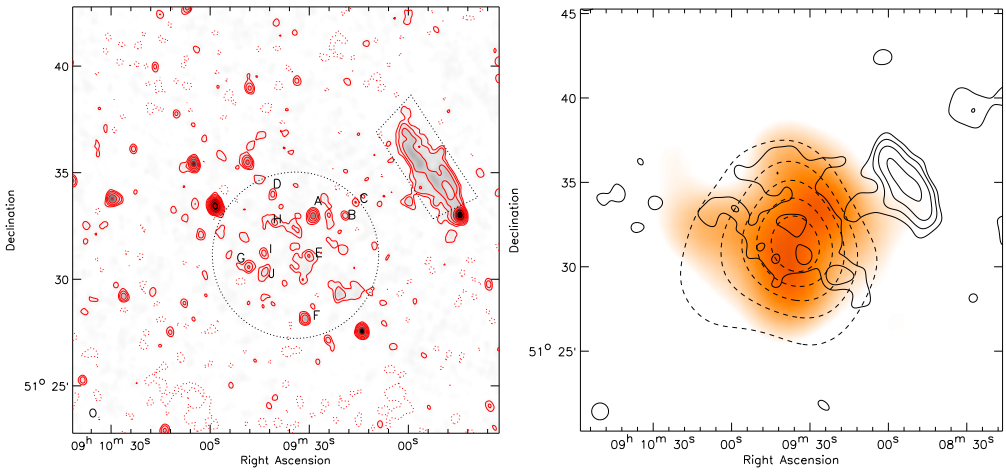

Figure 4.4: Left: WSRT 1382 MHz image of A746. Contour levels are drawn as in Fig. 4.1. Black dotted lines indicate the integration areas for the flux measurements. Discrete sources embedded in the diffuse emission are alphabetically labeled, see Table 4.3. Right: A746 X-ray emission from ROSAT in orange. The original image from the ROSAT All Sky Survey was convolved with a 225″ FWHM Gaussian. Solid contours are from the WSRT 1382 MHz natural weighted image convolved to a resolution of 60″. Compact sources were subtracted and contours are drawn at levels of $[1, 2, 4, 8, \ldots] \times 0.4$ mJy beam^{-1}. Dashed contours show the galaxy iso-density distribution derived from the SDSS survey. Contours are drawn at $[1.0, 1.4, 1.8, \ldots] \times 0.6$ galaxies arcmin^{-2} selecting only galaxies with $0.16 < z_{\rm phot} < 0.29$.

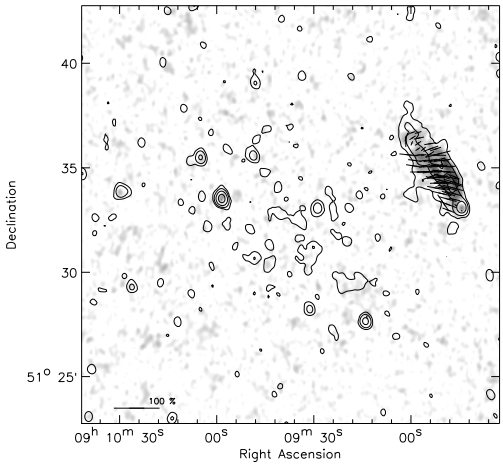

Figure 4.5: WSRT 1382 MHz polarization map of A746. Total polarized intensity is shown as a grayscale image. Vectors depict the polarization E-vectors, their length represents the polarization fraction. The length of the E-vectors are corrected for Ricean bias (Wardle & Kronberg 1974). A reference vector for a polarization fraction of 100% is shown in the bottom left corner. No vectors were drawn for pixels with a SNR < 4 in the total polarized intensity image. Contour levels are drawn at $[1, 4, 16, 64, \ldots] \times 4\sigma_{\rm rms}$ and are from the Stokes I image.

image (Fig. 4.6, left panel) reveals a large, irregular and diffuse radio source in the cluster as well as a number of compact sources related to AGN activity. Our radio image and galaxy distribution agree with the recent results from Giovannini et al. (2011) which showed the presence of diffuse radio emission in this cluster.

The brightest radio source is a tailed radio galaxy projected relatively close to the cluster center. The color of the optical counterpart is similar to other galaxies in the cluster making it likely that the radio source is associated with cluster. The optical INT image is shown in Fig. 4.7. We also detect some radio emission from the largest cD galaxy in the cluster located north of the tailed radio source. In the southern part of the cluster there is a brighter compact source associated with another large elliptical galaxy.

The diffuse source has a patchy morphology, with the brightest part of the diffuse source located to the northwest of the tailed radio source. To the west the diffuse source extends into two filamentary structures. The total flux of the diffuse radio source, minus the point sources and head-tail galaxy, is 61 ± 7 mJy. The diffuse source has a largest extent of 1.35 Mpc. Both numbers are consistent with the result from Giovannini et al. (2011).

The large extent and morphology make it unlikely that the diffuse sources is directly related to the tailed radio galaxy. Giovannini et al. (2011) classify the source as a radio halo. They note that the radio emission permeates both galaxy clumps. However, the possibility that the source is a radio relic projected onto central region of the cluster should also be considered. The source has a very patchy morphology unlike typical radio halos for which the surface brightness follows that of the X-ray emission. Currently we have too little constraints to completely rule out the relic scenario. Deep X-ray observations will be needed to characterize the dynamical

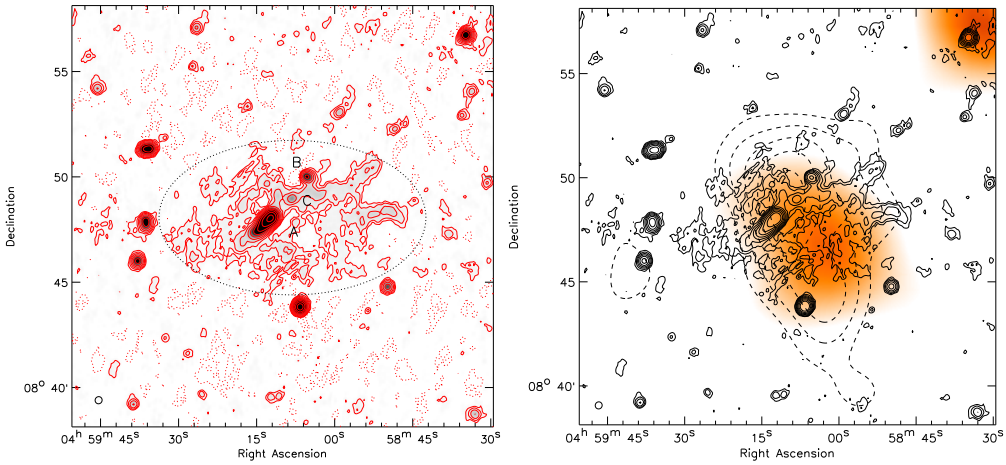

Figure 4.6: Left: A523 VLA 1.4 GHz image. Contour levels are drawn as in Fig. 4.1. Black dotted lines indicate the integration area for the flux measurement. Discrete sources embedded in the diffuse emission are alphabetically labeled, see Table 4.3. Right: A523 X-ray emission from in orange. The original image from the ROSAT All Sky Survey was convolved with a 225″ FWHM Gaussian. Solid contours are from the VLA 1425 MHz image and drawn at levels of $[1, 2, 4, 8, \ldots] \times 4\sigma_{\rm rms}$. Dashed contours show the galaxy iso-density distribution derived from INT images. Contours are drawn at $[1.0, 1.2, 1.4, \ldots] \times 1.6$ galaxies arcmin^{-2} selecting only galaxies with colors $1.12 < \mathrm{V-R} < 1.42$, $0.25 < \mathrm{R-I} < 0.55$, i.e., within 0.15 magnitudes the V–R and R–I color of the central cD galaxy.

state of the cluster. Polarization observations can be used to distinguish between the radio halo and relic scenarios as radio relics are usually strongly polarized (at the 10–20% level or more) while halos are mostly unpolarized.

4.3.4 Abell 697

Abell 697 is a massive Bautz-Morgan (B/M) type II-III cluster, located at $z = 0.282$, with a high X-ray luminosity of $L_{\rm X,\ 0.1-2.4\ keV} = 19.42 \times 10^{44}$ erg s^{-1} (Popesso et al. 2004). The ICM has an elliptical shape and an overall temperature of $8.8^{+0.7}_{-0.6}$ keV determined from Chandra observations by Maughan et al. (2008). Cavagnolo et al. (2009) reported a slightly higher temperature of 9.52 keV. Girardi et al. (2006) found a velocity dispersion of 1334^{+114}_{-96} km s^{-1} for the cluster. They noted this is expected in the case of energy-density equipartition between galaxies and gas. They suggested that the cluster has undergone a complex cluster merger event, occurring mainly along the LOS, with a transverse component in the SSE-NNW direction.

Kempner & Sarazin (2001) first suggested the presence of diffuse radio emission in the cluster. Venturi et al. (2008) showed the presence of a radio halo using 610 MHz GMRT observations, the halo was also reported by Rudnick & Lemmerman (2009) and Giovannini et al. (2009). Macario et al. (2010) presented a more detailed study which included GMRT 325 MHz observations. They found the radio halo to have a an ultra-steep spectrum ($\alpha^{1.4\ \rm GHz}_{325\ \rm MHz}$) with α about -1.7 to -1.8.

We detect the radio halo at both 1382 and 1714 MHz with better SNR than the previous

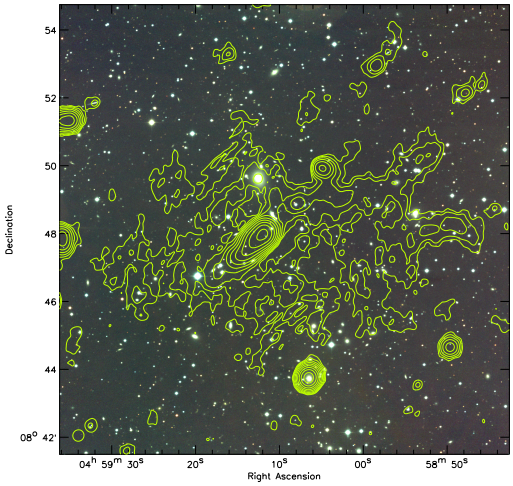

Figure 4.7: INT V, R, I color image of Abell 523. Overlaid are the radio contours from Fig. 4.6.

observations at 1.4 GHz. In our 1382 MHz image we find a total extent of about 750 kpc for the radio halo which is lower than the 1.3 Mpc reported by Macario et al. (2010) at 325 MHz. The lower 1382 MHz extent is expected due to the steep radio spectrum of the halo. To better image the diffuse emission and remove the contribution from compact sources, we made images with uniform weighting and excluded data $< 2.5\mathrm{k}\lambda$ at both 1382 and 1714 MHz. We then subtracted the clean components of the compact sources from the uv-data before re-imaging. To increase the SNR we combined the 21 and 18 cm images after convolving them to a common resolution of $29'' \times 17''$, see Fig. 4.9.

The discrete sources D, E, and F (see Fig. 4.9) were not detected with a SNR > 3. By using the positions from the 1382 MHz image, we could still get an approximate estimate of their fluxes. We subtracted the flux from the discrete sources (Table 4.3) and took the fluxes reported by Macario et al. (2010) to fit a power-law radio spectrum through the flux measurement with $\alpha = -1.64 \pm 0.06$, see Fig. 4.8. This confirms that the radio halo has a very steep spectral index, although it is marginally flatter than the -1.7 to -1.8 reported by Macario et al. (2010).

We do not detect any polarized flux from the radio halo in our WSRT observations. We set an upper limit on the radio halo polarization fraction of 6% at 1382 MHz.

4.3.5 Abell 2061

Abell 2061 is a Bautz-Morgan (B/M) type III cluster located at $z = 0.0784$. The cluster has a X-ray luminosity of $L_{\mathrm{X,\ 0.1-2.4\ keV}} = 3.95 \times 10^{44}$ erg s^{-1} (Ebeling et al. 1998). The cluster has a velocity dispersion of 673^{+49}_{-40} km s^{-1} (Oegerle & Hill 2001). The ROSAT image shows the cluster to be extended in the northeast-southwest direction, see Fig. 4.10 (left panel). Previous studies report that the cluster is part of the Corona Borealis supercluster (Small et al. 1998; Marini et al. 2004). The galaxy iso-density contours display three substructures located roughly along a northeast southwest axis.

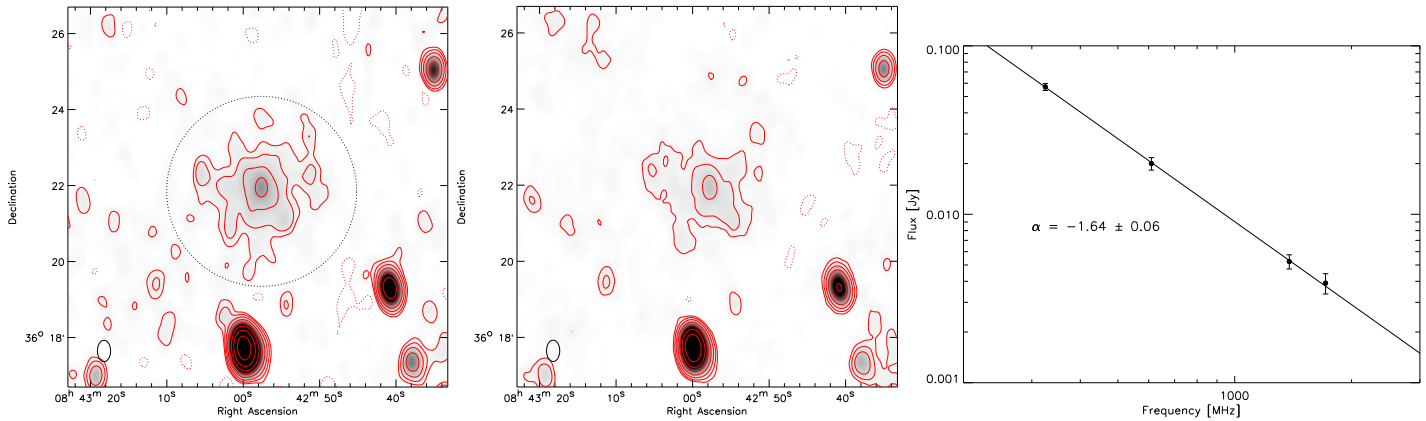

Figure 4.8: Left: WSRT 1382 MHz image of Abel 697. Contour levels are drawn as in Fig. 4.1. Black dotted lines indicate the integration area for the flux measurements. Middle: WSRT 1714 MHz image of Abell 697. Contour levels are drawn as in Fig. 4.1. Right: A697 radio halo spectrum. Flux measurements at 325 and 610 MHz are taken from Macario et al. (2010).

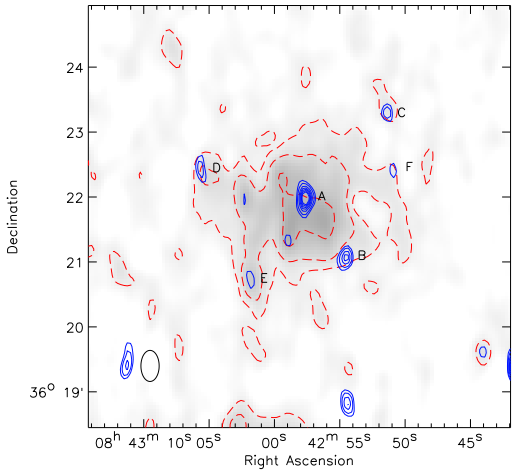

Figure 4.9: WSRT combined 1382 and 1714 MHz image of the radio halo in Abel 697, compact sources were subtracted from the uv-data. Dashed contour levels are drawn at $[1, 2, 4, 8 \ldots] \times 60$ μJy beam^{-1}. Solid contours display the compact sources at 1382 MHz. This high-resolution image ($19'' \times 10''$) was made with uniform weighting and data $< 2.5k\lambda$ was excluded. Contour levels are drawn at $\sqrt{[1, 2, 4, 8 \ldots]} \times 100$ μJy beam^{-1}. Discrete sources embedded in the diffuse emission are alphabetically labeled, see Table 4.3.

Abell 2067 is located at a projected distance of only 1.8 h^{-1} Mpc north from Abell 2061, and the cluster's systematic velocities are separated by $\sim$ 1600 km s $^{-1}$ (Oegerle & Hill 2001). Therefore, they probably form a bound system (Marini et al. 2004; Rines & Diaferio 2006) consisting of a massive cluster (A2061) with a smaller in-falling group/cluster (A2067). A2061 also contains an X-ray extension in the direction of A2067 (towards the north-east) which also suggests a dynamical connection between the two systems (Marini et al. 2004). According to Marini et al., the interaction between the clusters is in the phase in which the cores have not yet met and in which the formation of a shock is expected. The global temperature for A2061 is reported to be $4.53^{+0.48}_{-0.38}$ keV from BeppoSax observations (Marini et al. 2004). A region with a higher temperature is found in the northern part of A2061 with a temperature of $10.67^{+3.90}_{-2.47}$ keV. This region could correspond to the presence of an internal shock.

Kempner & Sarazin (2001) reported a possible relic in the southwest periphery of A2061 in WENSS images. They found a flux of 104 ± 15 and 19 ± 3 mJy at 327 MHz and 1.4 GHz, respectively. This would give a spectral index of $\alpha = -1.17 \pm 0.23$. Rudnick & Lemmerman (2009) also listed the presence of the diffuse peripheral source and measured a flux of 120 mJy in the WENSS image. They also claimed the presence of additional diffuse emission in the center of the cluster which could make up a radio halo.

With our WSRT observations we confirm the presence of the diffuse radio source in the southwestern periphery of A2061 and we also classify it as radio relic. We cannot confirm the presence of a radio halo. The radio relic is clearly seen in both the 21 and 18 cm WSRT images, Fig. 4.11. The relic is located at a distance of 1.5 Mpc from the cluster center and has a largest angular extent of 7.7′, corresponding to a physical size of 675 kpc. In the direction towards the

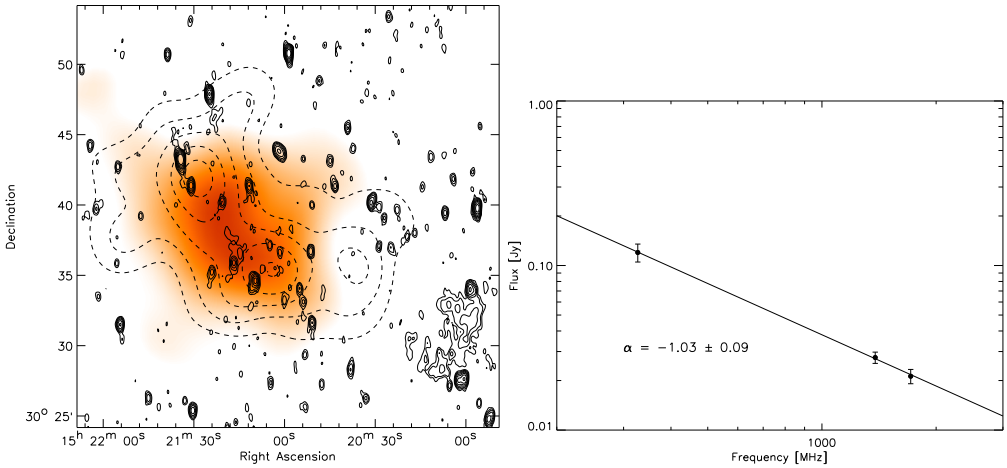

Figure 4.10: Left: A2061 X-ray emission from ROSAT in orange. The original image from the ROSAT All Sky Survey was convolved with a 225″ FWHM Gaussian. Solid contours are from the WSRT 1382 MHz image and drawn at levels of $[1, 2, 4, 8, \ldots] \times 4\sigma_{\rm rms}$. Dashed contours show the galaxy iso-density distribution derived from the SDSS survey. Contours are drawn at $[1.0, 1.4, 1.8, \ldots] \times 0.55$ galaxies arcmin^{-2} selecting only galaxies with $0.05 < z_{\rm phot} < 0.1$. Right: A2061 radio relic spectrum. Flux measurement at 325 MHz is taken from Rudnick & Lemmerman (2009).

cluster center the relic has an extent of $\sim$ 320 kpc. The western outer boundary of the relic is somewhat more pronounced, while the emission fades more slowly inwards to the cluster center. The relic consist of a northern and fainter southern component. Two compact sources are found directly to the north and south of the relic.

An optical color image at the location of the relic is shown in Fig. 4.12. This image does not reveal any obvious counterparts to the radio relic. One galaxy is located at the brightest region of the relic, but no compact radio source is associated with that galaxy. The bright compact sources to the north and south of the relic are both associated with background galaxies unrelated to A2061 because of their small angular sizes ($\lesssim 3''$) and very red color. For comparison, we have marked two galaxies located approximately at the distance of A2061 (Fig. 4.12).

The radio spectrum is fitted by a single power-law spectrum, see Fig. 4.10 (right panel). We find $\alpha = -1.03 \pm 0.09$. The 325 MHz WENSS flux is from Rudnick & Lemmerman. The 325 MHz measurement is however uncertain as the SNR on the relic is low. To better constrain the spectral index an additional low-frequency flux measurement is needed.

The picture that emerges from our observations is that of a radio relic tracing a shock wave from a cluster merger event. The merger event does not seem to be directly related to the cluster A2067, located north of A2061. Instead the shock wave is more likely related to the observed substructures seen in the SDSS galaxy iso-density contours.

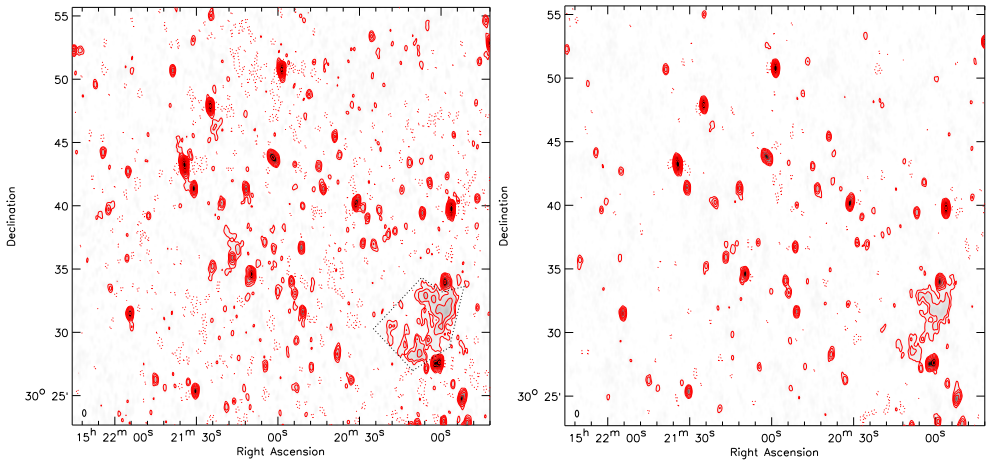

Figure 4.11: Left: A2061 WSRT 1382 MHz image. Contour levels are drawn as in Fig. 4.1. Black dotted lines indicate the integration area for the flux measurements. Right: A2061 WSRT 1714 MHz image. Contour levels are drawn as in Fig. 4.1.

4.3.6 Abell 3365

Abell 3365 (Abell et al. 1989) is located at a redshift of $z = 0.0926$ (Struble & Rood 1999). The cluster is listed as a Bautz-Morgan (B/M) type II cluster. The ESO Nearby Abell Cluster Survey (ENACS, Katgert et al. 1996) measured a velocity dispersion of 1153 km s^{-1} (Mazure et al. 1996) for A3365, quite high compared to other clusters in the sample. Galaxy cluster RXC J0548.8-2154 is located 9′ to the west of the NED listed position for A3365 at a redshift of $z = 0.0928$. The galaxy distribution, see Fig. 4.13 (right panel), peaks at the center of A3365, while the X-ray peak is located at the position of RXC J0548.8-2154. The galaxy distribution around A3365 is complex, with two main concentrations along an east-west axis and a smaller concentration at the far west. The ICM distribution is also complex and elongated in the east-west direction. Based on the very similar redshift, and complex X-ray emission and galaxy distribution, we conclude that A3365 and RXC J0548.8-2154 belong to the same merging system to which we will simply refer as A3365.

In the NVSS image we noted the presence of a peripheral elongated radio source to the east of the cluster center. The WSRT image (Fig. 4.13, left panel) reveals a second smaller diffuse source on the west side of the cluster. The diffuse sources are also detected in the VLA images (Fig. 4.14). For both sources we cannot identify obvious optical counterparts in our INT images (Fig. 4.15). The east and western sources have an angular extent of 5.5′ and 2.3′, which correspond to 560 and 235 kpc at the distance of A3365. We classify the eastern source as a radio relic. Most likely, the western source is another radio relic, which means that A3365 hosts a double radio relic system, but more observations are needed to confirm this classification. This interpretation is supported by the elongated X-ray and galaxy distribution which suggests a merger event along an east-west axis (Fig. 4.13 right panel). We also made an image where we subtracted the compact sources from the uv-data. To make this image, we subtracted the clean components from a uniformly weighted image (CnB array), from the DnC array data. This

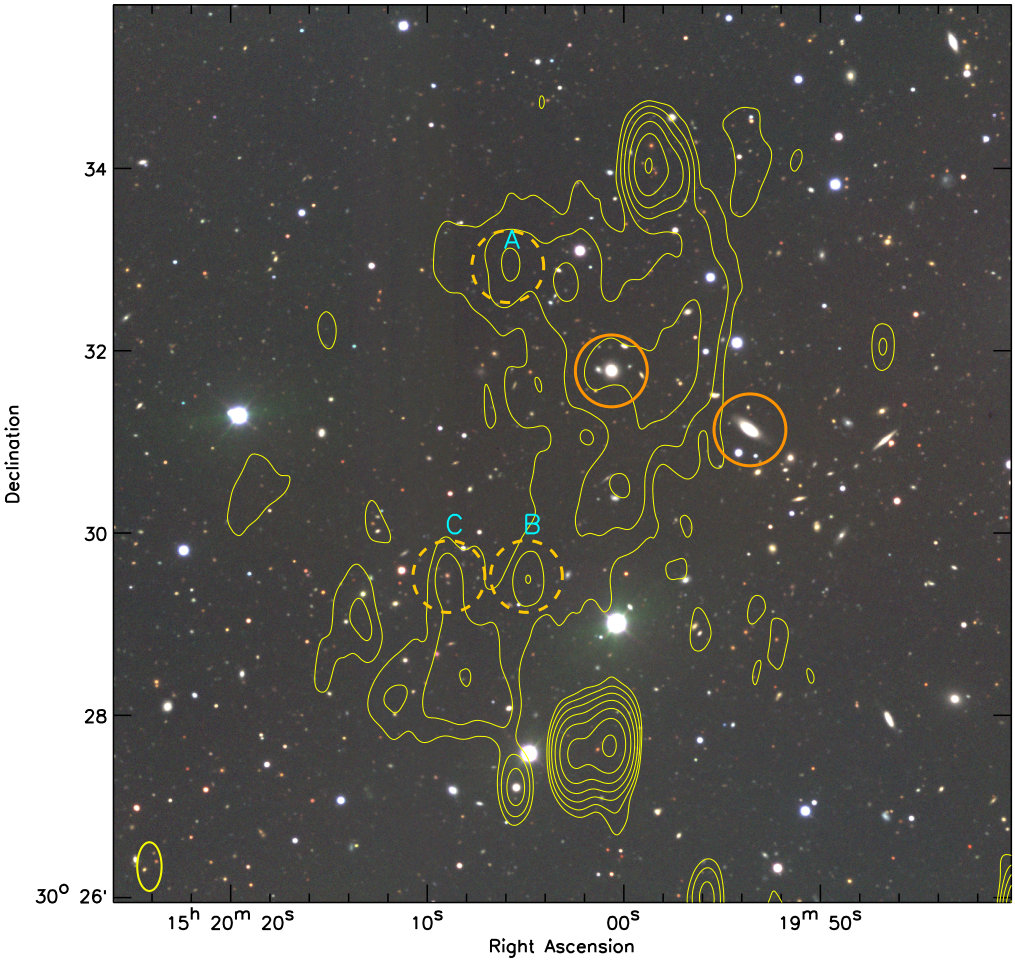

Figure 4.12: A2061 optical WHT V, R, I color image at the location of the radio relic. Radio contours are from Fig. 4.11. The two circles indicate galaxies with spectroscopic redshifts of 0.0815 (west) and 0.061 (east) (Abazajian et al. 2009). Discrete sources embedded in the diffuse emission are alphabetically labeled and marked with dashed circles, see Table 4.3.

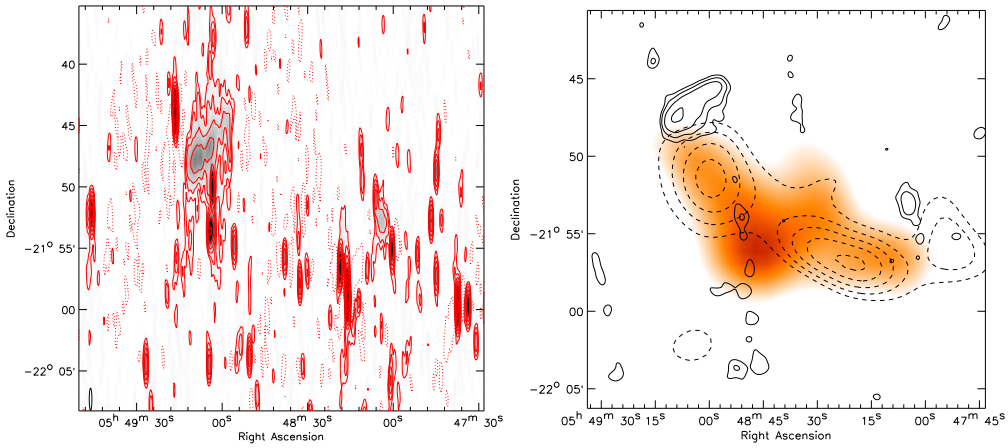

Figure 4.13: Left: A3365 WSRT 1382 MHz image. Contour levels are drawn as in Fig. 4.1. Right: A3365 X-ray emission from ROSAT in orange. The original image from the ROSAT All Sky Survey was convolved with a 225″ FWHM Gaussian. Solid contours are from a VLA 1.4 GHz image with compact sources subtracted from the uv-data. This DnC array image has a resolution of 47″ × 42″. Contours are drawn at levels of $[1, 2, 4, 8, \ldots] \times 0.4$ mJy beam^{-1}. Dashed contours show the galaxy iso-density distribution derived from INT images. Contours are drawn at $[1.0, 1.1, 1.2, \ldots] \times 0.78$ galaxies arcmin^{-2} selecting only galaxies with colors $0.6 < V - R < 0.9$, $0.54 < R - I < 0.84$, i.e., within 0.15 magnitudes the V–R and R–I color of the largest cD galaxy.

image is overlaid in Fig. 4.13.

4.3.7 CIZA J0649.3+1801

CIZA J0649.3+1801 is a little studied galaxy cluster located at $z = 0.064$ discovered by Ebeling et al. (2002) at a galactic latitude of $b = 7.668°$. The cluster has a moderate X-ray luminosity of $L_{\mathrm{X,\ 0.1-2.4\ keV}} = 2.38 \times 10^{44}$ erg s^{-1}. The cluster forms part of a supercluster in the Zone of Avoidance hidden by the Milky Way (Kocevski et al. 2007).

We discovered the presence of a diffuse ∼ 10′ elongated source to the west of the cluster in the NVSS survey. We do not find an optical counterpart for the source in our WHT images. In the GMRT image, see Fig. 4.16 (left panel), the source has a total extent of 10.6′ which corresponds to a size of about 800 kpc at the distance of CIZA J0649.3+1801. We therefore classify the source as a peripheral radio relic located at 0.8 Mpc from the cluster center. The relic is also visible in the 241 MHz image, although the SNR on the relic is very low (Fig. 4.16 right panel).

The ROSAT image reveals another fainter X-ray source located between the radio relic and the cluster center. The source is not resolved and therefore it could be unrelated to the cluster. Also we do not detect any group or cluster of galaxies associated with this source in our optical WHT images. Therefore, this X-ray source seems to be unrelated to CIZA J0649.3+1801.

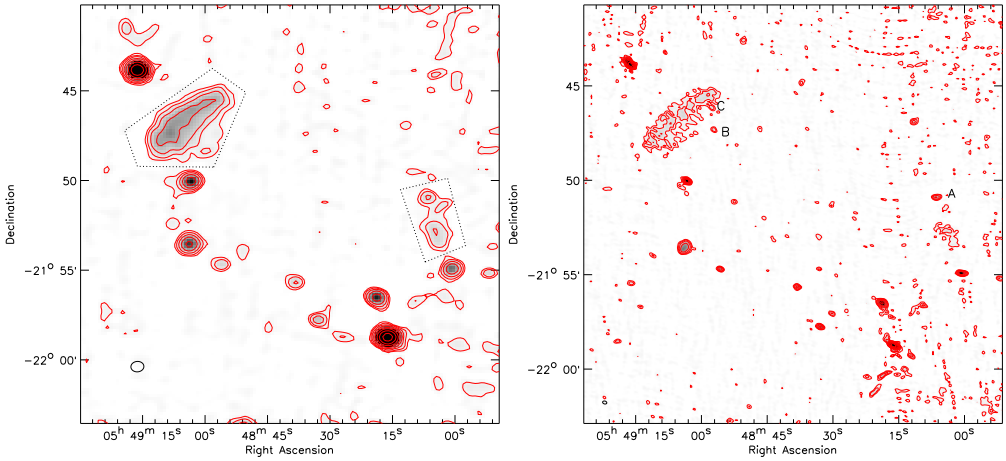

Figure 4.14: A3365 VLA 1.4 GHz DnC (left) and CnB (right) array images. Contour levels are drawn as in Fig. 4.1. Black dotted lines indicate the integration areas for the flux measurements. Discrete sources embedded in the diffuse emission are alphabetically labeled, see Table 4.3.

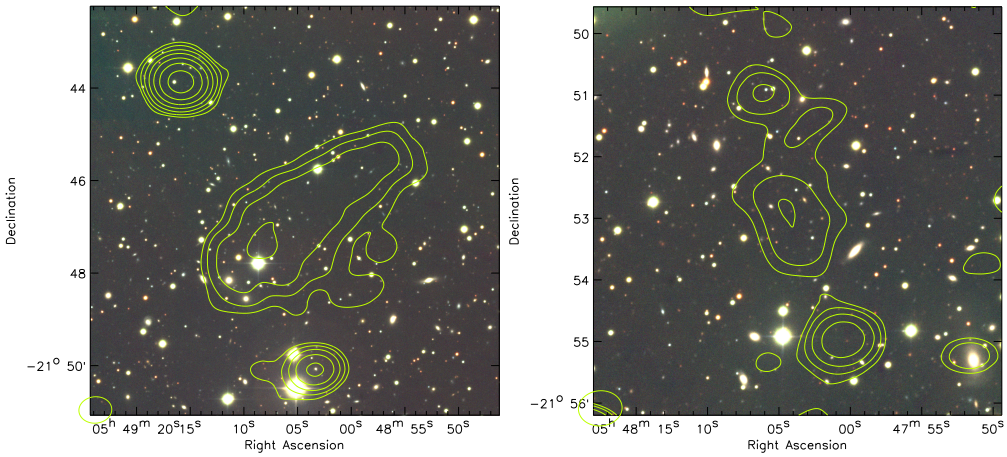

Figure 4.15: A3365 optical INT V, R, I color images at the location of the radio relics. Radio contours are from Fig. 4.14 (right panel).

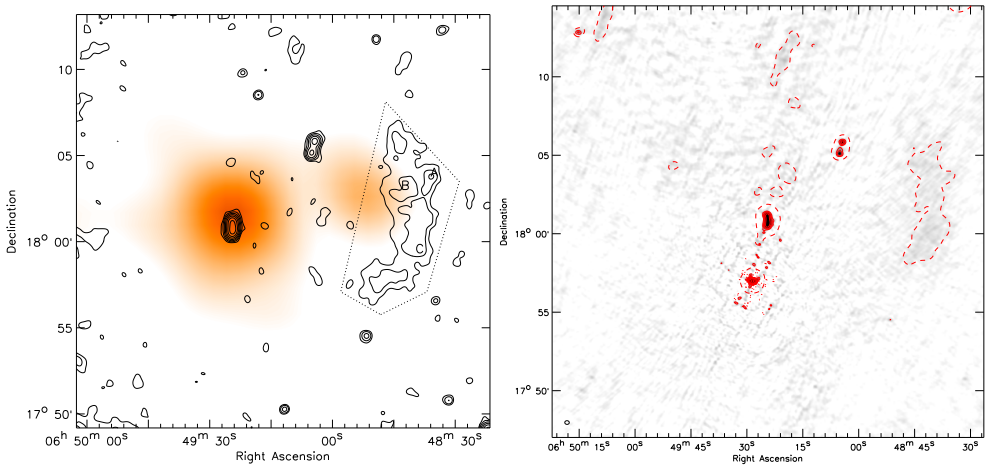

Figure 4.16: Left: CIZA J0649.3+1801 X-ray emission from ROSAT in orange. The original image from the ROSAT All Sky Survey was convolved with a 225″ FWHM Gaussian. Solid contours are from the GMRT 610 MHz image convolved to a resolution of 25″ and drawn at levels of $[1, 2, 4, 8, \ldots] \times 4\sigma_{\rm rms}$. The source NVSS J064928+175700 was removed using the "peeling"-method (e.g., Noordam 2004). Black dotted lines indicate the integration area for the flux measurement. Discrete sources embedded in the diffuse emission are alphabetically labeled, see Table 4.3. Right: CIZA J0649.3+1801 GMRT 241 MHz image. Contour levels are drawn as in Fig. 4.1. The dashed line is the 15 mJy beam^{-1}contour of the 241 MHz images convolved to a circular beam of 45″.

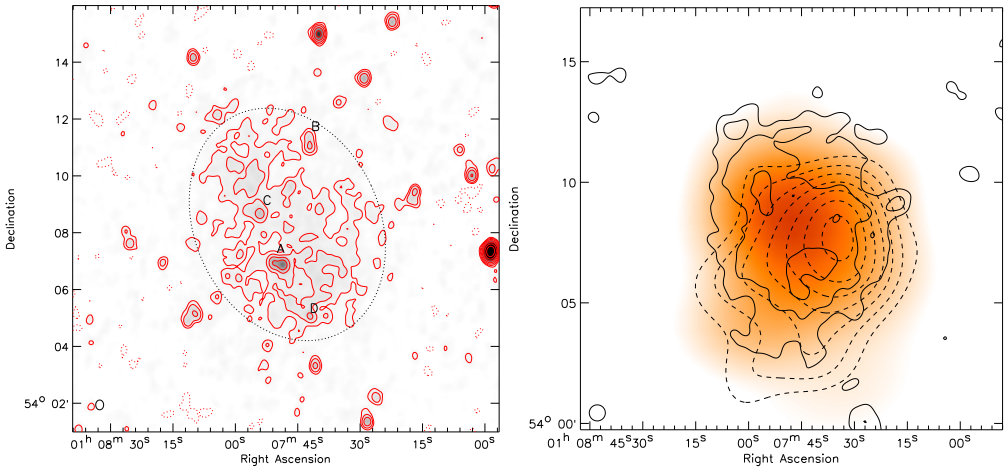

Figure 4.17: Left: CIZA J0107.7+5408 WSRT 1382 MHz image. Contour levels are drawn as in Fig. 4.1. Black dotted lines indicate the integration area for the flux measurement. Discrete sources embedded in the diffuse emission are alphabetically labeled, see Table 4.3. Right: CIZA J0107.7+5408 X-ray emission from ROSAT in orange. The original image from the ROSAT All Sky Survey was convolved with a 225″ FWHM Gaussian. Solid contours are from the WSRT 1382 MHz image convolved to a resolution of 40″. Compact sources were subtracted and contours are drawn at levels of $[1, 2, 4, 8, \ldots] \times 0.3$ mJy beam^{-1}. Dashed contours show the galaxy iso-density distribution derived from INT images. Contours are drawn at $[1.0, 1.2, 1.4, \ldots] \times 0.3$ galaxies arcmin^{-2} selecting only galaxies with colors $0.85 < \mathrm{V-R} < 1.15$, $0.6 < \mathrm{R-I} < 0.9$, i.e., within 0.15 magnitudes the V–R and R–I color of the central cD galaxy.

4.3.8 CIZA J0107.7+5408

CIZA J0107.7+5408 is located at $z = 0.1066$ (Crawford et al. 1995) and has quite a high X-ray luminosity of $L_{\mathrm{X,\ 0.1-2.4\ keV}} = 5.42 \times 10^{44}$ erg s^{-1} (Ebeling et al. 2002). The cluster is projected relatively close to the galactic plane with $b = -8.65°$. Both the NVSS and WENSS survey images display an extended diffuse radio source located roughly at the cluster center. Our WSRT image clearly reveals the presence of a somewhat elongated radio halo with a largest extent in the north-south direction of 1.1 Mpc. The galaxy and ICM distribution are also elongated along the major axis of the radio halo, see Fig. 4.17, which supports the scenario that the cluster is currently undergoing a merger event. An image of the radio halo with the discrete sources subtracted (using the same technique as described in Sect. 4.3.4) is overlaid with contours. The radio power of 3.8×10^{24} W Hz^{-1} is consistent with the L_{X}–$P_{1.4\mathrm{GHz}}$ correlation for giant radio halos.

4.3.9 Abell 2034

Abell 2034 is a merging galaxy cluster as revealed by a Chandra X-ray study from Kempner et al. (2003). White (2000) reported a global cluster temperature of 7.6 keV in agreement with the value of 7.9 ± 0.4 keV found by Kempner et al. (2003). Kempner & Sarazin (2001) suggested the presence of a radio relic on the basis of a WENSS image. The diffuse emission is located

close to the position of a cold front found by Kempner et al. (2003). The presence of diffuse emission was confirmed by Giovannini et al. (2009) and was classified as an irregular elongated radio halo.

We also observe the diffuse emission to brighten at the position of the cold front in the WSRT image. The SDSS galaxy distribution (Fig. 4.18, right panel) is bimodal which supports the scenario that the cluster is undergoing a merger event. We consider the classification of the source uncertain, since the radio emission does not show a very clear correlation with the X-rays. It could therefore also be a radio relic. The radio power ($P_{1.4\mathrm{GHz}} = 0.28 \times 10^{24}$ W Hz^{-1}) though is in agreement with the L_{X}–$P_{1.4\mathrm{GHz}}$ correlation for giant radio halos (e.g., Liang et al. 2000; Cassano et al. 2006). The total flux we find is 7.3 ± 2.0 mJy, lower than the 13.6 ± 1.0 mJy reported by Giovannini et al. (2009). The reason for the difference is unclear because Giovannini et al. (2009) do not report the integration area and the fluxes of the discrete sources that were subtracted. Deeper observations which sufficient resolution are needed to classify the nature of the diffuse emission. Polarimetric observations could be very helpful here as radio relics are usually highly polarized.

We report the detection of a new relatively small radio relic located west of the cluster center (NVSS J150940+333119, WN B1507.6+3342, 7C 150739.39+334252.00). This relic is already visible in the previous studies mentioned above but was not recognized as a radio relic probably because it is quite compact. The source has a size about 220 by 75 kpc and a spectral index ≈ -1.2, including flux measurements from the NVSS, WENSS and 7C (Hales et al. 2007) surveys . A high-resolution 610 MHz GMRT of the relic overlaid on an optical WHT image is shown in Fig. 4.19. The source does not have an optical counterpart which should have easily been visible in the WHT image. The radio plasma could have originated from the compact radio source located immediately south of the relic. On the other hand the spectral index is more typical of a relic directly tracing a shock wave.

4.3.10 RXC J1053.7+5452

RXC J1053.7+5452 is located at $z = 0.0704$. Aguerri et al. (2007) reported a velocity dispersion of 665^{+51}_{-45} km s^{-1} and an r_{200} radius of 1.52 Mpc based on SDSS data. Rudnick & Lemmerman (2009) mentioned the presence of a diffuse radio relic with an extent of about 1 Mpc on the west side of the cluster. Rudnick & Lemmerman reported a total flux of 0.36 Jy at 325 MHz. The low-surface brightness radio relic is also visible in the WSRT image. We find a total extent of 600 kpc, lower than that of Rudnick & Lemmerman (2009). The ROSAT image overlaid with SDSS galaxy iso-density contours and the 1382 MHZ WSRT image are shown in Fig. 4.20. The galaxy distribution seems irregular with the main peak to the southeast of the X-ray center and a second peak to the northwest. The radio relic is roughly located along a line connecting these two galaxy concentrations. This is expected for a cluster merger event, with the shock waves traveling outwards along the merger axis. Deeper radio observations are necessary to better map the extent of this faint radio relic.

4.4 Discussion

Giant radio relics are proposed to directly trace merger shock waves in galaxy clusters. Simulations show that in the case of a binary merger event two shell-like shock waves form at the

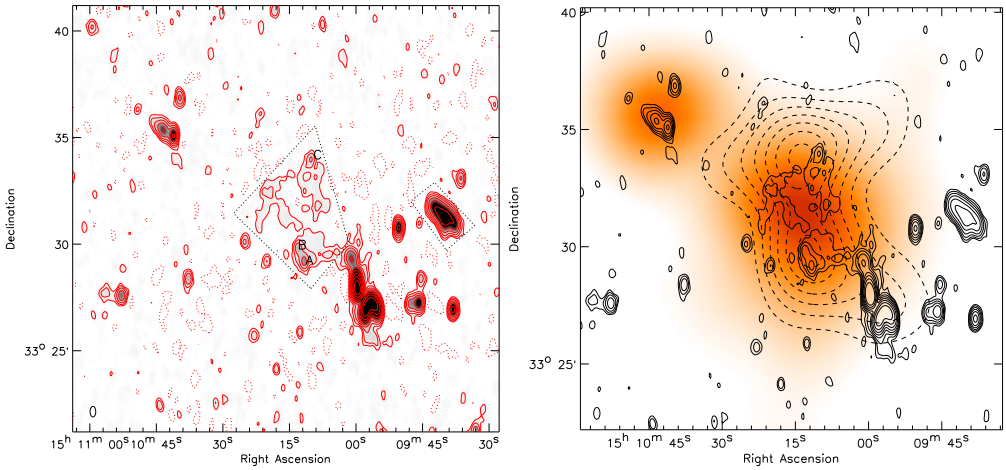

Figure 4.18: Left: A2034 WSRT 1382 MHz image. Contour levels are drawn as in Fig. 4.1. Black dotted lines indicate the integration areas for the flux measurements. Discrete sources embedded in the diffuse emission are alphabetically labeled, see Table 4.3. Right: A2034 X-ray emission from ROSAT in orange. The original image from the ROSAT All Sky Survey was convolved with a 180″ FWHM Gaussian. Solid contours are from the WSRT 1382 MHz image and drawn at levels of $[1, 2, 4, 8, \ldots] \times 4\sigma_{\rm rms}$. Dashed contours show the galaxy iso-density distribution derived from the SDSS survey. Contours are drawn at $[1.0, 1.2, 1.4, \ldots] \times 1.1$ galaxies arcmin^{-2} selecting only galaxies with $0.07 < z_{\rm phot} < 0.16$.

moment of core passage (e.g., Roettiger et al. 1999a; Ricker & Sarazin 2001). These shock waves then move outwards into the lower density ICM of the cluster's outskirts. Double radio relics are thought to trace these binary merger events, with two symmetric shock waves on each side of the cluster center. However, often merger events are more complex with multiple sub-structures merging, so that relics are not necessarily symmetric structures and not always come in pairs. Also, the shock structures may break up when they interact with the galaxy filaments connected to the cluster (e.g., Paul et al. 2011). Still, it is expected that relics are mainly found along the main axis of a merger event, while their orientation is perpendicular to this axis.

We have tested this prediction by constructing a sample of 35 relics, taking relics from the literature and those presented in this paper (see Table 4.4). We did not include any radio relics classified as AGN relics or radio phoenices and selected only relics in clusters which are detected in the ROSAT All Sky Survey (RASS) images.

For every relic we record the end positions of their largest spatial extent (R1, R2), see Fig. 4.21. The line connecting these two points we define as the relic's major axis. The midpoint between the two extrema we take as a the relic's center position. The RASS image can be used to estimate the position of a possible merger axis. We convolve the ROSAT X-ray images for each cluster to the same spatial resolution of 650 kpc. We then fit a 2-dimensional elliptical Gaussian to the X-ray emission. We record both the position of the major axis and the center of the fitted Gaussian. For the merger axis we take as a proxy the major axis of the fitted X-ray emission. Finally, we compute the angle ($\alpha_{\rm r}$) between the major axis of the ICM and the line cluster center–radio relic center. The resulting histogram is shown in Fig. 4.21. From this

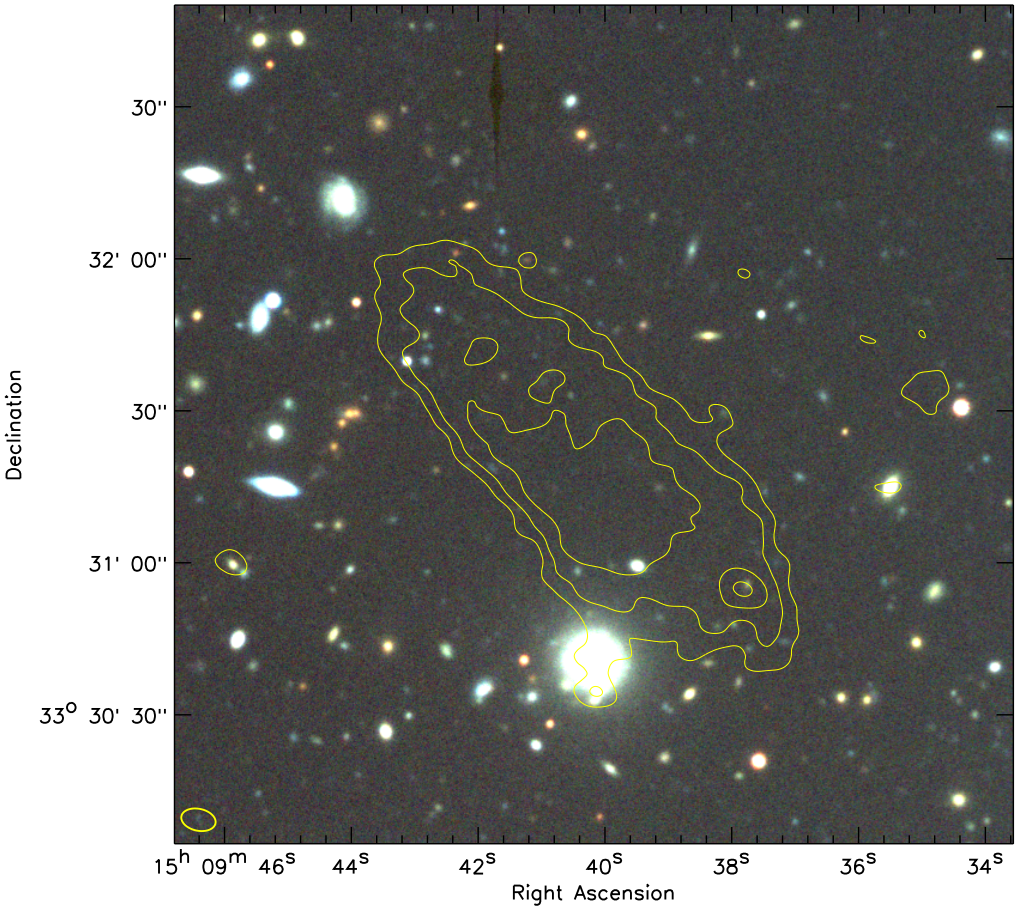

Figure 4.19: A2034 WHT V, R, I color image around the small radio relic. Contours at 610 MHz from the GMRT are overlaid and drawn at levels of $[1, 2, 4, 8, \ldots] \times 4\sigma_{\rm rms}$. The noise level in the image is 41μ Jy beam^{-1} and the beam size is $6.8'' \times 4.3''$.

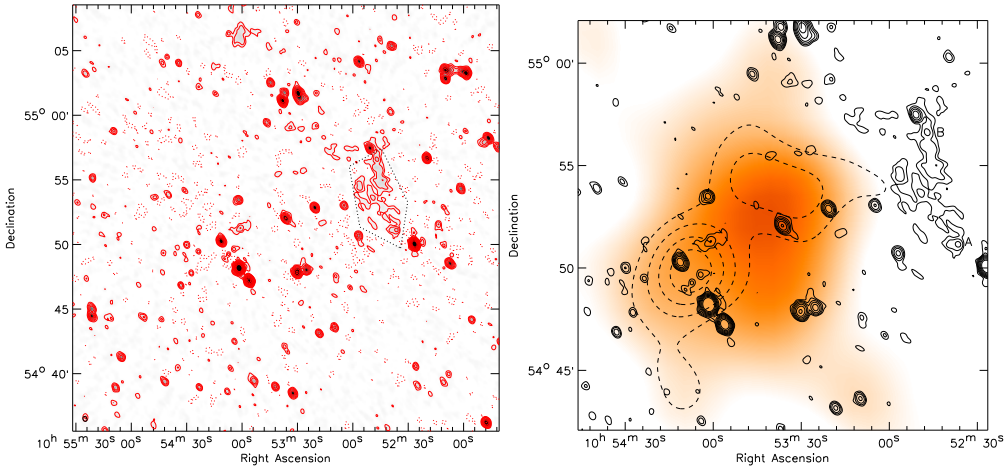

Figure 4.20: Left: RXC J1053.7+5452 WSRT 1382 MHz image. Contour levels are drawn as in Fig. 4.1. Black dotted lines indicate the integration area for the flux measurement. Right: RXC J1053.7+5452 X-ray emission from ROSAT in orange. The original image from the ROSAT All Sky Survey was convolved with a 225″FWHM Gaussian. Solid contours are from the WSRT 1382 MHz image and drawn at levels of $[1, 2, 4, 8, \ldots] \times 4\sigma_{\rm rms}$. Dashed contours show the galaxy iso-density distribution derived from the SDSS survey. Contours are drawn at $[1.0, 1.2, 1.4, \ldots] \times 0.25$ galaxies arcmin^{-2} selecting only galaxies with $0.05 < z_{\rm phot} < 0.1$. Discrete sources embedded in the diffuse emission are alphabetically labeled, see Table 4.3.

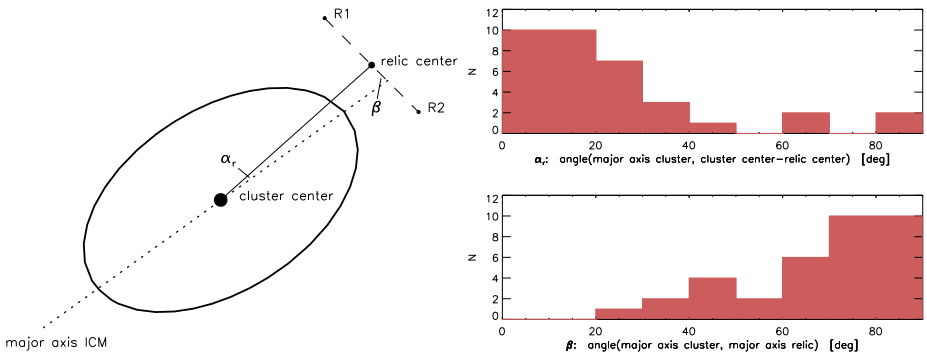

Figure 4.21: Left: Schematic illustration of the angle between the major axis of the ICM and the line relic center–cluster center ($\alpha_{\rm r}$), and the angle between the relic orientation and major axis of the ICM (β), see Table 4.4. Top Right: Histogram of angles between the major axis of the X-ray emission and the line connecting the cluster center with the center of the relic. Bottom Right: Histogram of angles between the major axis of the X-ray emission and the relic's major axis.

histogram we see that relics are preferably found along the major axis of the ICM. This is in line with the simple picture that shock waves propagate outwards along the merger axis. We also calculate the angle (β) between the major axis of the ICM and the relic's major axis. We find that most relics are oriented perpendicular to the ICM major axis, also in agreement with a proposed shock origin for radio relics.

4.4.1 Comparison with the REFLEX and NORAS X-ray clusters

We also compared the properties of cluster hosting radio relics with the X-ray clusters from the NORAS (Böhringer et al. 2000) and REFLEX (Böhringer et al. 2004) surveys. The NORAS survey contains 378 galaxy clusters and has an estimated completeness of about 50% at an X-ray Flux of $F_{\mathrm{X,\ 0.1-2.4\ keV}} = 3.0 \times 10^{-12}$ erg s^{-1} cm^{-2}. The REFLEX sample contains 447 galaxy clusters and has and a completeness of about 90% at the same flux level as the NORAS survey. For each cluster in this sample, we fitted a 2-dimensional elliptical Gaussian to the X-ray emission from the RASS image, using the same procedure as for the clusters hosting giant relics. For some clusters the fitting procedure did not converge because of nearby bright confusing X-ray sources, these cluster were not included in the analysis. The resulting histogram is displayed in Fig. 4.22. The distribution of the major-minor axis ratios for the relic cluster sample is broader. This is expected since relics should be found in merging cluster which are typically more elongated.

In addition, we compare both the X-ray luminosity and redshift distribution of the NORAS-REFLEX sample with the relic sample. We selected all clusters with a flux larger than 3.0×10^{-12} erg s^{-1} cm^{-2} in the ROSAT band. Below this flux limit the NORAS is more than 50% incomplete, see Fig. 4.23 (left panel). The total number of clusters above this flux limit is 540, and the number of clusters with relics is 16 (using the same flux cutoff). From this we find that the currently observed fraction of clusters hosting relics is 3% in this sample. The list of relics is given in Table 4.5 and the radio power are plotted as function of redshift are plotted in Fig. 4.23 (right panel).

The resulting histograms are displayed in Fig. 4.24. Although the number of known relics is rather small, and the relics were selected using various methods, there are few interesting trends visible. Apparently, the fraction of clusters with relics increases with the X-ray luminosity, from about a percent at $L_{\mathrm{X,\ 0.1-2.4\ keV}} = 1 \times 10^{44}$ erg s^{-1} to more than 10% above $\sim 1 \times 10^{45}$ erg s^{-1}. Also, the redshift distribution for cluster with relics is somewhat broader than the corresponding NORAS-REFLEX sample. Therefore, the chance of finding a relic above a certain flux density increases with redshift for clusters selected from flux-limited X-ray surveys. Since the number of clusters with relics is small this might be a statistical fluctuation. However, given that the average fraction of clusters with relics is 3 %, the probability to find four (or even more) in the 26 clusters with $L_{\mathrm{X}} > 10^{45}$ erg s^{-1} is 0.7%. Hence, a pure statistical fluctuation is rather unlikely. This rises the question if selection effects may causes this trend.

As discussed above, the NORAS-REFLEX sample is roughly complete to a flux of 3×10^{-12} erg s^{-1} cm^{-2}. The relic sample in contrast is probably not complete up to a specific flux limit. For example, large low-surface brightness relics could be missed, as are relics in more distant clusters because they are barely resolved in the NVSS and WENSS surveys images and therefore not easily recognizable. The construction of a flux-limited relic sample is therefore challenging as selection effects due to angular size, morphology and surface brightness need to be properly taken into account. In addition, one needs to properly identify other diffuse radio

Table 4.4: Clusters with radio relics and measured orientations

Cluster name	z	α_r "location PA" (deg)	β "orientation PA" (deg)
Abell 115	0.197	45	78
Abell 521	0.247	6	64
Abell 523[a]	0.100	23	39
Abell 548b[b]	0.042	87(A), 40(B)	84(A), 48(B)
Abell 746	0.232	25	56
Abell 1240	0.159	13(N), 15(S)	85(N), 85(S)
Abell 1612	0.179	62	69
Abell 1664	0.128	3	78
Abell 2061	0.078	15	77
Abell 2163	0.203	1	67
Abell 2255	0.081	61	38
Abell 2256	0.059	26	77
Abell 2345	0.176	13(W), 24(E)	87(W), 43(E)
Abell 2744	0.308	20	81
Abell 3365	0.093	20(W), 141(E)	82(W), 43(E)
Abell 3376	0.046	3(W), 8(E)	85(W), 67(E)
Abell 3667	0.055	13(W), 0(E)	75(W), 75(E)
Coma cluster	0.023	22	60
CIZA J2252.8+5301	0.192	27 (N), 4(S)	67(N), 84(S)
MACS J0717.5+3745	0.555	2	79
RXC J1053.7+5452	0.070	19	76
RXCJ1314.4-2515	0.244	30(W), 99(E)	26(W), 46(E)
ZwCl 0008.8+5215	0.104	10(W), 11(E)	76(W), 85(E)
ZwCl 2341.1+0000	0.270	14(N), 8(S)	88(N), 63(S)

- for double relics two values are measured (N=north, S=south, E=east, W=west)
- references: Abell 2255 (main relic only) Pizzo & de Bruyn (2009); Govoni et al. (2005), MACS J0717.5+3745 van Weeren et al. (2009d); Bonafede et al. (2009a), Abell 548b (2 relics) Feretti et al. (2006), Abell 2256 Clarke & Ensslin (2006), Abell 521 Giacintucci et al. (2008), Coma Cluster Giovannini et al. (1991); Brown & Rudnick (2011), Abell 2163 Feretti et al. (2001), Abell 2744 Govoni et al. (2001), Abell 115 and Abell 1664 Govoni et al. (2001). Symmetric double relics included from the literature are: Abell 1240 and Abell 2345 Bonafede et al. (2009b), Abell 3376 Bagchi et al. (2006), Abell 3667 Röttgering et al. (1997), ZwCl 0008.8+5215 van Weeren et al. (2011c), CIZA J2242.8+5301 van Weeren et al. (2010), ZwCl 2341.1+0000 van Weeren et al. (2009b); Giovannini et al. (2010), RXC J1314.4-2515 Venturi et al. (2007).

[a] identification uncertain (either relic or halo)

[b] A548b: A and B refer to the names used in Feretti et al. (2006)

sources (such as radio halos and giant radio galaxies) to prevent them from ending up in the relic sample. Rudnick & Lemmerman (2009) give a good overview of some of the problems involved in constructing these samples. The important question is whether there is any systematic effect which leads to a preferential detection of relics in luminous clusters. Since the luminous clusters are on average at higher redshift, see Fig. 4.23, relic detection is less affected by a too low surface brightness. However, it is possibly affected by resolution effects. This will only decrease the detection probability at higher redshift (luminosity) and hence there is no evident reason why relics in more luminous clusters should have a better chance of being discovered.

Skillman et al. (2011) found in simulations, based on DSA, that the radio power of clusters with relics scatters largely for a given X-ray luminosity. In addition, they found that the mean radio power strongly correlates with the X-ray luminosity. Hence, the fraction of clusters with relics should increase with X-ray luminosity. To compute the actual fractions many factors need to be considered, namely the X-ray flux limit, the discovery probability for radio relics, the radio power distribution of relics and the abundance of clusters as function of X-ray luminosity and redshift. In Nuza et al. (2011) we cary out this analysis in detail. We postulate a radio relic probability density based on numerical simulations $p(P, M_{\rm vir}, z, \nu_{\rm obs})$, where P is the radio luminosity, $M_{\rm vir}$ is the virial mass of the cluster and $\nu_{\rm obs}$ is the observing frequency. We convolve this with the cosmological abundance of dark matter halos. As a result we indeed find that the fraction of radio relics in the NORAS-REFLEX sample should increase with both the X-ray luminosity and the redshift, see Fig. 4.24 (solid lines).

The reason why in simulations more massive clusters show on average much brighter radio relics is unclear. We speculate that multiple aspects contribute: temperature and density are higher and shock fronts are larger in more massive clusters. It seems also likely that mergers of more massive clusters result in higher Mach numbers. Since according to the sub-grid models used in the simulation the radio emission strongly increases with Mach number (Hoeft & Brüggen 2007), a rather small increase of the Mach numbers would have a large effect on the resulting radio luminosity. (We note that the simulation of Hoeft & Brüggen (2007) is also based on DSA.) Finally, the merger rate increases with redshift. However, it needs to be clarified from simulations why an increase of the radio power with X-ray luminosity is expected. The fractions of relics in X-ray selected cluster samples is therefore a powerful tool to put constraints on the models used in the simulations, and hence on the evolution of magnetic fields and on particle acceleration in the ICM.

4.4.2 X-ray peak and galaxy distribution separation

Cluster mergers are thought to decouple the baryonic matter component from the dark matter (DM). This causes and offset between the gravitational center (measured from lensing) and X-ray center of the cluster. A clear example is the “Bullet cluster” (e.g., Clowe et al. 2006), but the effect has also been measured for other clusters (e.g., Shan et al. 2010). Radio relics and halos are mostly found in merger cluster and are thus good candidates to measure this effect. We do not have lensing measurements for the clusters in our sample, but simply taking the galaxy distribution as a proxy for the dark matter distribution we note offsets between the X-ray emission from ROSAT and the galaxy distribution in the clusters A2034, A3365, A2061, A523 and RXC J1053.7+5452 for example. These clusters would therefore make interesting targets for future X-ray and lensing observations.

Table 4.5: Clusters with radio relics in the NORAS and REFLEX surveys

Cluster name	z	$P_{1.4\mathrm{GHz}}$ (total for cluster) 10^{24} W Hz^{-1}	$L_{\mathrm{X,\ 0.1-2.4\ keV}}$ 10^{44} erg s^{-1}
A3376	0.0468	1.6	1.01
A2744	0.3066	7.7	11.68
A4038[c]	0.0292	0.1	1.00
A0548W[b]	0.0424	0.5	0.10
RXC J1314.4-2515	0.2439	8.2	9.92
A133[c]	0.0569	1.1	1.40
A1300	0.3075	6.3	12.12
A13[c]	0.0940	0.9	1.24
A2345	0.1760	6.2	3.91
A521	0.2475	3.4	7.44
A754	0.0542	0.04	3.79
A85[c]	0.0555	0.3	5.18
A2163	0.2030	2.8	19.62
A1612	0.1797	7.9	2.41
A523[a]	0.1034	1.8	0.89
Coma cluster	0.0231	0.29	3.63
A781[b]	0.2952	5.8	4.15
A2034[a]	0.1130	1.17	3.56
A1758	0.2799	4.1	10.90
A746[b]	0.232	6.8	3.68
RXC J1053.7+5452	0.0704	0.2	0.44
A2255	0.0809	0.8	3.08
A2256	0.0581	4.2	3.69

references: Abell 754 Macario et al. (2011); Abell 1758 Giovannini et al. (2009); Abell 781 Venturi et al. (2011); Abell 1300 Reid et al. (1999); Abell 13, 85, 133, and 4038 Slee et al. (2001); for other clusters see Table 4.4

[a] identification uncertain (either relic or halo)

[b] below X-ray flux limit of $F_{\mathrm{X,\ 0.1-2.4\ keV}} = 3 \times 10^{-12}$ erg s^{-1} cm^{-2}

[c] radio phoenix, not included in sample

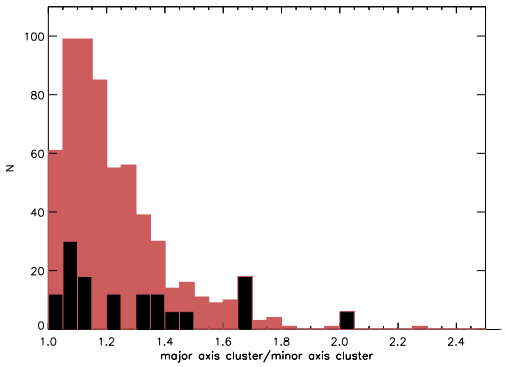

Figure 4.22: Histograms showing the distribution of the major and minor axis ratio. The red histogram is for clusters from the NORAS and REFLEX surveys, the black histogram is for clusters containing giant radio relics (see the caption of Fig. 4.21). The black histogram was scaled by a factor of six for easier comparison with the NORAS-REFLEX sample. Clusters for which the 2 dimensional Gaussian fit did not converge were not included.

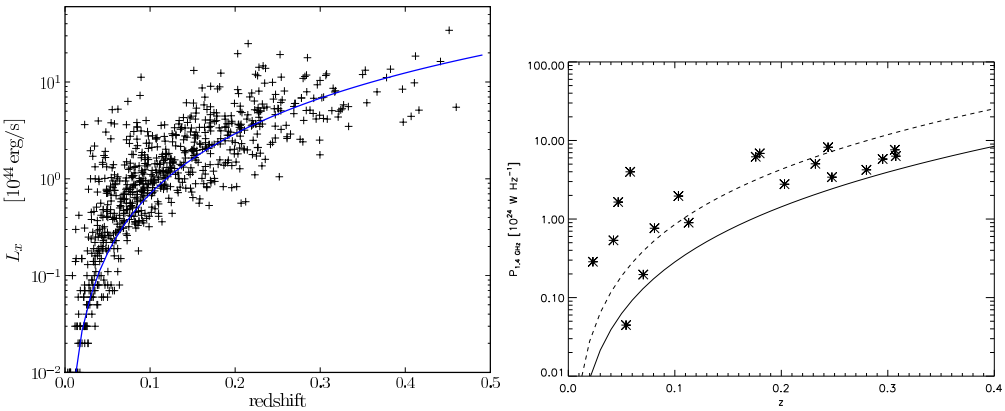

Figure 4.23: Left: L_X-redshift distribution for the NORAS and REFLEX surveys. The solid blue line is the flux cutoff of 3.0×10^{-12} erg s^{-1} cm^{-2} we use for comparison with the relic cluster sample. Right: $P_{1.4\mathrm{GHz}}$-redshift distribution for the relics in Table 4.5. The solid line is for a relic flux limit of 10 mJy, the dashed line for 30 mJy. Radio phoenices are not included.

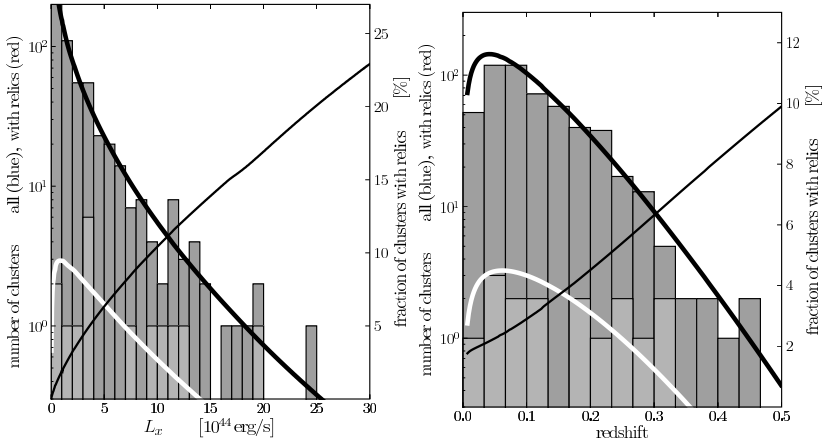

Figure 4.24: Histograms showing the X-ray luminosity (left) and redshift (right) distribution. Dark grey histograms shows the NORAS-REFLEX sample, light grey the relic cluster sample. The solid thick black line displays the predicted luminosity/redshift distributions from Nuza et al. (2011) for clusters with fluxes $> 3.0 \times 10^{-12}$ erg s^{-1} cm^{-2} , while the thick white line is the prediction for clusters hosting relics in the simulation. The fraction of clusters with relics is given by the black thin solid line (the ratio of the two thick lines).

4.5 Conclusions

We have presented WSRT, VLA and GMRT observations of galaxy clusters with diffuse emission selected from the WENSS and NVSS surveys. We find peripheral radio relics in the clusters Abell 1612, Abell 746 and CIZA J0649.3+1801 and a smaller relic Abell 2034. Abell 3365 seems to host a double radio relic system. Our observations reveal radio halos in the clusters Abell 746 and RX J0107.8+5408. We confirm the presence of radio relics in Abell 2061, RXC J1053.7+5452 and diffuse emission in Abell 523 and Abell 2034 (for which the classification is uncertain). In addition, we detect the radio halo Abell 697 providing additional flux measurements around 1.4 GHz.

By constructing a sample of 35 relics we have found that relics are generally located along the major axis (which can be used as a proxy for the merger axis) of the cluster's elongated ICM. Their orientation is mostly perpendicular to this major axis. The distribution of the major-minor axis ratios for the relic cluster sample is broader than that of the NORAS-REFLEX sample. These results are consistent with the scenario that relics trace shock waves which form along the merger axis of clusters. We also compared the redshift and X-ray luminosity distributions of clusters with relics to a sample of clusters from the NORAS and REFLEX surveys. Interestingly, we find indications that the observed fraction of clusters hosting relics increases with X-ray luminosity and redshift. However, selection biases for radio relics play a role and this needs to be investigated further. The significantly improved sensitivity of upcoming radio telescopes (e.g., the EVLA and LOFAR) will allow to find many more radio relics. Correlating this larger relic sample with cluster samples selected at X-rays wavelengths will provide a powerful tool to constrain the evolution of relics in galaxy clusters.

Acknowledgements. We would like to thank the anonymous referee for useful comments. We thank the staff of the GMRT who have made these observations possible. The GMRT is run by the National Centre for Radio Astrophysics of the Tata Institute of Fundamental Research. The Westerbork Synthesis Radio Telescope is operated by ASTRON (Netherlands Institute for Radio Astronomy) with support from the Netherlands Foundation for Scientific Research (NWO). The National Radio Astronomy Observatory is a facility of the National Science Foundation operated under cooperative agreement by Associated Universities, Inc. The William Herschel Telescope and Isaac Newton Telescope are operated on the island of La Palma by the Isaac Newton Group in the Spanish Observatorio del Roque de los Muchachos of the Instituto de Astrofsica de Canarias. The National Radio Astronomy Observatory is a facility of the National Science Foundation operated under cooperative agreement by Associated Universities, Inc. RJvW acknowledges funding from the Royal Netherlands Academy of Arts and Sciences. MB and MH acknowledge support by the research group FOR 1254 funded by the Deutsche Forschungsgemeinschaft.

CHAPTER 5

Diffuse radio emission in the merging cluster MACS J0717.5+3745: the discovery of the most powerful radio halo

Abstract. Hierarchical models of structure formation predict that galaxy clusters grow via mergers of smaller clusters and galaxy groups, as well as through continuous accretion of gas. MACS J0717.5+3745 is an X-ray luminous and complex merging cluster, located at a redshift of 0.5548. The cluster is suspected to host a bright radio relic, but up until now no detailed radio observations have been reported. Here we present Giant Metrewave Radio Telescope (GMRT) radio observations at 610 MHz of this cluster, complemented by Very Large Array (VLA) archival observations at 1.4, 4.9 and 8.5 GHz. We have find a radio halo in the cluster MACS J0717.5+3745 with a size of about 1.2 Mpc. The monochromatic radio power at 1400 MHz ($P_{1.4}$) is 5×10^{25} W Hz^{-1}, which makes it the most powerful radio halo known to date. A 700 kpc radio structure, which we classify as a radio relic, is located in between the merging substructures of the system. The global spectral index of radio emission within the cluster is found to be -1.24 ± 0.05 between 4.9 GHz and 610 MHz. We derive a value of 5.8 μG for the equipartition magnetic field strength at the location of the radio halo. The location of the relic roughly coincides with regions of the intra-cluster medium (ICM) that have a significant enhancement in temperature as shown by Chandra. The major axis of the relic is also roughly perpendicular to the merger axis. This shows that the relic might be the result of a merger-related shock wave, where particles are accelerated via the diffusive shock acceleration (DSA) mechanism. Alternatively, the relic might trace an accretion shock of a large-scale galaxy filament to the southeast.

R. J. van Weeren, H. J. A. Röttgering, M. Brüggen, and A. Cohen
Astronomy & Astrophysics, **505**, 991, 2009

Table 5.1: Observations

	GMRT 610 MHz	VLA 1.4 GHz	VLA 4.9 GHz	VLA 8.5 GHz
Frequency (VLA band)	610 MHz	1385, 1465 MHz (L)	4835, 4885 MHz (C)	8435, 8485 MHz (X)
Bandwidth	2×16 MHz	2×50 MHz	2×50 MHz	2×50 MHz
Channel width	125 kHz	50 MHz	50 MHz	50 MHz
Observation dates	6 & 8 Nov 2008	15 Jul 2002, 22 Aug 1997	27 Nov 2001	22 Aug 1997
Project Code	15HRa01	AE0147, AE0111	AH0748	AE0111
Total on-source time	~ 4 hrs	49 min, 18 min	89 min	8 min
VLA configuration		B, C	D	C
Beam size	$8.2'' \times 6.0''$	$6.1'' \times 6.1.''$	$17'' \times 17''$	$3.0'' \times 2.9''$
rms noise (σ)	78 μJy beam^{-1}	49 μJy beam^{-1}	22 μJy beam^{-1}	...
Largest angular scale	$\sim 4'$	$15'$	$5'$	$\sim 1.5'$ [a]

[a] the largest detectable angular scale is about two times smaller than the theoretical value for short integration times

5.1 Introduction

According to hierarchical structure formation, galaxy clusters grow via mergers of smaller clusters and galaxy groups. During cluster mergers an enormous amount of energy is released. This energy can heat the intra-cluster medium and accelerate particles to highly relativistic energies (e.g., Sarazin 2002; Dolag et al. 2008; Takizawa & Naito 2000). In the presence of magnetic fields these particles will emit diffuse synchrotron radiation, known as radio relics and halos (see the reviews by Feretti & Giovannini 1996; Feretti 2005; Ferrari et al. 2008, and references therein). Radio halos have a typical size of about 1 Mpc and the radio emission has a regular smooth morphology that follows the thermal X-ray emission from the ICM. Radio halos are unpolarized up to a few percent level. One of the main problems for understanding the presence of halos in clusters is the origin of the synchrotron-emitting electrons. The lifetime of these particles is much shorter than their diffusion time over the full extent of the halo (Jaffe 1977). Two main possibilities have been proposed to explain the presence of the relativistic particles producing the radio halos: (i) the re-acceleration models, where relativistic particles are re-accelerated in situ by turbulence in the ICM generated by merger events (e.g., Brunetti et al. 2001; Petrosian 2001; Fujita et al. 2003), and (ii) the secondary models, where the energetic electrons are secondary products of proton-proton collisions (e.g., Dennison 1980; Blasi & Colafrancesco 1999; Dolag & Enßlin 2000). Currently, the re-acceleration models provide a better explanation for the occurrence of radio halos since (i) halos seem to occur only in clusters which are undergoing a merger (e.g., Venturi et al. 2007, 2008), and (ii) the spectra of some radio halos show the expected high frequency cutoff (e.g., Brunetti et al. 2008). This in contrast to secondary models that predict that halos should be present in all massive clusters and the spectral indices should follow simple power-laws, both of which appears to contradict observations.

Unlike halos, radio relics are irregular structures and can be highly polarized. Their sizes vary but relics with sizes of megaparsecs have been found in some clusters. These giant radio relics are thought to trace merger shocks, where particles are accelerated through the diffusive shock acceleration (DSA) mechanism (Drury 1983; Ensslin et al. 1998; Miniati et al. 2001).

An extreme example of a merging cluster is MACS J0717.5+3745 (Ebeling et al. 2001; Edge

et al. 2003). This massive X-ray luminous cluster ($L_X = (24.6 \pm 0.3) \times 10^{44}$ erg s^{-1}) is located at $z = 0.5548$, with an overall ICM temperature of 11.6 ± 0.5 keV (Ebeling et al. 2007). The cluster shows pronounced substructure in optical images. A large-scale filamentary structure of galaxies connected with the cluster was discovered by Ebeling et al. (2004). Steep spectrum[1] radio emission ($\alpha = -1.15$, between 1400 and 74 MHz) in the direction of the cluster is found in the NVSS (Condon et al. 1998), WENSS (Rengelink et al. 1997) and VLSS (Cohen et al. 2007) surveys. The radio emission within the cluster was classified as a radio relic by Edge et al. (2003), no radio halo was found. Ma et al. (2009) presented X-ray (Chandra) and optical observations (Hubble Space Telescope (HST), ACS; Keck-II, DEIMOS) of the cluster. Instead of just two clusters merging, as is the case for 1ES0657-56 (Markevitch et al. 2002), they found the situation in MACS J0717.5+3745 to be more complex. A comparison of the galaxy and gas distribution with the radial velocity information showed the cluster to be undergoing a triple merger event. As pointed out by Ma et al., the partial alignment of the merger axes for the subclusters suggests that these mergers are linked to the large-scale filament to the southeast of the cluster. ICM temperatures exceeding 20 keV were found in some regions of the merging system. Near two of the merging subclusters regions with decrements in the ICM temperature were observed. These regions are probably remnants of cool cores.

One of the main questions is whether the radio relic in MACS J0717.5+3745 is the result of a large shock wave, where particles are accelerated via the DSA mechanism. According to Ma et al., the high temperature of the ICM in the cluster could to some extent be explained by shock heating from the ongoing mergers. However, the size of the high temperature ICM regions is very large (~ 1 Mpc). Therefore they conclude that it is more likely we are seeing the result of contiguous accretion of gas along the cluster-filament interface.

In this paper we present 610 MHz continuum observations of MACS J0717.5+3745 with the GMRT. These observations are complemented by unpublished VLA archival observations. The layout of this paper is as follows. In Sect. 5.2 we give an overview of the observations and data reduction. The radio images, spectral index maps, and X-ray overlay are presented in Sect. 5.3. This is followed by a discussion and conclusions in Sects. 5.4 and 5.5. Throughout this paper we assume a ΛCDM cosmology with $H_0 = 71$ km s^{-1} Mpc^{-1}, $\Omega_m = 0.3$, and $\Omega_\Lambda = 0.7$.

5.2 Observations & data reduction

MACS J0717.5+3745 was observed with the GMRT as part of a larger sample of diffuse steep spectrum sources selected from the 74 MHz VLSS survey. Here we shortly describe the reduction of these observations, for further details the reader is referred to van Weeren et al. 2009 (submitted). The cluster was observed in the 610 MHz band on 6 and 8 November, 2008. The total on-source time was about 4 hours, see Table 5.1. The observations recorded both RR and LL polarizations in two intermediate frequency bands (IFs), each having 128 channels, with a total bandwidth of 32 MHz. We used the NRAO Astronomical Image Processing System (AIPS) for reducing the data. The data was flux and bandpass calibrated using the primary calibrators 3C48, 3C147 and 3C286. We used the Perley & Taylor (1999) extension to the Baars et al. (1977) scale for the absolute flux calibration. Special care was taken to remove radio frequency interference (RFI). To track gain variations during the observations the secondary calibrator 0713+438 was observed several times. After this initial calibration several rounds of phase selfcalibration were

[1] $F_\nu \propto \nu^\alpha$, with α the spectral index

carried out followed by two final rounds of amplitude and phase selfcalibration. We used the polyhedron method (Perley 1989; Cornwell & Perley 1992) for making images to minimize the effects of non-coplanar baselines. Both IFs were simultaneously gridded, imaged and cleaned. About two times the primary beam radius was covered with 199 facets to remove sidelobes from sources away from the field center.

MACS J0717.5+3745 was observed with the VLA, in the L-band on 15 July 2002 in B-array, in the C-band on 27 November 2001 in D-array, and in the L and X-bands on 22 August 1997 in C-array, see Table 5.1. These observations were carried out in single channel continuum mode with two IFs, each with a bandwidth of 50 MHz. The L-band B-array data was calibrated in the standard way using the flux calibrator 3C48 and phase calibrator 0713+438. Several rounds of phase only selfcalibration was followed by a final round of amplitude and phase selfcalibration. The L and X-band C-array observations lacked a usable scan on a flux calibrator, so we could only use the secondary calibrator 0713+438. Flux calibration for the L-band data was carried out by an amplitude and phase selfcalibration against the B-array clean-component model, restricting the UV-range to avoid the inclusion of short baselines. This produced the desired result after checking the flux of the compact sources in the corrected images. The B and C-array L-band UV-datasets were then combined and imaged simultaneously. An extra round of amplitude and phase selfcalibration was carried out on the combined data. Flux calibration for the X-band data was not carried out as we only used the images to identify compact sources related to AGN. The calibrated C-band observations were taken from the NRAO VLA Archive Survey[2]. We carried out an additional round of amplitude and phase selfcalibration.

5.3 Results: images, equipartition magnetic field & spectral index maps

Our GMRT radio image with a noise of 78 μJy beam^{-1} (using robust weighting 0.5; Briggs 1995) is shown in Fig. 5.1 (left panel). The 1.4, 4.9 and 8.5 GHz images are shown in Figs. 5.1 (right panel) and 5.5 (the 4.9 GHz image as overlay on the spectral index map). The noise levels are 49 and 22 μJy beam^{-1} for the 1.4 and 4.9 GHz images, respectively, see Table 5.1. We have indicated the various sources found in Fig. 5.1 (right panel). The 610 MHz, 1.4 and 4.9 GHz images reveal a bright elongated source, defined as R, which we have further subdivided into R1 to R4. The source runs from north to south and then turns southwest at a compact source HT. In the north and in the southwest, at the end of the elongated structure R, there are two regions with enhanced emission R1 and R4. The linear size of the entire structure is about 700 kpc. On the basis of the spectral index map and location within the merging system we classify this source, except the central component (HT), as a radio relic (see Sects. 5.3.2 and 5.4). The bright, relatively compact region, HT, is located roughly halfway along this elongated source. To the southwest a straight elongated linear source (FR-I) is seen, most likely related to a nearby AGN. Around the radio relic (R), both to the south (H1) and northwest (H2), we detect faint diffuse radio emission with a total size of about 1.2 Mpc.

The 8.5 GHz image, Fig. 5.1, shows four compact sources. HT is located on the elongated radio relic. A hint of diffuse emission is seen from the northern brighter region R1. The second compact source is located halfway along the fainter linear structure (FR-I) to the southeast.

[2]This NVAS image was produced as part of the NRAO VLA Archive Survey, (c) AUI/NRAO. The NVAS can be browsed through http://www.aoc.nrao.edu/~vlbacald/

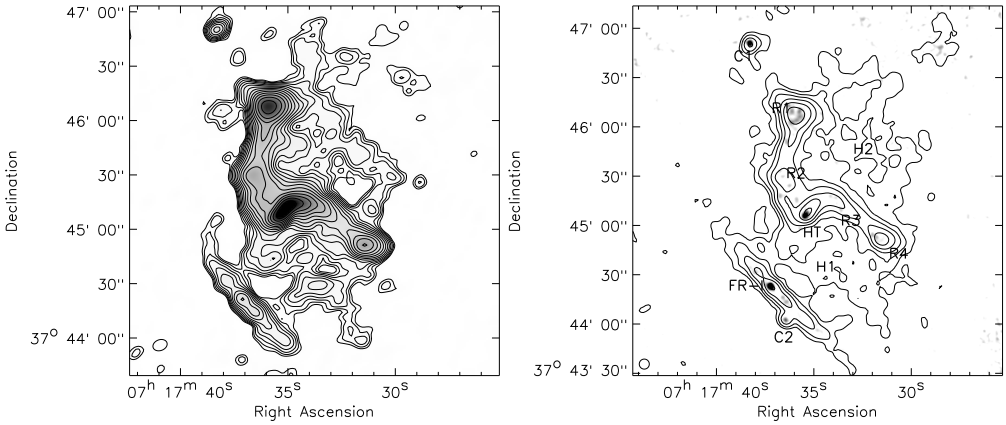

Figure 5.1: Left: GMRT 610 MHz radio image. Contour levels are drawn at $\sqrt{[1,2,4,6,8,16,32,...]} \times 234\ \mu$Jy beam^{-1}. The image has a noise of 78 μJy beam^{-1}. The beam size is $8.2'' \times 6.0''$ and is indicated in the bottom left corner. Right: Greyscale 8.5 GHz VLA C-array image with a resolution of $3.0'' \times 2.9''$. Contours are from the VLA B+C array 1.4 GHz radio image. This image has a restoring beam size of $6.1'' \times 6.1''$ (shown at the bottom left corner) and a rms noise of 49 μJy beam^{-1}. Contours levels are drawn at $[1,2,4,8,16,32,...] \times 3\sigma_{\rm rms}$. Indicated in the figure are the radio halo (H1 & H2), radio relic (R1–R4), central head-tail source (HT), source FR-I to the southeast, and two other compact sources (C1 & C2).

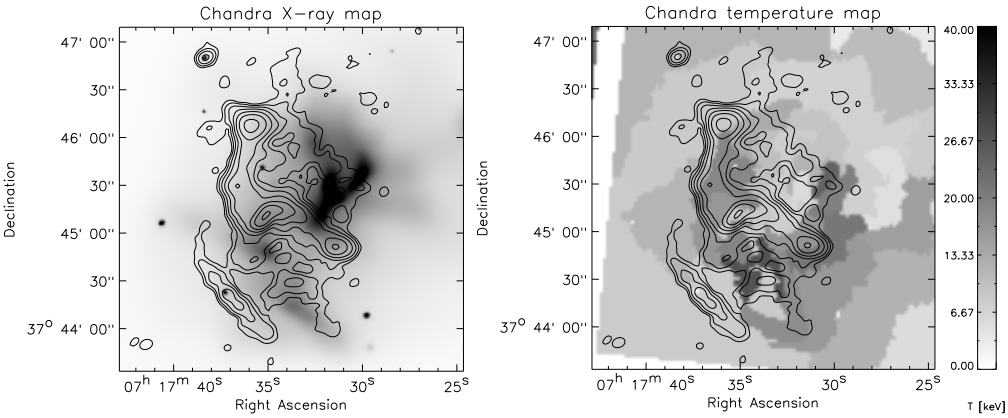

Figure 5.2: Left: Chandra X-ray image overlaid with radio contours at 610 MHz from the GMRT. The beam size is $8.2'' \times 6.0''$ and is indicated in the bottom left corner. The greyscale image shows the X-ray emission from 0.5 – 7.0 keV. The image has been adaptively smoothed (3σ confidence) using the `ASMOOTH` algorithm (Ebeling et al. 2006). Contour levels are drawn at $[1,2,4,8,16,32,...] \times 0.312$ mJy beam^{-1}. Right: Temperature map (Fig. 2 from Ma et al. 2009) overlaid with 610 MHz radio contours. Contour levels are drawn as in the left panel.

Compact source C2 is located just south of FR-I, and compact source C1 is located to the north of R1. All these compact sources are related to AGN. No obvious optical counterpart was found for the central compact radio source (HT) by Edge et al. (2003). We identify an elliptical galaxy located within the cluster at RA $07^h\ 17^m\ 35^s.5$, DEC $+37°\ 45'\ 05''.5$ as a likely counterpart. The source can be classified a "head-tail" source. The tail is not visible in the 8.5 GHz image due to its steep spectral index, but it is detected at all three frequencies below 8.5 GHz. The spectral index map clearly shows spectral steepening along the 20″ long tail as expected, see Fig. 5.4. The southeast source FR-I with its compact core is associated with a bright elliptical foreground galaxy (RA $07^h\ 17^m\ 37^s.2$, DEC $+37°\ 44'\ 23''$). The faint linear extensions on both sides of the compact radio core probably make up a FR-I type (Fanaroff & Riley 1974) radio source.

The large-scale diffuse radio emission, H1+H2, is classified as a radio halo given the large size of about 1.2 Mpc and the emission following roughly the galaxy distribution and X-ray emission from the ICM. The monochromatic radio power ($P_{1.4}$) is estimated to be $(5 \pm 1) \times 10^{25}$ W Hz^{-1} using the 610 MHz image, a spectral index of -1.1 (see Fig. 5.5), an extent of 1.2 Mpc, and the AIPS task 'TVSTAT'[3]. The uncertainty in the radio power is based on a spectral index error of about 0.3. We have extrapolated the halo flux at the location of the bright radio relic using the average flux from the halo per unit surface area outside the relic region. This increased the radio power by a factor of 1.23. This makes it the most powerful radio halo known as the radio power is higher than the halo in 1E0657-56 which has $P_{1.4} = 3 \times 10^{25}$ W Hz^{-1} (Liang et al. 2000). In fact, we could have underestimated the radio power as we may have missed some additional diffuse emission due to our limited sensitivity on large angular scales. The high radio power is in agreement with the X-ray luminosity-radio power ($L_X - P_{1.4}$) and temperature-radio power ($T - P_{1.4}$) correlations (Liang et al. 2000; Enßlin & Röttgering 2002; Cassano et al. 2006), see Fig. 5.3.

A radio overlay on Chandra image is shown in Fig. 5.2 (left panel). The radio relic is roughly located between the merging substructures as indicated by Ma et al. (2009).

5.3.1 Equipartition magnetic field strength

The existence of a radio halo reveals the presence of magnetic fields within the cluster on a scales of about 1 Mpc. We can estimate the equipartition magnetic field strength on the basis of the minimum energy density of the magnetic field for the radio halo. We use the same procedure as in van Weeren et al. (2009b) and take $d = 1.2$ Mpc (the depth of the source), $k = 100$ (the ratio of energy in relativistic protons to that in electrons), and a spectral index of -1.1. Using these values and a flux of 6.8 μJy arcsec^{-2} (integrated flux of the halo divided by the surface area) gives $B_{\rm eq} = 3.2\ \mu$G. For different values of k, the equipartition magnetic field strength scales with $(1 + k)^{2/7}$. This method assumes fixed frequency cutoffs ($\nu_{\rm min} = 10$ MHz and $\nu_{\rm max} = 100$ GHz). This is not entirely correct, rather low and high energy cutoffs ($\gamma_{\rm min}, \gamma_{\rm max}$) for the particle distribution should be used (Brunetti et al. 1997; Beck & Krause 2005). Assuming that $\gamma_{\rm min} \ll \gamma_{\rm max}$ and using a lower energy cutoff $\gamma_{\rm min} = 100$, the revised equipartition magnetic field strength $B'_{\rm eq}$ is 5.8 μG. For different values of k, the revised equipartition magnetic field strength ($B'_{\rm eq}$) scales with $(1 + k)^{1/(3-\alpha)}$. These equipartition magnetic field strength values are similar to those found for other radio halos (e.g., Giovannini et al. 1993; Kim 1999; Thierbach et al. 2003; Clarke & Ensslin 2006).

[3]TVSTAT measures the integrated flux in a user defined region of an image

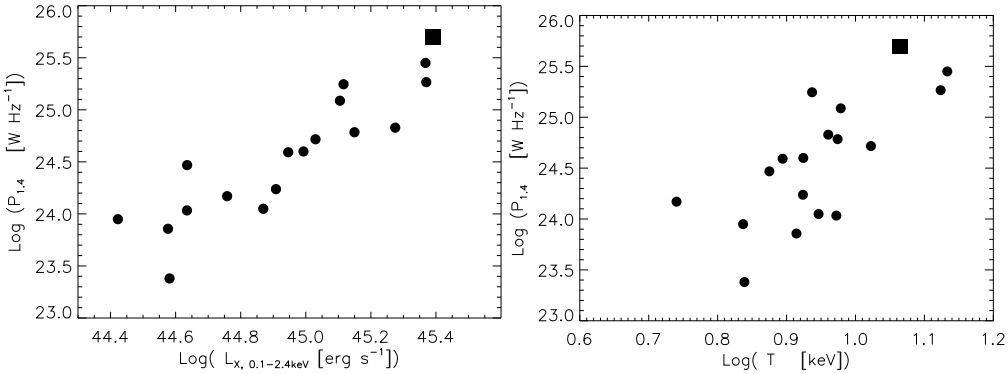

Figure 5.3: Left: X-ray luminosity versus 1.4 GHz radio power. The circles are radio halos from the list compiled by Cassano et al. (2006). The square represents the radio halo in MACS J0717.5+3745. Right: ICM temperature versus 1.4 GHz radio power. The circles are radio halos from the list compiled by Cassano et al. (2006). The square represents the radio halo in MACS J0717.5+3745.

The equipartition energy density in the magnetic field can be compared to the thermal energy density for the cluster. For the density profile of the cluster we use the β-model (e.g., Cavaliere & Fusco-Femiano 1976) derived by Ma et al. (2008). We find that in the cluster center the thermal energy density is 1.9×10^{-10} erg cm^{-3}, the equipartition energy density in the magnetic field is 9.4×10^{-13} erg cm^{-3}. At a distance of 0.6 Mpc from the cluster center the thermal energy density drops to 5.9×10^{-11} erg cm^{-3}. The thermal energy density is about two orders of magnitude higher than the equipartition energy density in the magnetic field. This is consistent with the fact that a small fraction of the thermal energy is being used to accelerate particles to highly relativistic energies.

5.3.2 Spectral index

We have created a spectral index map between 1.4 GHz and 610 MHz at a resolution of 6.1″(see Fig. 5.4). Pixels below $5\sigma_{\rm rms}$ in each of the images were blanked before computing the spectral index map. A second, lower resolution 17″ spectral index map, see Fig. 5.5, was created by fitting single power-law spectra to the combined images at 0.61, 1.4 and 4.9 GHz. The spectral index is only shown in regions where the flux is larger than $2.5\sigma_{\rm rms}$ at all three frequencies. Differences in the UV coverage and calibration errors may have resulted in additional errors in the spectral index.

Steepening along the tail of the central compact source (HT) is clearly visible in Fig. 5.4. This is most likely caused by spectral aging due to synchrotron and Inverse Compton (IC) losses. The spectral index of the head-tail source is steeper than that of the surrounding halo and relic. The origin of the synchrotron emitting electrons in HT and the halo/relic are different. For HT the relativistic electrons are produced in an AGN, after that spectral aging in the tail produces the steep spectrum. The electrons in the relic/halo are probably continuously being accelerated, the spectral index thus depends on the balance between aging and acceleration. On top of that, the equipartition magnetic field strength in the tail is higher than that of the surrounding radio

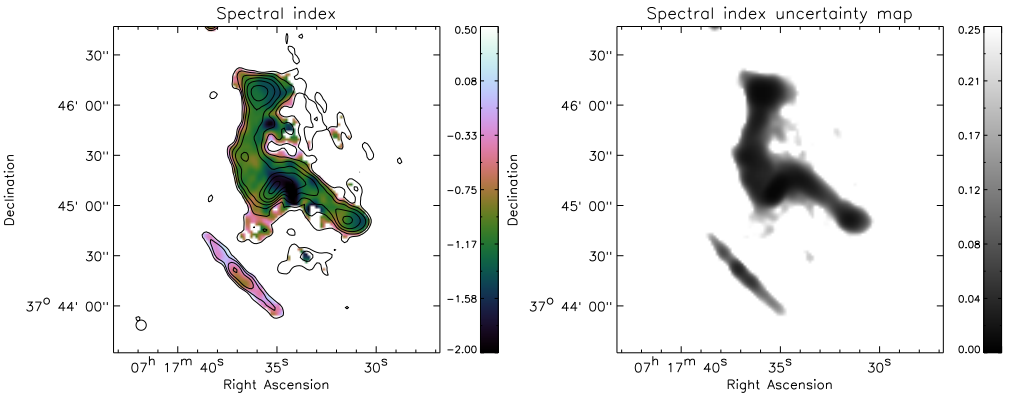

Figure 5.4: Left: Spectral index map between 610 MHz and 1.4 GHz at a resolution of 6.1″ × 6.1″. Contours are from the 610 MHz image and drawn at levels of $[1, 2, 4, 8, 16, 32, ...] \times 0.468$ mJy beam^{-1}. Right: Spectral index uncertainty map between 1.4 GHz and 610 MHz based on the rms noise in both radio images. The absolute flux calibration uncertainty is not included.

halo. The values of the (equipartition) magnetic field strength for the halo, tail, and equivalent magnetic field strength of the microwave background ($B_{\rm IC} = 3.25(1+z)^2$ in units of μG, e.g., Miley 1980; Slee et al. 2001) are 3.2, 36, and 7.8 μG, respectively. Comparing these values, we find that the energy losses are higher in the tail compared to the halo, also resulting in a steeper spectral index.

In the high-resolution spectral index map (Fig. 5.4), the spectral index in the two regions with enhanced emission (R1 and R4), at the north and southwest end of the relic, steepens to the west. This might be caused by spectral aging behind a shock front, where particles are accelerated by the DSA mechanism, located on the west side of R1 and R4 (see also Sect. 5.4.2). This effect is also visible to some extent at R2 in Fig. 5.4. Alternatively, the relic traces a wider region with multiple shocks. Variations in the Mach number of the shocks would then cause variation in the (injection) spectral indices. The overall spectrum is thus determined by the balance between spectral aging, acceleration of particles, and the injection spectral index (determined by the Mach number of the shock). At present, it is not possible to separate between these effects. Furthermore, spectral index variations on scales smaller than the beam size have been smoothed out.

The low-resolution spectral index map is similar to the higher resolution one. However, the tail of the central compact radio source HT has a spectral index of only −1.55 compared to −2.2 in the high-resolution map. This is explained by the lower resolution of the second spectral index map. In this map the tail has been partly blended with the emission from regions surrounding it having a shallower spectrum. The low-resolution spectral index map provides us with some indication of the spectral index of the radio halo. We find that on average $\alpha \approx -1.1$ for the radio halo. More observations are needed to better constrain this value and create a good spectral index map of the radio halo.

The total integrated spectral index, excluding the southeast FR-I source, is −1.04 ± 0.13 between 610 MHz and 1.4 GHz, −1.37 ± 0.06 between 1.4 and 4.9 GHz, and −1.24 ± 0.05

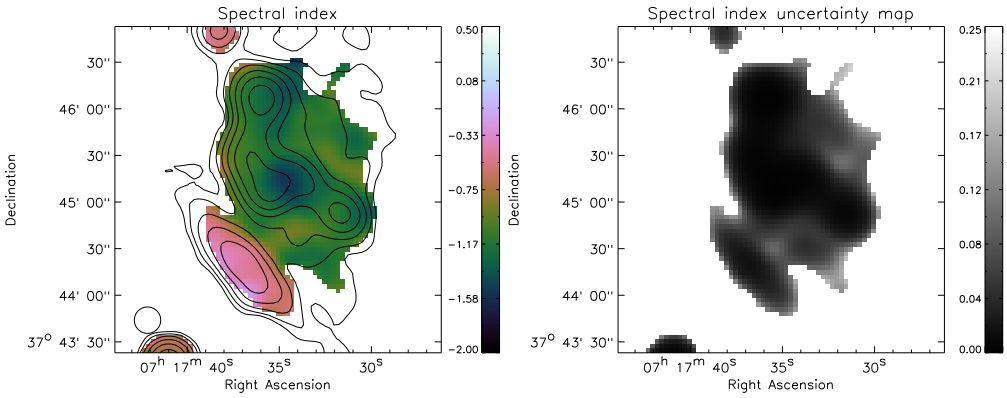

Figure 5.5: Left: Power-law spectral index fit between 0.61, 1.4, and 4.9 GHz at a resolution of $17'' \times 17''$. Contours are from the 4.9 GHz image and drawn at levels of $[1, 2, 4, 8, 16, 32, ...] \times 0.14$ mJy beam^{-1}. Right: Spectral index uncertainty map between 4.9 GHz, 1.4 GHz and 610 MHz based on the rms noise in the three radio images. The absolute flux calibration uncertainty is not included.

between 610 MHz and 4.9 GHz. The errors in the spectral indices are dominated by the absolute flux calibration uncertainty which we have taken to be 5% for the VLA[4] and 10% for the GMRT (Chandra et al. 2004). These values for the spectral index are consistent with the spectral index of -1.15 ± 0.04 derived from the 1.4 GHz NVSS, 325 MHz WENSS, and 74 MHz VLSS fluxes. The radio spectrum is thus relatively straight, although there is evidence for a small amount of spectral steepening at the higher frequencies due to spectral aging. This indicates particle acceleration is currently still ongoing, as otherwise a strong high frequency cutoff would be expected.

The southeast linear structure (FR-I) has a relatively shallow spectral index of -0.52 ± 0.13 between 610 MHz and 4.9 GHz. In the high resolution map (Fig. 5.4) the spectral index seems to flatten somewhat (from -0.6 to -0.3) away from the center of this source (the compact core seen in Fig. 5.1). This could be explained by the presence of hotspots at the end of the lobes from the FR-I source. The flattening is not seen in the low-resolution spectral index map (Fig. 5.5).

5.4 Discussion

5.4.1 Alternative explanations for the elongated radio structures

The bright elongated radio structure R could be a 700 kpc wide angle tail (WAT) source, with the enhanced regions of emission to the north and southwest (R1 and R4) the lobes/hotspots of this WAT. However, the spectral index map does not support such an explanation as there is no obvious connection with the central head-tail source (HT). The central head-tail source has a size of about 115 kpc, much smaller than the total extent of the bright elongated radio structure. Furthermore, the proposed lobes have a spectral index of about -1.1 and steepen towards the

[4]VLA Calibrator Manual

west. If the source was a 700 kpc WAT source, then a steepening of the spectral index along the proposed tails would be expected. This is not observed.

Another possible interpretation for the fainter diffuse linear structure to the southeast (FR-I) is that of a second radio relic since the linear structure lies parallel to a "ridge" of X-ray emission visible in Chandra image (Fig.5.2). This relic would then be seen in projection against the compact radio source located in front of it. However, we prefer a FR-I interpretation since (i) the source has a shallow spectral index of -0.5, and (ii) a central component is associated with a nearby active elliptical galaxy, also detected in the Chandra observations. This component is located halfway along the linear structure. High-resolution observations ($\lesssim 5''$) will be needed to confirm our proposed classification.

5.4.2 Origin of the radio relic

The projected merger axes of the subgroups in the plane of the sky run in a direction that all point towards the large-scale galaxy filament to the southeast. The large elongated radio source (R) has an orientation roughly perpendicular to the merger axis which is expected for a relic tracing a large shock front, where electrons are accelerated via the DSA mechanism in a first-order Fermi process (e.g., Hoeft et al. 2008). Since the relic is expected to trace a shock wave in the ICM, it is interesting to compare our radio image with the low-resolution temperature maps that have been published by Ma et al. (2009), see Fig. 5.2 (right panel). The south part of the relic (R3) is located north, but relatively close to a region having $kT \sim 25$ keV. The northern part of the relic (R1 and R2) directly follows a $kT \sim 20$ keV extension to the north of cluster. The spectral index for the north part of the relic seems to steepen away from these hot ICM regions. This is expected in the case of an outwards (to the east) traveling shock front where particles lose energy by synchrotron and IC losses in the post-shock region. The southern part of the relic (R4) also passes through regions having $kT \sim 20$ keV. Close to HT the relic does not directly trace any regions with a high temperature. However, the temperature map from Ma et al. has a fairly low resolution so a one-to-one comparison with the position of the relic is currently not possible. The temperature map also does not have the resolution to identify the location of a shock wave related to the ongoing merger.

Because of the large 1 Mpc extent of the high-temperature regions, Ma et al. conclude that it is more likely that the ICM is heated as a result of contiguous accretion of gas along the cluster-filament interface. In this case, the radio relic might trace an accretion shock rather than a merger shock. Merger and accretion shocks generally differ in their location with respect to the cluster and also in Mach numbers (Miniati et al. 2000; Miniati 2002; Ryu et al. 2003; Pfrommer et al. 2006; Hoeft & Brüggen 2007; Hoeft et al. 2008; Vazza et al. 2009). Accretion shocks have high mach numbers ($\mathcal{M} \gg 1$) and process the low-density, un-shocked inter-galactic medium (IGM). Merger shocks have lower Mach numbers and occur within the cluster, at radii smaller than about 1 Mpc. The relic in MACS J0717.5+3745 is located relatively close to the cluster center, although this may (partly) be the result of projection. The spectral index over the relic varies roughly between -0.8 and -1.5. Therefore the radio observations do not exclude any of the two scenarios. Additional Chandra observations will be needed to establish the location of the proposed shock front and link this to the location of the radio relic.

Polarization observations of the radio relic will be important to investigate the relation between the relic and the suggested shock wave that has either been created by the merger or by the accretion of gas. Shocks waves in the ICM/IGM can compress and order magnetic fields.

If the magnetic field is seen under some angle (between the normal of the shock front and the line of sight) the projected magnetic field is expected to be parallel to the major axis of the relic (Ensslin et al. 1998). The polarization E-vectors are then perpendicular to the shock front. This is indeed what has been observed for the double relics in Abell 1240 and Abell 2345 by Bonafede et al. (2009b) for example. Therefore, future polarization observations of the relic in MACS J0717.5+3745 will be important to test the shock wave scenario, where particles are accelerated by the DSA mechanism (either created by a cluster merger or by accretion of gas).

5.5 Conclusions

We have presented GMRT 610 MHz radio observations of the complex merging cluster MACS J0717.5+3745. We confirm the presence of a bright radio relic. We also report on the presence of additional diffuse emission in the cluster in the form of a radio halo, with $\alpha \approx -1.1$. The radio halo has the highest radio power ($P_{1.4}$) known to date. This high radio power is in line with scaling relations, relating it to X-ray luminosity and ICM temperature. The integrated spectral index of the radio emission within the cluster is -1.24 ± 0.05 between 610 MHz and 4.9 GHz. We have derived an equipartition magnetic field strength of 3.2 μG for the radio halo. A somewhat higher value of 5.8 μG is obtained by using lower and higher energy cutoffs instead of fixed frequency cutoffs.

The location of the bright relic roughly coincides with regions in the cluster having higher temperatures. The major axis of the relic is orientated approximately perpendicular to the merger axis of the system. This shows that the relic is probably the result of a large-scale shock wave within the cluster where particles are accelerated via the DSA mechanism. Spectral index maps created using additional archival VLA observations show the presence of a 115 kpc head-tail source located roughly halfway the bright radio relic.

Follow-up polarization observations will be important to test the prosed shock wave scenario for the origin of the relic. High sensitivity radio observations at 8 GHz with a resolution $\lesssim 2''$ will allow a more detailed morphological study of the radio relic. This would also provide spectral indices with lower errors due to the larger spectral baseline and allow a search for spectral breaks or curvature.

Deep Chandra observations will be needed to create high spatial resolution temperature maps and pinpoint the location of the proposed shock wave. These observations might also be able to discriminate between the merger and accretion shock scenarios.

Acknowledgements. We thank the staff of the GMRT who have made these observations possible. GMRT is run by the National Centre for Radio Astrophysics of the Tata Institute of Fundamental Research. The National Radio Astronomy Observatory is a facility of the National Science Foundation operated under cooperative agreement by Associated Universities, Inc. We would like to thank H. Ebeling for providing the Chandra X-ray image and temperature map. RJvW acknowledges funding from the Royal Netherlands Academy of Arts and Sciences.

CHAPTER 6

Radio observations of ZwCl 2341.1+0000: a double radio relic cluster

Abstract. Hierarchal models of large-scale structure (LSS) formation predict that galaxy clusters grow via gravitational infall and mergers of smaller subclusters and galaxy groups. Diffuse radio emission, in the form of radio *halos* and *relics*, is found in clusters undergoing a merger, indicating that shocks or turbulence associated with the merger are capable of accelerating electrons to highly relativistic energies. Double relics are a rare class of radio sources found in the periphery of clusters, with the two components located symmetrically on the opposite sides of the cluster center. These relics are important probes of the cluster periphery as (i) they provide an estimate of the magnetic field strength, and (ii) together with detailed modeling can be used to derive information about the merger geometry, mass, and timescale. Observations of these double relics can thus be used to test the framework of LSS formation. Here we report on radio observations of ZwCl 2341.1+0000, a complex merging structure of galaxies located at $z = 0.27$, using Giant Metrewave Radio Telescope (GMRT) observations. The main aim of the observations is to study the nature of the diffuse radio emission in the galaxy cluster ZwCl 2341.1+0000. We carried out GMRT 610, 241, and 157 MHz continuum observations of ZwCl 2341.1+0000. The radio observations are combined with X-ray and optical data of the cluster. The GMRT observations show a double peripheral radio relic in the cluster ZwCl 2341.1+0000. The spectral index is -0.49 ± 0.18 for the northern relic and -0.76 ± 0.17 for the southern relic. We have derived values of $0.48 - 0.93\,\mu$Gauss for the equipartition magnetic field strength. The relics are probably associated with outward traveling merger shock waves.

R. J. van Weeren, H. J. A. Röttgering, J. Bagchi, S. Raychaudhury, H. T. Intema,
F. Miniati, T. A. Enßlin, M. Markevitch, and T. Erben
Astronomy & Astrophysics, **506**, 1083, 2009

6.1 Introduction

Galaxy clusters grow by mergers of smaller subclusters and galaxy groups as predicted by hierarchical models of large-scale structure formation. During a clusters merger a significant amount of energy is released, of $10^{63} - 10^{64}$ ergs for the most massive mergers according to these models. All massive clusters have undergone several mergers in their history and presently clusters are still in the process of accreting matter. Key properties for testing models of large-scale structure (LSS) formation include the total energy budget and the detailed temperature distribution within a cluster, which are both strongly affected by the cluster's merger history. Moreover, the physics of shock waves in the tenuous intra-cluster medium (ICM) and the effect of cosmic rays on galaxy clusters are all fundamental for our understanding of LSS formation.

Diffuse radio sources with relatively steep spectra[1] ($\alpha \lesssim -0.5$), which are not directly associated with individual galaxies, are observed in a number of clusters (e.g., see the review by Ferrari et al. 2008). The vast majority of clusters with diffuse extended radio sources are massive, X-ray luminous and show signs of undergoing a merger. Shocks and turbulence associated with the merger are thought to be responsible for (re)accelerating electrons to highly relativistic energies and synchrotron radiation is produced in the presence of magnetic fields (e.g., Ensslin et al. 1998; Miniati et al. 2000; Brunetti et al. 2001; Petrosian 2001; Fujita et al. 2003). The correlation between cluster mergers and diffuse radio emission is strongly suggested by current observational and theoretical work, however the connection between the diffuse radio emission and clusters mergers has still not been fully understood.

The diffuse radio sources in clusters are commonly divided into three groups: radio halos, radio mini-halos, and relics. Radio halos have smooth morphologies, are extended with sizes $\gtrsim$ 1 Mpc, unpolarized (with upper limits of a few percent, except Abell 2255; Govoni et al. 2005), and are found in the center of clusters. Radio halos follow the thermal X-ray emitting gas from the ICM. Radio mini-halos are not associated with merging clusters and are found in the centers of cool core clusters (e.g., Fabian et al. 1991; Peterson & Fabian 2006). They are associated with the central, brightest cluster galaxy and have typical sizes $\lesssim$ 500 kpc (e.g., Govoni et al. 2009). Radio relics can be highly polarized, are usually found in the periphery of clusters, and have a filamentary or elongated irregular morphology. Their polarization fraction, morphology, and location can vary significantly, possibly reflecting different physical origins or conditions in the ICM; see Kempner et al. (2004).

Giant radio relics are observed in the cluster periphery, with sizes up to several Mpc (e.g., Giovannini et al. 1991; Röttgering et al. 1994; Clarke & Ensslin 2006). These giant radio relics sometimes show symmetric or ring-like structures and are highly polarized (10 – 50% at 1.4 GHz). They are probably signatures of electrons accelerated at large-scale shocks. Smaller relics have been found closer to cluster centers. In this case they could be "radio ghosts", i.e., remnants of past AGN activity. All known radio relics and halos are found in clusters that show signs of undergoing a merger. This gives strong support for the scenario in which the electrons are accelerated by merger-induced shocks or turbulence. Giacintucci et al. (2008) reported that the location of the peripheral relic in Abell 521 coincided with an X-ray brightness edge. This edge could well be the shock front where particles are accelerated. The spectral index of -1.48 ± 0.01 for the A521 relic is in agreement with the low Mach numbers expected in clusters mergers (see below). This suggests that at least in some clusters, the relativistic particles responsible for the presence of a peripheral radio relic are accelerated in a shock front. However, not all merging

[1] $F_\nu \propto \nu^\alpha$, with α the spectral index

clusters host a diffuse radio source, indicating that other processes must be identified for a full understanding of this phenomena.

The class of double radio relics is particular interesting because, based on current models of electron acceleration for this class of radio sources, it enables us to explore the connection between clusters mergers and shock waves (e.g., Roettiger et al. 1999a; Ensslin et al. 1998). In this case two (sometimes ring-like) relics are found in the periphery, symmetric with respect to the cluster center as traced by the X-ray emission. These relics are thought to trace an outward traveling shock emanating from the cluster center, which was created during a cluster merger with a smaller substructure. An alternative shockwave-inducing mechanism is that of external "accretion" shocks where the intergalactic medium (IGM) in filaments of galaxies funnels deep into the cluster (Miniati et al. 2000; Miniati 2003; Keshet et al. 2003). The merger shocks are weaker than external accretion shocks, since the gas has already been heated by these external shocks. The external accretion shocks occur farther out than the merger shocks up to a few times the virial radius of a cluster. However, the gas density is much higher closer to the cluster center so the energy densities in cosmic ray (CR) electrons and magnetic fields are also higher. Accretion shocks of filaments can therefore also be responsible for the occurrence of peripheral radio relics (Miniati et al. 2001). While double relics are allowed in the filament accretion picture, they are not necessarily symmetric with respect to the X-ray elongation axis. A symmetric configuration arises naturally in the binary cluster merger picture (e.g., Roettiger et al. 1999a).

Double relics are rare, with only five of them known in total. Abell 3667 hosts a giant double relic (Röttgering et al. 1997) with a total size of 3.8 Mpc. A numerical model for the diffuse radio and X-ray emission in A3667 was presented by Roettiger et al. (1999a) where the formation of the double relics was explained by an outgoing merger shock front. The model suggested that the two relics were produced by a slightly off-axis merger about 1 Gyr ago, with the merging subcluster having 20% of the mass of the primary cluster. Their model correctly predicted (i) the orientation of the X-ray emission, (ii) the spectral index gradients of the radio relics with steeper spectra farther away from the shock front due to spectral aging, (iii) the approximate location of the radio emission with respect to the X-ray emission, and (iv) roughly the shape of the two relics.

The double radio relic around Abell 3376 (Bagchi et al. 2006) has a maximum size of about 2 Mpc. Bagchi et al. (2006) argue that the relics can be explained by outgoing merger shocks or by accretion shocks tracing the infall of the IGM or warm-hot intergalactic medium (WHIM) onto the cluster at approximately the viral radius. RXC J1314.4−2515 (Valtchanov et al. 2002; Feretti et al. 2005; Venturi et al. 2007) also hosts a double relic. This is the only cluster known to have a radio halo and a double radio relic.

Bonafede et al. (2009b) present observations of double relics in Abell 2345 and Abell 1240. The polarization fraction for the relics in A2345 was found to be 22% and 14%. For A1240, values of 26% and 29% were derived. Steepening of the spectral index was observed away from the shock front towards the center of the cluster for one relic in A1240 (the data for the other relic was consistent with this trend), as well as for one relic in A2345. They concluded that these trends are consistent with shock model predictions. An opposite trend has been seen for the second relic in A2345, i.e., steeper spectra farther away from the cluster center. This trend could be explained by the peculiar position of the relic between two merging substructures.

In this paper we present deep low-frequency Giant Metrewave Radio Telescope (GMRT) observation of the merging system ZwCl 2341.1+0000 at 610, 241, and 157 MHz. These observations were taken to investigate the nature of the diffuse radio emission within the cluster

and explore the connection between the radio and the X-ray emission. ZwCl 2341.1+0000 ($\alpha = 23^h43^m40^s$, $\delta = 00°16'39''$) is a complex cluster galaxies, composed out of several different subclusters, probably at the junction of supercluster filaments (Raychaudhury et al. in prep.; Bagchi et al. 2002). The system is located at a redshift of $z = 0.27$ (using SDSS DR7 spectroscopic redshifts of several galaxies in the vicinity). The cluster is also listed as SDSS CE J355.930756+00.303606 and NSCS J234339+001747. Galaxy isodensity maps, derived from SDSS imaging data, show an elongated cluster of galaxies, including several subclusters distributed roughly along a north-south axis. A galaxy filament is seen branching off from the main structure towards the northeast.

Bagchi et al. (2002) discovered the presence of diffuse radio emission in 1.4 GHz NVSS images (FWHM 45″ Condon et al. 1998), as the emission was not seen in higher resolution 5″ FIRST images (White et al. 1997; Becker et al. 2003) around ZwCl 2341.1+0000. Very Large Array (VLA) observations at 325 MHz confirmed the presence of diffuse emission in the cluster, although the resolution in the corresponding images was rather low (108″), making it difficult to disentangle the diffuse emission from compact sources. At 325 MHz an extension of diffuse emission towards the northeast was suggested, with a spectral index < -0.9, as well diffuse radio emission following the north-south galaxy distribution. The spectral index (between 1400 and 325 MHz) of the diffuse emission was found to be ~ -0.5, which is not steep compared to other diffuse radio sources in clusters. The derived equipartition magnetic field strength was $0.3 - 0.5\mu$Gauss. Bagchi et al. also found the system to be an extended source in ROSAT PSPC All-Sky X-ray Survey. They concluded that the diffuse radio emission was the first evidence of cosmic-ray particle acceleration taking place at cosmic shocks in a magnetized IGM on scales ≥ 5 Mpc.

Raychaudhury et al. (in prep.) obtained high sensitivity X-ray observations of the cluster ZwCl 2341.1+0000 with the Chandra and XMM-Newton satellites. They find the X-ray emission span about 3.3 Mpc in the north-south direction. An extension towards the east is also visible (see Fig. 6.1). The X-ray data show a complex, clearly disturbed ICM, indicating a merger in progress.

The layout of this paper is as follows. In Sect. 6.2 we give an overview of the observations and data reduction. In Sects. 6.3 and 6.4 we present the radio maps and compare them to the X-ray and galaxy distribution. In Sect. 6.5 we present the spectral index maps and derive the equipartition magnetic field strength. We end with a discussion and conclusions in Sects. refsec:discussionzwcl and 6.7.

Throughout this paper we assume a ΛCDM cosmology with $H_0 = 71$ km s^{-1} Mpc^{-1}, $\Omega_m = 0.27$, and $\Omega_\Lambda = 0.73$. At a distance of $z = 0.27$, 1′ corresponds to a physical scale of 246 kpc.

6.2 Observations & data reduction

High-sensitivity radio observations of the merging cluster ZwCl 2341.1+0000 were carried out with the GMRT at 610, 241, and 157 MHz. The 241 and 610 MHz observations were carried out simultaneously using the dual-frequency mode. At 610 MHz only the righthanded circular polarization (RR) was recorded and at 241 MHz only the left-handed circular polarization (LL). Both upper (USB) and lower (LSB) sidebands were recorded at 610 MHz resulting in a total bandwidth of 32 MHz. At 241 MHz only the USB was recorded with a effective bandwidth of 6 MHz (see below). The data were collected in spectral line mode with 128 channels per side-

Table 6.1: Observations

	610 MHz	241 MHz	157 MHz
Bandpass & flux calibrator(s)	3C 48, 3C 147	3C 48, 3C 147	3C 48, 3C 286
Phase calibrator(s)	2225-049	2225-049	0025-260
Bandwidth	32 MHz	6 MHz[a]	8 MHz
Channel width	125 kHz	125 kHz	62.5 kHz
Polarization	RR	LL	RR+LL
Sidebands	USB+LSB	USB	USB
Observation dates	3, 4, 5, 6 Sep 2003	3, 4, 5, 6 Sep 2003	2, 3 Jun 2006
Integration time per visibility	16.9 s	16.9 s	16.9 s
Total duration[b]	12.90 hr	12.90 hr	6.25 hr
Beam size[c]	$6.9'' \times 4.3''$	$17.5'' \times 10.3''$	$21.1'' \times 17.1''$
rms noise (σ)	28 μJy beam^{-1}	297 μJy beam^{-1}	1.36 mJy beam^{-1}

[a] the total bandwidth is 16 MHz but only 6 MHz is usable due to RFI
[b] on-source time (not including calibrators and slewing time)
[c] restoring beam, robust weighting parameter was set to 0.5 (Briggs 1995)

band (IF), resulting in a spectral resolution of 125 kHz per channel. The 157 MHz observations recorded the LSB sideband and included both LL and RR polarizations. The data were also collected in spectral line mode with 128 channels and a total bandwidth of 8 MHz (62.5 kHz per channel). The total integration time for the dual-frequency 610 and 241 MHz observations was 12.9 hours. For the 157 MHz observations this was 6.25 hours. A summary of the observations is given in Table 6.1.

The data was reduced and analyzed with the NRAO Astronomical Image Processing System (AIPS) package. Bandpass calibration was carried out using the standard flux calibrators: 3C48, 3C147, and 3C286. The flux densities for our primary calibrators were taken from the Perley & Taylor (1999) extension to the Baars et al. (1977) scale. This results in 29.43 Jy for 3C48 and 38.26 Jy for 3C147 at 610 MHz; 51.05 Jy and 59.42 Jy at 241 MHz. At 157 MHz, the flux density scale gives 62.71 Jy for 3C 48 and 31.02 Jy for 3C 286. A set of channels (typically 5) free of radio frequency interference (RFI) were taken to normalize the bandpass for each antenna. We removed strong radio frequency interference (RFI) automatically with the AIPS task ‘FLGIT’, but also carefully visually inspected the data for remaining RFI using the AIPS tasks ‘SPFLG’ and ‘TVFLG’. The RFI was partially strong at 241 and 157 MHz. The antenna gains were set using the primary (bandpass) and secondary calibrators and applied to our target source. We have not chosen to average any channels to aid further removal of RFI at a later stage. The first and last few channels of the data were discarded as noisy. At 241 MHz, only the first ~50% of the 16 MHz bandwidth is usable.

For making the images (used subsequently in the selfcalibration), we used the polyhedron method (Perley 1989; Cornwell & Perley 1992) to minimize the effects of non-coplanar baselines. At 610 MHz the USB and LSB were reduced separately. We used a total of 199 facets covering ~2 times the full primary beam in order to remove sidelobes from strong sources far away from the field center. After a first round of imaging, “ripples” in the background were subsequently removed by identifying corresponding bad baseline(s). Several rounds of phase

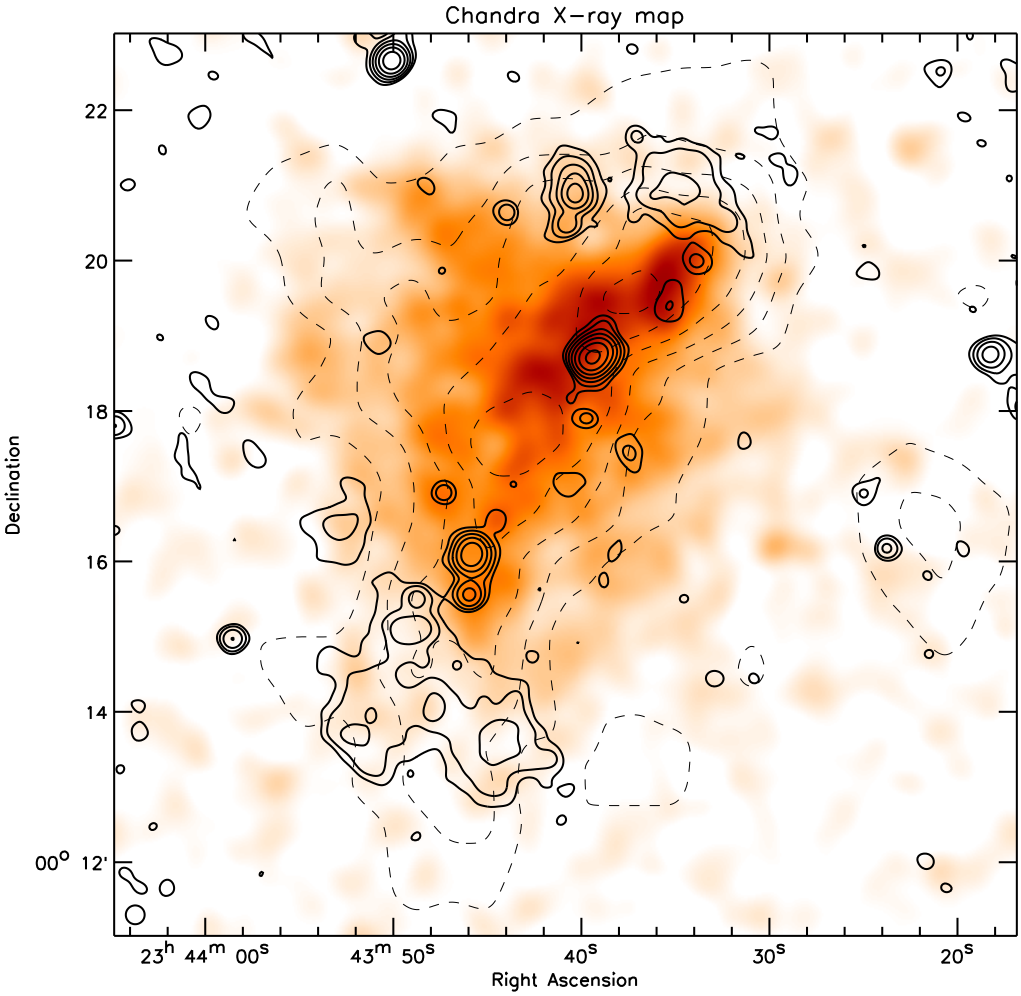

Figure 6.1: X-ray emission from Chandra in the 0.5 – 3.0 keV energy band. Point sources were excluded from the image, see Raychaudhury et al. (in prep.). The image has been convolved with a circular Gaussian of 24″. The solid contours represent the radio emission at 610 MHz from the GMRT. The radio map has been convolved to a circular beam of 15″ to better show the diffuse radio emission. The radio contours are drawn at $[1, 2, 4, 8, 16, 32, ...] \times 0.224$ mJy beam^{-1}. Dashed contours show the galaxy isodensity contours from SDSS, corresponding roughly to a limit of $M_V = -18.1$ (i.e., $M^* + 2.4$). The dashed contours are drawn at $[2, 3, 4, 5, ...]$ galaxies arcmin^{-2}, using the redshift cuts described in the text.

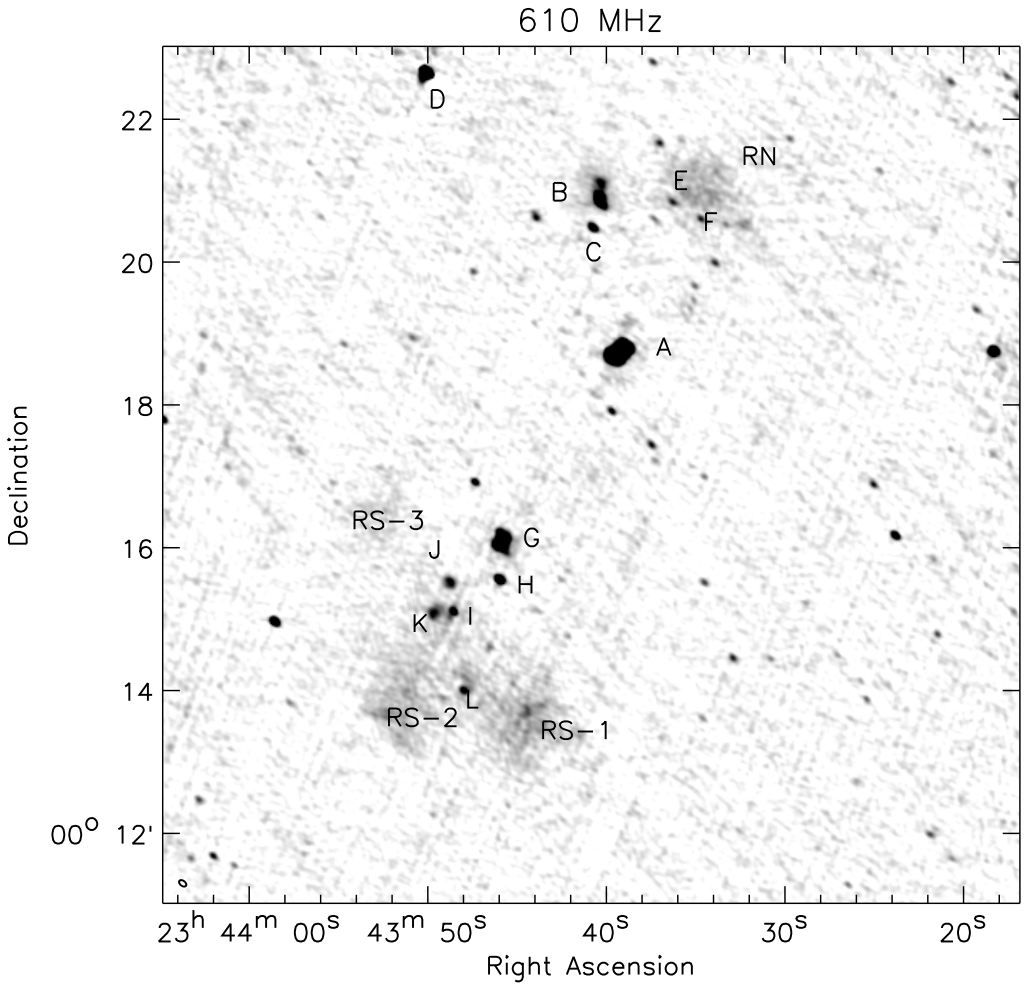

Figure 6.2: Radio map at 610 MHz. The greyscale image represent the high-resolution map with a restoring beam size of 6.9″ × 4.3″, indicated in the bottom left corner.

selfcalibration were carried out before doing a final amplitude and phase selfcalibration. A deep image was made, and the corresponding clean component model was subtracted from the UV-data. This data was then visually inspected for remaining low-level RFI and flagged automatically with 'FLGIT' using a 6σ rms clip before adding back the clean component model to the UV-data. The data was then averaged to 22 (610 MHz), 8 (241 MHz), and 11 (157 MHz), channels. The 610 MHz USB and LSB were combined using the tasks 'UVFLP'[2] (Garn et al. 2007) written by D. A. Green, 'BLOAT', and 'DBCON' so they could be simultaneously imaged and cleaned.

The 157 MHz data was further calibrated for ionospheric phase distortions, because they can become quite severe at this frequency, using the SPAM package by Intema et al. (2009). Phase solutions of the 10 brightest sources within the field of view were used to fit an ionospheric model to the data. The resulting direction-dependent phase corrections were applied during imaging using the Cotton-Schwab clean algorithm (Schwab 1984; Cotton 1999; Cornwell et al. 1999). This lowered the rms noise in the image by factor of 1.2 with respect to conventional self-calibration. The final 610 and 241 MHz images were made using CASA (formerly AIPS++)[3], using w-projection (Cornwell et al. 2005, 2008) with 512 internal planes[4]. We weighted our UV-data using robust weighting 0.5 (Briggs 1995), increasing the noise level in the maps by about 15%. The 610 and 241 MHz were cleaned with the Multi-scale CLEAN algorithm (Cornwell 2008) yielding significantly better results than Clark CLEAN for large-scale diffuse emission. Five different convolving scales were used at 610 MHz (0.0″, 3.6″, 18.0″, 60.0″, 120.0″) and three at 241 MHz (0.0″, 9.3″, 15.5″). We checked absolute flux calibration by obtaining flux measurements from the literature for 15 strong compact sources within our field from 74 MHz to 4.8 GHz. These flux measurements were fitted with second order polynomials in log-space to obtain the radio spectra. The fitted spectra were then compared to fluxes measured from the GMRT maps. The accuracy of the absolute flux calibration was found to be about 5 – 10% at all three frequencies, in agreement with values derived by Chandra et al. (2004).

The theoretical thermal noise in the image is given by[5]

$$\sigma_{\rm thermal} = \frac{\sqrt{2}T_{\rm sys}}{G\sqrt{n(n-1)N_{\rm IF}\Delta\nu t_{\rm int}}}\,, \tag{6.1}$$

with the $T_{\rm sys}$ the system temperature ($T_{\rm sys} = T_{\rm R} + T_{\rm sky} + T_{\rm ground}$, with $T_{\rm R}$, $T_{\rm sky}$, and $T_{\rm ground}$ the receiver, sky, and ground temperatures respectively), $G = 0.32$ K Jy^{-1} the antenna gain, $n \approx 26$ the number of working antennas, $N_{\rm IF}$ the number of sidebands used (both recording RR and LL polarizations), $\Delta\nu$ the bandwidth per sideband, and $t_{\rm int}$ the net integration time. At 610 MHz $T_{\rm sys} = 92$ K, $N_{\rm IF} = 1$[6], $\Delta\nu = 13.5$ MHz, and $t_{\rm int} = 12.9$ hrs. The expected thermal noise for 12.9 hrs integration time is about 22 μJy beam^{-1}, where we take into account that typically 25% of the data is flagged due to RFI. The noise level in our maps is 28μJy beam^{-1}, which is close to the thermal noise since weighting increased our noise level by about 10%. The system temperature at 157 MHz is 482 K and 177 K at 241 MHz. In both cases $T_{\rm sky}$ dominates the contribution over $T_{\rm R}$ (at all frequencies $T_{\rm ground} < T_{\rm R}$). The thermal noise at 241 MHz ($\Delta\nu = 6.9$ MHz, $N_{\rm IF} = 0.5$,

[2] http://www.mrao.cam.ac.uk/~dag/UVFLP/

[3] http://casa.nrao.edu/

[4] The 157 MHz images could not be made with the CASA imager since the direction-dependent phase corrections could only be applied using specialized imaging routines from the SPAM package.

[5] http://www.gmrt.ncra.tifr.res.in/gmrt_hpage/Users/doc/manual/UsersManual/node13.html

[6] There are two sidebands but only one polarization is recorded

$t_{\rm int}$ = 12.9 hrs) is expected to be 96 μJy beam^{-1}. At 157 MHz we expect 245μJy beam^{-1} ($\Delta\nu$ = 6.0 MHz, $N_{\rm IF}$ = 1, and $t_{\rm int}$ = 6.25 hrs). The noise levels in our 241 and 157 MHz images are 297 μJy beam^{-1} and 1.36 mJy beam^{-1}, respectively. These are a factor 3.1 and 5.5 higher than the expected thermal noise. This is probably caused by remaining RFI, pointing errors, and other phase/amplitude errors, which cannot be solved for in our calibration. A significant amount of RFI is still present on short baselines at 157 MHz. By flagging these baselines, the noise level decreases to about 0.97 mJy beam^{-1}. We have, however, not chosen to use this map as the diffuse emission from the cluster is removed together with the RFI.

6.3 Results

A summary of the maps made, the corresponding restoring beam values and noise levels, is given in Table 6.1. The high-resolution maps at three different frequencies are shown Figs. 6.2 and 6.3.

We labeled the compact ($\lesssim$ 30″) radio sources alphabetically in order to clarify the discussion of the different sources found in the maps, see Fig. 6.2 and Appendix 6.8. We only chose to label the brightest sources and those located close to regions with diffuse emission. The 610 MHz, as well as the 241 MHz image, show two regions of diffuse emission, one to the north of the cluster center (RN: relic north) and one in the south (RS: relic south). The southern diffuse region consists of three different components labeled RS-1, RS-2, and RS-3. RS-3 seems to be detached from RS-1 and RS-2. A hint of the diffuse emission is visible in the 157 MHz map at the 3σ level. Given that the diffuse sources are located in the periphery of the cluster and the diffuse emission does not seem to be associated with any of the radio galaxies, we will refer to them as relics (see Sect. 6.6). Several compact sources related to AGNs, including several possible head-tail sources, are located within the cluster. Other compact sources are related to AGNs located behind or in front of the cluster. An overview of the labeled sources with their flux densities and spectral indices is given in Table 6.2.

Source A is located in the center of the clusters (near the X-ray emission peak, see Sect. 6.4). Other bright sources include B northeast to RN, D in the far north, and G in the south north of RS-2. Several fainter sources are visible close to relic RN, namely E and F, and nearby RS, namely H, I, J, K, and L.

Sources A, B, and D are also detected by the 1.4 GHz FIRST survey. Source G is not listed in the FIRST catalog, but a hint is seen in the FIRST image. In the 1.4 GHz NVSS image sources A, B, D, and G are visible, and the combined emission from sources I, J, K, L, RS-2, and RS-1. A hint of source RN is seen (blended with B). In the 325 MHz image from Bagchi et al. (2002) source A and B are visible, although the resolution is not high enough to separate source B from the relic RN. The northeast extension of diffuse emission towards source D, which was detected at the 2σ-level in the 325 MHz image from Bagchi et al., is not visible in any of our maps, indicating that this feature is not real.

The deep high-resolution 610 MHz map shows that the radio relics RN and RS are truly diffuse and do not originate from compact sources. RN has a size of about 1.5′ by 1′ (0.37 by 0.25 Mpc) and a total flux of 14, 21, and 36 mJy at 610, 241, and 157 MHz, respectively. RS (RS-1 + RS-2 + RS-3) has a size of about 5′ by 2′ (1.2 by 0.49 Mpc) and a total flux of 43 mJy (610 MHz), 72 (241 MHz), and 70 mJy (157 MHz), see Table 6.2. We subtracted the flux contribution of the compact sources (E, F, I, J, K, and L) at 610 MHz from RS and RN. At 241

Table 6.2: Source properties

Source	RA[a]	DEC	F_{610} mJy	F_{241} mJy	F_{157} mJy	α^b	resolved/unresolved	morphology/type
A	23 43 39.3	00 18 43.6	29.6 ± 2.9	69.4 ± 7.0	69.7 ± 7.8	−0.92 ± −0.15	resolved	head-tail
B	23 43 40.3	00 20 52.8	10.1 ± 1.2	20.4 ± 2.6	38.5 ± 7.6	−0.76 ± 0.19	resolved	head-tail
C	23 43 40.7	00 20 29.3	1.53 ± 0.18	...	...	...	unresolved	...
D	23 43 50.1	00 22 39.7	12.9 ± 1.2	15.8 ± 1.6	19.5 ± 3.0	−0.22 ± 0.15	unresolved	...
E	23 43 36.2	00 20 51.0	0.79 ± 0.12	...	...	...	unresolved	...
F	23 43 34.6	00 20 36.5	0.66 ± 0.11	...	...	...	unresolved	...
G	23 43 45.8	00 16 05.8	10.2 ± 1.2	42.2 ± 4.7	53.2 ± 5.3	−1.53 ± 0.17	resolved	head-tail
H	23 43 46.0	00 15 33.5	2.33 ± 0.25	6.36 ± 1.2	...	−1.08 ± 0.23	unresolved	...
I	23 43 48.6	00 15 06.5	1.30 ± 0.37	...	...	...	unresolved	...
J	23 43 48.7	00 15 30.9	1.44 ± 0.25	...	...	...	resolved	...
K	23 43 49.6	00 15 05.5	1.76 ± 0.43	...	...	...	resolved	...
L	23 43 47.9	00 14 00.4	1.33 ± 0.32	...	...	...	unresolved	...
RN	~23 43 35	~00 21 00	14 ± 3	21 ± 7	~36	−0.49 ± 0.18[c]	resolved	diffuse, relic
RS-1 + RS-2	~23 43 50	~00 14 20	37 ± 13	72 ± 21	~70	−0.76 ± 0.17[c]	resolved	diffuse, relic
RS3	~23 43 52	~00 16 15	6 ± 3	...	...	...	resolved	diffuse, relic

[a] position (peak flux) derived from the 610 MHz map
[b] spectral index between 610 and 241 MHz
[c] Spectral index was calculated using our fluxes at 610, 241, and 157 MHz, combined with the fluxes at 325 and 1400 MHz from Bagchi et al. (2002), see Sect. 6.5.1

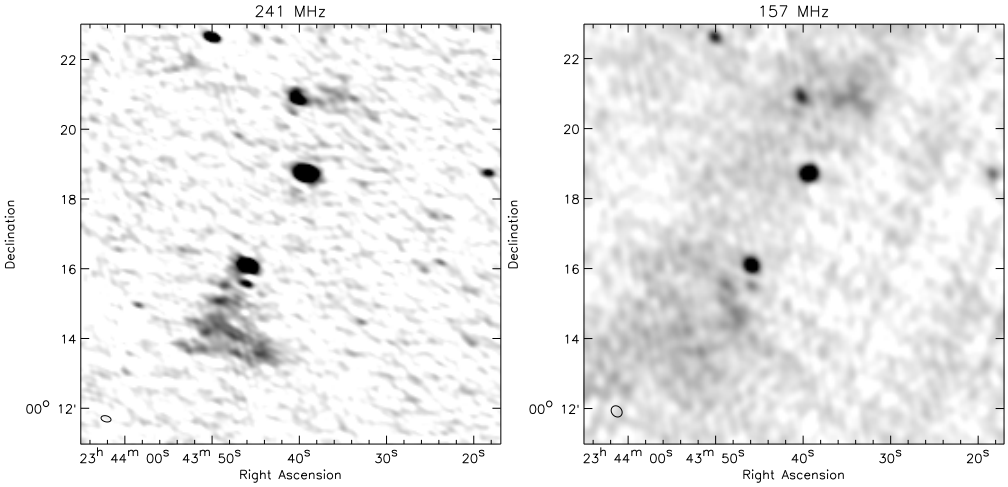

Figure 6.3: Left: Radio map at 241 MHz. The restoring beam size is 17.4″ × 10.3″. Right: Radio map at 157 MHz. The restoring beam size is 21.1″ × 17.1″.

and 157 MHz we assumed a spectral index of −0.5, because the resolution at those frequencies was too low to properly identify these sources within the diffuse emission. The flux of RN and RS was determined by measuring the flux within a region showing the diffuse emission (using the lowest contour visible in the convolved 610 MHz image in Fig. 6.1) with the AIPS task 'TVSTAT'.

A description of the compact sources and their optical counterparts is given in Appendix 6.8.

6.4 Radio, X-ray, and galaxy distribution comparison

An X-ray map of 0.5 – 3.0 keV X-ray emission from Chandra with radio contours is shown in Fig. 6.1. The Chandra image was taken from Raychaudhury et al. (in prep). These observations had a net exposure time of 29.5 ks, and the cluster was placed on the ACIS I3 CCD array. Point sources were removed from the maps based on the criteria described in Raychaudhury et al.. The X-ray image shows extended emission roughly in the north-south direction. A fainter northeastern extension is also visible. The morphology clearly shows a highly distorted ICM, an indication of a recent or ongoing merger. The global temperature in the cluster was found to be $\sim$ 5 keV. The cluster has a total X-ray luminosity ($L_{\rm X}$, 0.3−8.0 keV) of 3×10^{44} erg s^{-1}. The combined (restframe) radio power $P_{1.4\ \rm GHz}$ of the two relics is $\sim 5\times10^{24}$ W Hz^{-1}. The two diffuse radio structures are located to the north and the south of the X-ray emission, symmetrically with respect to the cluster center. The radio emission is located outside the X-ray bright area, similar to the double relics found in A3667, A3376, A2345, and A2140 (Röttgering et al. 1997; Bagchi et al. 2006; Bonafede et al. 2009b). The relics appear elongated perpendicular to the direction of the main merger apparent from the X-ray data (the main merger axis is orientated north-south). No central radio halo is detected, with a limit on the surface brightness of $\sim$ 1.5 μJy arcsec^{-2}. The largest spatial scale detectable in the 610 MHz map is about 4′, which corresponds to a

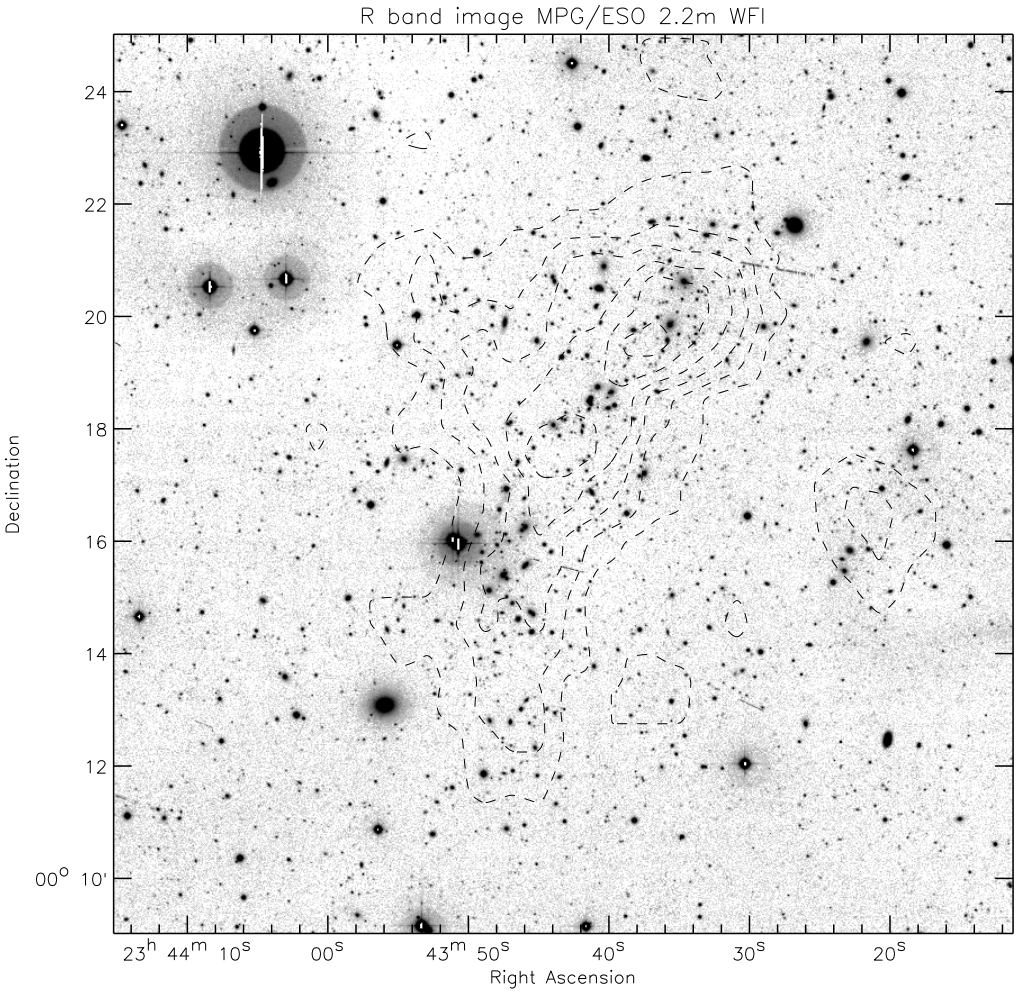

Figure 6.4: Large-scale galaxy distribution around ZwCl 2341.1+0000. The optical R band image, a combination of several individual exposures resulting in a total exposure time of 7800 s, was obtained with the WFI at the MPG/ESO 2.2m telescope. Dashed contours show the galaxy isodensity contours from SDSS, for details see Fig. 6.1. The image shows an area of $16' \times 16'$ (~ 4 Mpc $\times$ 4 Mpc) in size.

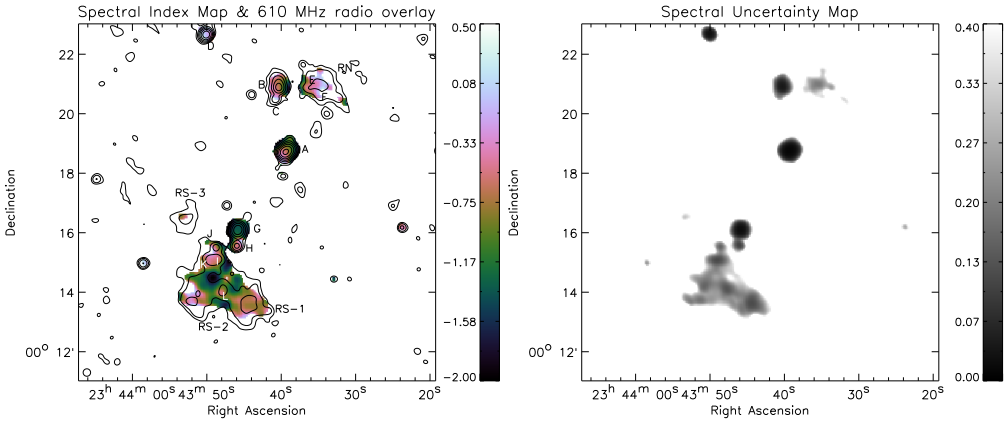

Figure 6.5: Left: Spectral index map between 610 and 241 MHz with a resolution of 18″. The black contours show the 610 MHz radio map convolved to a resolution of 15″. The radio contours are drawn at $[1, 2, 4, 8, 16, 32, ...] \times 0.224$ mJy beam^{-1}. Right: Spectral index uncertainty map between 610 and 241 MHz. The uncertainty of about 10% in the absolute flux calibration, resulting in an additional uncertainty of ±0.15 in the spectral index, is not included.

physical size of 1 Mpc. This indicates that a possible radio halo in ZwCl 2341.1+0000 has a size $\gtrsim 1$ Mpc, or a very low surface brightness; or alternatively, it does not exist at all.

An optical R band image from the Wide Field Imaging (WFI) system at the MPG/ESO 2.2m telescope, showing the large-scale galaxy distribution around ZwCl 2341.1+0000, is shown in Fig. 6.4. For more details about this image see Raychaudhury et al. (in prep.). The galaxy isodensity contours are also indicated in Figs. 6.1 and 6.4. The surface density of galaxies (per square arcmin) was computed using the photometric redshifts from the SDSS DR7 catalogs. Galaxies between $0.24 + z_{\rm err} < z < 0.31 - z_{\rm err}$ were selected from the catalogs, with $z_{\rm err}$ (typically between 0.02 and 0.06) the error in the photometric redshift. This assures that galaxies at approximately the distance of the cluster are selected while fore-/background galaxies are omitted. The galaxy distribution more or less follows the X-ray emission. The fainter northeastern extension in the X-ray emission is associated with a galaxy filament extending roughly in the same direction. Several substructures are visible within the main north-south galaxy structure.

6.5 Spectral index & equipartition magnetic field strength

6.5.1 Spectral index

Radio spectra can be an important tool for understanding the origin of the relativistic electrons. We have created a spectral index map between 610 and 241 MHz, by convolving the 610 MHz image to the 241 MHz resolution, see Fig. 6.5 (left panel). We blanked pixels with a signal-to-noise ratio (SNR) below 3 in both maps. The errors in the spectral index are displayed in Fig. 6.5 (right panel) and are based on the rms noise in the images. Taking the uncertainty of about 10% in the absolute flux calibration into account results in an additional systematic error

in the spectral index of ±0.15.

Spectral index variations are visible for RS and RN. At the location of compact sources (I, J, K, and L) embedded within the relic RS, the spectral index is relatively flat, around −0.5. A region with steep steep spectra is found in the northern region of RS-2. The spectral index of RN seems to steepen towards the east. However one has to be careful not to overinterpret these variations, as residual calibration errors may have resulted in artificial variations. Furthermore, differences in the UV-coverage can also have introduced spurious variations in the spectral index map. For source A, there is an indication of spectral steepening towards the northwest consistent with the hypothesis that the core of the radio source is located southeast. The same is observed for source B, with steepening towards the north.

The integrated spectral index for RN (excluding the compact sources) is $-0.49 \pm 0.10 \pm 0.15$, with the second error the previously reported systemic flux calibration error. The spectral index of −0.49 is consistent with the value of -0.47 ± 0.2 measured by Bagchi et al. (2002). For RS (not including RS-3), we find $-0.76 \pm 0.09 \pm 0.15$, somewhat steeper than the value of -0.5 ± 0.15 reported by Bagchi et al. but consistent within the errors. The spectral indices were determined by fitting a simple power-law spectra through the integrated fluxes for RN and RS. The flux measurements in this work were combined with those measured from the images presented by Bagchi et al. (2002). The fluxes were determined in a fixed region, which was the same at all frequencies (without blanking). Compact sources were subtracted using the flux measurements at 610 MHz and a spectral index of −0.5.

6.5.2 Equipartition magnetic field

The presence of magnetic fields in the cluster on scales ∼1 Mpc is demonstrated from the observed synchrotron radiation from the two radio relics (RN and RS). The strength of the magnetic field can be estimated by assuming minimum energy densities in the radio sources. The minimum energy density (in units of erg cm^{-3}) is given by

$$u_{\rm min} = \xi(\alpha, \nu_1, \nu_2)(1+k)^{4/7} \nu_0^{-4\alpha/7} (1+z)^{(12-4\alpha)/7} I_0^{4/7} d^{-4/7} \tag{6.2}$$

with $\xi(\alpha, \nu_1)$, a constant tabulated in Govoni & Feretti (2004), typically between $10^{-12} - 10^{-14}$, I_0 the surface brightness (mJy arcsec^{-2}) at frequency ν_0 (MHz), d the depth of the source (kpc), and k the ratio of the energy in relativistic protons to that in electrons (taken often as $k = 1$ or $k = 0$, behind a shock k is in the range $1 - 100$). A volume-filling factor of one has been assumed in the above equation. The equipartition magnetic field strength can then be calculated as

$$B_{\rm eq} = \left(\frac{24\pi}{7} u_{\rm min} \right)^{1/2} . \tag{6.3}$$

This method calculates the synchrotron luminosity using a fixed high and low-frequency cutoff (ν_1 and ν_2). However, this is not entirely correct since the upper and lower limits should not be fixed during the integration because they dependent on the energy of the radiating electrons. Instead, low and high energy cutoffs for the particle distribution should be used (Brunetti et al. 1997; Beck & Krause 2005). Taking this into account (and assuming that $\gamma_{\rm min} \ll \gamma_{\rm max}$, the energy boundaries indicated by the Lorentz factor), the revised equipartition magnetic field strength ($B'_{\rm eq}$) is

$$B'_{\rm eq} \sim 1.1 \gamma_{\rm min}^{(1+2\alpha)/(3-\alpha)} B_{\rm eq}^{7/(6-2\alpha)} . \tag{6.4}$$

Using a ratio of unity for the energy in relativistic protons to that in electrons (i.e., $k = 1$) and applying the first of the previous two methods, we derive an equipartition magnetic field of $B_{\rm eq} = 0.59\ \mu$Gauss for the northern relic ($\xi = 2.13 \times 10^{-12}$, $\nu_1 = 10$ MHz, $\nu_2 = 10$ GHz), and $B_{\rm eq} = 0.55\ \mu$Gauss for the southern relic ($\xi = 8.75 \times 10^{-13}$). For the depth along the line of sight, we have taken the average of the major and minor axis of the relics. Using the lower and higher energy cutoff limits results in $B'_{\rm eq} = 0.64\ \mu$Gauss (RN) and $0.93\ \mu$Gauss (RS), assuming $\gamma_{\rm min} = 100$. Using $\gamma_{\rm min} = 5000$ leads to $B'_{\rm eq} = 0.66\ \mu$Gauss and $0.48\ \mu$Gauss, respectively. The exact value for the lower cutoff is difficult to estimate. The Lorentz factor (γ) can be estimated according to $\gamma \sim 5 \times 10^2 \times (\nu[\mathrm{MHz}]/B_\perp[\mu\mathrm{Gauss}])$. The exact value for $\gamma_{\rm min}$ depends on the shape of the radio spectrum. Taking $k = 100$ results in magnetic field strengths of about a factor of three higher than $k = 1$.

6.6 Discussion

We have interpreted the diffuse radio emission in the periphery of ZwCl 2341.1+0000 as a double radio relic, arising from outgoing shock fronts because of a cluster merger. This interpretation is based on (i) the location of the diffuse radio emission with respect to the X-ray emission, (ii) the presence of an elongated structure of galaxies in optical images, (iii) the orientation of the symmetry axis of the double relic perpendicular to the elongation axis of the X-ray and optical emission, (iv) the morphology of the X-ray emission, (v) the lack of a direct connection between the diffuse emission and the radio galaxies within the cluster, and (vi) the presence of head-tail galaxies, which are commonly found in merging clusters (e.g., Burns et al. 1994a). This is all clear evidence that we are witnessing a merging system of subclusters where electrons are (re-)accelerated by large-scale shocks. Neither the Chandra nor the XMM-Newton X-ray images (Raychaudhury et al.) show any shock fronts at the location of the relics. However, both observations are probably too short to see any sharp details in the low-brightness X-ray regions so far from the cluster center.

6.6.1 Alternative explanations

AGN also provides a source of relativistic electrons, and the question arises whether the diffuse radio emission could be related to an AGN. In particular, could RS and RN be the lobes of a giant radio galaxy located within the cluster? This seems unlikely, as (i) no host galaxy is visible located roughly halfway between RN and RS. The most likely candidate would then be source A, but this source has the morphology of a compact head tail source, with no indication of a large-scale jet. The arm-length ratio of 1.9 between the two lobes and the core would also be quite extreme, because arm-length ratios are typically smaller than 1.5 (e.g., Konar et al. 2008). A faint 0.6 mJy source (RA $23^h\ 43^m\ 39.7^s$, DEC $00^\circ\ 17'\ 55''.0$) is located below A, resulting in a more reasonable arm-length ratio of about 1.3. But this source seems to be associated with a much more distant $z_{\rm phot} = 0.70$ galaxy. It could also be that the host galaxy is no longer active and therefore no central radio source is visible; however, in this case the spectral index of the lobes is expected to be steeper than about -1, which is not observed. (ii) This would make it one of the largest radio galaxies known with a size of 2.2 Mpc, but radio galaxies of this size are very rare. The largest known radio source is J1420−0545, with a projected size of 4.69 Mpc (Machalski et al. 2008), and (iii) these giant radio galaxies do not reside in a high-

density cluster environment. Bagchi et al. (2002) came to the same conclusion that sources RN and RS are probably not related to a giant radio galaxy. Another possibility is that the electrons originate from some of the compact sources located in or around the regions with diffuse emission. However, RN does not seem to be associated with the proposed head-tail source B, with the tail pointing north and RN located to the west. Source E and F are located within the diffuse emission but are unresolved. Source F would then be the most likely candidate because it is located at the distance of the cluster (source E is located behind the cluster with $z_{\rm phot} = 0.45$). However, in that case we would expect some head-tail morphology, but the source is compact.

RS-1 and RS-2 could be the radio lobes from source L, which coincides with an elliptical galaxy (probably a member of the cluster, $z_{\rm phot} = 0.30$). The radio source would then span a size of about 700 kpc. However the morphology of RS-1 and RS-2 is not entirely consistent with this scenario because no obvious lobe structure is visible. Furthermore there are no jets originating from L and the radio bridge connecting the two relics (RS-1 and RS-2) is very wide. In fact source L is completely embedded within the diffuse emission. The diffuse emission could also be associated with sources J, K, which could have supplied the radio plasma. However, no clear connection is visible although sources J and K are resolved. Both of these scenarios also fail to explain the presence of RS-3. An association with source G is also unlikely since it seems to be completely detached from the diffuse emission.

6.6.2 Comparison of spectral indices and magnetic field strengths with other double relics

Röttgering et al. (1997) report a spectral index of ~ -1.1 for the northern relic of A3667 (between 85.5, 408, and 843 MHz). For RXC J1314.4−2515, Venturi et al. (2007) report a spectral index of about -1.4 for both relics between 1400 and 610 MHz. Bonafede et al. (2009b) report integrated spectral indices of -1.5 and -1.3 between 1400 and 325 MHz for A2345 and -1.2, -1.3 for A1240. Spectral steepening was observed away from the shock front towards the center of the cluster for one relic in A1240 (the data for the other relic was consistent with this trend) as well as for one of the relics in A2345. If the relics trace outward traveling shock fronts, spectral steepening towards the cluster center is expected because of spectral aging. Our low SNR in the 241 MHz map means that this cannot be tested for the double relics in ZwCl 2341.1+0000, although this prediction relies on several assumptions about the viewing angle, the magnetic field structure, and some assumptions about the merger geometry. A detailed merger scenario is presently unavailable from optical and X-ray observations.

Our derived spectral indices of -0.49 (RN) and -0.76 (RS) are not particularly steep, although the errors in the spectral indices are relatively large. We also note that some large-scale variations in the background flux level are present, in particular east of the northern relic. By measuring the total flux within with an area just east of RN, we estimate that this could have potentially resulted in the flux loss of 10 mJy. If correct, this suggests a spectral indices of ~ -0.6 for RN. High-sensitivity observations, at for example 325 MHz, are needed to resolve this issue and create better spectral index maps.

Equipartition magnetic fields of about 1μGauss have been derived for several clusters having radio halos or relics (e.g., Govoni & Feretti 2004). Our derived equipartition magnetic field strength of approximately 0.6 μGauss is comparable to values derived for other double relics. Bagchi et al. (2006) derive a value of 0.5 – 3.0 μGauss for the double relics in A3376, and

Bonafede et al. (2009b) derived field strengths of 1.0−2.5 μGauss for A1240 and 0.8−2.9 μGauss for A2345.

Equipartition field strength should be used with caution, not only for their dependence on merely guessed properties of the electron spectrum, but also for the assumption of equipartition between relativistic particle and magnetic field energies, which may or may not be established by physical processes in the synchrotron emitting region. Faraday rotation and inverse Compton (IC) scattering of CMB photons by relativistic electrons in the relics can also give an independent estimate of the magnetic field strength. Both techniques give similar results (within a factor of 10) to the derived equipartition magnetic field strength, indicating that the assumptions made are reasonable (see Govoni & Feretti 2004; Ferrari et al. 2008; Bonafede et al. 2009b, and references therein).

6.6.3 Origin of the double relic

The presence of Mpc scale radio emission in the periphery of the cluster requires an acceleration mechanism for emitting relativistic particles. This is naturally provided by the diffusive shock acceleration mechanism (DSA; Krymskii 1977; Axford et al. 1977; Bell 1978a,b; Blandford & Ostriker 1978; Drury 1983; Blandford & Eichler 1987; Jones & Ellison 1991) via the Fermi-I process (Ensslin et al. 1998; Miniati et al. 2001). In this scenario the synchrotron spectral index, α, of the relativistic electrons is determined by the slope, q, of the underlying CR distribution function, which in turn depends on the shock Mach number, $\mathcal{M}$ (Landau & Lifshitz 1959; Sarazin 2002). The relevant expressions (in linear theory) are

$$\alpha = -\frac{q-3}{2},\ q = \frac{4}{1-\mathcal{M}^{-2}} \text{ or, } \alpha = -\frac{3\mathcal{M}^{-2}+1}{2-2\mathcal{M}^{-2}}\ . \tag{6.5}$$

For strong shocks, $\mathcal{M} \gg 1$, resulting in a flat spectral index of about −0.5.

However, the high-energy electrons responsible for the synchrotron emission have a finite lifetime given by

$$t_{\rm age} = 1060\frac{B^{0.5}}{B^2+B_{\rm IC}^2}[(1+z)\nu_b]^{-0.5}\ [\text{Myr}]\ , \tag{6.6}$$

with B the magnetic field strength and $B_{\rm IC} = 3.25(1+z)^2$ the equivalent magnetic field strength of the microwave background both in units of μGauss (e.g., Miley 1980; Slee et al. 2001). We have no information about the break frequency ν_b (expressed in GHz) but assume a reasonable value of $\gtrsim 1$ GHz, because the spectral indices between 241 and 610 MHz are not particularly steep. Then for a magnetic field strength of 0.6 μGauss $t_{\rm age} \lesssim 50$ Myr.

In the post-shock flow, the accelerated particles are most likely trapped by the strong turbulent field generated by the shock itself. Then, the extent of the region within which diffuse radio emission is expected to be visible can be roughly estimated by taking the product of the particles cooling time and the shock speed (Miniati et al. 2001). This typically gives a few hundred kpc, roughly consistent with the thickness of the sources observed in Fig. 6.1. The lateral extent, on the other hand, is related to the size and strength of the shock. In addition, the energy losses mean that the longer the distances from the acceleration site (shock front), the lower the energy cutoff appearing in the particle distribution function. As it turns out, the combination of the particles distribution functions at different locations has a slope that is steeper by one unit with respect to the one at the acceleration site (Bagchi et al. 2002). As a result, although the

spectrum is flat at the acceleration site ($\alpha \sim -0.5$), we expect to measure a spectral index closer to minus one. Higher values than this (i.e., flatter radio spectra) can either indicate a continuous acceleration in the post-shock region, incomplete shock acceleration model, a systematic error in the calculation of the spectral index, or a combination thereof.

Our spectral spectral indices are relatively flat and marginally consistent with the above description in which the radio emitting electrons are shock-accelerated. Such flat spectral indices have also been found for other merger related relics. An example is the relic in Abell 2256. Brentjens (2008) measures a spectral index of ~ -0.5 for some parts of the relic between 338 and 365 MHz. The integrated spectral index for the relic was found to be -0.72 ± 0.02, similar to that in ZwCl 2341.1+0000.

High mach number shocks are required for efficient particle acceleration (Blandford & Eichler 1987). Numerical simulations indicate the development of different types of shocks during structure formation, including external accretion shocks, as well as merger and flow shocks, both of which are internal to a galaxy cluster (Miniati et al. 2000). These shocks differ in their respective Mach number, (e.g., Miniati et al. 2000; Miniati 2002; Ryu et al. 2003; Pfrommer et al. 2006; Skillman et al. 2008). External accretion shocks, which process the low-density, unshocked IGM, have $\mathcal{M} \gg 1$, which result in flat spectral indices at the acceleration site of about -0.5. Although some level of diffuse radio emission is expected there, the surface brightness is too low to be detected by current facilities, owing to the expected low density of both magnetic field energy and CR particles there (Miniati et al. 2001; Hoeft et al. 2008; Pfrommer et al. 2008). Nevertheless, these shocks could possibly shine and be detected in gamma rays (Loeb & Waxman 2000; Miniati 2002, 2003; Keshet et al. 2003; Miniati et al. 2007). Internal shocks produced by accretion through filaments are weaker than the external accretion shocks but still strong enough to produce flat spectra at the shock front. In addition, unlike external accretion shocks, they occur in a high enough density environment to be detected by current radio facilities. Finally, binary merger shocks are weak and inefficient in the initial stages of the impact. As the shocks propagate outward into the lower density environment, however, they steepen and evolve into high Mach number shocks. Therefore, these shocks too are viable candidates for the origin of the observed radio emission. Also, a weak shock with $\mathcal{M} \sim 2.3$ seems to be able to produce a peripheral radio relic in A521 (Giacintucci et al. 2008), so it may be that the Mach numbers do not need to be that high for efficient particle acceleration.

While, in principle, according to simulations double relics are allowed in the filament-shock-accretion picture discussed above, there is no reason why they should be symmetric with respect to any particular axis. Instead, a symmetric configuration with respect to the X-ray elongation axis arises quite naturally in the binary merger picture (Roettiger et al. 1999a). Thus the morphological and symmetry properties of the source as they emerge from the combined X-ray and radio image seem to strongly suggest that the double radio relic is associated with a binary merger scenario.

6.7 Conclusions

We have presented low-frequency radio observations of the merging cluster ZwCl 2341.1+0000 at 610, 241, and 157 MHz taken with the GMRT. The radio maps show two diffuse structures to the north and south of the cluster, which we classify as a double radio relic, where the particles are accelerated by the DSA mechanism in an outward moving shock. Our interpretation is

different from Bagchi et al. (2002), which proposed that the radio emission originated from cosmic shocks in the IGM. The relics are located along the elongated X-ray axis (i.e, the merger axis). Their orientation is perpendicular to this axis and the radio emission straddles the outer boundary of the X-ray emission. Several possible head-tail sources are also found within the cluster.

The derived galaxy distribution shows an elongated structure consisting out of several substructures, and a galaxy filament extending towards the northeast that seems to be connected to the main structure. This extension is also visible in the Chandra X-ray images. The radio spectral indices found are relatively flat, -0.49 ± 0.18 for the northern relic and -0.76 ± 0.17 for the southern relic. The derived equipartition magnetic field strength is $\sim 0.6\ \mu$Gauss, comparable to values derived for other double relics. The two radio relics on both sides of the cluster are probably outward traveling shocks caused by a major merger event. High SNR radio spectral index maps, together with more detailed optical and X-ray analyses of the cluster, will be needed to further test the merger scenario, in particular whether radial spectral steepening of the relics is observed towards the cluster center. This would be evidence of an outward traveling shock.

Acknowledgements. We would like to thank T. E. Clarke for her help with the GMRT proposal. We thank the staff of the GMRT who have made these observations possible. GMRT is run by the National Centre for Radio Astrophysics of the Tata Institute of Fundamental Research. RJvW acknowledges funding from the Royal Netherlands Academy of Arts and Sciences.

Funding for the SDSS and SDSS-II has been provided by the Alfred P. Sloan Foundation, the Participating Institutions, the National Science Foundation, the U.S. Department of Energy, the National Aeronautics and Space Administration, the Japanese Monbukagakusho, the Max Planck Society, and the Higher Education Funding Council for England. The SDSS Web Site is http://www.sdss.org/. The SDSS is managed by the Astrophysical Research Consortium for the Participating Institutions. The Participating Institutions are the American Museum of Natural History, Astrophysical Institute Potsdam, University of Basel, University of Cambridge, Case Western Reserve University, University of Chicago, Drexel University, Fermilab, the Institute for Advanced Study, the Japan Participation Group, Johns Hopkins University, the Joint Institute for Nuclear Astrophysics, the Kavli Institute for Particle Astrophysics and Cosmology, the Korean Scientist Group, the Chinese Academy of Sciences (LAMOST), Los Alamos National Laboratory, the Max-Planck-Institute for Astronomy (MPIA), the Max-Planck-Institute for Astrophysics (MPA), New Mexico State University, Ohio State University, University of Pittsburgh, University of Portsmouth, Princeton University, the United States Naval Observatory, and the University of Washington.

This research has made use of the NASA/IPAC Extragalactic Database (NED), which is operated by the Jet Propulsion Laboratory, California Institute of Technology, under contract with the National Aeronautics and Space Administration. This research has made use of the VizieR catalogue access tool, CDS, Strasbourg, France.

6.8 Appendix: Compact sources at 610 MHz and optical counterparts

To identify optical counterparts for the radio sources we have overlaid the 610 MHz radio contours on SDSS images, see Figs. 6.6 and 6.7.

Source A is resolved, 13″ by 19″, with the brightest part of the emission located to the southeast. The resolution is insufficient to classify the source, but the morphology is consistent with a head-tail source. A spectral index gradient is also observed towards the northwest (Sect. 6.5.1). An optical counterpart is visible to the southwest of the center of the radio source, close to the peak of the radio emission (see Fig. 6.6). The photometric redshift ($z_{\rm phot}$) of this galaxy is 0.32, consistent with being a cluster member. The E/S0 galaxy ($\rm mag_r$ = 18.65) has a close companion ($\rm mag_r$ = 21.12) about 3″ to the southwest. The spectral index of A is −0.92, between 157 and 1400 MHz, typical for a radio galaxy. The source therefore does not seem to be directly related to the diffuse emission within the cluster, as suggested by Bagchi et al. (2002).

Source B has a peculiar morphology, resembling a head-tail galaxy. A $\rm mag_r$ = 18.65 E/S0 counterpart is located at $z_{\rm phot}$ = 0.29. The direction of the tail suggest the galaxy is falling in from the north towards the cluster center. The spectral index of the source is −0.76 (between 241 and 610 MHz). Other sources north of the cluster center are sources C, E, and F. Source C has a blue star-forming galaxy ($\rm mag_r$ = 17.87) as an optical counterpart at z = 0.261 (spectroscopic redshift). The SDSS DR6 spectrum of this galaxy shows strong emission lines (in particular Hα). A close companion is located about 4″ to the west. The E/S0 $\rm mag_r$ = 18.06 counterpart of source F has a spectroscopic redshift of 0.269, and the SDSS spectrum shows a strong Balmer break. The $\rm mag_r$= 20.11 optical counterpart of E is located at $z_{\rm phot}$ = 0.45 and may therefore not be associated with the cluster.

To the south of the cluster center we have sources G, H, I, J, K, and L. Source G is probably a head-tail source, with the tail pointing south, indicating the galaxy is also falling towards the cluster center. The spectral index α_{241}^{610} of −1.53 is consistent with such an identification, and there is a hint of spectral steepening towards the south. The counterpart of source G is an E/S0 $\rm mag_r$ = 18.35 galaxy (located at $z_{\rm phot}$ = 0.35) with two close companions. The counterpart of source H is a blue $\rm mag_r$ = 18.02 galaxy at $z_{\rm phot}$ = 0.28. The spectral index α_{241}^{610} of ∼−1.08, quite steep for a star-forming galaxy (e.g., Windhorst et al. 1993; Thompson et al. 2006; Bondi et al. 2007), this indicates that an AGN may also be present. The counterpart of source I is an E/S0 $\rm mag_r$ = 18.45 galaxy located at $z_{\rm phot}$ = 0.26. The counterpart of source L is an E/S0 $\rm mag_r$ = 19.84 galaxy with $z_{\rm phot}$ = 0.30 and $\alpha_{241}^{610} \sim -0.5$. The galaxy is located roughly in the middle between RS-1 and RS-2. Radio sources J and K are diffuse with sizes of about 10″. Source K has no counterpart, while source J has a possible $\rm mag_r$= 22.23, $z_{\rm phot}$ = 0.18 counterpart. However, J and K could also be the two lobes of a distant radio galaxy.

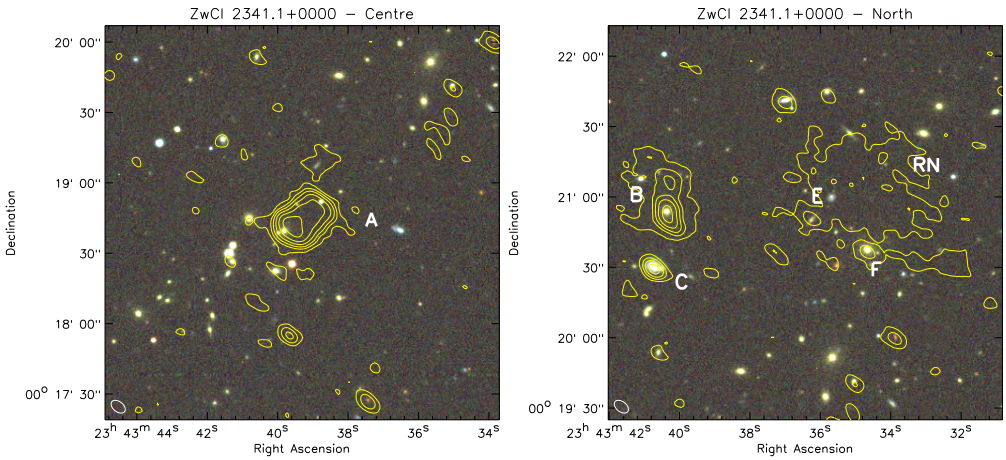

Figure 6.6: SDSS DR7 color images (g, r, and i bands) of the cluster center (left panel) and northern part of the cluster (right panel), overlaid with radio contours. The 610 MHz contour levels are drawn at $\sqrt{[1, 8, 32, 128, ...]} \times 84\ \mu$Jy beam^{-1}. The beam size of $6.9'' \times 4.3''$ is indicated in the bottom left corner.

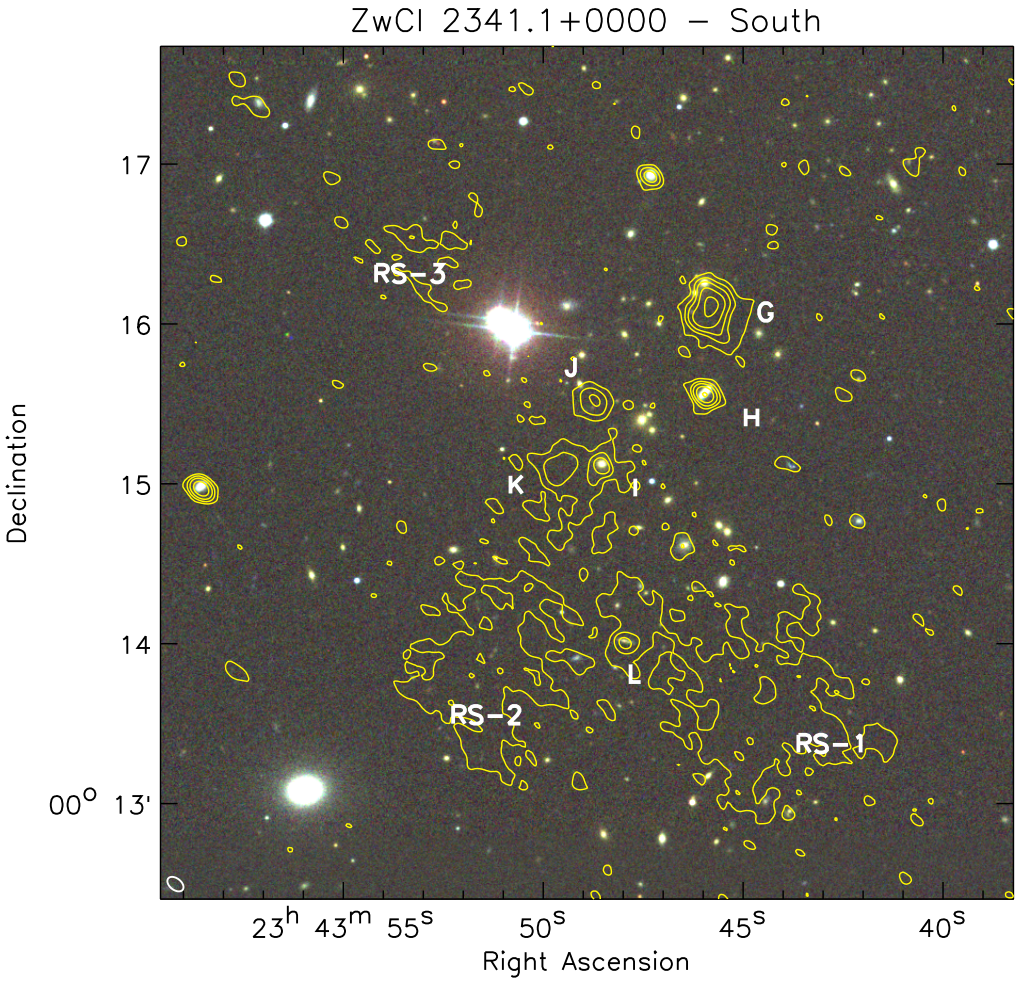

Figure 6.7: SDSS DR7 color image (*g*, *r*, and *i* bands) of the southern part of the cluster overlaid with 610 MHz radio contours. Contours are drawn at the same levels as in Fig. 6.6.

CHAPTER 7

A double radio relic in the merging galaxy cluster ZwCl 0008.8+5215

Abstract. Some merging galaxy clusters host diffuse elongated radio sources, also called radio relics. It is proposed that these radio relics trace shock waves in the intracluster medium (ICM) created during a cluster merger event. Within the shock waves particles are accelerated to relativistic energies, and in the presence of a magnetic field synchrotron radiation will be emitted. Here we present Giant Metrewave Radio Telescope (GMRT) and Westerbork Synthesis Radio Telescope (WSRT) observations of a new double relic in the galaxy cluster ZwCl 0008.8+5215. The aim of the observation is to understand the phenomenon of radio relics. We carried out radio continuum observations at 241 and 610 MHz with the GMRT, and 1.3 – 1.8 GHz observations with the WSRT in full polarization mode. Optical V, R, and I band images of the cluster were taken with the 2.5m Isaac Newton Telescope (INT). An optical spectrum, to determine the redshift of the cluster, was taken with the William Herschel Telescope (WHT). Our observations show the presence of a double radio relic in the galaxy cluster ZwCl 0008.8+5215, for which we find a spectroscopic redshift of $z = 0.1032 \pm 0.0018$ from an optical spectrum of one of the cD galaxies. The spectral index of the two relics steepens inwards to the cluster center. For part of the relics, we measure a polarization fraction in the range $\sim 5 - 25\%$. A ROSAT X-ray image displays an elongated ICM and the large-scale distribution of galaxies reveals two cluster cores, all pointing towards a binary cluster merger event. The radio relics are located symmetrically with respect to the X-ray center of the cluster, along the proposed merger axis. The relics have a linear extent of 1.4 Mpc and 290 kpc. This factor of five difference in linear size is unlike that of previously known double relic systems, for which the sizes do not differ by more than a factor of two. We conclude that the double relics in ZwCl 0008.8+5215 are best explained by two outward moving shock waves in which particles are (re)accelerated through the diffusive shock acceleration (DSA) mechanism.

R. J. van Weeren, M. Hoeft, H. J. A. Röttgering, M. Brüggen, H. T. Intema, and S. van Velzen
Astronomy & Astrophysics, **528**, 38, 2011

7.1 Introduction

Radio relics are filamentary structures often located in the periphery of galaxy clusters. It is proposed that large radio relics trace shock waves generated by cluster merger events (Ensslin et al. 1998; Miniati et al. 2001). At the shock front particles from the thermal gas are accelerated to relativistic energies by DSA mechanism in a first-order Fermi process (Krymskii 1977; Axford et al. 1977; Bell 1978a,b; Blandford & Ostriker 1978; Drury 1983; Blandford & Eichler 1987; Jones & Ellison 1991; Malkov & O'C Drury 2001). In the presence of a magnetic field these particles emit synchrotron radiation at radio wavelengths. Another possibility mentioned by Markevitch et al. (2005), is that the shock re-accelerates relativistic fossil electrons injected previously into the ICM by for example AGN. They note that from an observational point of view, this case will probably be indistinguishable from the direct shock acceleration mentioned above. An alternative scenario has been recently proposed, namely that relics arise from emission of secondary cosmic ray electrons (Keshet 2010).

Some smaller radio relics ($\lesssim$ 500kpc) have been been explained by old ("fossil") radio plasma from a previous episode of AGN activity. These sources are called *AGN relics* (see Kempner et al. 2004, for an overview of the classification of diffuse radio sources). The fossil radio plasma could also have been compressed, creating a radio *phoenix* (Enßlin & Gopal-Krishna 2001; Enßlin & Brüggen 2002). Both radio phoenices and AGN relics, are characterized by a very steep ($\alpha \lesssim -1.5$, $F_\nu \propto \nu^\alpha$, where α is the spectral index) and curved radio spectra due to synchrotron and Inverse Compton (IC) losses.

In the hierarchical model of structure formation galaxy cluster grow by the accretion of gas from the surrounding intergalactic medium (IGM) and through mergers with other clusters and galaxy groups. Large radio relics are exclusively found in disturbed clusters, indicative of merger activity. This supports the idea that shocks generated during cluster merger events can be responsible for the non-thermal radio emission. Hydrodynamical models of structure formation, including particle acceleration mechanisms (e.g., Hoeft & Brüggen 2007; Hoeft et al. 2008; Pfrommer 2008; Battaglia et al. 2009) make predictions about the location, orientation and radio power of relics in merging clusters. Amongst the several dozen radio relics known to date (e.g., van Weeren et al. 2009c; Rudnick & Lemmerman 2009; Pizzo & de Bruyn 2009; Giacintucci et al. 2008; Brentjens 2008; Kempner & Sarazin 2001; Giovannini et al. 1999, 1991), there are a few rare double relic systems, with two relics located symmetrically on opposite sites of the cluster center (e.g., van Weeren et al. 2010; Brown et al. 2011; Bonafede et al. 2009b; van Weeren et al. 2009b; Venturi et al. 2007; Bagchi et al. 2006; Röttgering et al. 1997). These double relics can be used to constrain the merger geometry and timescales involved (Roettiger et al. 1999a). If radio relics trace outward traveling shock waves in which DSA takes place, then the radio plasma in the post-shock region should have a steeper spectrum due to IC and synchrotron losses. For a relic seen close to edge-on, the luminosity profile across the width of the relic can then be used to constrain the magnetic fields strength at the location of the shock (Markevitch et al. 2005; Finoguenov et al. 2010). This is because the downstream luminosity profile should directly reflect the synchrotron losses, which in turn depend on the magnetic field strength. In van Weeren et al. (2010) we presented observations of a double relic in the merging cluster CIZA J2242.8+5301, which provided evidence for DSA in galaxy cluster merger shocks. For the largest relic we derived a magnetic field strength of about 5–7 μGauss by modeling the relic's luminosity profile across the width of the relic (although a strength of about 1.2 μGauss could not be completely ruled out).

Because there are only a few double relics systems known, we carried out an extensive search in the 1.4 GHz NVSS (Condon et al. 1998), 325 MHz WENSS (Rengelink et al. 1997), and 74 MHz VLSS (Cohen et al. 2007) surveys for the presence of arc-like radio structures around X-ray selected galaxy clusters from the ROSAT All-Sky Survey. This search already resulted in the discovery of several new radio relics, see van Weeren et al. (2009b,c,d). In this paper we present the discovery of a double relic in the galaxy cluster ZwCl 0008.8+5215 which showed faint elongated structures in both NVSS and WENSS images.

The layout of this paper is as follows. In Sect. 7.2 we give an overview of the observations and the data reduction. In Sect. 7.3 we present the radio and spectral index maps as well as optical images around the radio sources. In Sect. 7.4 we discuss the merger scenario and the magnetic field strength at the location of the relics. We end with conclusions in Sect. 7.5.

Throughout this paper we assume a ΛCDM cosmology with $H_0 = 71$ km s^{-1} Mpc^{-1}, $\Omega_m = 0.3$, and $\Omega_\Lambda = 0.7$. All images are in the J2000 coordinate system.

7.2 Observations & data reduction

7.2.1 GMRT observations

The GMRT observations were taken in dual-frequency mode, recording RR polarization at 610 MHz and LL polarization at 241 MHz. Total useable bandwidth was 30 MHz at 610 MHz and 6 MHz at 241 MHz. The GMRT software backend (GSB; Roy et al. 2010) was used giving 512 spectral channels. The total on source time was 220 min (3.7 hr). A summary of the observations is given in Table 7.1.

For the reduction we used the NRAO Astronomical Image Processing System (AIPS) package. The 610 MHz dataset was visually inspected for the presence of radio frequency interference (RFI) which was subsequently removed. Strong RFI on short baselines was present in the 241 MHz band. This RFI was fitted and subtracted from the data using the technique described by Athreya (2009) which was implemented in Obit (Cotton 2008). Summarized, the fringe-stopped correlator output of a baseline oscillates with the fringe-stop period in the presence of RFI. The fitting routine tries to fit such a signal and subtracts it from the data (Athreya 2009). This has the advantage that most of the visibilities from the short baselines are not removed (i.e., flagged) and hence spatial structure on large angular scales is preserved. We assumed the RFI to be constant over periods of 10 min and required a minimal amplitude of 5 Jy for the RFI to be subtracted. Further visual inspection of the data was carried out to remove some remaining RFI which could not be fitted because of short timescale variations of the RFI signal.

Amplitude and phase corrections were obtained for the calibrator sources using 5 neighboring channels free of RFI. These solutions were applied to the data before determining the bandpass. The bandpass was then applied and gain solutions for the full channel range were determined. The fluxes of the primary calibrators were set according to the Perley & Taylor (1999) extension to the Baars et al. (1977) scale. Several rounds of phase self-calibration and two final rounds of amplitude and phase self-calibration were carried out. We used the polyhedron method (Perley 1989; Cornwell & Perley 1992) for making the images to minimize the effects of non-coplanar baselines. Both in the 610 and 241 MHz images, there were several bright sources in the field that limited the dynamic range. Direction dependent gain solutions for these sources were obtained and these sources were subtracted from the data. This method is commonly referred to as “peeling” (e.g., Noordam 2004).

Table 7.1: GMRT observations

	241 MHz	610 MHz
Observation date	November 22, 2009	November 22, 2009
Usable bandwidth	6 MHz	30 MHz
Channel width	62.5 kHz	62.5 kHz
Polarization	LL	RR
Integration time	8 sec	8 sec
Total on-source time	220 min	220 min
Beam size	$14.65'' \times 12.5''$	$6.3'' \times 5.3''$
Rms noise ($\sigma_{\rm rms}$)	483 μJy beam^{-1}	38 μJy beam^{-1}

Table 7.2: WSRT observations

Frequency bands 21 cm (IFs)	1311, 1330, 1350, 1370, 1392, 1410, 1432, 1450 MHz
Frequency bands 18 cm (IFs)	1650, 1668, 1686, 1704, 1722, 1740, 1758, 1776 MHz
Bandwidth per IF	20 MHz
Number of channels per IF	64
Channel width	312.5 kHz
Polarization	XX, YY, XY, XY
Observation dates	28 March, 25 & 31 May, 7 & 16 June 7, 2009
Integration time	30 sec
Total on-source time	12.5 hr (21cm) , 12.5 hr (18cm)
Beam size	$23.5'' \times 17.0''$ (21cm), $23.5'' \times 17.0''$ (18cm)
Rms noise ($\sigma_{\rm rms}$)	27 μJy beam^{-1} (21cm), 33 μJy beam^{-1} (18cm)

Final images were made using "briggs" weighting (with robust set to 0.5, Briggs 1995). Images were cleaned down to 2 times the rms noise level ($2\sigma_{\rm rms}$) within the clean boxes. The images were corrected for the primary beam response[1]. The uncertainty in the calibration of the absolute flux-scale is between 5 – 10%, see Chandra et al. (2004).

7.2.2 WSRT 1.3–1.7 GHz observations

WSRT observations of ZwCl 0008.8+5215 were taken in the L-band, see Table 7.2. The observations were spread out over various runs of several hours, resulting in more or less full 12 hours synthesis coverage. Frequency switching, between the 18 and 21 cm setups, was employed every 5 min to increase the spectral baseline of the observations. Each setup had a total bandwidth of 160 MHz, evenly divided over 8 sidebands (IF). All four polarization products were recored with 64 channels per IF.

The data were calibrated using the CASA[2] package. The L-band receivers of the WSRT

[1] http://gmrt.ncra.tifr.res.in/gmrt_hpage/Users/doc/manual/UsersManual/node27.html
[2] http://casa.nrao.edu/

antennas have linearly polarized feeds[3]. Bandpass and gain solutions were determined from observations of the standard calibrators 3C48, 3C138, 3C147, 3C286, and CTD93. Time ranges for antennas affected by shadowing were removed. Some IFs were also affected by RFI and had to be partly flagged. The fluxes for the calibrators were set according to the Perley & Taylor (1999) extension to the Baars et al. (1977) scale. Frequency (channel) dependent leakage terms (D-terms) were calculated from observations of a bright unpolarized point source, while the polarization angles were set using either 3C138 or 3C286. We assumed −66.0° and 15.0° for the R-L phase difference of 3C286 and 3C138, respectively. The data were then exported into AIPS and several rounds of phase self-calibration, followed by two rounds of amplitude and phase self-calibration, were carried out. The solutions for the amplitude and phase self-calibration were determined combining both XX and YY polarizations because Stokes Q is not necessarily zero. Separate images for each IF were made (16 in total) using robust weighting of 0.75 (21 cm) and 1.25 (18 cm) giving roughly the same resolution. These images were corrected for the primary beam attenuation ($A(r)$)

$$A(r) = \cos^6 (r \times \nu \times C) \,, \tag{7.1}$$

with r the distance from the pointing center in degrees, ν the observing frequency in GHz and $C = 68$, a constant[4].

Images were cleaned to about $2\sigma_{\rm rms}$ and clean boxes were used. For each frequency setup the eight images from each IF were combined, convolving the images to the same resolution of $23.5'' \times 17.0''$ and weighting the images inversely proportional to $\sigma^2_{\rm rms}$. The images are centered at frequencies of 1382 and 1714 MHz. The final noise levels are 27 and 33 μJy beam^{-1} for the 21 cm and 18 cm images, respectively.

7.2.3 Optical images & spectroscopy

Optical images of the cluster were made with the Wide Field Camera (WFC) on the INT. The observation were taken between 1 and 8 October, 2009. The seeing varied between 0.9 and 1.3″ during the observations. Most nights were photometric. Total integration time was about 6000 sec per filter. The data were reduced in a standard way using IRAF (Tody 1986, 1993) and the *mscred* package (Valdes 1998). The R and I band images were fringe corrected. The individual exposures were averaged, pixels were rejected above $3\sigma_{\rm rms}$ to remove cosmic rays and other artifacts. Observations of standard stars on photometric nights were used to calibrate the flux scale. The images have a depth (signal to noise radio (SNR) of 5 for point sources) of approximately 24.5, 23.9, 23.3 magnitude (Vega) in the V, R and I band, respectively.

To determine the redshift of the cluster a 600 sec WHT ACAM long-slit spectrum, with the V400 grating, was taken of 2MASX J00112171+5231437 (Skrutskie et al. 2003). On the INT images this galaxy was identified being the largest cD galaxy of the cluster. The spectrum was taken on November 2, 2010 with a slit width of 1.5″. Standard long-slit calibration was done in IRAF.

[3]The WSRT records XX = I − Q, YY = I − Q, XY = −U + iV, and XY = −U − iV. I, Q, U, and V are the standard Stokes parameters

[4]from the WSRT Guide to Observations

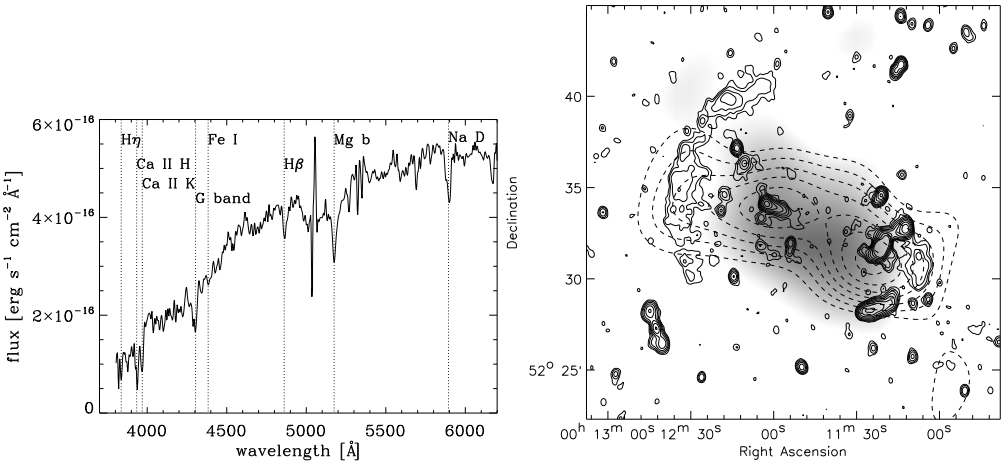

Figure 7.1: Left: Spectrum of the galaxy 2MASX J00112171+5231437 taken with the WHT ACAM V400 grating. Various absorption features are indicated. Right: X-ray emission from ROSAT, tracing the thermal ICM, is shown by the greyscale image. The original image from the ROSAT All Sky Survey was convolved with a 200″ FWHM Gaussian. Solid contours are from the WSRT 1382 MHz image and drawn at levels of $[1, 2, 4, 8, \ldots] \times 4\sigma_{\rm rms}$. The resolution of the WSRT image is 23.5″ × 17.0″. Dashed contours show the galaxy iso-density distribution derived from the INT images. Contours are drawn at $[1, 1.1, 1.2, 1.3, 1.4 \ldots] \times 0.38$ galaxies arcmin^{-2} using the color cuts as described in Sect. 7.3.2.

7.3 Results

7.3.1 Redshift of ZwCl 0008.8+5215

No redshift is available in the literature for the galaxy cluster ZwCl 0008.8+5215, with coordinates RA $00^{\rm h}11^{\rm m}25.6^{\rm s}$, DEC +52°31′41″. The cluster is located relatively close to the galactic plane at a galactic latitude $b = -9.86°$. Galactic extinction is 0.812 mag in the R-band and 0.111 in the K-band according to Schlegel et al. (1998). The spectrum of cD galaxy 2MASX J00112171+5231437 is shown in Fig. 7.1 (left panel). From this spectrum we determine a redshift of 0.1032 ± 0.018 for the galaxy, which we adopt as the redshift for ZwCl 0008.8+5215. 2MASX J00112171+5231437 is associated with a complex disturbed radio source, see Sect. 7.3.5.

7.3.2 Thermal ICM and galaxy distribution

ZwCl 0008.8+5215 is seen in the ROSAT All-Sky Survey as an east-west elongated source, see Fig. 7.1 (right panel), and listed as 1RXS J001145.3+523147 (Voges et al. 1999). Using the redshift and the ROSAT count rate we find an X-ray luminosity ($L_{\rm X,\ 0.1-2.4\ keV}$) of $\sim 5 \times 10^{43}$ erg s^{-1}. With the $L_{\rm X,\ 0.1-2.4\ keV}$-temperature scaling relation from Pratt et al. (2009), Table B.2 *BCES Orthogonal Fitting Method*, we find a corresponding temperature of ∼ 3 to 4 keV.

We computed galaxy iso-densities from the INT images. We first created a catalog of objects using Sextractor (Bertin & Arnouts 1996). We then removed all point-like objects (i.e., stars)

Table 7.3: Relic & source properties

Source	$S_{241\ \mathrm{MHz}}$ Jy	$S_{610\ \mathrm{MHz}}$ mJy	$S_{1382\ \mathrm{MHz}}$ mJy	$S_{1714\ \mathrm{MHz}}$ mJy	$\alpha^{1714\ \mathrm{MHz}}_{241\mathrm{MHz}}$	$P_{1.4\ \mathrm{GHz}}$ 10^{24} W Hz^{-1}	LLS[b] kpc
RW	0.11 ± 0.03	56 ± 8	11 ± 1.2	8.9 ± 1.2	−1.49 ± 0.12[a]	0.37	290
RE	0.82 ± 0.09	230 ± 25	56 ± 3.5	37 ± 2.7	−1.59 ± 0.06[a]	1.8	1400
A	0.186 ± 0.020	86 ± 9.0	37 ± 1.9	29 ± 1.6	−0.96 ± 0.06	1.1	270
B	0.112 ± 0.015	87 ± 9.0	34 ± 1.9	28 ± 1.6	−0.81 ± 0.06	0.99	289
C	0.423 ± 0.045	205 ± 21	88 ± 4.6	69 ± 3.6	−0.94 ± 0.06	2.6	249
D	...	2.2 ± 0.3	1.06 ± 0.1	1.2 ± 0.1	−0.63 ± 0.16[c]	0.030	...
E	2.81 ± 0.28	1016 ± 102	387 ± 20	302 ± 15	−1.14 ± 0.05	11.9	200
F	0.280 ± 0.030	135 ± 14	58 ± 3	47 ± 3	−0.93 ± 0.06	1.7	151
G	0.040 ± 0.005	16 ± 2	7.3 ± 0.4	6.3 ± 0.4	−0.94 ± 0.07	0.22	38
H	...	8.7 ± 1.2	2.6 ± 0.2	2.7 ± 0.2	−1.18 ± 0.15[c]	0.081	60
I	...	2.8 ± 0.5	1.2 ± 0.19	0.76 ± 0.18	−1.15 ± 0.23[c]	0.037	45

[a] see also Fig. 7.10 (left panel)
[b] largest linear size
[c] between 610 and 1714 MHz

from the catalogs. To exclude galaxies not belonging to the cluster we selected only galaxies with R−I and V−R colors within 0.15 magnitude from the average color of the massive elliptical cD galaxy 2MASX J00112171+5231437 (see Fig. 7.9 and Sect. 7.3.1). The range of 0.15 in the colors was taken to maximize the contrast of the cluster with respect to the fore and background galaxies in the field, but not being too restrictive so that a sufficient number of candidate cluster members was selected. The galaxy iso-density contours are shown in Fig. 7.1. The cluster shows a pronounced bimodal structure, with two cores separated by about 700 kpc. The cluster extends somewhat further in the east-west direction than the X-ray emission from ROSAT. The cD galaxy 2MASX J00112171+5231437 belongs to the western subcluster (i.e., it is located at the center of the subcluster). The eastern subcluster also hosts a separate cD galaxy (2MASX J00121892+5233460, see Fig. 7.8 (right panel)). Although we do not have a spectroscopic redshift for this galaxy, the (i) color and (ii) R and K magnitudes are in agreement with a subcluster located at the same redshift as the western subcluster (e.g., Willott et al. 2003; de Vries et al. 2007). The same is true for the other massive elliptical galaxies found in both subclusters, see Sect. 7.3.5. Therefore, both the X-ray and optical observations point towards a bi-modal galaxy cluster, indicative of an ongoing merger event. As we will show in the next sections, the radio observations also point towards a merger scenario.

7.3.3 Radio continuum maps

The WSRT 1382 MHz image is shown in Fig. 7.2 (left panel). It reveals a large arc of diffuse emission on the east side of the cluster and a smaller faint diffuse source on the west side of the cluster, symmetrically with respect to the cluster center. We classify these sources as radio relics based on their location with respect to the cluster center, their morphology, and the lack of optical counterparts. The relics are located about 850 kpc from the center of the X-ray emission.

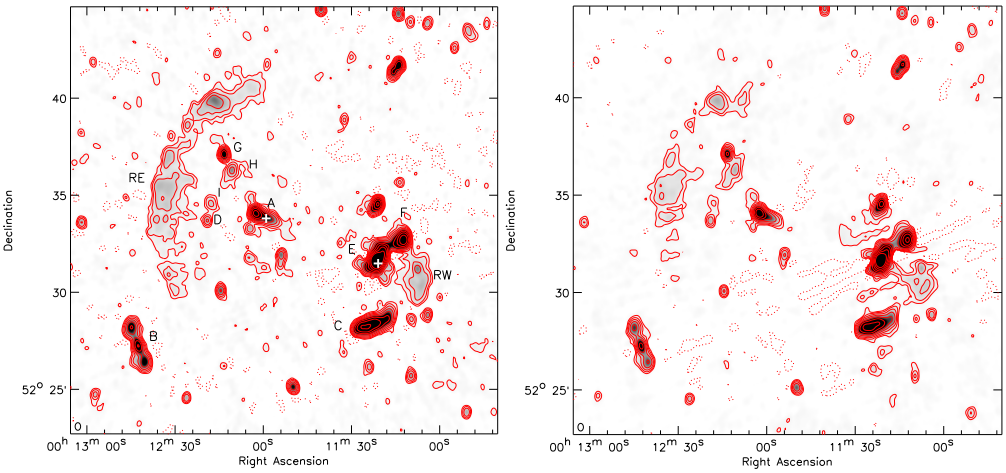

Figure 7.2: Left: WSRT 1382 MHz image. Contour levels are drawn at $[-1, 1, 2, 4, 8, \ldots] \times 4\sigma_{\rm rms}$. Negative contours are shown by the dotted lines. The beam size is $23.5'' \times 17.0''$ and shown in the bottom left corner of the image. Sources are labeled as in Fig. 7.4 (right panel). The white + symbols mark the centers of the two subclusters based on the iso-density contours from Fig. 7.3.2 (right panel). Right: WSRT 1714 MHz image. Contour levels are drawn at $[-1, 1, 2, 4, 8, \ldots] \times 4\sigma_{\rm rms}$. Negative contours are shown by the dotted lines. The beam size is $23.5'' \times 17.0''$ and shown in the bottom left corner of the image.

Several complex tailed radio sources, related to AGN activity, are also visible. The WSRT 1714 MHz image is similar to the 1382 MHz image, although the overall signal to noise ratio is less, therefore revealing less of the diffuse extended relics. The radio relics are also visible in the GMRT 610 and 241 MHz images (Figs. 7.3 and 7.4), although at 241 MHz the SNR on the relics is $\lesssim 5$ per beam.

To facilitate the discussion we have labeled various sources in Figs. 7.2 and 7.4 (right panel). Optical overlays can be found Sect. 7.3.5. The integrated fluxes, spectral indices, radio power and largest linear size for the two relics (RE & RW) are displayed in Table 7.3.

Relic RE consist of two parts, a smaller region of emission to the north and a larger one in the south (most clearly seen in Figs. 7.3 and 7.4, right panel). In the 1382 MHz image the two regions are seen connected. The eastern boundary of RE is somewhat more pronounced, while on the western side the emission fades more slowly in the direction of the cluster center. The relic has a total extent of 1.4 Mpc. The surface brightness varies across the relic fading at the extreme northern and southern ends. The northern diffuse patch has a “notch” like region of higher surface brightness. Relic RW has a much smaller extent of 290 kpc. The western boundary is more pronounced in the WSRT images. A compact source in the middle of RW is associated with a background galaxy.

The cluster also hosts a number of complex radio sources related to AGN activity, for a short discussion on these sources see Sect. 7.3.5.

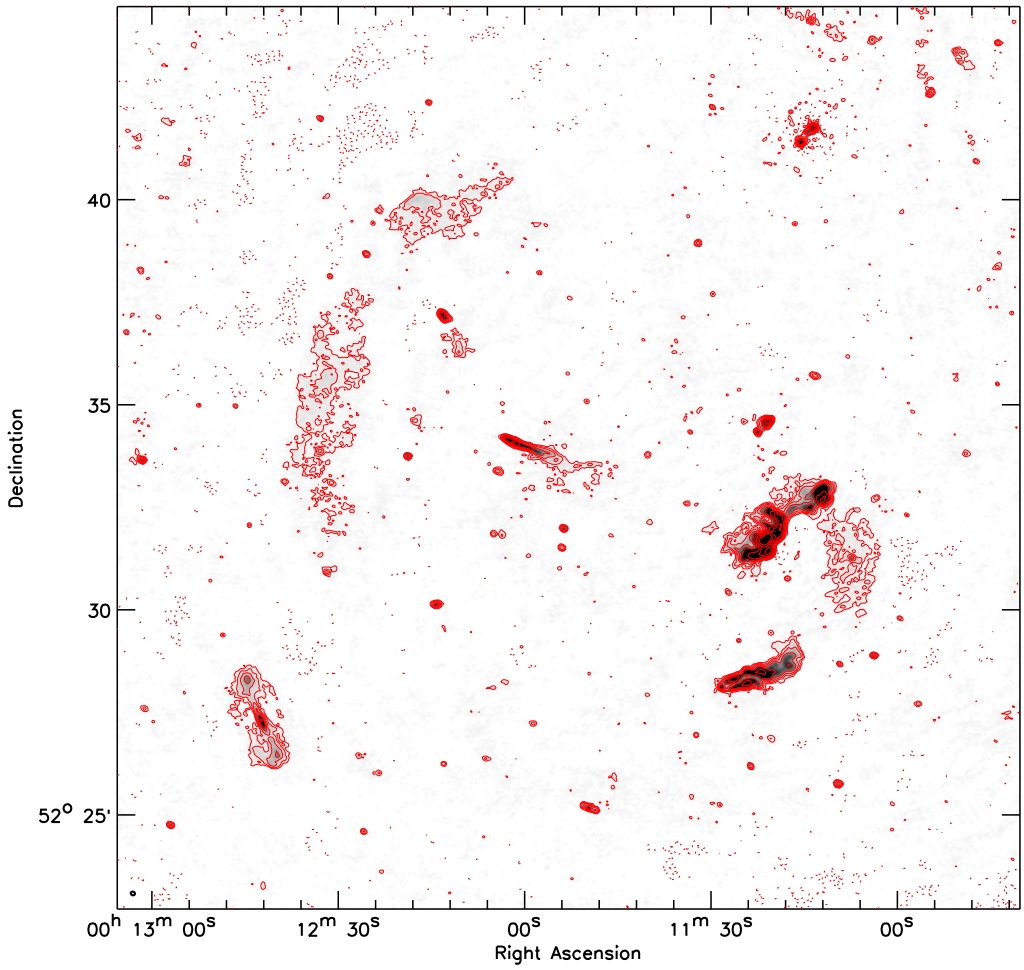

Figure 7.3: GMRT 610 MHz image. Contour levels are drawn at $[-1, 1, 2, 4, 8, \ldots] \times 4\sigma_{\rm rms}$. Negative contours are shown by the dotted lines. The beam size is $6.3'' \times 5.3''$ and shown in the bottom left corner of the image.

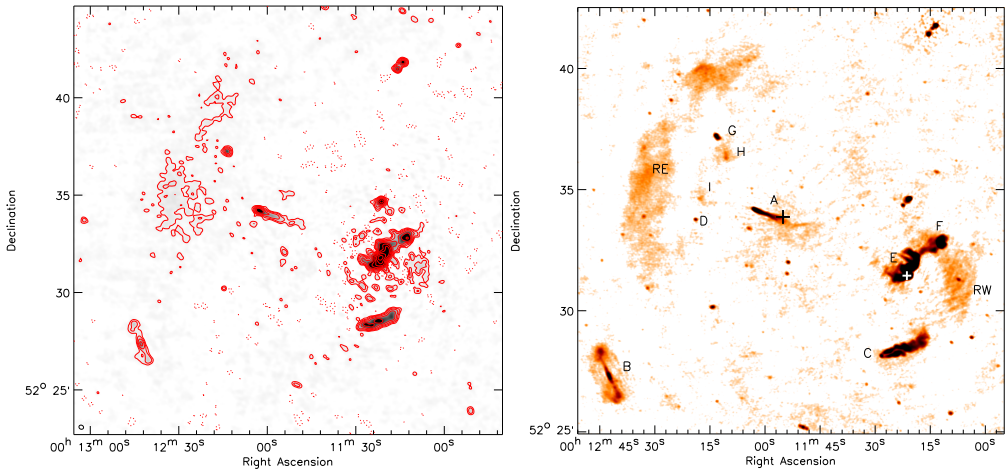

Figure 7.4: Left: GMRT 241 MHz image. Contour levels are drawn at $[-1, 1, 2, 4, 8, \ldots] \times 4\sigma_{\rm rms}$. Negative contours are shown by the dotted lines. The beam size is $14.65'' \times 12.50''$ and shown in the bottom left corner of the image. Right: GMRT 610 MHz image with sources labeled. The + symbols mark the centers of the two subclusters based on the iso-density contours from Fig. 7.1 (right panel).

7.3.4 Spectral index and polarization maps

A spectral index map was computed using both the WSRT and GMRT images, including only common UV ranges. Both the WSRT and GMRT datasets have relatively good inner UV-coverage. The largest detectable angular scale is limited to about 16′ at 610 MHz, which is sufficient not to resolve out the extended radio relics. The inclusion of maps at four different frequencies enables us to map the spectral index over the low surface brightness radio relics. Spectral index maps made with only two frequency images were too noisy to map the spectral index across the relics. The spectral index map was created by fitting a single power-law through the flux measurements at 241, 610, 1382, and 1714 MHz. In this way, we only fitted for the slope and normalization of the radio spectrum, ensuring the number of free variables in the fit remains as low as possible (at the cost of detecting spectral curvature). The technique of combining maps at more than two frequencies has another advantage that errors in the maps arising from RFI, calibration errors, deconvolution errors, slightly different UV coverage, etc., are suppressed in the spectral index map as long as they do not correlate at the same location and spatial frequencies on the sky.

Pixels in the spectral index map were blanked if any of corresponding pixels in the individual maps fell below $1.5\sigma_{\rm rms}$. Special care was taken about the precise alignment of the maps, we slightly shifted the GMRT maps by about a quarter of the synthesized beam, removing a small spectral index gradient visible across all the point sources. The result is shown in Fig. 7.5.

For relic RW, the spectral index steepens to the north and eastwards to the cluster center, from −0.9 to −2.0. The spectral index for relic RE also varies roughly between −0.9 and −2.0. The overall spectral index at the east side of relic RE is about −1.2 There is an overall trend of spectral steepening towards the west, see also Fig. 7.10 (right panel). The spectral index is

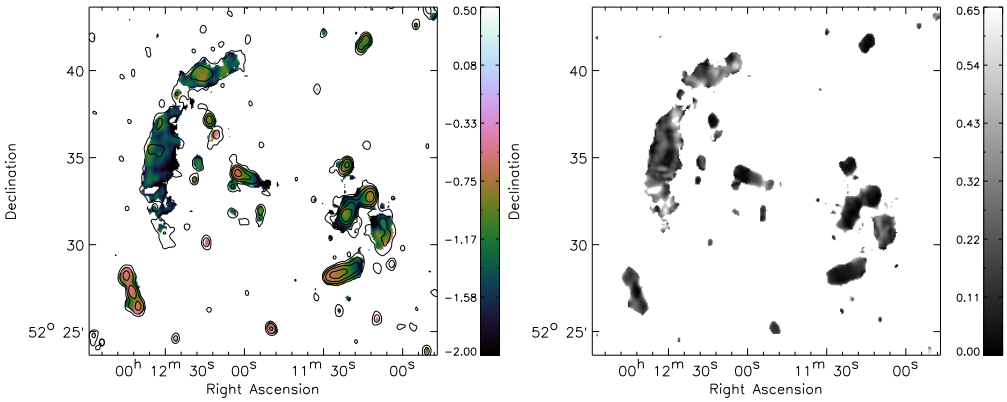

Figure 7.5: Left: Spectral index map. Spectral indices were computed by fitting a single power-law radio spectrum through the fluxes at 241, 610, 1382, and 1714 MHz. Solid contours are from the 1382 MHz WSRT map and drawn at levels of $[1, 4, 16, 64, \ldots] \times 6\sigma_{\rm rms}$. The resolution of the map is $23.5'' \times 17.0''$. Right: Spectral index uncertainty map. The map is computed on the basis of $\sigma_{\rm rms}$ values for the individual maps.

correlated with the surface brightness of the relic, the brightest parts have a flatter spectral index.

The polarization map from the WSRT at 1382 MHz is shown in Fig. 7.6. No useful polarization information could be extracted from the WSRT 18 cm observations. The polarization map reveals that most of the compact sources are polarized below the 5% level. Some polarized emission is detected from the two radio relics, although at low SNR. For relic RW the polarization fraction is around 5 – 10% (reported polarization fractions are corrected for Ricean bias; Wardle & Kronberg 1974). For RE the polarization fraction varies, with a maximum of ∼ 25%. For the fainter parts of the relics no polarized emission is detected, but this is expected if the relics are polarized at the 30% level or less. Most polarization E-vectors are aligned perpendicular to the major axis of the two relics (for the parts where polarized emission was detected).

Spectral index and polarization properties for the compact sources are discussed in Sect. 7.3.5.

7.3.5 Radio galaxies in the cluster

The cluster hosts several interesting tailed radio sources. Radio overlays on optical images are shown in Figs. 7.7 to 7.9. Sources are referred to as in Fig. 7.4 (right panel). The morphology of these radio sources is as expected for a system undergoing a merger, with high galaxy velocities with respect to the ICM. The radio powers reported for the sources in Table 7.3, are consistent with them being FR-I sources (Fanaroff & Riley 1974) located in the cluster (e.g., Owen & White 1991; Owen & Ledlow 1994; Baum et al. 1995).

Source A is a “head-tail” source belonging to the elliptical galaxy 2MASX J00120320 +5234132. The spectral index steepens along the tail, from −0.6 to −2.1 to the west. The “head” is polarized at the 1% level. The tail has a total extent of 270 kpc in the 610 MHz image. Source B is a double-lobe radio source (also listed as NVSS J001242+522717 or B0010.0+5210) consisting of a central core and two radio lobes. Additional diffuse emis-

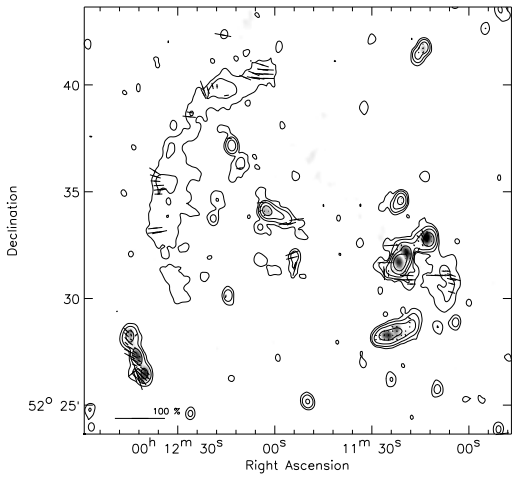

Figure 7.6: WSRT 1382 MHz polarization E-vector map. Total polarized intensity is shown as grayscale image. Vectors depict the polarization E-vectors, their length represents the polarization fraction. The length of the E-vectors are corrected for Ricean bias (Wardle & Kronberg 1974). A reference vector for a polarization fraction of 100% is shown in the bottom left corner. No vectors were drawn for pixels with a SNR < 5 in the total polarized intensity image. Contour levels are drawn at $[1, 2, 4, 8, \ldots] \times 5\sigma_{\rm rms}$ and are from the Stokes I 1382 MHz image. The beam size is $23.5'' \times 17.0''$ and shown in the bottom left corner of the image.

sion is seen surrounding the lobes and the central radio core. The spectral index does not vary much over the core and radio lobes, the average spectral index is about −0.6. The radio emission from the source has a polarization fraction between 10 and 20%. An optical counterpart (2MASX J00124217+5227182) is centered on the radio core. The source could be a cluster member as its color is similar to that of other galaxies in the cluster.

Source C is a narrow angle tailed (NAT) radio source with 2MASX J00112859+5228096 being the optical counterpart. The spectral index steepens from −0.6 to −1.7 along the tails as expected for a radio galaxy moving eastwards with respect to the ICM. The radio emission is polarized at the 2 – 4% level. Source D belongs to the cD galaxy 2MASX J00121892+5233460 in the eastern part of the cluster and has a spectral index of −0.8. No polarized emission is detected from the source.

Source E is the brightest radio source (4C +52.01) in the cluster and has a very complex morphology. The radio emission has a sharp western boundary, while the eastern boundary is more diffuse with "fans" of emission. The counterpart is the galaxy 2MASX J00112171+5231437, which has a close companion to the west. The spectral index steepens to the north and south from −0.9 to −1.7. Fractional polarization for the brightest emission is below 1%.

Source F has a complex morphology and is located to the northwest of E. There is a bridge of steep spectrum emission (with $\alpha \sim -1.4$) between E and F. The polarization fraction of F varies between 2 and 10%. The brighter parts of the source have a spectral index of −0.75. Because the spectral index here is flatter than the bridge of emission between E and F, this suggests the source is a separate radio galaxy with the emission not coming from E. The most likely counterpart is the galaxy 2MASS J00111135+5232421. The complex morphology of both E and F suggest that the radio sources are significantly disturbed, possibly due to the merger event. The radio morphology of both E and F suggest the sources moves westwards with respect to the ICM.

We could not identify optical counterparts for sources G, H and I. However, a diffraction spike in the INT images from a nearby bright star partly covers source G, likely blocking our view of the optical counterpart. The high surface brightness of G indicates the source is probably associated with an AGN.

7.4 Discussion

7.4.1 Origin of the double radio relic

Hydrodynamical simulations of cluster mergers show that the process takes of the order of 10^9 yr (e.g., Vazza et al. 2010; Paul et al. 2011; Battaglia et al. 2009; Skillman et al. 2008; Hoeft et al. 2008; Pfrommer et al. 2008; Ricker & Sarazin 2001). During a cluster merger, "internal" shock waves are generated. Typically, these have lower Mach numbers ($\mathcal{M} \lesssim 5$) than "external" shock waves which are generated by the infall of unprocessed gas from the surrounding IGM and having $\mathcal{M} > 10$. The Mach numbers of internal shocks are low because the sound speed in the gas of the main (bigger) cluster and the velocity of the in-falling subcluster both reflect the same gravitational potential of the main cluster. Merger events which generate shock waves with $\mathcal{M} \gtrsim 3$ are rare, and these are mainly formed in major merger events, with the mass ratio of the two merging clusters approaching unity. In the case of a binary cluster, merger two shocks are produced along the merger axis. As the shock waves propagate outward into a lower density environment their Mach number increases. The shock structure may get broken when it interacts

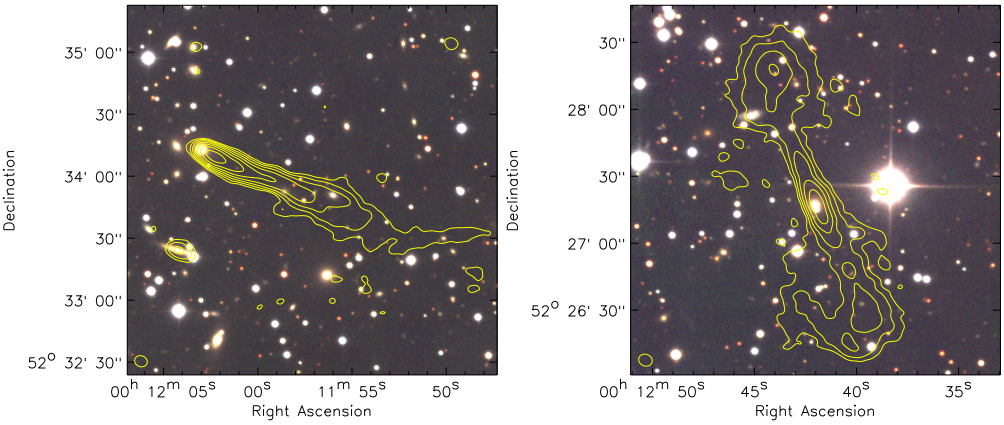

Figure 7.7: Left: Source A. GMRT 610 MHz contour are drawn at levels of $\sqrt{[1,2,4,8,\ldots]} \times 4\sigma_{\rm rms}$. The beam size is $11.75'' \times 7.65''$ and shown in the bottom left corner of the image. Right: Source B. GMRT 610 MHz contour levels are displayed as in the left panel.

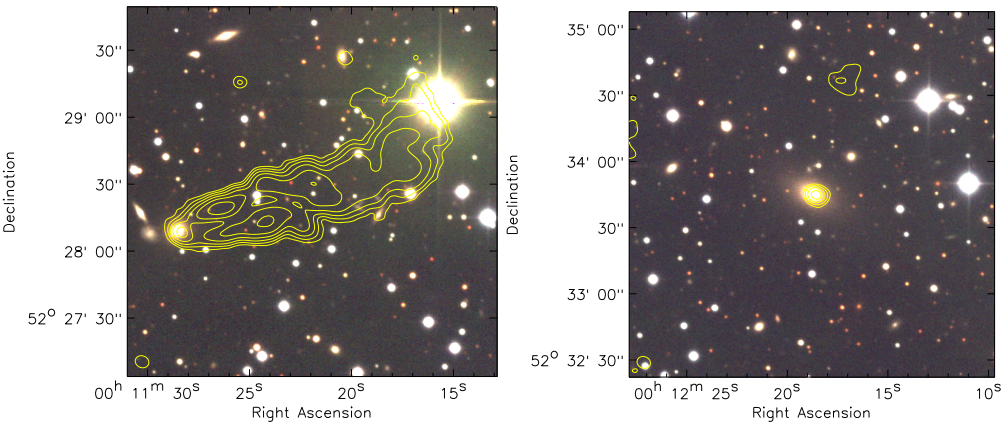

Figure 7.8: Left: Source C. GMRT 610 MHz contour levels are displayed as in Fig. 7.7. Right: Source D. GMRT 610 MHz contour levels are displayed as in Fig. 7.7.

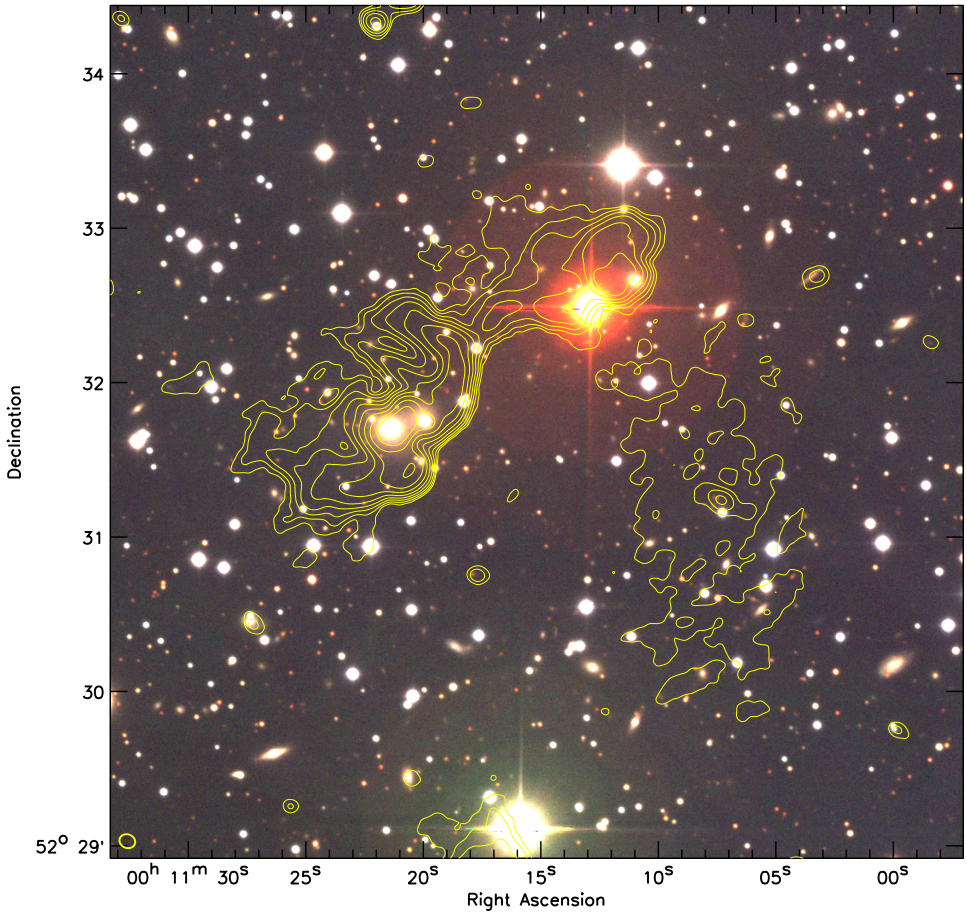

Figure 7.9: Source E & F. GMRT 610 MHz contour levels are displayed as in Fig. 7.7.

with the galaxy filaments connected to the cluster. This may explain the presence of the "notch-like" feature observed in the north of relic RE (Paul et al. 2011). These notch-like structures are also observed for the double relics in Abell 3376 (Bagchi et al. 2006) and Abell 3667 (Röttgering et al. 1997).

At the location of the shock front particles are proposed (Ensslin et al. 1998) to be accelerated (or re-accelerated) by the DSA mechanism. In this case, the injection spectral index of the radio emission is related to the Mach number of the shock. Behind the shock front particles cool through IC and synchrotron losses. The spectral index should thus steepen inwards to the cluster center. The overall integrated spectral is still a power-law though, but steeper by about 0.5 unit (e.g., Blandford & Eichler 1987; Sarazin 1999, 2002) than the injection spectral index. Relics which such power-law spectra have been found for example in Abell 521 and the Coma cluster (Giacintucci et al. 2008; Giovannini et al. 1991).

We have fitted a power-law radio spectrum for the integrated fluxes of the radio relic reported in Table 7.3. The fitted radio spectra for the two relics are displayed in Fig. 7.10 (left panel). RE is well fitted by a single power-law spectrum with a spectral index of -1.59 ± 0.06. For the western relic we find a spectral index of -1.49 ± 0.12. We note that the 241 MHz flux measurement and the corresponding error are somewhat difficult to estimate as the noise in the image increases sharply towards bright radio source E because of residual calibration errors, see also Fig. 7.4.

As reported in Sect. 7.3.4, the spectral indices at the front of the relics are about -1.2 ± 0.2 and -1.0 ± 0.15 for RE and RW, respectively. The errors give the variation in spectral index across the outer edges of the relic. The integrated spectral indices are consistent with this values (if we assume that DSA takes place), being steeper by about 0.5 units. We take the values at the front of the relic as the injection spectral indices. This then gives Mach numbers of $2.2^{+0.2}_{-0.1}$ and $2.4^{+0.4}_{-0.2}$ for relics RE and RW, respectively (van Weeren et al. 2009b). The uncertainties in the Mach number are based on the variation in spectral index at the front of the relics of about -0.15 units. These Mach number are in agreement with those found in other merging clusters, typically being between 1.5 and 3 (Markevitch et al. 2002, 2005; Markevitch 2006; Russell et al. 2010; Finoguenov et al. 2010).

Compression of fossil radio plasma (Enßlin & Gopal-Krishna 2001) does not seem to be a likely scenario to explain the relics in ZwCl 0008.8+5215, because regions with a spectral index of -0.9 are seen in front of the relic, not very steep for a radio phoenix. The integrated radio spectra do also not reveal significant spectral curvature (see for example Slee et al. 2001). Furthermore, relic RE has a size of 1.4 Mpc and the time to compress such a large radio ghost would have removed most of the energetic particles responsible for the radio emission (Clarke & Ensslin 2006). Relic RW is located not far from the complex sources E and F. If RW is directly associated with E and F, one would not expect the spectral index to steepen across RW in the direction of E and F. Also, the overall polarization fraction of RW is considerably higher than that of sources E and F. Therefore, our preferred scenario is that of relics tracing shock fronts where particles are accelerated or re-accelerated by the DSA mechanism.

The large difference of a factor of five in linear extent for relic RE and RW, is unlike that of previously known double relics. This large ratio in linear size could be explained by a relatively large mass ratio between the merging clusters, as the size of the shock waves formed during a binary cluster merger event roughly scale with the radii/masses of the merging components. The galaxy iso-density contours in Fig. 7.1 show two subclusters, with the eastern subcluster being slightly larger. Another possibility is that the shock front on the west side of the cluster is partly

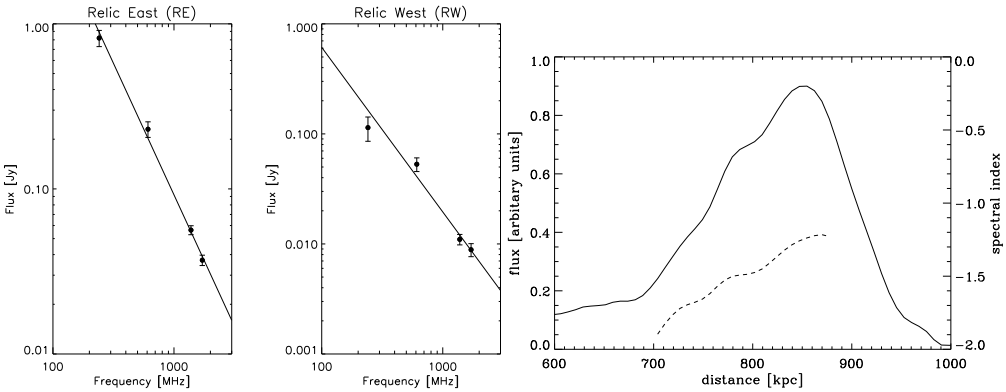

Figure 7.10: Left: Integrated fluxes for the relics. We find a spectral index of −1.59 for relic RE and −1.49 for relic RW by fitting a single power-law spectrum through the flux measurements at 241, 610, 1382, and 1714 MHz. Right: Radio luminosity profile across the width of relic RE. Solid line displays the 1382 MHz luminosity profile, averaged over the full 1.4 Mpc extent, of the relic RE. Dashed line displays the resulting spectral index profile (labeling on the right axis), also averaged over the full 1.4 Mpc extent, between 1382 and 241 MHz. The averaging was done by adding up the total flux at each frequency in a spherical shell and then calculating the spectral index.

broken up due to the presence of substructures or galaxy filaments. In case of re-acceleration, a supply of fossil electrons is needed. Therefore, a third possibility is that if these electrons have a limited spatial distribution, the shock front might be illuminated only locally.

The overall configuration of the relics is largely symmetric around the east-west merger axis, indicating that the impact parameter for the merger is close to zero (Ricker & Sarazin 2001).

7.4.2 Radio luminosity profile for the eastern relic

The width of a relic ($l_{\rm relic}$), tracing a plane shock wave, to first order reflects the downstream velocity of the shock v_2, a characteristic timescale due to spectral ageing $t_{\rm ageing}$, and the angle ϕ between the shock front normal and the plane of the sky

$$l_{\rm relic} \approx \frac{v_2 \times t_{\rm ageing}}{\cos\phi} \ . \tag{7.2}$$

The characteristic timescale due to spectral ageing is given by

$$t_{\rm ageing}\ [{\rm yr}] = 3.2 \times 10^{10} \frac{B^{1/2}}{B^2 + B_{\rm CMB}^2}\ [(1+z)\nu]^{-1/2} \ , \tag{7.3}$$

with B the magnetic field at the shock front in μGauss, $B_{\rm CMB}$ the equivalent magnetic field strength of the CMB in μGauss, and ν the observed frequency in MHz. At $z = 0.103$, $B_{\rm CMB}$ is 4.0 μGauss. If v_2 and ϕ are known this gives a method for determining the magnetic field strength. Even if ϕ is not known, limits on the magnetic field can be obtained if the observed width ($l_{\rm relic}$) is smaller than the maximum width allowed from Eq. 7.2.

To get an estimate of v_2, we use a temperature in the post-shock region of 6 keV, i.e, about twice the average cluster temperature. This factor of two increase is roughly what has been observed in other clusters with shocks (e.g., Russell et al. 2010; Ma et al. 2009). We use Rankine-Hugoniot jump conditions (Landau & Lifshitz 1959), with an adiabatic index $\gamma = 5/3$, and take the Mach number from the injection spectral index. This gives

$$\frac{T_2}{T_1} = \frac{5\mathcal{M}^4 + 14\mathcal{M}^2 - 3}{16\mathcal{M}^2} , \tag{7.4}$$

with indices 1 and 2 referring to the pre-shock and post-shock regions. The downstream speed is given by $v_2 = \mathcal{M}c_{s,1}/C$, with $c_{s,1}$ the pre-shock sound speed, $(\gamma k_{\rm B} T_1/m_{\rm H}\mu)^{1/2}$, with $\mu = 0.6$ the mean molecular weight. The compression ratio C is given by

$$\frac{1}{C} = \frac{3}{4\mathcal{M}^2} + \frac{1}{4} . \tag{7.5}$$

Filling in the numbers gives $C = 2.4$ and $c_{s,1} = 1100$ km s^{-1}. We then obtain $v_2 = 750$ km s^{-1}. The downstream velocity depends only weakly on the adopted downstream temperature. For example, using a downstream temperature of 10 keV increases of v_2 to about 950 km s^{-1}. For the remainder we will adopt $v_2 = 750$ km s^{-1}. This then gives for the width of the relic (FWHM) observed at 1382 MHz

$$l_{\rm relic}\ [{\rm kpc}] \approx 628 \times \frac{B^{1/2}}{B^2 + B_{\rm CMB}^2} \cos^{-1}\phi , \tag{7.6}$$

with the magnetic field strengths in units of μGauss.

For $\phi = 0°$, the maximum width is 46 kpc, which corresponds to $B \approx 2$ μGauss. This is smaller than the observed width of about 150 kpc (see Fig. 7.10, right panel) and hence no constraints on the magnetic field can be put since the angle ϕ is not known. It is possible to set limits on ϕ using the observed polarization fraction (Ensslin et al. 1998). A 20% polarization fraction implies $\phi < 50°$. This limit on ϕ is not consistent with the observed width which would require $\phi > 72°$. Although, for large sections of the relic the polarization fraction is unknown and could be smaller than 20%.

7.4.3 Simulated radio luminosity and spectral index profiles

In the above analysis we assumed that a relic traces a planar shock wave. In a more realistic model of a relic would trace a shock wave that forms a part of a sphere. This is illustrated by the curved shape of relic RE. The observed width is about a factor of three larger than the maximum intrinsic allowed width, $\max(l_{\rm relic}(\phi = 0, B))$. This implies that projection effects probably play an important role. The questions is then why do we still see a clear spectral index gradient (Fig. 7.10) across the relic?

To answer this questions we use a more realistic model of a shock front. The spherical shock subtends an angle Ψ into the plane of the sky and has a radius of curvature $R_{\rm projected}$. The total angle subtended by the relic is 2Ψ. We compute the radio luminosity profiles at the observed frequencies of 241 and 1382 MHz. The injection spectral index is taken to be -1.0. Synchrotron cooling processes, based on the distance of the emitting radio plasma from the front of the shock, which in turn depend on the downstream velocity $v_2 = 750$ km s^{-1}, are taken into account. For the magnetic field we assume $B = 2$ μGauss, which maximizes the intrinsic

width of the relic to 46 kpc. A spectral index profile is computed using the profiles at the two different frequencies. The resulting intrinsic luminosity profiles (with intrinsic referring to a planar shock wave without any projection effects) and profiles for $R_{\rm projected} = 0.75$ and 1.0 Mpc, with opening angles $\Psi = 22, 30, 40°$ are shown in Fig. 7.11. For $R_{\rm projected} = 0.75$ Mpc, we find that the profile with an opening angle between 30 and 22°(∼ 26°) provides the best match to the observed profile. For $R_{\rm projected} = 1.0$ Mpc, we find the best match for $\Psi = 22°$.

Our computed luminosity profiles do no provide a very good match to the observed profile at distances of more than 0.85 Mpc from the cluster center. The observed profile is more symmetric, while the computed profiles are rather asymmetric with a strong luminosity decrease at large radii. This may be caused by the fact that the actual 3D shape of the shock front differs somewhat from a sphere. Also, we assumed a uniform surface brightness over the front of the shock surface (which forms part of a segment of a sphere). At the edges of this surface the radio emission drops to zero abruptly. This causes the discontinuities in the modeled profiles inwards of the peak luminosity towards the cluster center. In the GMRT and WSRT images, the relic's surface brightness fades towards the northern and southern ends. This could (partly) be explained by the spherical shell model we use for the relic, as the relic's extent into the plane of the sky decreases at the northern and southern ends. It is also possible that the surface brightness across the shell decreases towards the edges. This effect is not included in our model. However, our goal was not to reproduce the exact profile of the relic, but rather to show that although projection effects can be significant, a clear spectral index gradient can remain. Even for an opening angle of 40°(a total of 80° into and out of the plane of the sky), a steepening of more than 0.5 units in the spectral index is predicted towards the cluster center.

Based on this we argue that although relic RE is widened significantly by projection effects, the fact the we see a clear spectral index gradient is not surprising. This could also explain the spectral index gradients visible for the relics observed by Röttgering et al. (1997); Clarke & Ensslin (2006); Orrú et al. (2007); Giacintucci et al. (2008); Bonafede et al. (2009b), even though the observed widths are significantly larger than the maximum intrinsic widths.

7.4.4 Equipartition magnetic field strength

Since the width of the relic is larger than the maximum intrinsic width, we estimate the magnetic field at the location of the relics by assuming minimum energy densities in the relics. We use the same procedure as described in van Weeren et al. (2009b) and take $k = 100$, i.e, the ratio of energy in relativistic protons to that in electrons. For relic RW, we have a spectral index of -1.49, and a surface brightness of 1.2 μJy arcsec^{-2}. We take 290 kpc for the depth (d) along the line of sight. This gives $B_{\rm eq} = 3.4\,\mu$Gauss. For RE we have a spectral index of -1.59, a surface brightness of 0.96 μJy arcsec^{-2}, and we assume $d = 1$ Mpc. This gives $B_{\rm eq} = 2.5\,\mu$Gauss. The equipartition magnetic field strength scales with $(1 + k)^{2/7}$. In the above calculation, we used fixed frequency cutoffs ($\nu_{\rm min} = 10$ MHz and $\nu_{\rm max} = 100$ GHz), which is not entirely correct (Beck & Krause 2005; Brunetti et al. 1997). With low and high energy cutoffs ($\gamma_{\rm min}$, $\gamma_{\rm max}$), $\gamma_{\rm min} \ll \gamma_{\rm max}$, and fixing $\gamma_{\rm min}$ to 100, we find a revised magnetic field strength ($B'_{\rm eq}$) of 7.9 and 6.6 μGauss for RW and RE, respectively. For a lower cutoff of $\gamma_{\rm min} = 5000$, we get 1.4 and 1.0 μGauss for RW and RE, respectively. The revised equipartition magnetic field strength ($B'_{\rm eq}$) scales with $(1 + k)^{1/(3-\alpha)}$, for different values of k.

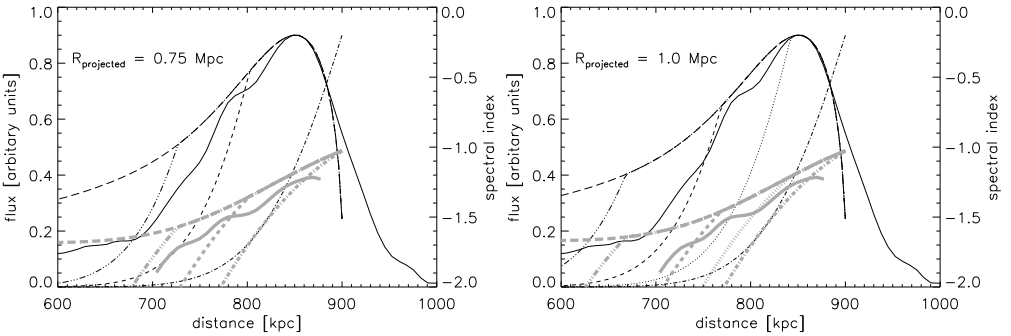

Figure 7.11: Left: Radio luminosity profile for $R_{\rm projected}$ = 0.75 Mpc and B = 2 μGauss. Thin black lines are the 1382 MHz luminosity profiles, the thicker grey lines represent the spectral index profiles. Solid lines are the observed profiles. The simulated intrinsic profiles (i.e., without any projection effects) are shown by the dashed-dotted lines. The simulated profiles, including the projection effects, are shown with the following line styles: dashed for an opening angle of 22°, dashed-triple-dotted for an opening angle of 30°, and long dashes for an opening angle of 40°. Right: Radio luminosity profile for $R_{\rm projected}$ = 1.0 Mpc. In addition to the left panel, the simulated luminosity and spectral index profiles for an opening angle of 15° are shown with dotted lines.

7.5 Conclusions

We discovered a double radio relic in the galaxy cluster ZwCl 0008.8+5215, located at $z = 0.103$ (based on a single spectroscopic redshift). A ROSAT X-ray image and galaxy iso-density map show that the cluster is undergoing a binary merger event, with the merger axis oriented roughly east-west. The two radio relics are located along this merger axis, while their orientation is perpendicular to this axis. The relics probably trace shocks waves in the ICM, created by the merger event, in which particles are (re)accelerated by the DSA mechanism. Integrated radio spectra are consistent with particle acceleration in the shock by DSA and indicate Mach numbers of ~ 2 for the shocks. The spectral index for both relics shows a steepening towards the cluster center. Parts of the relics have a polarization fraction in the range of $5 - 25\%$, but further observations are needed to better map the polarization properties. The relics have an extent of 1.4 Mpc and 290 kpc. This factor of five difference in their linear extent is unlike that of other known double relic systems. The size difference could be related to a relatively large mass ratio between the two merging clusters, although galaxy iso-density contours do not indicate a large difference in masses between the two subclusters. Alternatively, the second shock front is partly broken up due to interaction with substructures, or the small size of the western relic reflects the limited spatial distribution of fossil electrons.

We modeled the radio luminosity and spectral index profiles of the eastern relic, assuming that the relic traces a curved shock front. We conclude that projection effects play an important role in increasing the observed s width of the relic. However, we find that a clear spectral index gradient remains visible for large opening angles.

Future X-ray observations will be needed to investigate the dynamical state of the cluster, determine the mass ratio of the merging systems, and search for shock waves associated with the relics.

Acknowledgements. We thank the staff of the GMRT who have made these observations possible. The GMRT is run by the National Centre for Radio Astrophysics of the Tata Institute of Fundamental Research. The Westerbork Synthesis Radio Telescope is operated by ASTRON (Netherlands Institute for Radio Astronomy) with support from the Netherlands Foundation for Scientific Research (NWO). The National Radio Astronomy Observatory is a facility of the National Science Foundation operated under cooperative agreement by Associated Universities, Inc. The Isaac Newton Telescope and William Herschel Telescope are operated on the island of La Palma by the Isaac Newton Group in the Spanish Observatorio del Roque de los Muchachos of the Instituto de Astrofísica de Canarias. This publication makes use of data products from the Two Micron All Sky Survey, which is a joint project of the University of Massachusetts and the Infrared Processing and Analysis Center/California Institute of Technology, funded by the National Aeronautics and Space Administration and the National Science Foundation. This research has made use of the VizieR catalogue access tool, CDS, Strasbourg, France.

RJvW acknowledges funding from the Royal Netherlands Academy of Arts and Sciences. MB acknowledges support by the research group FOR 1254 funded by the Deutsche Forschungsgemeinschaft

CHAPTER 8

Particle acceleration on megaparsec scales in a merging galaxy cluster

Abstract. Galaxy clusters form through a sequence of mergers of smaller galaxy clusters and groups. Models of diffusive shock acceleration (DSA) suggest that in shocks that occur during cluster mergers, particles are accelerated to relativistic energies, similar to supernova remnants. Together with magnetic fields these particles emit synchrotron radiation and may form so-called radio relics. Here we report the detection of a radio relic for which we find highly aligned magnetic fields, a strong spectral index gradient, and a narrow relic width, giving a measure of the magnetic field in an unexplored site of the universe. Our observations provide strong evidence for DSA on scales much larger than in supernova remnants and this implies that shocks in galaxy clusters are capable of producing extremely energetic cosmic rays.

R. J. van Weeren, H. J. A. Röttgering, M. Brüggen, and M. Hoeft
Science, **330**, 347, 2010

In the universe structure forms hierarchically with smaller structures merging to form bigger ones. On the largest scales, clusters of galaxies merge releasing energies of the order of 10^{64} erg on timescales of 1–2 Gyr Roettiger et al. (1999a); Hoeft et al. (2008). During such merger events, large-scale shock waves with moderate Mach numbers of 1–5, should be created. In such shocks, DSA is expected to accelerate electrons to high energies; in the presence of a magnetic field, these particles are expected to form large regions emitting synchrotron radiation at radio wavelengths Miniati et al. (2001); Hoeft et al. (2008); Pfrommer et al. (2008). The accelerated particles at the shock front have a power-law energy distribution which directly translates into an integrated power-law radio spectrum (flux $\propto \nu^{\alpha}$, with α the spectral index and ν the frequency). The slope of the particle distribution (s) in the linear test particle regime, and thus the radio spectral index ($\alpha = (1 - s)/2$), only depends on the compression ratio (r) of the shock Drury (1983); Blandford & Eichler (1987), with $s = (r + 2)/(r - 1)$. At the shock front, the intracluster medium (ICM) is compressed such that magnetic fields align parallel to the shock front Ensslin et al. (1998). These ordered and aligned magnetic fields cause the radio emission to be highly polarized. Synchrotron and inverse Compton (IC) losses cool the radio plasma behind the shock, creating a strong spectral index gradient in the direction towards the cluster center. It has been suggested that such synchrotron emitting regions from shocks can be identified with radio relics Ensslin et al. (1998); Miniati et al. (2001). These are elongated radio sources located mostly in the outskirts of massive merging galaxy clusters Feretti (2005); Bagchi et al. (2006); Clarke & Ensslin (2006); Bonafede et al. (2009a,b); van Weeren et al. (2009d,b).

Here we present the detection of a 2 Mpc radio relic (Figs. 8.1 and 8.2) located in the northern outskirts of the galaxy cluster CIZA J2242.8+5301 ($z = 0.1921$). This X-ray luminous cluster Kocevski et al. (2007) ($L_X = 6.8 \times 10^{44}$ ergs^{-1}, between 0.1 and 2.4 keV) shows a disturbed elongated morphology in ROSAT X-ray images Voges et al. (1999), indicative of an undergoing major merger event. The relic is located at a distance of 1.5 Mpc from the cluster center. Unlike other known radio relics, the northern relic is extremely narrow with a width of 55 kpc. Deep Westerbork Synthesis Radio Telescope (WSRT), Giant Metrewave Radio Telescope (GMRT) and Very Large Array (VLA) observations (SOM) show a clear unambiguous spectral index gradient towards the cluster center (Fig. 8.3). The spectral index, measured over a range of frequencies between 2.3 and 0.61 GHz, steepens from -0.6 to -2.0 across the width of the narrow relic. The gradient is visible over the entire 2 Mpc length of the relic, constituting clear evidence for shock acceleration and spectral ageing of relativistic electrons in an outward moving shock. The relic's integrated radio spectrum is a single power-law, with $\alpha = -1.08 \pm 0.05$, as predicted Drury (1983); Blandford & Eichler (1987). The relic is strongly polarized at the 50–60% level, indicating a well ordered magnetic field, and polarization magnetic field vectors are aligned with the relic. In the southern part of the cluster, located symmetrically with respect to the cluster center and the northern relic, there is a second fainter broader relic. The elongated radio relics are orientated perpendicular to the major axis of the cluster's elongated X-ray emitting ICM, as expected for a binary cluster merger event in which the second southern relic traces the opposite shock wave Roettiger et al. (1999a). Furthermore, there is a faint halo of diffuse radio emission extending all the way towards the cluster center connecting the two radio relics (Fig. 8.1). This emission extends over 3.1 Mpc, making it the largest known diffuse radio source in a cluster to date.

The source cannot be a gravitational lens because it is too large and located too far from the cluster center. The morphology, spectral index, and association with a cluster exclude the possibility of the source being a supernova remnant. The source is also not related to the radio

AGN located at the eastern end of the relic. High-resolution observations show this source to be detached from the relic (Fig. 8.2). The spectral and polarization properties are also unlike that of any known tailed radio sources Miley (1973); Sijbring & de Bruyn (1998). The power-law radio spectral index, clear spectral index gradient and enormous extent, exclude the possibility the source is tracing (compressed) fossil radio plasma from a radio source whose jets are now off Enßlin & Gopal-Krishna (2001); Enßlin & Brüggen (2002). The integrated radio spectra of such fossil sources are very steep ($\alpha < -1.5$) and curved, because the radio emitting plasma is old and has undergone synchrotron and IC losses. In addition, the shell-like (and not lobe-like) morphology does not support the above scenario.

Instead, all the observed properties of the relic perfectly match that of electrons accelerated at large-scale shocks via DSA. The characteristics of the bright relic provide evidence that (at least some) relics are direct tracers of shocks waves, and a way to determine the magnetic field strength at the location of the shock using similar arguments to those that have been used for supernova remnants Vink & Laming (2003).

The configuration of the relic arises naturally for a roughly equal mass head-on binary cluster merger, without much substructure, in the plane of the sky with the shock waves seen edge-on. First, the polarization fraction of 50% or larger can only explained by an angle of less than 30 degrees between the line-of-sight and the shock surface Clarke & Ensslin (2006). Second, because there is evidence for spectral ageing across the relic, only part of the width can be caused by projection effects.

The amount of spectral ageing by synchrotron and IC losses is determined by the magnetic field strength, B, the equivalent magnetic field strength of the cosmic microwave background (CMB), $B_{\rm CMB}$, and the observed frequency. The result is a downward spectral curvature resulting in a steeper spectral index in the post-shock region (i.e., lower α). For a relic seen edge-on the downstream luminosity and spectral index profiles thus directly reflect the ageing of the relativistic electrons Markevitch et al. (2005). To first approximation, the width of the relic ($l_{\rm relic}$) is determined by a characteristic timescale ($t_{\rm sync}$) due to spectral ageing, and the downstream velocity (v_d): $l_{\rm relic} \approx t_{sync} \times v_d$, with $t_{sync} \propto \left(B^{1/2}/(B^2 + B^2_{\rm CMB})\right) \times \left(1/(\nu(1+z))^{1/2}\right)$. Conversely, from the width of the relic and its downstream velocity, a direct measurement of the magnetic field at the location of the shock can be obtained. Using standard shock jump conditions, it is possible to determine the downstream velocity, from the Mach number and the downstream plasma temperature.

The spectral index at the front of the relic is -0.6 ± 0.05 which gives a Mach number of $4.6^{+1.3}_{-0.9}$ for the shock van Weeren et al. (2009b) in the linear regime. Using the $L_X - T$ scaling relation for clusters Markevitch (1998) we estimate the average temperature of the ICM to be ~ 9 keV. Behind the shock front the temperature is likely to be higher. Temperatures in the range between 1.5 and 2.5 times the average value have previously been observed Ma et al. (2009). The derived Mach number and the advocated temperature range, imply downstream velocities between 900 and 1,200 km s^{-1} (we used an adiabatic exponent of 5/3). For the remainder we will adopt a value of 1,000 km s^{-1}. Using the redshift, downstream velocity, spectral index, and characteristic synchrotron timescale we have for the width of the relic

$$l_{\rm relic,\ 610\ MHz} \approx 1.2 \times 10^3 \frac{B^{1/2}}{B^2 + B^2_{\rm CMB}} \ \ [\rm kpc]\,, \tag{8.1}$$

with B and $B_{\rm CMB}$ in units of μGauss. Because $B_{\rm CMB}$ is known, the measurement of $l_{\rm relic}$ from the radio maps, directly constrains the magnetic field. From the 610 MHz image (the image

with the best signal to noise ratio and highest angular resolution), the relic has a deconvolved width (full width at half maximum) of 55 kpc (Fig. 8.4). Because Eq. 8.1 has two solutions, the strength of the magnetic field is 5 or 1.2 μGauss. However, projection effects can increase the observed width of the relic and affect the derived magnetic field strength. Therefore, the true intrinsic width of the relic could be smaller, which implies that $B \geq 5$ or ≤ 1.2 μGauss (Eq. 8.1). We investigated the effects of projection using a curvature radius of 1.5 Mpc, the projected distance from the cluster center. Instead of using Eq. 8.1, we computed full radio profiles Hoeft & Brüggen (2007) for different angles subtended by a spherical shock front into the plane of the sky (Ψ; the total angle subtended is 2Ψ for a shell-like relic). The profile for $\Psi = 10$ deg and $B = 5$ μGauss agrees best with the observations (Fig. 8.4). For $\Psi = 15$ deg, B is 7 or 0.6 μGauss. Values of Ψ larger than ~ 15 deg are ruled out. Lower limits placed on the IC emission Nakazawa et al. (2009); Finoguenov et al. (2010) and measurements of Faraday rotation Clarke et al. (2001) indicate magnetic fields higher than ~ 2 μGauss. We therefore exclude the lower solutions for the magnetic field strength and conclude that the magnetic field at the location of the bright radio relic is between 5 and 7 μGauss.

Magnetic fields within the ICM are notoriously difficult to measure. No methods have yielded precise magnetic field strengths as far from the center as the virial radius; only lower limits using limits on IC emission have been placed. Equipartition arguments have been used van Weeren et al. (2009b); Bagchi et al. (2006); Clarke & Ensslin (2006); Bonafede et al. (2009b) but this gives only a rough estimate for the magnetic field strength and it relies on various assumptions that cannot be verified. The value of 5–7 μGauss we find shows that a substantial magnetic field exists even far out from the cluster center.

Because radio relics directly pinpoint the location of shock fronts they can be used to get a complete inventory of shocks and their associated properties in galaxy clusters, important to understand the impact of shocks and mergers on the general evolution of clusters. Because less energetic mergers are more common and have lower Mach numbers, there should be many fainter relics with steep spectra which have currently escaped detection. Interestingly, these large-scale shocks in galaxy clusters have been suggested as acceleration sites for highly relativistic cosmic rays Ryu et al. (2003). As the radiation losses for relativistic cosmic ray protons are negligible, the maximum energy to which they can be accelerated is only limited by the lifetime of the shock, which can last for at least 10^9 yr. This means that in merging clusters protons can be accelerated up to extreme energies of 10^{19} eV, much higher than that in supernova remnants.

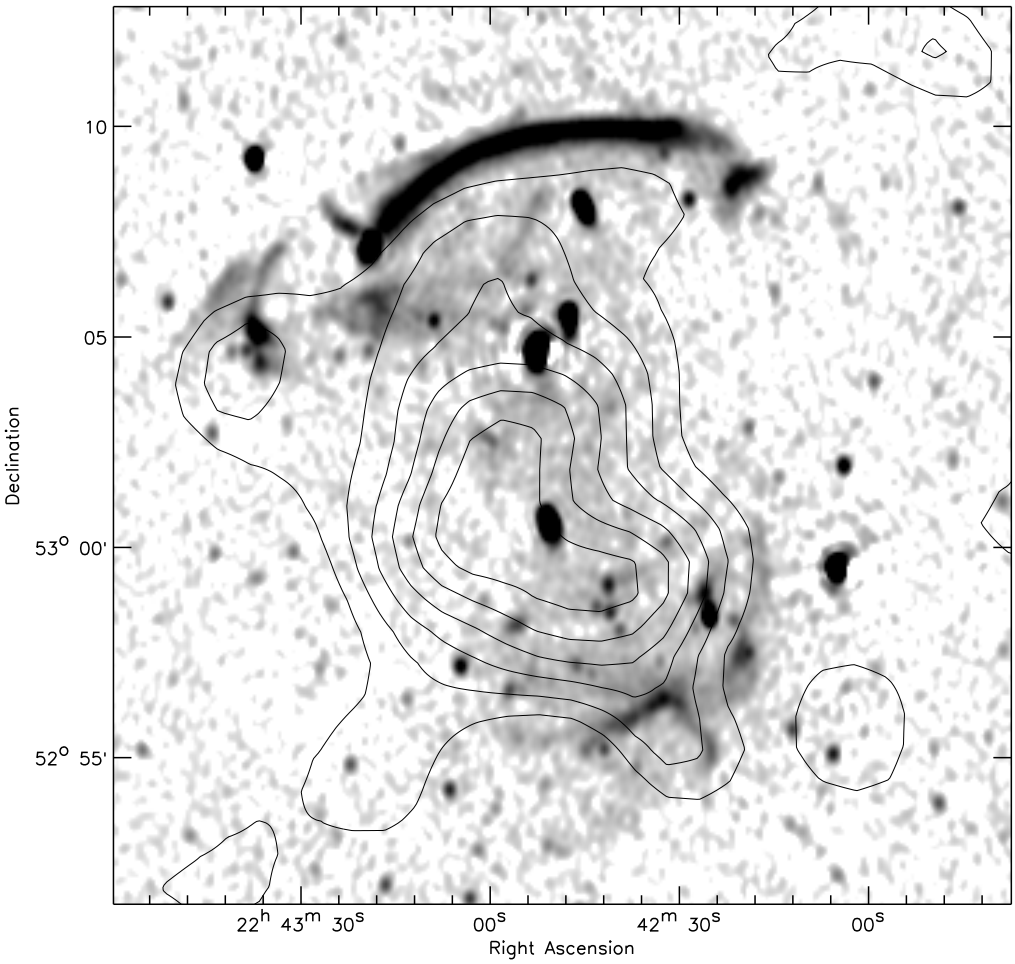

Figure 8.1: WSRT radio image at 1.4 GHz. The image has a resolution of 16.5 arcsec × 12.9 arcsec and the rms noise is 19 μJy beam^{-1}. Contours (linearly spaced) represent the X-ray emission from ROSAT showing the hot ICM.

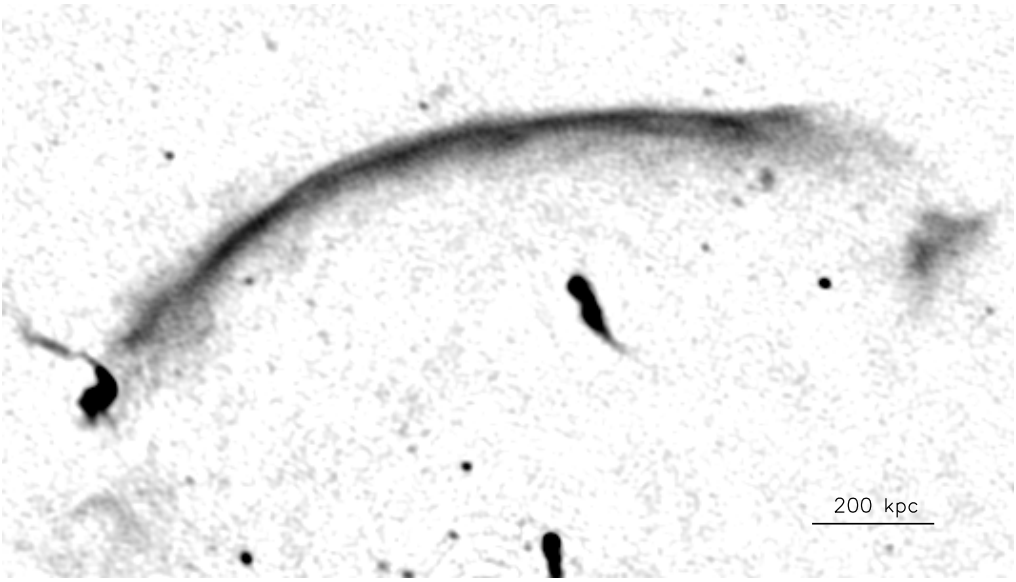

Figure 8.2: GMRT 610 MHz radio image. The image has a rms noise of 23 μJy beam^{-1} and a resolution of 4.8 arcsec $\times$ 3.9 arcsec.

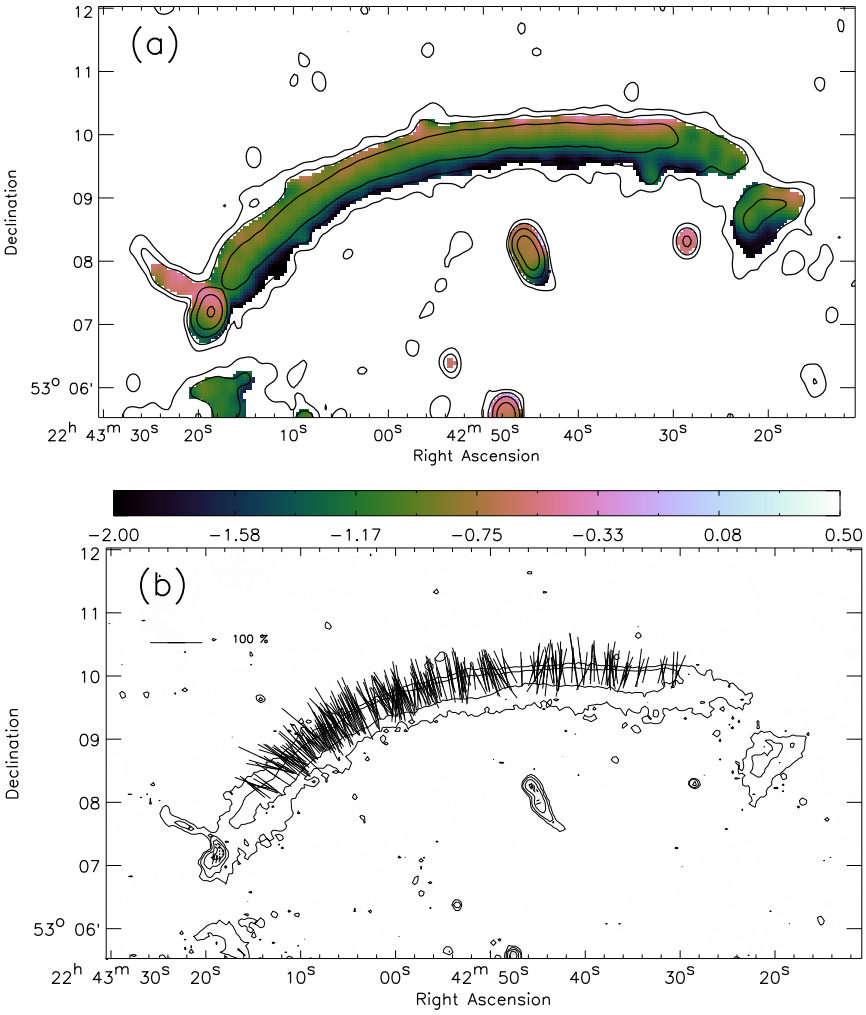

Figure 8.3: Radio spectral index and polarization maps. *a*: The spectral index was determined using matched observations at 2.3, 1.7, 1.4, 1.2, and 0.61 GHz, fitting a power-law radio spectrum to the flux density measurements. The map has a resolution of 16.7 arcsec × 12.7 arcsec. Contours are from the WSRT 1.4 GHz image and are drawn at levels of $[1, 4, 16, \ldots] \times 36\ \mu$Jy beam^{-1}. *b*: The polarization electric field vector map was obtained with the VLA at a frequency of 4.9 GHz and has a resolution of 5.2 arcsec × 5.1 arcsec. The contours are from Fig. 8.2 and are drawn at levels of $[1, 4, 16, \ldots] \times 70\ \mu$Jy beam^{-1}. The length of the vectors is proportional the polarization fraction, which is the ratio between the total intensity and total polarized intensity. A reference vector for 100% polarization is drawn in the top left corner. The vectors were corrected for the effects of Faraday rotation using a Faraday depth of −140 rad m^{-2} determined from the WSRT 1.2 – 1.8 GHz observations.

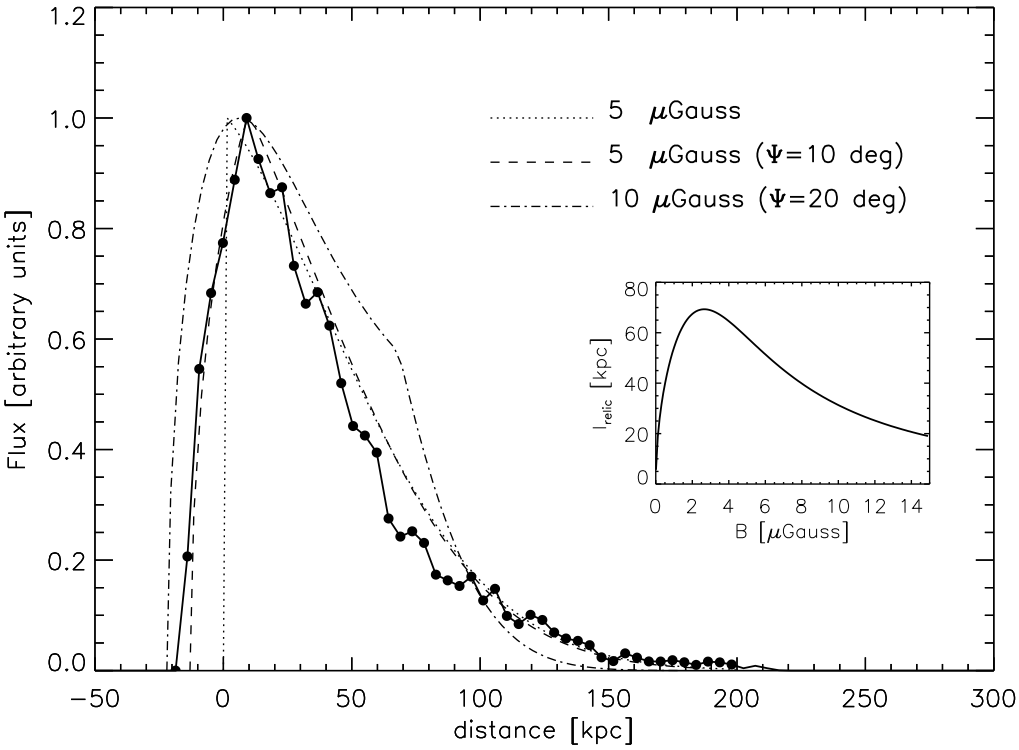

Figure 8.4: The deconvolved profile at 610 MHz, averaged over the full length of the relic, is shown by the solid line and dots. Models for different magnetic field strengths and projection angles (Ψ; i.e., the angle subtended by the relic into the plane of the sky) are overlaid. We used an equivalent magnetic field strength of the CMB at $z = 0.1921$ of 4.6 μGauss and a downstream velocity of 1,000 km s^{-1}. The model (dashed lines) for $\Psi = 10$ deg and $B = 5$ μGauss provides the best fit. A model for $B = 5$ μGauss without any projection effects is overlaid with dotted lines. For $\Psi > 15$ deg no good fit to the data could be obtained, as an example we have plotted the profile (dashed-dotted) for $\Psi = 20$ deg and $B = 10$ μGauss. *(inset)* The intrinsic width of the relic as function of magnetic field strength (Eq. 1), it shows that for a given width usually two solutions for the magnetic field strength can be obtained.

8.1 Appendix: Data reduction

We carried out radio observations of CIZA J2242.8+5301 with the WSRT in the L-band (at 1.2, 1.4 and 1.7 GHz) and at 2.3 GHz recording full polarization products. The total integration time was 12 hr at 2.3, 1.2 and 1.7 GHz, and 30 hr at 1.4 GHz. The observations were spread out over various runs between March and November 2009. For each different frequency setup the total bandwidth was 160 MHz. The 160 MHz was further divided over 8 sub-bands (IFs) with 20 MHz bandwidth and 64 spectral channels. GMRT observations at 610 MHz were carried out with 32 MHz bandwidth in spectral line mode with 512 channels on November 19, 2009. The total integration time was 9 hr. Only RR and LL polarization, to create a total intensity image, were recorded. VLA C-array 4.9 GHz observations were taken on August 17, 2009 in single channel continuum mode recording all four polarization products. Total integration time was about 7.5 hr.

We reduced the data using AIPS[1] (Astronomical Image Processing System, NRAO) and CASA[2] (Common Astronomy Software Applications). After inspection for the presence of radio frequency interference and other problems, bad data was subsequently removed (i.e., "flagged"). Bandpass[3] and gain calibration were carried out using several bright unresolved calibrator sources. The flux scale was set using standard primary calibrators Baars et al. (1977); Perley & Taylor (1999). For the WSRT observations the channel dependent polarization leakage terms were determined using a bright unpolarized calibrator source. The polarization angles were set using the polarized calibrators 3C138 and 3C286 for the WSRT and VLA observations. Subsequent rounds of self-calibration were carried out to improve the dynamic range of the images. Several bright nearby sources still limited the dynamic range in the 610 MHz GMRT image. These sources were subtracted from the data using the "peeling-method" Noordam (2004); Intema et al. (2009). The 610 MHz high-resolution image of the relic was made using robust weighting Briggs (1995) set to -1.0. A 610 MHz image of the cluster, with robust weighting set to 0.5, is shown in Fig. 8.5.

We made a radio spectral index map using images at 2.3, 1.7, 1.4, 1.2, and 0.61 GHz, fitting a power-law spectral index through the flux measurements. We limited the UV-ranges (to include only common UV-coverage) for the images that were used to compute the spectral index map. The spectral index map for the full cluster is shown in Fig. 8.6. Both the northern and southern relics show steepening of the spectral index towards the cluster center.

We used the technique of Rotation Measure Synthesis Brentjens & de Bruyn (2005) to determine the Faraday depth of the northern relic. We found an average Faraday depth of about -140 rad m^{-2} and used that to correct for the effect of Faraday Rotation by de-rotating the electric/magnetic field vectors.

Acknowledgements. The WSRT is operated by ASTRON (Netherlands Institute for Radio Astronomy) with support from the Netherlands Foundation for Scientific Research (NWO). We thank the staff of the GMRT who have made these observations possible. The GMRT is run by the National Centre for Radio Astrophysics of the Tata Institute of Fundamental Research. The National Radio Astronomy Observatory is a facility of the National Science Foundation operated under cooperative agreement by Associated Universities, Inc. R.J.v.W. acknowledges funding from the Royal Academy of Arts and Sciences (KNAW). The authors thank G. Brunetti for discussions.

[1] http://www.aips.nrao.edu/
[2] http://casa.nrao.edu/
[3] only for the GMRT & WSRT observations

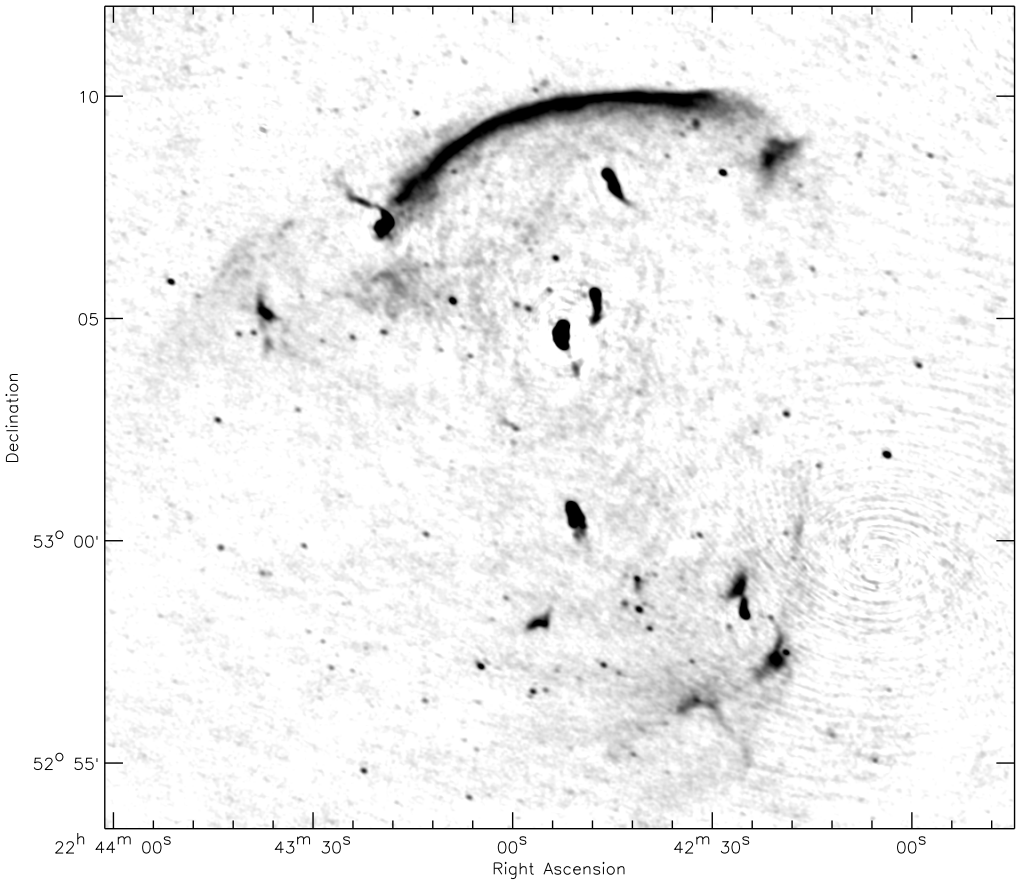

Figure 8.5: GMRT 610 MHz radio image with a resolution of 5.8 arcsec × 4.4 arcsec. The rms noise in the image is 24 μJy beam^{-1}.

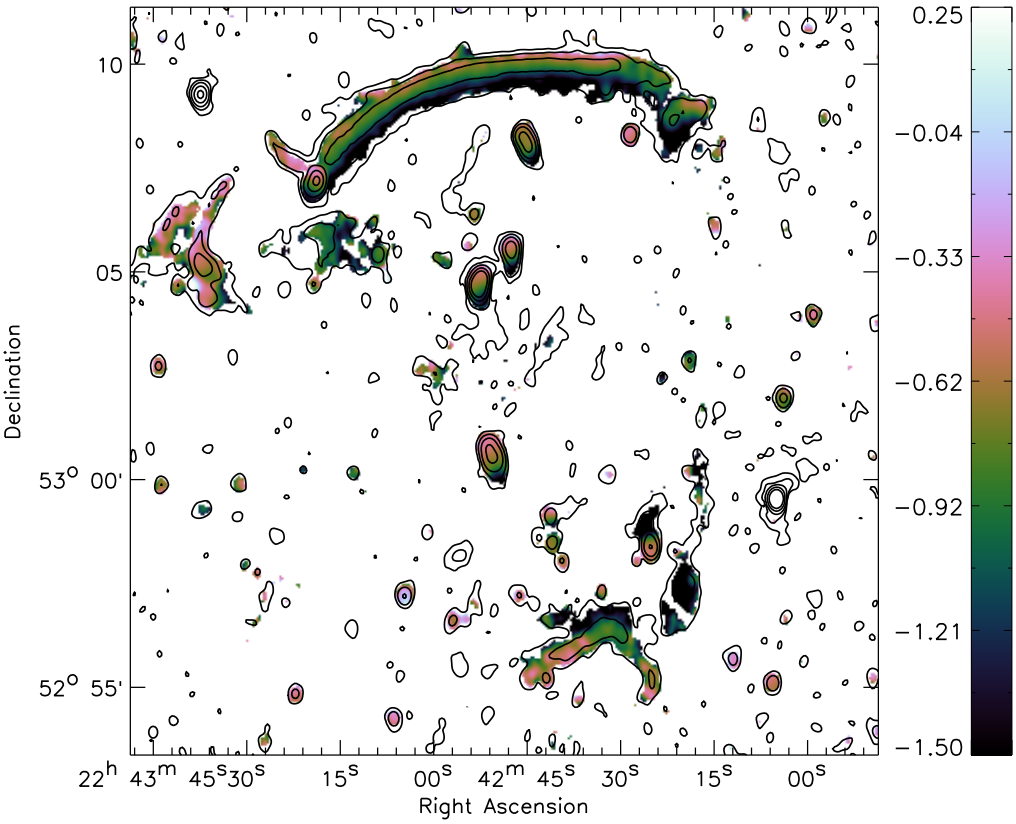

Figure 8.6: Radio spectral index map. The spectral index map has a resolution of 16.7 arcsec × 12.7 arcsec. Contours are from the WSRT 1.4 GHz image and are drawn at levels of $[1, 4, 16, \ldots] \times 57$ μJy beam^{-1}.

CHAPTER 9

The “toothbrush-relic”: evidence for a coherent linear 2-Mpc scale shock wave in a massive merging galaxy cluster?

Abstract. Some merging galaxy clusters host diffuse extended radio emission, so-called radio halos and relics, which origin is still being debated. Here we present WSRT and GMRT observations of a new radio-selected galaxy cluster 1RXS J0603.3+4214 at $z = 0.225$. The cluster is detected in the ROSAT All Sky Survey with an X-ray luminosity of $L_{\mathrm{X,\ 0.1-2.4\ keV}} \sim 1{\times}10^{45}$ erg s^{-1}. The cluster hosts a large bright 1.9 Mpc radio relic, an elongated $\sim$ 2 Mpc radio halo, and two fainter smaller radio relics. The large radio relic has a peculiar linear morphology. For this relic we observe a clear spectral index gradient from the front of the relic towards the back. Parts of this relic are highly polarized with a polarization fraction of up to 60%. We performed Rotation Measure (RM) Synthesis between 1.2 and 1.7 GHz. The results suggest that for the west part of the large relic some of the Faraday rotation is caused by ICM and not only due to galactic foregrounds. We also carried out a detailed spectral analysis of this radio relic and created radio color-color diagrams. We find (i) an injection spectral index of -0.6 to -0.7, (ii) steepening spectral index and increasing spectral curvature in the post-shock region, and (iii) an overall power-law spectrum between 74 MHz and 4.9 GHz with $\alpha = -1.10 \pm 0.02$. Mixing of emission in the beam from regions with different ages is probably the dominant factor that determines the shape of the radio spectra. Changes in the magnetic field, total electron content, or adiabatic gains/losses do not play a major role. A model in which particles are (re)accelerated in a first order Fermi process at the front of the relic provides the best match to the observed spectra. We speculate that in the post-shock region particles are re-accelerated by merger induced turbulence to form the radio halo as the relic and halo are connected. The orientation of the bright relic and halo indicate a north-south merger event, but the peculiar linear shape and the presence of another relic, perpendicular to the bright relic, suggest a more complex merger event. Deep X-ray observations will be needed to determine the merger scenario.

R. J. van Weeren, H. J. A. Röttgering, H. T. Intema, L. Rudnick,
M. Brüggen, M. Hoeft, J. B. R. Oonk
to be submitted

9.1 Introduction

Radio halos and relics are diffuse sources found in galaxy clusters that show signs of an ongoing merger event (see Feretti 2005; Ferrari et al. 2008; Brüggen et al. 2011, for an overview). These sources reveal the presence of relativistic particles and cluster-wide magnetic fields (e.g., Jaffe 1977) within the intracluster medium (ICM). In the hierarchical model of structure formation galaxy cluster form through a sequence of mergers with smaller substructures. These merger events create shocks and turbulence in the ICM and could amplify magnetic fields. Several models have been put forward which link the presence of these diffuse radio sources to cluster merger events (e.g., Ensslin et al. 1998; Brunetti et al. 2001; Petrosian 2001; Cassano & Brunetti 2005; Keshet 2010; Enßlin et al. 2011).

Radio halos are smooth extended radio sources that roughly follow the X-ray emission from the ICM. They are typically unpolarized and have an extent of about a Mpc. Radio halos have been explained by the turbulence re-acceleration model (e.g., Brunetti et al. 2001; Petrosian 2001; Cassano & Brunetti 2005; Brunetti et al. 2008; Cassano 2010). In an alternative model, the energetic electrons are secondary products of proton-proton collisions (e.g., Dennison 1980; Blasi & Colafrancesco 1999; Dolag & Enßlin 2000). Simulations from Donnert et al. (2010a,b), observed radial radio profiles (e.g., Brown & Rudnick 2011), upper limits on the Gamma ray emission (Jeltema & Profumo 2011), and the existence of ultra-steep spectrum radio halos (Brunetti et al. 2008) put tension on the secondary models. Clusters with and without radio halos also show a bimodal distribution in the $P_{1.4\ \mathrm{GHz}} - L_{\mathrm{X}}$ diagram, i.e., a fraction of clusters hosts giant radio halos, while the majority of clusters do not show evidence of radio emission (Brunetti et al. 2007), in agreement with the turbulent re-acceleration model (Brunetti et al. 2009). However, it has been claimed that cosmic ray transport in clusters can also induce the radio bimodality that is observed (Enßlin et al. 2011).

Radio relics are usually divided up into three different classes (see Kempner et al. 2004, for an overview). (1) *Radio Gischt* are large extended sources mostly found in the outskirts of galaxy clusters. They are proposed to trace shock waves (Ensslin et al. 1998; Miniati et al. 2001), in which particles are accelerated by the diffusive shock acceleration mechanism (DSA; e.g., Krymskii 1977; Axford et al. 1977; Bell 1978a,b; Blandford & Ostriker 1978; Drury 1983; Blandford & Eichler 1987; Jones & Ellison 1991; Malkov & O’C Drury 2001) in a first-order Fermi process. However, the efficiency with which collisionless shocks can accelerate particles is unknown and may not be enough to produce the observed radio brightness of relics. A closely linked scenario is that of shock re-acceleration of pre-accelerated electrons in the ICM, which is a more efficient mechanism for weak shocks (e.g., Markevitch et al. 2005; Giacintucci et al. 2008; Kang & Ryu 2011). (2) *AGN relics* trace old radio plasma from previous episodes of AGN activity. (3) *Radio phoenices* are AGN relics that have been compressed adiabatically by merger shock waves boosting the radio emission (Enßlin & Gopal-Krishna 2001; Enßlin & Brüggen 2002). The radio spectra of these sources should be steep ($\alpha \lesssim -1.5$, $F_\nu \propto \nu^\alpha$, where α is the spectral index) and curved due to synchrotron and Inverse Compton (IC) losses.

A different model for radio relics (radio gischt) and halos has been proposed by Keshet (2010). It is based on a secondary cosmic ray electron model, where the time evolution of the magnetic fields and cosmic ray distribution are taken into account to explain both halos and gischt. For the outer edges of relics it is predicted that the spectral index should be $\alpha \simeq -1$. In addition, the magnetic fields (B) are expected to be strong, with $B \gtrsim B_{\mathrm{CMB}} > 3\ \mu$Gauss, and B_{CMB} the equivalent magnetic field strength of the cosmic microwave background.

Table 9.1: GMRT observations

	147 MHz	241 MHz (dual)	325 MHz	610 MHz (dual), 610 MHz	1280 MHz
Observation date	Apr 29, 2010	Nov 20, 2009	Apr 25, 2010	Nov 20, 2009 & 30 Apr, 2010	Nov 12, 2009
Usable bandwidth	15 MHz	6 MHz	30 MHz	30 MHz	30 MHz
Channel width	31.25 kHz	62.5 kHz	62.5 kHz	62.5 kHz	62.5 kHz
Polarization	RR+LL	LL	RR+LL	RR, RR+LL	RR+LL
Integration time	4 sec	8 sec	8 sec	8 sec	16 sec
Total on-source time	5.5 hr	3.5 hr	6.5 hr	3.5 + 6.0 hr	4.0 hr
Beam size	$26'' \times 22''$	$16'' \times 12''$	$12'' \times 8.7''$	$5.1'' \times 4.1''$	$5.8'' \times 2.0''$
Rms noise ($\sigma_{\rm rms}$)	0.92 mJy beam^{-1}	300 μJy beam^{-1}	79 μJy beam^{-1}	26 μJy beam^{-1}	32 μJy beam^{-1}
Briggs weighting	0.5	0.5	0.0	0.0	0.5

Table 9.2: WSRT observations

	25 cm, 1221 MHz	21 cm, 1382 MHz	18 cm, 1714 MHz	13 cm, 2272 MHz	6 cm, 4.9 GHz
Bandwidth	8×20 MHz	8×20 MHz	8×20 MHz	8×20 MHz	8×20 MHz
Number of channels per IF	64	64	64	64	64
Polarization	XX, YY, XY, XY	XX, YY, XY, XY	XX, YY, XY, XY	RR, LL, RL, LR	XX, YY, XY, XY
Observation dates	Aug 28, 2010	Sep 10, 2010	Sep 3, 2010	Sep 9, 2010	Sep 2 &6, 2010
Total on-source time	12 hr	12 hr	12 hr	12 hr	24hr
Beam size	$29.0'' \times 19.0''$	$27.1'' \times 16.4''$	$23.6'' \times 15.6''$	$16.1'' \times 9.8''$	$7.0'' \times 4.7''$
Rms noise ($\sigma_{\rm rms}$)	39 μJy beam^{-1}	27 μJy beam^{-1}	25 μJy beam^{-1}	40 μJy beam^{-1}	41 μJy beam^{-1}
Briggs weighting	0.0	0.5	1.0	0.5	0.5

Although there is now substantial evidence that radio relics and halos are related to galaxy cluster mergers (e.g., Cassano et al. 2010b), the detailed physics are still not understood. Radio spectra are a crucial way to separate between the physical models for the origin of radio relics and halos. Obtaining high-quality spectra is however difficult as these sources are extended and have a low surface brightness. In particular, spectral curvature provides important information about the underlying physical processes. However, curvature in the synchrotron spectrum is only observable if the observed frequency range is wide enough. In addition, obtaining images at matched resolutions over a wide-frequency range is often not possible.

We carried out an observing campaign to search for new diffuse radio sources in clusters (van Weeren et al. 2011c,b). By inspecting the WENSS (Rengelink et al. 1997) and NVSS (Condon et al. 1998) surveys we came across the complex radio source B3 0559+422B. The radio source roughly coincided with an extended X-ray source in the ROSAT All Sky Survey. In addition, an overdensity of galaxies following the X-ray emission, was visible in 2MASS images. The diffuse radio source, extended X-ray emission and galaxy overdensity strongly suggested the presence of a previously unidentified galaxy cluster located at moderate redshift. In this paper we present detailed radio observations of this new galaxy cluster 1RXS J0603.3+4214 and investigate the spectral and polarimetric properties of the diffuse emission.

The layout of this paper is as follows. In Sect. 9.2 we give an overview of the observations and the data reduction. The WSRT and GMRT images are presented in Sect. 9.3. The radio spectra and polarization data are analyzed in Sects 9.4 to 9.6. We end with a discussion and conclusions in Sects. 9.7 and 9.8.

Throughout this paper we assume a ΛCDM cosmology with $H_0 = 71$ km s^{-1} Mpc^{-1}, $\Omega_m = 0.3$, and $\Omega_\Lambda = 0.7$. All images are in the J2000 coordinate system.

9.2 Observations & data reduction

9.2.1 GMRT observations

GMRT observations were taken using the GMRT software backend (GSB; Roy et al. 2010). An overview of the observations is given in Table 9.1.

The data were reduced with the NRAO Astronomical Image Processing System (AIPS) package. The data were visually inspected for the presence of RFI which was subsequently removed. For the 147 and 241 MHz data, RFI was fitted and subtracted using the technique described by Athreya (2009), implemented in Obit (Cotton 2008). Standard bandpass and gain calibration were carried out, followed by several rounds of phase self-calibration and two final rounds of amplitude and phase self-calibration. The fluxes for the calibrator sources were set by the Perley & Taylor (1999) extension to the Baars et al. (1977) scale. Images were made using "briggs" weighting (Briggs 1995), see Table 9.1. were cleaned down to 2 times the rms noise level ($2\sigma_{\rm rms}$) within the clean boxes and corrected for the primary beam attenuation[1]. For more details about the data reduction see van Weeren et al. (2011e). The 147 MHz data were further calibrated for ionospheric phase distortions, as these can become quite severe at this frequency, with the SPAM package (Intema et al. 2009). At 325 MHz we removed several sources using the "peeling"-method (e.g., Noordam 2004).

[1] http://gmrt.ncra.tifr.res.in/gmrt_hpage/Users/doc/manual/UsersManual/node27.html

9.2.2 WSRT observations

WSRT observations of 1RXS J0603.3+4214 were taken in the L-band, 13cm and 6cm bands, see Table 9.2 for details. The data were calibrated with the CASA[2] package. We first removed time ranges affected by shadowing and RFI. The data were then calibrated for the bandpass response and subsequent gain solutions were transferred to the target source. Channel dependent leakage terms were found using an unpolarized calibrator source and the polarization angles were determined from 3C286. The fluxes for the calibrator sources were set by the Perley & Taylor (1999) extension to the Baars et al. (1977) scale. The data were exported into AIPS for several rounds of phase self-calibration, followed by two rounds of amplitude and phase self-calibration, see also van Weeren et al. (2011e). Images were cleaned with manually placed clean boxes and corrected for the primary beam attenuation. A deep image was created by combining the images from individual IF’s from the 18, 21, and 25 cm bands. The images were convolved to the same resolution and combined with a spectral index scaling of -1. The resolution of this combined image is $29'' \times 19''$.

We used the WSRT L-band observations to perform RM-Synthesis (see Sect. 9.6.2). For this, we created full polarization maps of every two neighboring frequency channels (i.e., the image bandwidth is 62.5 kHz). We inspected all these images and removed maps that had high noise levels, were affected by RFI or had other artifacts. In the end, 280 channels maps between 1170 and 1786 MHz were retained for RM-synthesis.

9.2.3 WHT spectroscopy & imaging

Optical images of 1RXS J0603.3+4214 were taken with the PFIP camera on the 4.2m William Herschel Telescope (WHT) between 15 and 19 April, 2009 with V, R and I filters. The seeing varied between 1.0″ and 1.5″and the total integration time was 1500 s per filter. The data were reduced with IRAF (Tody 1986, 1993) and the *mscred* package (Valdes 1998). Images were flat-fielded and corrected for the bias offset. R and I band images were also fringe corrected. The individual exposures were averaged, with pixels being rejected above $3.0\sigma_{\rm rms}$ to remove cosmic rays and other artifacts. The optical images were strongly affected by the bright star BD+42 1474 ($V_{\rm mag}$= 8.62), see Fig. 9.1.

To determine the redshift of the cluster, WHT ISIS spectra of galaxies located on the optical images were taken on 10 and 11 February, 2011. For the blue arm we used the R300B grating and for the red arm the R316R grating. The slit-width was 1.5″. Flat-fielding, bias correction, and wavelength calibration were performed in IDL[3]. The total exposure time per galaxy was 1500 s in both the blue and red arms. In the end, the spectra for the blue and red arm were merged into single spectrum for each galaxy.

9.3 Results: redshift, X-rays, and radio continuum maps

9.3.1 Redshift of 1RXS J0603.3+4214

The brightest cluster members are visible in the 2MASS survey images (Skrutskie et al. 2006) and some of them are also listed in the 2MASS Extended sources catalog (Skrutskie et al. 2003).

[2]http://casa.nrao.edu/
[3]http://www.ittvis.com

Table 9.3: Redshifts

Galaxy	2MASS K mag	z
2MASX J06031667+4214416	13.204	0.227
2MASX J06030757+4216215	13.610	0.222
2MASS J06032605+4214050	15.075	0.228
2MASS J06030644+4215241	15.201	0.227
2MASX J06032432+4209306	13.858	0.220

The cluster is not listed in NED or SIMBAD and probably remained unidentified because it is located relatively close to the galactic plane at a galactic latitude $b = 9.4°$ and nearby the bright star BD+42 1474.

No published redshifts are available for any of the galaxies in the cluster. Galaxies for which WHT ISIS spectra were obtained are listed in Table 9.3 and the spectra are shown in Fig. 9.2. The spectra are typical for passive red elliptical galaxies mostly found in clusters. We find that the five galaxies are located at $0.220 \leq z \leq 0.228$. Taking the average value we adopt $z = 0.225 \pm 0.04$ for the cluster, with the uncertainty in the redshift given by the standard deviation.

9.3.2 X-ray emission from the ICM

1RXS J0603.1+4214 is seen the ROSAT All-Sky Survey as an extended source and listed as 1RXS J060313.4+421231, 1RXS J060322.3+421305, and 1RXS J060314.8+421439 (Voges et al. 1999, 2000), see Fig. 9.3 (left panel). Using the redshift and ROSAT count rate (0.21 PSPC cts s^{-1}) we find an X-ray luminosity ($L_{\mathrm{X,\ 0.1-2.4\ keV}}$) of $\sim 1 \times 10^{45}$ erg s^{-1}. The X-ray emission is extended in the north-south direction. Additional emission extends to the east and west of the main X-ray peak. The high X-ray luminosity and extended emission are consistent with a massive cluster undergoing a major merger event.

9.3.3 Radio continuum maps

The WSRT L-band map is displayed in Fig. 9.3. We labeled some of the most prominent sources in this image. The GMRT 147, 241, 325, 610, 1280 MHz, and 13 cm WSRT images are shown in Figs. 9.4 to 9.7 (for the 4.9 GHz image see Fig. 9.16). The properties of the diffuse source in the cluster are summarized in Table 9.4.

Source A (B3 0559+422A) is a compact flat spectrum source with a flux of 0.29 Jy at 1.4 GHz (Jackson et al. 2007; Beasley et al. 2002; Marecki et al. 1999; Patnaik et al. 1992). The radio source is associated with a star-like object in the WHT images and listed as a quasar by Andrei et al. (2009), but no redshift is reported. Source F is a compact source (but resolved in the 1280 and 610 MHz images) and has an optical counterpart in the WHT images.

The most prominent source in the GMRT and WSRT images is B3 0559+422B (source B). The source is also visible in the 74 MHz VLSS survey (Cohen et al. 2007) and listed as VLSS J0603.2+4217. In the L-band image, the source has a largest angular size of 8.7′, which corresponds to a physical size of almost 1900 kpc. The source consists of a bright western

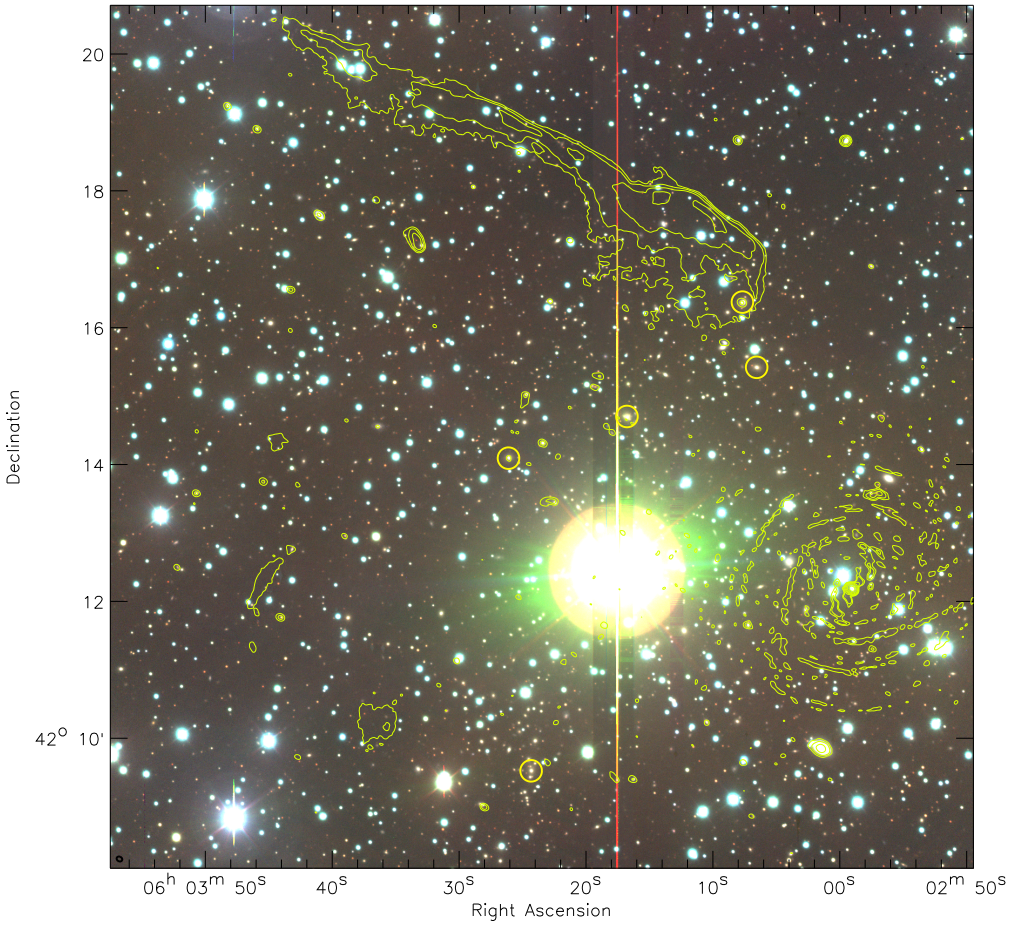

Figure 9.1: WHT V, R, I color image. Yellow contours are from the GMRT 610 MHz image (Fig. 9.4) and drawn at levels of $[1, 2, 4, 8, \ldots] \times 0.15$ mJy beam^{-1}. Galaxies for which spectra were obtained are marked with circles, see also Table 9.3 and Fig. 9.2. The spiral pattern at the bottom right is due to residual calibration errors around the source B3 0559+422A.

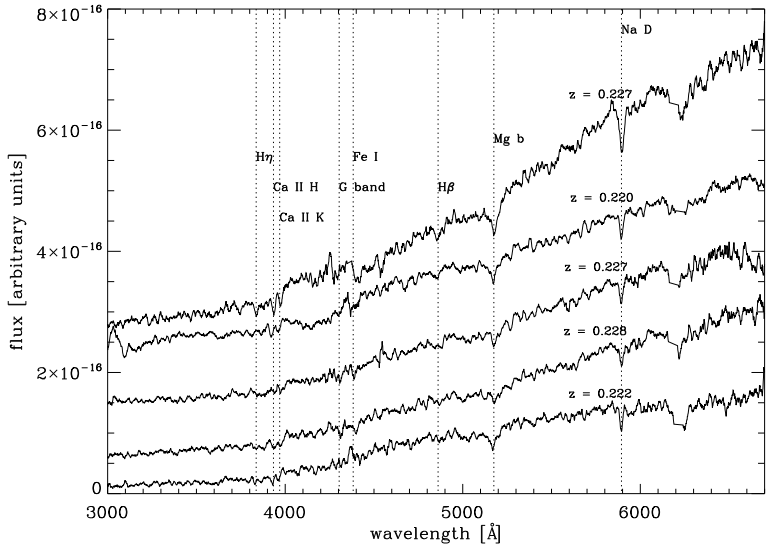

Figure 9.2: Rest-frame WHT ISIS spectra for the galaxies listed in Table 9.3. The order (from top to bottom) is the same as in Table 9.3. Various absorption features are indicated.

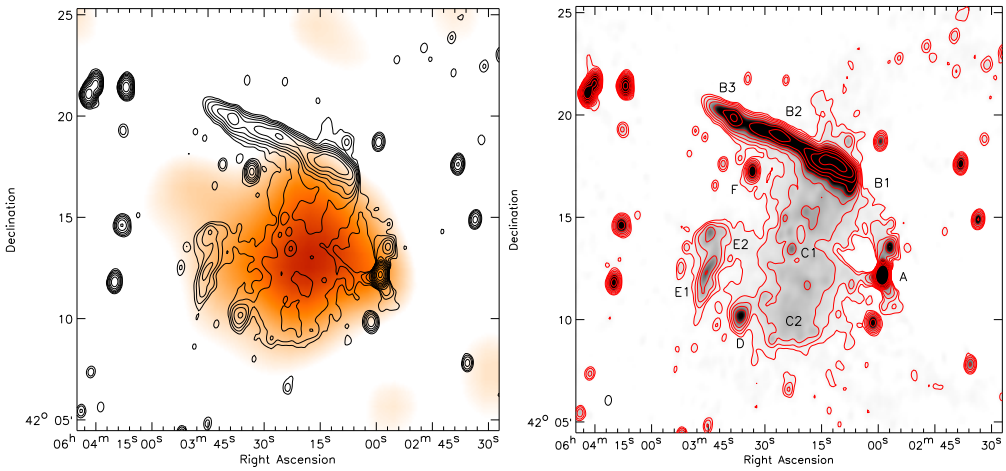

Figure 9.3: Left: X-ray emission from ROSAT. The image from the ROSAT All Sky Survey was smoothed with a 200″ FWHM Gaussian and is shown in orange colors. Solid contours are from the WSRT L-band image and drawn at levels of $[1, 2, 4, 8, \ldots] \times 0.15$ mJy beam^{-1}. Right: WSRT L-band image (1160–1780 MHz) with sources labelled. Contour levels are drawn at $[1, 2, 4, 8, \ldots] \times 80$ μJy beam^{-1}. The beam size is 29″ × 19″ and indicated in the bottom left corner of the image.

Table 9.4: Diffuse radio sources in 1RXS J0603.3+4214

Source	$S_{1382\mathrm{MHz}}$ mJy	$P_{1.4\mathrm{GHz}}$ 10^{24} W Hz^{-1}	LLS kpc	α
B	319.5 ± 14.8	60	1870	−1.10 ± 0.02
C	35.9±1.7	6.8	1700–2100	−1.15 ± 0.06
D	5.38±0.27	1.0	215	−1.10 ± 0.05
E	9.48±0.90	1.8	860	−1.0 ± 0.2

part (B1) and a fainter linear extension to the northeast (B2, B3). The radio emission brightens and fades two times along this extension, while the width of the source also varies. In the high-resolution 1280, 610, and 325 MHz images, the source displays a complex filamentary morphology. Some “streams” of emission extent from the northern part of B1 to the south. The northern boundary of the source is sharp, while the emission fades more slowly at the southern part. We classify source B as a radio relic because of the lack of optical counterparts, its polarization and spectral properties (see Sects. 9.4 to 9.6), and the large physical elongated size and peripheral location in the cluster.

Extending from B1 to the south, there is a patch of low surface brightness emission (C: subdivided into C1and C2). A hint of emission is visible north of B1 in the L-band and 325 MHz images, possibly associated with C1. The surface brightness decreases more rapidly at the south side of C (C2) than at the east and west sides. If we consider the faint emission north of B1 to be part of C then the source has a largest angular size of about 10′ (i.e., a physical extent of 2.1 Mpc). Only counting the emission south of B1 the source extends about 8′. We classify source C as the giant elongated radio halo because it roughly follows the X-ray emission from the ICM and has different spectral index properties than source B. The radio power of 6.8×10^{24} W Hz^{-1} falls on the L_{X}–$P_{1.4\mathrm{GHz}}$ correlation for giant radio halos (e.g., Liang et al. 2000; Cassano et al. 2006). However, at the most southern part of C2 the surface brightness increases slightly. This is best seen in the 147 and 241 MHz images (Figs. 9.6 and 9.7). The southern end of C2 could therefore be the “counter” radio relic of B1 (see Sect. 9.7). Although, we can also not exclude the possibility that it is part of the radio halo.

Another diffuse elongated source is located to the east of C1. The source consist of two parts, E1 and E2. We classify source E as a radio relic because we could not find an optical counterpart associated with it and it is located at the eastern boundary of the X-ray emission. The extent of E is 4′which corresponds to 860 kpc. Source D is another diffuse source without any optical counterpart in the WHT images, which we also classify as a radio relic. It has a largest angular size of 1.0′ in the GMRT 610 MHz image and displays hints of a complex morphology (Fig. 9.5), very different from a typical radio galaxy.

9.4 Radio spectra

9.4.1 Spectral index maps

We created radio spectral index maps using the GMRT and WSRT data. We first made radio maps at roughly the same resolution applying suitable tapers in the uv-plane and using uniform

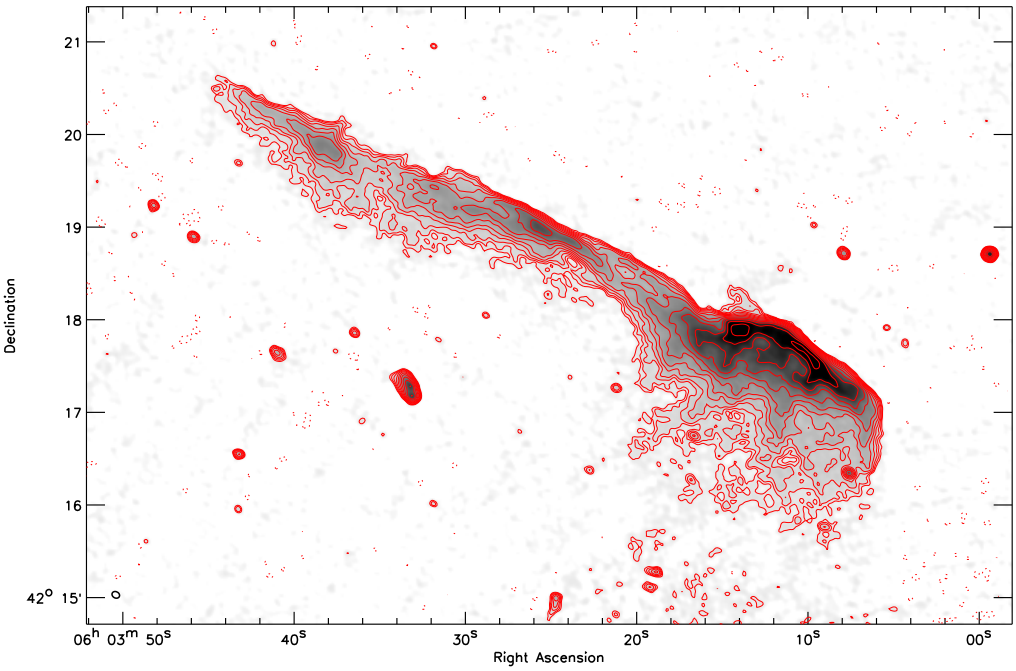

Figure 9.4: GMRT 610 MHz image. Contour levels are drawn at $\sqrt{[1,2,4,8,\ldots]}\times 4\sigma_{\rm rms}$. Negative $-3\sigma_{\rm rms}$ contours are shown by the dotted lines. The beam size is $5.1'' \times 4.1''$ and indicated in the bottom left corner of the image.

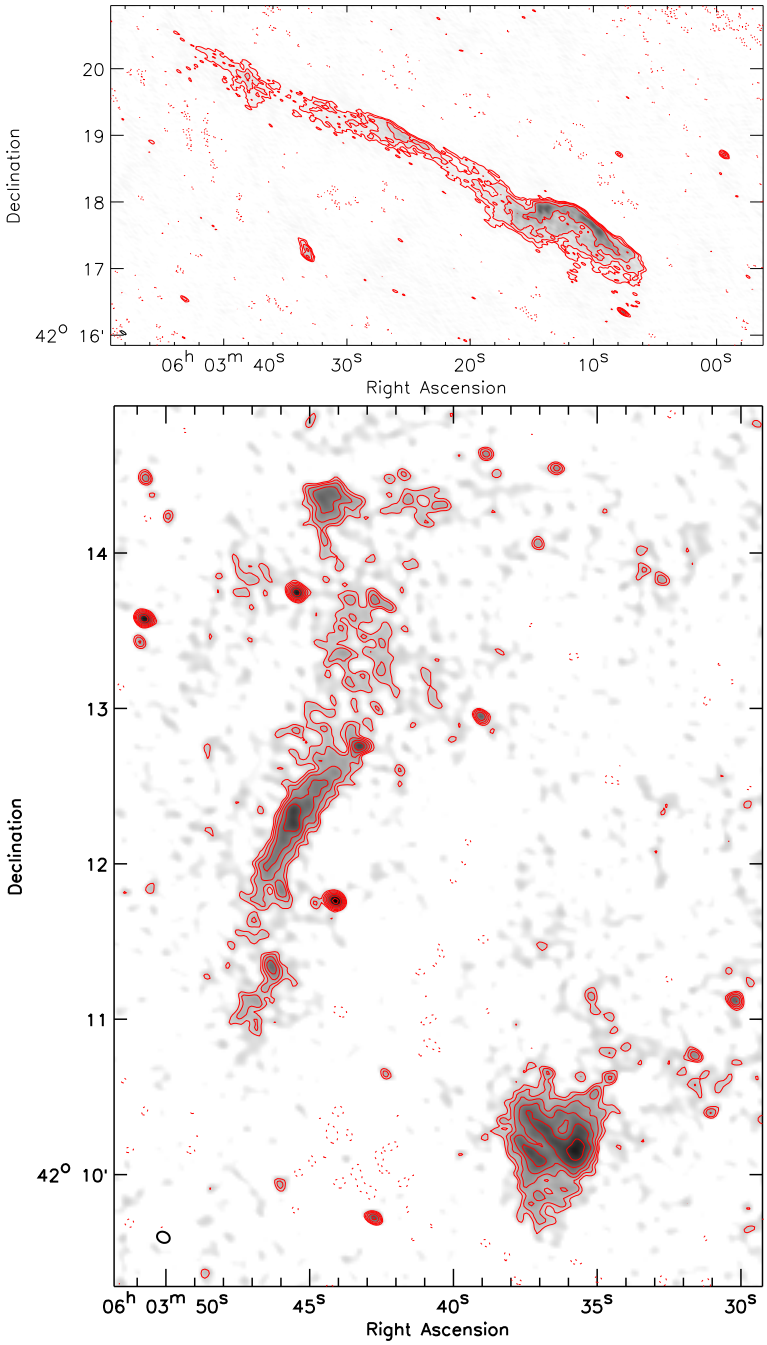

Figure 9.5: Top 1280 MHz image. Contour levels are drawn at $[1, 2, 4, 8, \ldots] \times 4\sigma_{\rm rms}$. Negative $-3\sigma_{\rm rms}$ contours are shown by the dotted lines. The beam size is $5.8'' \times 2.0''$ and indicated in the bottom left corner of the image. Bottom: GMRT 610 MHz cutout around sources D and E. Contours are drawn as in Fig. 9.4.

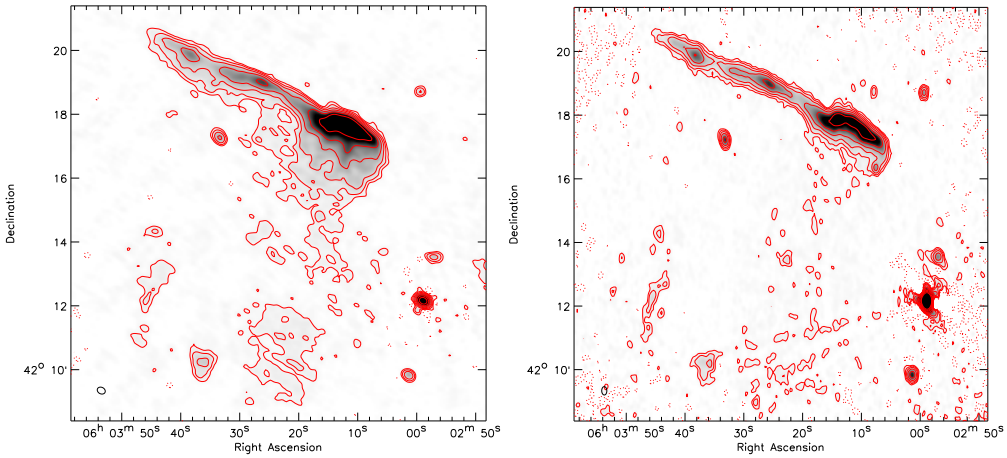

Figure 9.6: Left: GMRT 241 MHz image. Contour levels are drawn at $[1, 2, 4, 8, \ldots] \times 4\sigma_{\rm rms}$. Negative $-3\sigma_{\rm rms}$ contours are shown by the dotted lines. The beam size is shown in the bottom left corner of the image. Right: WSRT 2272 MHz image, contours are drawn as in the left panel.

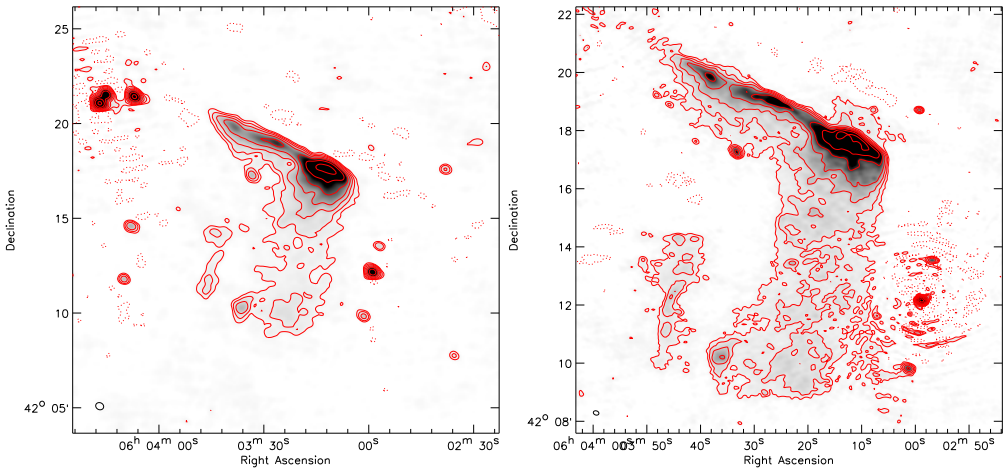

Figure 9.7: Left: GMRT 147 MHz image. Contour levels are drawn at $[1, 2, 4, 8, \ldots] \times 4\sigma_{\rm rms}$. Negative $-3\sigma_{\rm rms}$ contours are shown by the dotted lines. The beam size is shown in the bottom left corner of the image. Right: GMRT 325 MHz image. Contour levels are drawn at $[1, 2, 4, 8, \ldots] \times 5\sigma_{\rm rms}$. Negative $-5\sigma_{\rm rms}$ contours are shown by the dotted lines.

weighting. We discarded data below 0.25 kλ to select only common inner uvranges. The maps were then convolved to the same resolution. A high-resolution (7.9″ × 6.2″) spectral index map between 610 and 325 MHz is shown in Fig. 9.8. Pixels with values below $5\sigma_{\rm rms}$ were blanked. A medium-resolution (20″ × 18″) spectral index map between 2272 and 147 MHz was also made by fitting a second order polynomial in $\log(S) - \log(\nu)$ space through the flux measurements at 2272, 1714, 1382, 1221, 610, 325, 241, and 147 MHz, see Fig. 9.9 (left panel). Pixels with values below $1.5\sigma_{\rm rms}$ were blanked. To map the spectral index across the low surface brightness halo emission in the cluster, we also made a low-resolution spectral index map. We convolved the eight maps with a 35″ FWHM Gaussian (giving a resolution of approximately 40″) and fitted a power-law spectral index to minimize the number of fitted parameters. Pixels with a spectral spectral index error > 0.7 were blanked (Fig. 9.9, right panel).

The spectral index across relic B displays a clear north-south gradient, with a spectral index of about −0.6 to −0.75 on the north side of the relic, steepening to ~ -1.9 at the south side of B2 and B3 and to $\lesssim -2.5$ for B1. The spectral index gradient is visible over the entire length of the relic. The high-resolution 610–325 MHz spectral index map reveals the same general trends for relic B as in the medium-resolution map. However, the SNR on the spectral index is somewhat lower, mainly because of the smaller frequency span. We note that the spectral index at the front of B2 and B3 has a steeper spectral index (about −0.9 to −1.1) in the region where the surface brightness drops (i.e., at the intersection B1–B2 and B2–B3).

The spectral index across Relic E varies mostly between −1.0 to −1.2. There are no systematic trends visible across the relic, except that the north part of E3 has a somewhat flatter spectral index, see Fig. 9.9. The spectral index for relic D steepens from −1.0 to −1.3 from south to north. The spectral index across the radio halo (C) is difficult to determine as the SNR is low, but it roughly varies between −1.5 and −0.8 with an average of −1.1. There is a hint of spectral flattening for the center of the halo, while to the north and south of it the spectral index is steeper on average.

9.4.2 Integrated radio spectra

We determined the integrated radio spectra of the components, taking the same maps which were used to create the medium-resolution (20″ × 18″) spectral index map to minimize the effects of different uv-coverage. In addition, we added flux measurements at 74 MHz and 4.9 GHz for relic B from the VLSS survey and the WSRT observations. The radio spectrum is shown in Fig. 9.10 and is well fitted by a single power-law with $\alpha = -1.10 \pm 0.02$ between 74 and 4900 MHz. For relics D and E we find integrated spectral indices of -1.10 ± 0.05 and -1.0 ± 0.2. For source C we find $\alpha = -1.15 \pm 0.06$. The integrated radio spectra do not show clear evidence for spectral breaks or turnovers, although the radio spectrum for E is poorly determined, see Fig. 9.11.

9.5 Radio color-color diagrams

We investigated the detailed spectral shape of the relic emission. We first divided the relic into two parts, B1 and B2+B3, which we analyzed separately. These parts were further subdivided into regions ($\alpha_{\rm ref}$) within a specific spectral index range of 0.1 units, using the spectral index map from Fig. 9.9 (left panel). The resulting spectra, including first order polynomial fits through the data points (in $\log(I) - \log(\nu)$ space) are shown in Fig. 9.12. The fluxes were normalized by

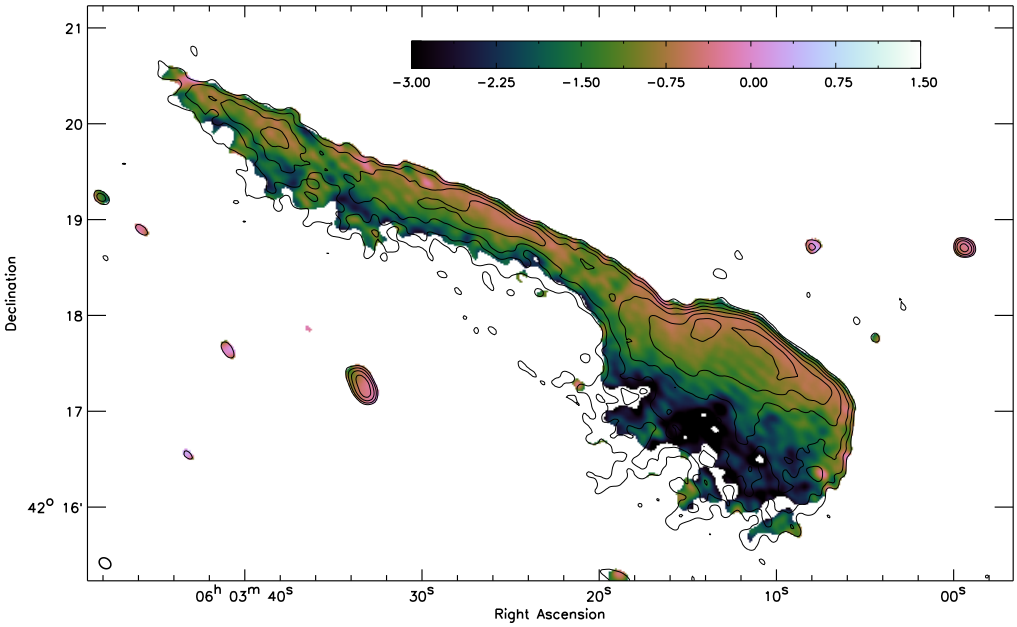

Figure 9.8: GMRT 610–325 MHz spectral index map. Contour levels from the GMRT 325 MHz image are drawn at $[1, 4, 16, 64, \ldots] \times 6\sigma_{\rm rms}$ and the spectral index map has a resolution of $7.9'' \times 6.2''$. Pixels below $5\sigma_{\rm rms}$ are blanked.

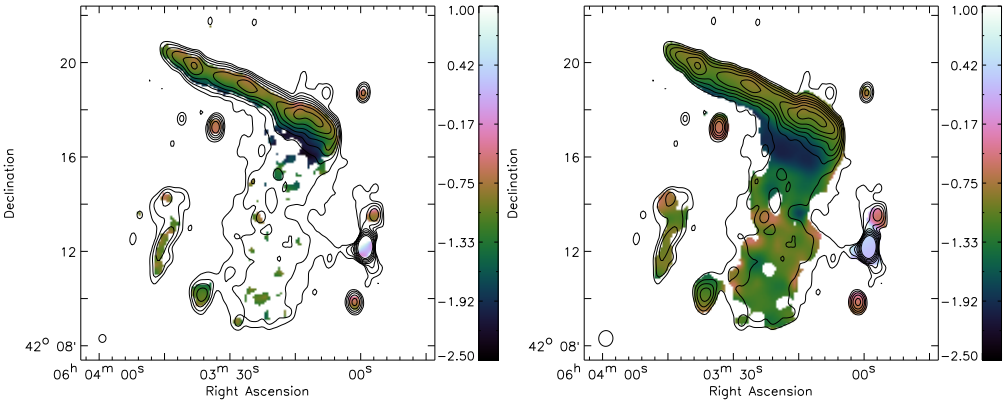

Figure 9.9: Left: Fitted spectral index map between 2272 and 147 MHz. The spectral index map was made by fitting a second order polynomial in $\log(S) - \log(\nu)$ for each pixel in the maps at 2272, 1714, 1382, 1221, 610, 325, 241 and 147 MHz. Contour levels are drawn at $[1, 2, 4, 8, \ldots] \times 0.175$ mJy beam^{-1} and are from the L-band image in Fig. 9.3. The spectral index map has a resolution of $20'' \times 18''$ and pixels below $1.5\sigma_{\rm rms}$ were blanked. Right: Fitted spectral index (2272 and 147 MHz) for each pixel in the maps at 2272, 1714, 1382, 1221, 610, 325, 241 and 147 MHz. The individual maps were convolved with Gaussians of $35''$ FWHM and pixels with a spectral index error > 0.7 were blanked, contours are drawn as in the left panel.

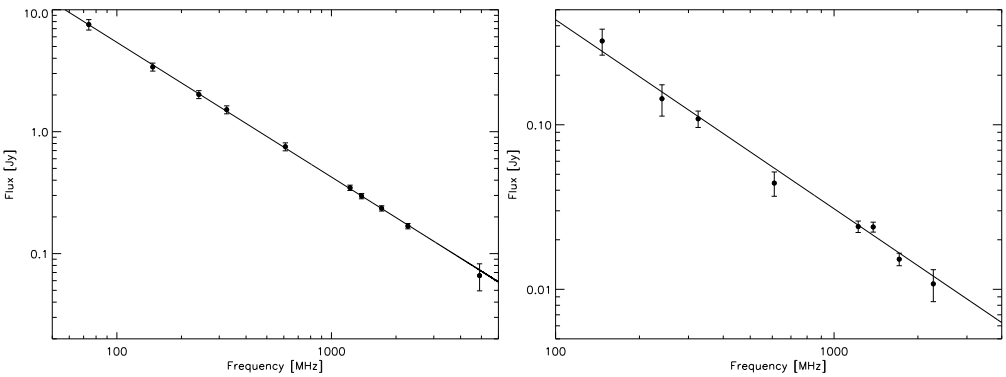

Figure 9.10: Integrated radio spectrum for radio relic B (left) and halo C (right). The lines are fitted straight power-laws with indices given in Table 9.4.

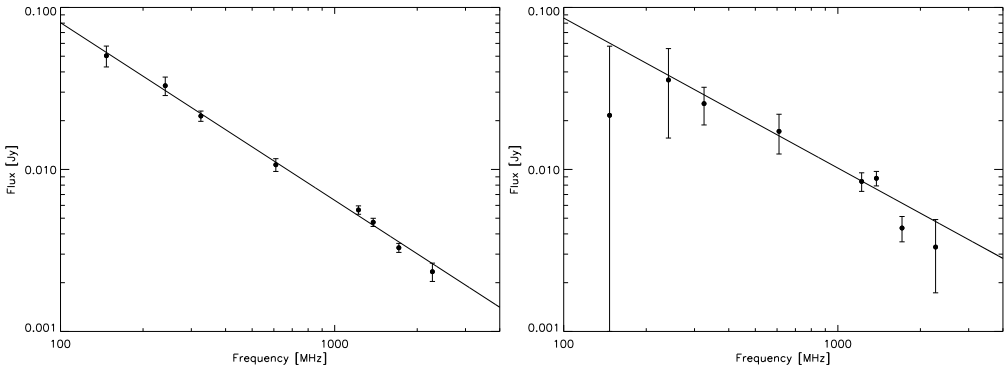

Figure 9.11: Integrated radio spectra for sources D (left), and E (right). The lines are fitted straight power-laws with indices given in Table 9.4.

dividing by the number of pixels found in each region, i.e., we work in surface brightness units. Each spectra thus corresponds to a region from the spectral index map where $\alpha_{\rm ref} - 0.05 < \alpha_{\rm ref} < \alpha_{\rm ref} + 0.05$, with $\alpha_{\rm ref} = -0.65, -0.75, -0.85$, etc. We limited $\alpha_{\rm ref}$ to -1.85 and -1.65 for B1 and B2+B3, respectively, to retain sufficient SNR at the highest frequency map (at 2272 MHz). We use these spectra as a starting point for creating the radio color-color diagrams.

9.5.1 Spectral models

In the model put forward by Ensslin et al. (1998), relics trace shock waves in which particles are accelerated by the DSA mechanism. Without projection effects and mixing of emission, and all properties of the shock remaining constant, the spectra at the different locations should simply reflect the energy losses of the radiating particles. Assuming an edge-on planar shock-wave, the time since acceleration for particles at a given location behind the front of the relic is simply $l/v_{\rm d}$, with l the distance from the front of the shock and $v_{\rm d}$ the shock downstream velocity. According to DSA-theory, the injection spectral index $\alpha_{\rm inj}$ is linked to the Mach number ($\mathcal{M}$) of the shock by (e.g., Blandford & Eichler 1987)

$$\alpha_{\rm inj} = \frac{1}{2} - \frac{\mathcal{M}^2 + 1}{\mathcal{M}^2 - 1} \ . \tag{9.1}$$

The integrated spectral index is steeper by about 0.5 units compared to $\alpha_{\rm inj}$ for a simple shock model where the electron cooling time is much shorter than the lifetime of the shock (Miniati 2002). Most of the synchrotron radiation we observe comes from the "critical" frequency $\nu_{\rm c}$

$$\nu_{\rm c} = \frac{3\gamma^2 e B_\perp}{4\pi m_{\rm e} c} \ . \tag{9.2}$$

Directly behind the front of the shock, the spectra should have a power-law shape of the form $I(\nu) = I_0 \nu^{\alpha_{\rm inj}}$, under the usual assumption that one starts with a power-law distribution of relativistic electrons $N(\gamma) = N_0 \gamma^{s_{\rm inj}}$, where $s_{\rm inj} = 1 - 2\alpha_{\rm inj}$. Synchrotron and IC (radiation) losses

steepen the distribution $N(\gamma)$ above certain break energy ($\gamma_{\rm brk}$). This also causes the radio spectrum to steepen above a corresponding break frequency ($\nu_{\rm brk}$), with

$$\nu_{\rm brk} \propto \frac{B}{\left(\left[B^2 + B^2_{\rm CMB}\right] t\right)^2}\,, \tag{9.3}$$

and t the time since injection.

The full spectral shapes are given by the Jaffe-Perola (Jaffe & Perola 1973) and Kardashev-Pacholczyk models (Kardashev 1962; Pacholczyk 1970). The JP-model takes into account the spectral ageing due to synchrotron and IC losses and that the pitch angles of the synchrotron emitting electrons are continuously isotropized on a timescale shorter than the radiative timescale. In the KP-model, the pitch angle of the electrons remains in its original orientation with respect to the magnetic field. The JP model is more realistic from a physical point of view, as an anisotropic pitch angle distribution will become more isotropic due to changes in the magnetic field strength between different regions and scattering by self-induced Alfvén waves (e.g., Carilli et al. 1991; Slee et al. 2001).

In addition to the above “single burst” models, there is the continuous injection (CI) model (Pacholczyk 1970), i.e., a fresh supply of particles is injected continuously and the so-called KGJP or KGKP models (Komissarov & Gubanov 1994), where particles are injected for a fixed period of time after which the supply of newly injected electrons is switched off.

9.5.2 Effect of resolution on surface brightness

If radiative losses are the dominant effect then all spectra for different parts of the relic should line up at some fiducial low energy/frequency where radiation losses are not important. The spectra displayed in Fig. 9.12 should therefore all line up at low enough frequencies. Part of such a trend is indeed visible. Although, the spectra with $\alpha_{\rm ref} = -0.65, -0.75$ have a lower surface brightnesses than we naively expect. We attribute this to the fact that the pixels, from which these spectra are determined, are all located on the sharp outer edge of the relic, where the emission drops abruptly to zero within a single beam element. Since the resolution of the spectral index map is only about 20″ and there are about 4 pixels per beam, the regions with the flattest spectral index are all located on pixels where the surface brightness drops at the front of the relic due to the finite beam size. This can be seen by looking at the black contours in Fig. 9.9, i.e., the surface brightness does not peak at the region with the flattest spectral index. Comparing these contours to the higher resolution images in Figs. 9.4 and 9.5, we find however that the outer rim of the relic is indeed the brightest part of the relic. The lower surface brightness for the $\alpha_{\rm ref} = -0.65, -0.75$ regions is thus caused by the low spatial resolution of the spectral index map. This is also confirmed by the high-resolution 325–610 MHz spectral index map, see Fig. 9.8.

It is interesting to note that the spectra for the regions with a flattest spectral index are all relatively straight and show little deviations from a pure power-laws (Fig. 9.12). Going to the regions with a steeper $\alpha_{\rm ref}$, the spectral shapes change and display signs of curvature at the higher frequencies. These changes happens gradually from the regions with a flat $\alpha_{\rm ref}$ to a steeper $\alpha_{\rm ref}$.

9.5.3 Color-color diagrams

To better investigate the spectral shape we use so called three frequency "color-color" diagrams for which the spectral indices for different region of the source can all be put in a single diagram (Katz-Stone et al. 1993). On the x-axis we plot the low- frequency spectral index and on the y-axis the high-frequency one. Color-color diagrams are particularly useful to discriminate between theoretical synchrotron spectral models, such as the JP, KP, CI, KGJP, KGKP models described before.

Another advantage of color-color diagrams is that the shapes traced out in the diagrams are conserved for changes in the magnetic field, adiabatic expansion or compression, and the radiation losses, for standard spectral models. We observe a different portion of the spectrum for each different frequency or source physical condition (e.g., local B field). We can thus use the observed curve to constrain the different models (JP, CI, KP, etc.) and injection spectral indices. Mixing of emission, for example from regions with different B strengths or radiation losses, due the finite resolution of the observations or projection effects, will lead to different curves in the color-color diagrams. If a global spectral shape exists, it also allows for a better effective frequency sampling and provides sampling of a larger range of electrons energies.

9.5.3.1 Color-color diagrams for B1 and B2+B3

The color-color diagrams for B1 and B2+B3 are shown in Fig. 9.13 (left and right panels, respectively). The points in the color-color diagrams seem to trace out single curves. This suggests the existence of a global spectral shape for these regions. The curves are similar for the B1 and B2+B3 regions, but they slightly differ for $\alpha_{\rm ref} \lesssim -1.4$.

Tracing the curves back to the $\alpha_{241}^{610} = \alpha_{1382}^{2272}$ (i.e., power-law) line gives the injection spectral index. In both cases we find $\alpha_{\rm inj}$ is about -0.6 to -0.7 for B1 and B2+B3, in agreement with the spectral index maps. The color-color diagrams highlight the trend of increasing spectral curvature, i.e., distance from the power-law line, with decreasing $\alpha_{\rm ref}$ (Fig. 9.12). The spectra for $\alpha_{\rm ref} = -0.65, -0.75$ are power-laws. We also indicated varies spectral models in the diagrams. We compare the observed curves in the color-color diagrams to the some of the standard spectral models.

The observed curve is clearly different from the continuous injection spectral model. The CI model only steepens to $\alpha = \alpha_{\rm inj} - 0.5$ (Pacholczyk 1970). The KP model (with $\alpha_{\rm inj} = -0.6$) roughly follows the data for flat $\alpha_{\rm ref}$, but deviates for $\alpha_{\rm ref} \lesssim -1$. However, in the end the KP curve bends back and returns to the $\alpha_{241}^{610} = \alpha_{1382}^{2272}$ line. We do not see evidence for a turn back to the $\alpha_{241}^{610} = \alpha_{1382}^{2272}$ line in the data, although we do not sample this part of the diagram well because of insufficient SNR at high-frequencies.

The JP model (plotted for $\alpha_{\rm inj} = -0.6$ and -0.7) follows the KP model for flat $\alpha_{\rm ref}$. Instead of turning back to the $\alpha_{241}^{610} = \alpha_{1382}^{2272}$ line, the spectral curvature keeps increasing. The data also show this trend of increasing curvature, but less quickly than the JP curve. A KGJP model with $\alpha_{\rm inj} = -0.7$ matches the data for B2+B3 very well. The KGJP curves in Fig. 9.13 are for particles injected continuously for about 0.6×10^8 yr and $B = 9\ \mu$Gauss (see Sect. 9.7.3). The KGJP model also provides a better match for the B1 region compared to the KP and JP curves. Although, in the regions with the steepest $\alpha_{\rm ref}$ values the KGJP model still overestimates the amount of curvature. A KGJP model can be thought of as an integration of JP spectra with a range of spectral ages, up to the oldest population of electrons. At first, the KGJP model follows the CI model until at some point in time the supply of newly injected electrons is shut off.

9.5.3.2 The effect of resolution and mixing

One important effect is mixing of emission within the beam. Each beam samples superpositions of regions with potentially physical different conditions. To investigate the effect of resolution in the color-color diagrams, we decreased the resolution of the spectral index maps by convolving them with Gaussians of 60″ FWHM. The data for the lower resolution maps are also displayed in Fig. 9.13. The effect of the lower resolution is that the curve ends up closer to the $\alpha_{241}^{610} = \alpha_{1382}^{2272}$ line. This is expected because the total integrated spectrum of the relic has a power-law shape (Fig. 9.10).

We also investigated for B1, the effect of a possible underlying flux component from the radio halo C. For this, we determined the average spectrum of the radio halo and subtracted this flux contribution at each frequency. This however did not substantially change the resulting color-color diagram for B1 because the surface brightness of the relic is much higher than that of the radio halo.

Our conclusion is that mixing of emission (from regions with different *B*-fields or different electron energy distributions, etc.) pushes the spectra closer to power-law shapes. The spectral curvature we find can thus be regarded as a lower limit on the actual curvature and it is therefore important that when searching for spectral curvature one retains sufficient spatial resolution (enough to properly resolve the spectral variations).

9.5.4 Global spectrum

Since the data points trace out a well defined curve in the color-color diagrams, we have attempted to map the flux measurements onto a single spectral shape using the “shift-technique” described by Katz-Stone et al. (1993); Rudnick & Katz-Stone (1996); Rudnick (2001). This allows for a much better sampling in frequency, and maps out the spectrum over a larger range of electron energies. The idea is that the individual radio spectra for different $\alpha_{\rm ref}$ regions each trace some part of the “global spectrum” (or electron energy distribution) of the source, depending on the energy losses, and magnetic fields in these regions. The shifts (in $\log(I)$-$\log(\nu)$ space) remove the effects of possible different local magnetic field strengths, electron densities, radiative energy losses, and adiabatic energy gains/losses.

We shifted the spectra, displayed Fig. 9.12, in $\log(I)$-$\log(\nu)$ space and tried to line them all up. This went remarkably well, indicating we indeed have a single electron energy distribution (or global spectral shape) that is consistent with the spectra for each individual region. The two resulting spectra (for B1 and B2+B3) are displayed in Fig. 9.14. As can be seen it allows for an almost continuous sampling of the radio relic spectrum over about 4 orders of magnitude in frequency (two oders of magnitude in energy, see Eq. 9.2).

Similar to the color-color diagrams we find that the low-frequency part of the global spectrum has a power-law shape, with $\alpha = -0.6$ to -0.7. At higher frequencies the spectrum steepens. We also compare the global spectra with some of the standard models in Fig. 9.14. The results are the same as for the color-color diagrams, i.e., the best match we find for a KGJP model and for B1 the KGJP spectral curvature is somewhat too high for $\nu_{\rm eff} \gtrsim 20$ GHz.

9.5.4.1 Shift diagrams

Interestingly, the shifts made to align up all the individual radio spectra to create Fig. 9.14 provide information about changes in the underlying physical parameters (Katz-Stone & Rudnick

1994). The shifts made in the frequency direction ($\log(\nu)$), to line up the spectra, are related to $\gamma^2 B$. The shifts in $\log(I)$ are related to $N_{\rm T}B$, where $N_{\rm T}$ is the total number of relativistic electrons in the volume determined by the beam size.

By plotting the shifts which we needed to align up the individual spectra ($\log(\nu)$ shifts against $\log(I)$ shifts), we can investigate the contributions of the above mentioned quantities, i.e., which quantities cause the spectra to differ from region to region. The shift diagrams are shown in Fig. 9.15. For example, a slope ($\delta\log(I)/\delta\log(\nu)$) of +1 indicates mainly variations in the magnetic field strength, a slope of infinity indicates density variations, and a slope of zero energy variations. If every line of sight samples the same physical conditions (i.e., the same magnetic field, path length through the source, number of relativistic particles at some fiducial low energy), then ageing alone would give a slope equal to the injection spectral index. The idea is that for spectral ageing you need to shift in $\log(\nu)$ space to match up the break frequency, but then the spectrum will fall below the initial power-law injection spectrum, so a shift (up) in $\log(I)$ is also required.

We find slopes of −0.83 and −0.67 in the shifts diagrams for B1 and B2+B3, respectively. We did not include the first three (B1) and two (B2+B3) points for fitting the slope. This because the $\log(I)$-shifts for these points are affected by the reduced surface brightness at the outer edge of the relic, see Sect. 9.5.2. The slopes are close to the injection spectral indices of −0.6 to −0.7 we found from the color-color diagrams. The slope for B1 deviates a little more, but overall the shift diagrams indicate that spectral ageing is likely the dominant factor in explaining the different spectral shapes from region to region. Apparently, the magnetic field and total number of number of relativistic electrons remain more or less constant for the different $\alpha_{\rm ref}$ regions.

9.6 RM-synthesis & polarization maps

9.6.1 Polarization maps

The distribution of the polarization E-vectors at 4.9 and 1.382 GHz are shown in Fig. 9.16. In the 4.9 GHz map, we find the relic to be polarized over its entire length (in the region with sufficient SNR). The E-vectors are mainly perpendicular to the relic's orientation, except at the eastern end of B1 (where the relic bends and is connected to the linear eastward extension B2). The polarization fraction across the relic varies between 10 and 60%, where it can be measured. At the front of B1, the polarization fraction is mostly between 15 and 30%, while at the front of B2 the fraction is 50% or higher. In the 4.9 GHz map we cannot determine the polarization fraction for B3 because the attenuation of the primary beam . It should be noted that the spatially averaged polarization fractions are lower.

At 1382 MHz the polarization fraction drops significantly for B1 and B2, compared to at 4.9 GHz. For region B3 we measure a polarization fraction as high as 40%, while for the brightest part of B2 it is about 5%, and for B1 it drops below 1%. The average polarization fractions and depolarization properties for relic B are described in Sect. 9.6.3.

9.6.2 RM-synthesis

Faraday rotation changes the intrinsic polarization angle (χ_0) depending on the wavelength (λ) or frequency of the radiation. The Faraday depth (ϕ) is related to the properties of the plasma

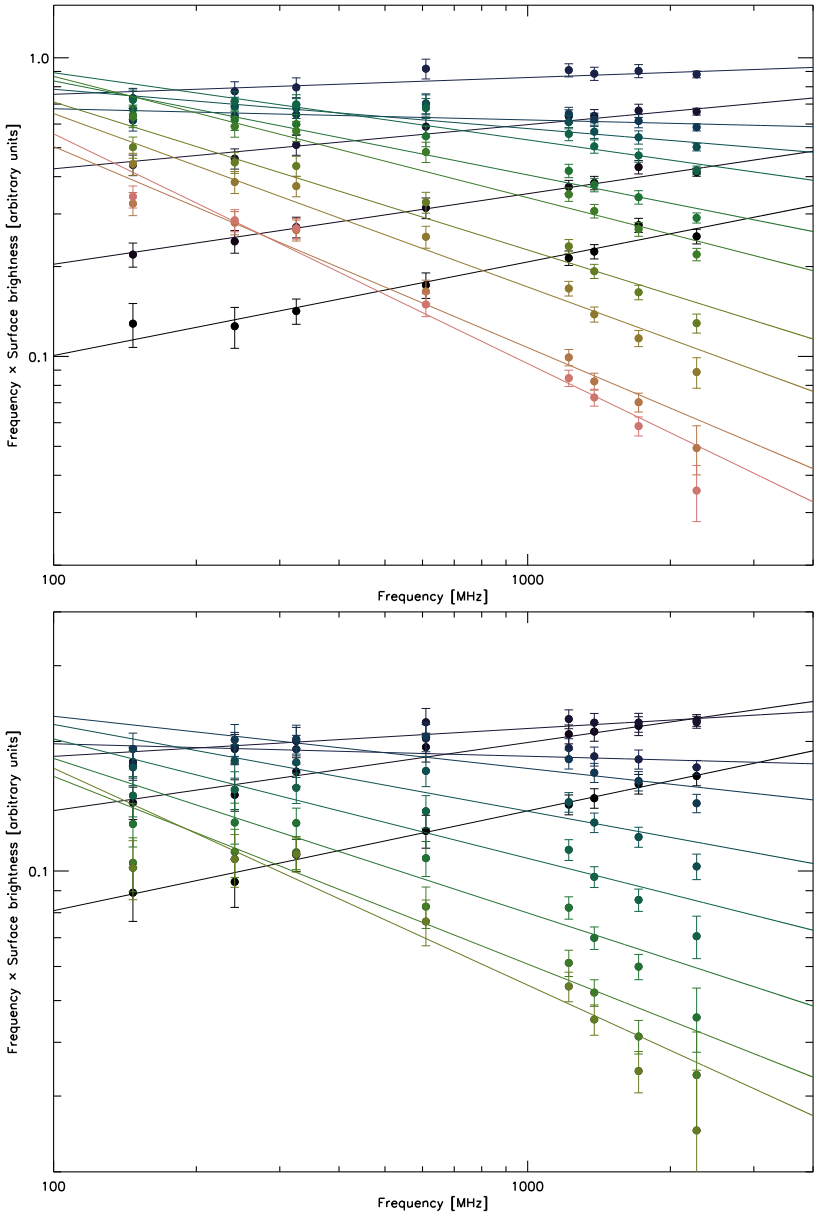

Figure 9.12: Normalized radio spectra for relic B1 (top) and B2+B3 (bottom). Each spectrum corresponds to a region from the spectral index map where $\alpha_{\rm ref} - 0.05 < \alpha_{\rm ref} < \alpha_{\rm ref} + 0.05$, with $\alpha_{\rm ref} = -0.65, -0.75, \ldots, -1.85$ for B1, and $\alpha_{\rm ref} = -0.75, -0.85, \ldots, -1.65$ for B2+B3. The spectra are plotted in $\nu \log(I) - \log(\nu)$ space to emphasize the differences between the spectra. First order polynomial fits in $\log(I) - \log(\nu)$ space are shown by the solid lines to emphasize possible deviations from power-law radio spectra. Colors correspond to the different $\alpha_{\rm ref}$ and go from black, blue, green, to red (or from black to white in the greyscale version of the figure).

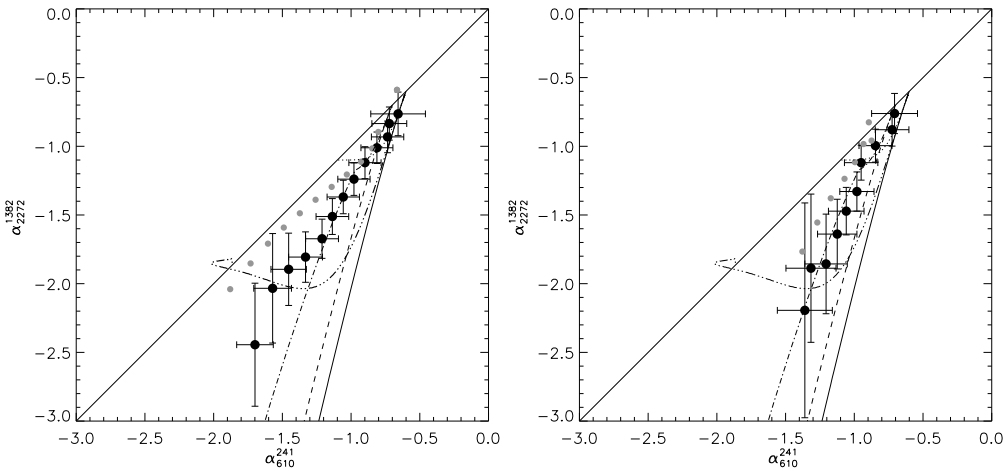

Figure 9.13: Color-color diagrams for B1 (left) and B2+B3 (right). Black data points are from the spectra displayed in Fig. 9.12. The solid black (slightly curved) line is a JP model with $\alpha_{\rm inj} = -0.6$, the dashed black line a JP model with $\alpha_{\rm inj} = -0.7$, the dash-triple-dotted line a KP model with $\alpha_{\rm inj} = -0.6$, the dotted line a CI model with $\alpha_{\rm inj} = -0.6$, and the dash-dotted line a KGJP model with $\alpha_{\rm inj} = -0.7$. The grey data points are for the same data as the black points, except the maps were smoothed with a 60″ FWHM Gaussian. The $\alpha^{610}_{241} = \alpha^{2272}_{1382}$ line is also shown for reference.

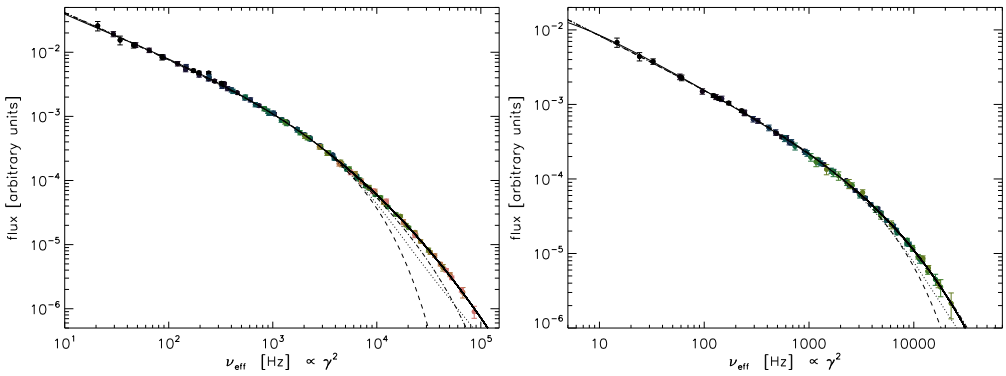

Figure 9.14: "Global" radio spectra for B1 (left) and B2+B3 (right). The spectrum for each $\alpha_{\rm ref}$ spectral region from Fig. 9.12 has been shifted in $\log(I) - \log(\nu)$ space to create the "global" spectral shape. Fourth order polynomial fits through these data points are shown by the solid thin black lines. JP (dashed), KP (dotted) and KGJP (dash-dotted) models are also plotted. The color coding, based on the $\alpha_{\rm ref}$ regions, is the same as in Fig. 9.12.

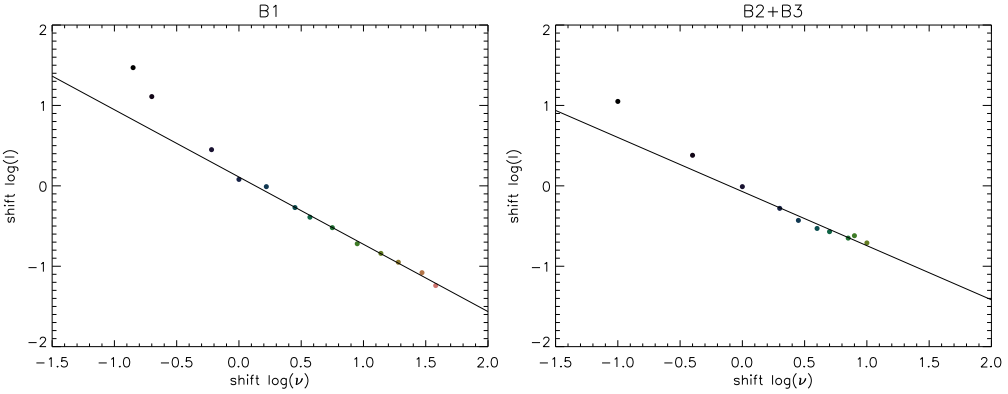

Figure 9.15: Shifts in $\log(I) - \log(\nu)$ space, for B1 (left) and B2+B3 (right), needed to line up the radio spectra displayed in Fig. 9.14. A line is fitted through the data points, excluding the first three (B1) or two (B2+B3) points. Color coding for the $\alpha_{\rm ref}$ regions is the same as in Fig. 9.12.

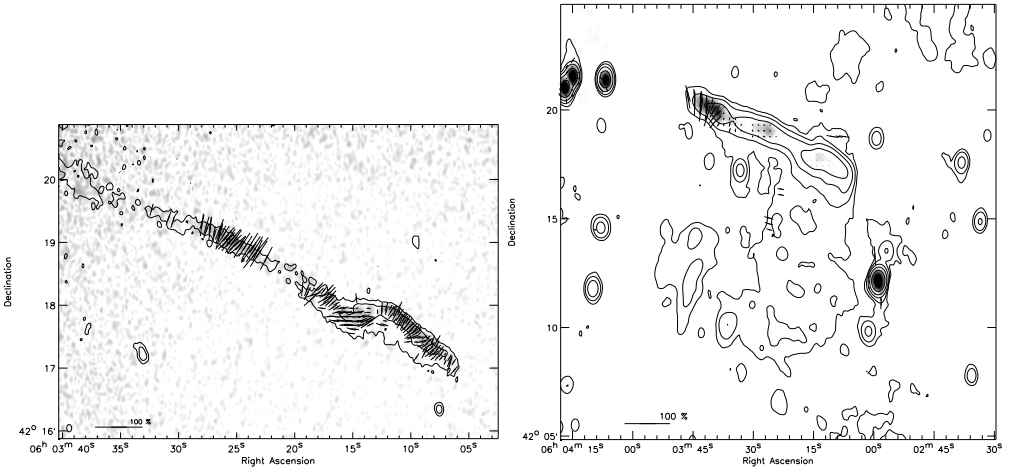

Figure 9.16: Left: WSRT 4.9 GHz polarization E-vector map. Total polarized intensity is shown as greyscale image. Vectors depict the polarization E-vectors, their length represents the polarization fraction. The length of the E-vectors are corrected for Ricean bias (Wardle & Kronberg 1974). A reference vector for a polarization fraction of 100% is shown in the bottom left corner. No vectors were drawn for pixels with a SNR < 3 in the total polarized intensity image. Contour levels are drawn at $[1, 4, 16, 64, \ldots] \times 3\sigma_{\rm rms}$ and are from the Stokes I image. The beam size is $7.0'' \times 4.7''$ and indicated in the bottom left corner of the image. Right: WSRT 1382 MHz polarization E-vector map. Total polarized intensity is shown as grayscale image. No vectors were drawn for pixels with a SNR < 4 in the total polarized intensity image. Contour levels are drawn at $[1, 4, 16, 64, \ldots] \times 3\sigma_{\rm rms}$ and are from the Stokes I image.

casing the Faraday rotation (Burn 1966; Brentjens & de Bruyn 2005)

$$\phi(\mathbf{r}) = 0.81 \int_{\text{source}}^{\text{telescope}} n_{\text{e}}\mathbf{B} \cdot \, d\mathbf{r} \; [\text{rad m}^{-2}] \, , \tag{9.4}$$

where $d\mathbf{r}$ is an infinitesimal path length in parsec along the line of sight, $\mathbf{B}$ the magnetic field in μGauss and n_{e} the electron density in cm^{-3}. The sign is defined to be positive for a magnetic field pointing towards the observer. The rotation measure (RM) is defined as

$$\text{RM} = \frac{d\chi(\lambda^2)}{\lambda^2} \, . \tag{9.5}$$

If there is only one source along the line of sight (without internal Faraday rotation), the Faraday depth is equal the rotation measure (RM) at all wavelengths. In other words, all polarized emission is observed at a single Faraday depth ϕ. The observed polarization angle (χ) is then

$$\chi = \chi_0 + \phi\lambda^2 \, . \tag{9.6}$$

In more complicated situations this relation is not valid (e.g., Vallee 1980; Sokoloff et al. 1998). By expressing the polarization as a complex vector $P = pe^{2i\chi} = Q + iU$, with p the intrinsic polarization Burn (1966) showed that

$$P(\lambda^2) = \int_{-\infty}^{+\infty} F(\phi) e^{2i\phi\lambda^2} \, d\phi \, , \tag{9.7}$$

where $F(\phi)$ is the Faraday dispersion function, i.e., the complex polarized surface brightness per unit Faraday depth. Eq. 9.7 is invertible if the intrinsic polarization angle χ_0 is constant as function of λ, then $F(\phi)$ can be found by measuring $P(\lambda^2)$

$$F(\phi) = \int_{-\infty}^{+\infty} P(\lambda^2) e^{-2i\phi\lambda^2} \, d\lambda^2 \, . \tag{9.8}$$

With modern correlator backends, such as the one at the WSRT or EVLA, $P(\lambda^2)$ can measured over a large number of frequency channels. If $\phi\delta\lambda^2 \ll 1$, with $\delta\lambda^2$ the channel width in wavelength squared, Brentjens & de Bruyn (2005) showed that Eq. 9.8 can be approximated as

$$\tilde{F}(\phi) \approx K \sum_{i=1}^{N} w_i P_i e^{-2i\phi(\lambda_i^2 - \lambda_0^2)} \, , \tag{9.9}$$

with w_i being some weights and K a normalization factor

$$K = \left(\sum_{i=1}^{N} w_i \right) \, . \tag{9.10}$$

An extra λ_0^2 has been added in the exponent in Eq. 9.9 by Brentjens & de Bruyn who showed that this results in a better behaved or rotation measure spread function (RMSF), with

$$\lambda_0^2 = \frac{\sum_{i=1}^{N} w_i \lambda_i^2}{\sum_{i=1}^{N} w_i} \, , \tag{9.11}$$

and the RMSF given by

$$\mathrm{RMSF}(\phi) = K \sum_{i=1}^{N} w_i e^{-2i\phi(\lambda_i^2 - \lambda_0^2)} \,. \tag{9.12}$$

Because P is not measured for every possible λ_i^2, the true Faraday depth function is related to Eq. 9.9 by a convolution

$$\tilde{F}(\phi) = F(\phi) * \mathrm{RMSF}(\phi) \,. \tag{9.13}$$

Depending on the sidelobe structure of the RMSF (which can be adjusted by choosing the weights w_i) a brighter component can contaminate the response of fainter components in $\tilde{F}(\phi)$ and therefore deconvolution might be necessary. The one-dimensional deconvolution algorithm which has been used is a simple extension of Högbom (1974) `RM-CLEAN` algorithm to the complex domain as described by Brentjens (2007), see also Heald et al. (2009). It works as follows

1. For a spatial pixel the maximum of $\left|\tilde{F}(\phi)\right|$ is found and the location of the peak is stored (ϕ_{peak}).

2. If this maximum value is higher than a user defined cutoff, the RMSF is shifted to the location of the peak (ϕ_{peak}) and a scaled version (i.e., using a gain of 0.1) is subtracted from $\tilde{F}(\phi)$. Since the RMSF is complex, a multiplication with a phase factor is needed which depends on the phase of $\tilde{F}(\phi_{\mathrm{peak}})$.

3. The complex scaling factor, which was used to shift and subtract the RMSF, is stored as a clean component.

4. Steps 2 – 4 are repeated until a user defined threshold is reached or the number of iterations has reached a predefined maximum.

5. Optionally, the clean components are restored with Gaussians with a FWHM matched to that of the RMSF. The Gaussians are again shifted to their respective locations (ϕ_{peak}), and since this happens in the complex domain, multiplied by a phase factor (i.e., the complex part of the clean component). The restored Gaussians are added to the residual from step 4. If there are multiple RM components within the beam it is however not a good idea to reconvolve the spectra with the RMSF if one wants to investigate the depolarization properties. This is related to the fact that the clean components are complex numbers and can interfere with each other (Farnsworth et al. 2011).

6. The algorithm then continues with the next spatial pixel.

The above described RM-synthesis technique works better than linear fitting techniques (e.g., Ruzmaikin & Sokoloff 1979; Dolag et al. 2005; Vogt et al. 2005), which break down in low signal to noise regimes and do not apply to more complex situations when Eq. 9.6 is not valid.

The RM-synthesis technique (i.e., Eq. 9.9) and `RM-CLEAN` algorithm were implemented in IDL.

9.6.2.1 Application to the L-band WSRT data

We performed RM-synthesis on the WSRT 25, 21 and 18 cm data using cubes of Stokes Q and U images with a resolution of $40'' \times 28''$, see also Sect. 9.2.2. These data give a sensitivity to polarized emission up to a maximum Faraday depth of $|\phi_{\rm max}| \approx \sqrt{3}/\delta\lambda^2 \approx 8.8 \times 10^4$ rad m^{-2} (Brentjens & de Bruyn 2005). The three bands provide a resolution of $\delta\phi \approx 2\sqrt{3}/\Delta\lambda^2 = 88$ rad m^{-2}, with $\Delta\lambda^2 = \lambda^2_{\rm max} - \lambda^2_{\rm min}$ the total bandwidth in wavelength squared. The maximum scale in ϕ space to which the sensitivity has dropped to 50% is approximately $\pi/\lambda^2_{\rm min} = 111$ rad m^{-2}. The RMSF is shown in Fig 9.17 (left panel). Since the first sidelobe of the RMSF is about 65% of the main lobe, we used the `RM-CLEAN` algorithm, cleaning down to a threshold of 0.12 mJy beam^{-1} RMSF^{-1}. The distribution of the peak of $\left|\tilde{F}(\phi)\right|$, the so-called "rotation measure map" (or Faraday depth map), is shown in Fig. 9.17 (right panel).

We extracted the location of the peak in the Faraday depth ($\phi_{\rm peak}$) for all compact sources within 0.5° radius of the cluster. In total for 17 sources we find an outlier-resistant mean of $+11.7 \pm 3.0$ rad m^{-2}, clipping values more than two standard deviations away from the median, with the uncertainty the standard deviation of the mean of the $\phi_{\rm peak}$ distribution. This is in agreement with the value of 11 rad m^{-2} from Taylor et al. (2009) derived from NVSS data measured over scales of 8°. The $\left|\tilde{F}(\phi)\right|$ spectra for seven compact sources are displayed in Fig. 9.18 (left panel).

For the relic, $\phi_{\rm peak}$ values vary spatially from about -53 to $+55$ rad m^{-2}. For B3, $\phi_{\rm peak}$ is about 10 rad m^{-2}, similar to the compact sources in the field. For B2, we find a strong gradient from -10 to $+55$ rad m^{-2} from east to west. For B1, $\phi_{\rm peak}$ varies between -10 and -53 rad m^{-2}. The "clean component" spectra are clearly resolved, see Fig. 9.18 (right panel).

Interestingly, the $\phi_{\rm peak}$ values for B1 and B2 deviate from the average galactic foreground of $+11.7 \pm 3.0$ rad m^{-2}, indicating that some of the Faraday rotation is probably caused by the ICM. The $\phi_{\rm peak}$ value for B3 indicates it is located in the cluster outskirts and the line of sight towards it does not pass deep into the ICM. B2 and B1 seem to be located progressively deeper into the ICM of the cluster (or more behind it) given the larger $\phi_{\rm peak}$ deviation from the galactic foreground. Although the number of counts is low in the ROSAT image (Fig. 9.3), it is indeed expected that $\int_{\rm source}^{\rm telescope} n_{\rm e}\, dr$ increases from B3, B2, to B1.

9.6.3 The depolarization properties of the radio relic

Our observations show a significant decrease in the polarization fraction towards lower frequencies. There are several factors that can cause such an effect. We rule out the effect of bandwidth depolarization, as the frequency resolution of the observations is sufficient to detected polarized emission with a Faraday depth $> 10^4$ rad m^{-2} using RM-synthesis. A second possibility is beam depolarization due to multiple RM components within the beam (spatially varying). These different RM components can be caused by variations of the magnetic field and/or electron density. The spatially averaged polarization fraction over B1 and B2 is about 13% at 4.9 GHz, 1.6% at 1714 MHz cm and $< 1\%$ at 1382 and 1221 MHz. We excluded B3 from the analysis because the SNR is too low at 4.9 GHz due to the primary beam attenuation.

Two types of depolarization, *internal* and *external*, have been identified (Burn 1966; Tribble 1991). Internal depolarization takes place within the radio source itself, while external depolarization takes place in a medium between the source and the observer, e.g., the ICM or magnetized plasma from our own galaxy. A simple case of internal depolarization is for a uniform

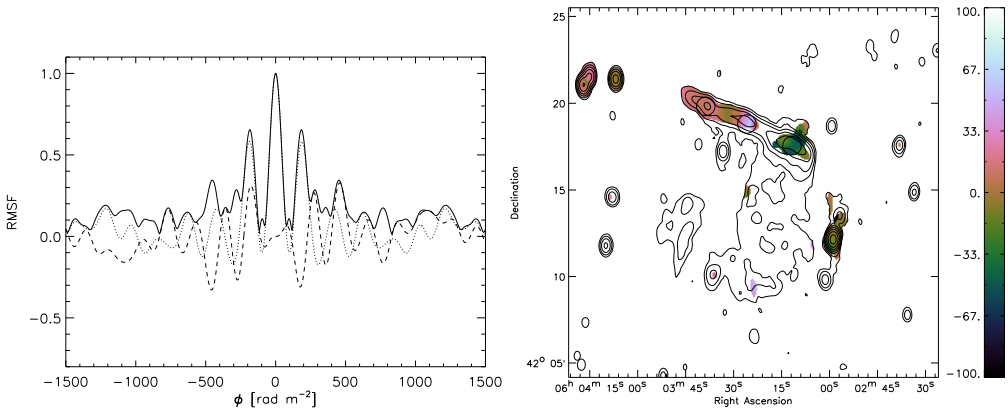

Figure 9.17: Left: RMSF from the 25, 21, 18 cm bands WSRT data. The solid line is the overall amplitude of the complex RMSF. Dotted line depicts the Real part of the RMSF and the dashed line the Imaginary part. The FWHM of the RMSF is 88 rad m^{-2}. Right: Faraday depth value of the peak in $F(\phi)$. Contours are from the WSRT 1382 MHz image and drawn at levels of $[1, 3, 9, 27, \ldots] \times 0.225$ mJy beam^{-1}.

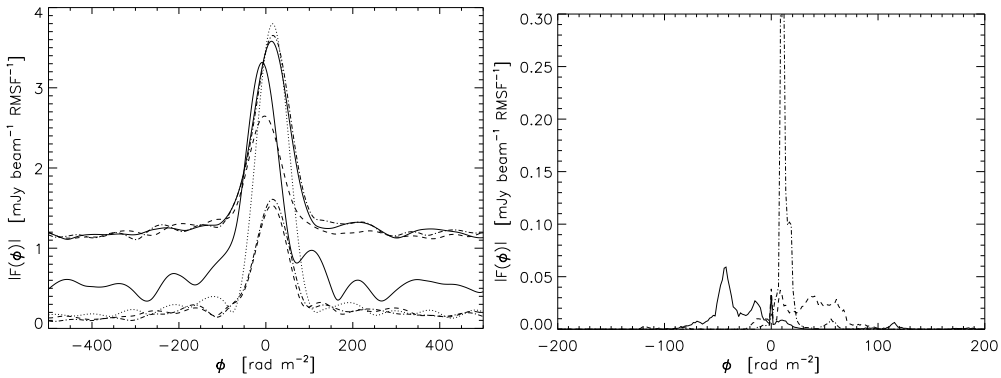

Figure 9.18: Left: Gaussian restored $|F(\phi)|$ spectra of compact sources. B3 0559+422A solid line, NVSS J060231+422811 (west component) dashed line, NVSS J060231+422811 (east component) dash-dotted line, and NVSS J060206+422045 dotted line, NVSS J060406+422125 dashed line (1 mJy beam^{-1} RMSF^{-1} offset), NVSS J060416+422110 (south component) solid line (offset), NVSS J060416+422110 (north component) dashed-dotted line (offset). The high “residuals” for B3 0559+422A are an artifact due to remaining calibration errors. Right: $|F(\phi)|$ spectra, consisting of clean components, extracted at three different positions from relic B. The positions are indicated by the circles drawn in Fig. 9.17 (right panel). Dash-dotted line: position B3, dashed line: position B2, and solid line: position B1 (see also Fig. 9.3).

magnetic field and electron density within the source. In this slab model (Burn 1966), the fractional polarization as function of λ^2 is given by a sinc-function. From this, the extent in Faraday depth of the source can be estimated. Observations indicate that the uniform slab model does not fit the data for the radio relics in A2256 and the Coma cluster (Brentjens 2008; Pizzo 2010).

For B1 and B2 there is a clear trend of depolarization towards higher λ^2. The only way to get depolarization as a function of wavelength is to have multiple RM components within the beam, either across it or along it – external –, or mixed with the synchrotron emitting plasma – internal. Therefore, the Faraday spectrum must be resolved wherever there is depolarization. In practice, because of the finite width of the RMSF, it may not always be possible to see these multiple RM components, even though they are depolarizing. In the case of B1 and B2, the spectra are indeed clearly resolved, consistent with the high amount of depolarization found for these regions. It cannot be directly determined whether this is due to beam depolarization (spatially varying RM components) or due to multiple RM components along the line of sight. In the first case, the depolarization should vanish when going to high enough spatial resolution. The fact that the RM varies spatially from beam to beam across B1 and B2 makes it very likely that at least a significant part of the depolarization is indeed caused beam depolarization.

The trend from east to west over the relic of (i) a larger $\phi_{\rm peak}$ deviation from the galactic foreground, and (ii) an increasing depolarization towards higher λ^2, suggest that most of the depolarization is probably due to the ICM of the cluster itself and not due to internal depolarization.

9.7 Discussion

The complex diffuse radio emission and extended X-ray emission give strong support for the fact that the cluster is currently undergoing a merger event. There are however a few puzzling aspects to the diffuse emission in this cluster. The linear extension of relic B to the east is quite peculiar. Usually shock surfaces are curved and not very linear over distances of more than a Mpc (e.g., Hoeft et al. 2008; Battaglia et al. 2009; Vazza et al. 2009; Skillman et al. 2011). The ongoing merger event for 1RXS J0603.3+4214 is probably more complex than the "simple" binary merger events that are thought to give rise to symmetric double radio relics (e.g., Roettiger et al. 1999a; van Weeren et al. 2011a). Deep X-ray observations will be needed to investigate whether the relic is indeed associated with such a linear shock front.

Relic E could also trace a shock wave with DSA, given its large extent and relatively flat integrated spectral index. The nature of relic D remains unclear, its small size and morphology would suggest a radio phoenix scenario, but the integrated spectral index of -1.10 ± 0.05 is not consistent with this interpretation. Higher-resolution observations ($\sim 1''$) would be helpful to better delineate the morphology.

An interesting point is the relation between relic B and the radio halo C. The radio halo is located directly south of B1, the brightest part of relic B. The halo and relic are connected by a region with $\alpha \lesssim -2$, but then the spectral index flattens to $\alpha \sim -1.2$ and increases a bit towards the center of the halo. We speculate that relativistic particles, previously accelerated at the shock front, are re-accelerated due to merger induced turbulence and then form the radio halo. Another interesting feature of the halo is the increased surface brightness at its southern end. Why does the surface brightness increase here? For a binary cluster merger event one expects two shock waves to form traveling diametrically outwards (e.g., Roettiger et al. 1999a).

If relic B traces the main shock wave one could also expect a second shock waves at the south side of the cluster center. This could be the region of increased surface brightness at the southern end of C. Although, this remains somewhat speculative, also because the merger event seems to be complex given the peculiar linear extension of relic B. X-ray observations could reveal whether the south part of radio halo C is associated with a shocked region with a higher ICM temperature.

There is also a possibility that source C is not a radio halo, but another relic seen close to face-on, because the surface brightness does not clearly peak at the location of the ROSAT X-ray peak. However, the radio power of source C is in agreement with the $L_{\rm X}$–$P_{1.4\rm GHz}$ correlation. Also, the brightness distribution over C is regular and quite smooth, which argues against a relic interpretation. Relics are often composed of smaller filamentary structures (e.g., Clarke & Ensslin 2006). We note that source C is somewhat similar to the diffuse emission seen between the relics in CIZA J2242.8+5301 (van Weeren et al. 2010).

9.7.1 Relic spectra

The analysis of the radio spectra for radio relic B are consistent with the existence a two global spectral shapes, one that describes the spectrum for the east part and one for the west part. This because it is possible to line up all radio spectra onto a single shape with shifts along $\log(I)$ and $\log(\nu)$.

The spectral shapes of the west (B1) and east (B2+B3) regions only differ in regions in the spectral index map with $\alpha \lesssim -1.4$ (e.g., see Fig. 9.13). At the front part of the relic we find power-law radio spectra, consistent with an injection spectral index of -0.6 to -0.7. The injection spectral index is also consistent with the total integrated spectral index of -1.1, i.e., the integrated spectral index should be -0.5 units steeper than the injection spectral index (e.g., Miniati 2002; Bagchi et al. 2002) for a simple shock model (with the properties of the shock not changing over time). We also find that the shape of the radio spectra are mostly governed by the effects of spectral ageing, by looking at the shifts made to align up all individual spectra to the global spectral shape (see Sect. 9.5.4.1). Changes in the magnetic field, total electron content, or electron energy (except energy changes due to ageing) do not seem to play a major role.

The observed radio spectra are not consistent with a JP model (which consists of a single burst of injection and spectral ageing). Instead, we find that the KGJP model, which consist of a sum of individual JP spectra with different amounts of ageing, provides a good match to the spectrum of the east part of the relic. This can be thought of as mixing of emission, most likely because of projection effects. For the west part of the relic (in the regions with the steepest spectral index), we find deviations from the KGJP model. We speculate that additional mixing of emission takes place here, or the spectra are contaminated by the emission from radio halo C (although we attempted to subtract this emission).

The KGJP spectra indicate that (1) at the front of the relic we see freshly injected radio plasma, giving a power-law spectrum. Little mixing of emission takes place here. (2) For the middle part of the relic (the region $-0.9 \lesssim \alpha \lesssim -1.1$ from the spectral index map), we observe a mix of radio aged radio plasma and freshly injected radio plasma. For the back part of the relic (the region with $\alpha \lesssim -1.1$), we see a mix of aged radio plasma, but no freshly injected plasma.

Mixing of emission thus seems to be an important factor determining the spectral shape. This suppresses spectral curvature and pushes back the radio spectra to power-law shapes. It is therefore crucial that this effect is considered. The lack of spectral curvature does therefore not

directly imply spectral ageing is not important.

An injection spectral index of −0.6 in combination with DSA, implicates a Mach number of 4.5, surprisingly high. These Mach numbers are rarely seen in simulations of cluster mergers. Instead of DSA, another possibility is shock re-acceleration of fossil electrons. In practice, these radio spectra will probably be indistinguishable from DSA (Markevitch et al. 2005).

9.7.2 Alternative models to explain the relativistic electrons from the radio relic

An alternative explanation for radio relics, based on a secondary cosmic ray electron model, has been proposed by Keshet (2010). This model predicts a spectral index of −1 at the front of the relic. We do not observe this, although there is a hint of a steeper spectral index at the front of B1 at some places in the 325–610 MHz spectral index map. However, this could be an artifact, as edge pixels is the spectral index map are not reliable. Also these steeper regions are smaller than the beam size. We do not find indications of magnetic field changes across the relic from the shifts needed to align up the spectra from individual regions. On the other hand, in the images we see a morphological connection between the radio relic and halo, these halo-relic "bridges" are included in the model from Keshet (2010).

Enßlin & Gopal-Krishna (2001) and Enßlin & Brüggen (2002) proposed that (some) radio relics could be the result of adiabatically compressed fossil radio plasma due to a shock wave. This could boost the radio luminosity by about two orders of magnitude. The question is whether the large relic in 1RXS J0603.3+4214 can be explained in this way. The model of Enßlin & Gopal-Krishna (2001) consist of five phases: (1) injection by a radio galaxy, (2) expansion of the radio cocoon, during this phase the cocoon becomes undetectable, (3) the "lurking"-phase, when pressure equilibrium is reached and the volume of the cocoon remains constant. Due to significant adiabatic losses most of the electrons reside at low energies which reduces the radiation losses. The losses can be further reduced by a low-magnetic field. (4) Adiabatic compression of the cocoon, the radio emission is boosted so it becomes visible again and the break frequency moves upwards. (5) The radio emission fades away due to synchrotron and IC losses.

In the case of 1RXS J0603.3+4214, the fossil plasma should be quite old ($\gtrsim$ 1 Gyr) as it takes a considerable amount of time for a radio galaxy to move over a distance of 2 Mpc and dump the radio plasma. The change in the break frequency from the adiabatic compression is (Giacintucci et al. 2008)

$$\frac{\nu_{\rm brk}^{\rm after}}{\nu_{\rm brk}^{\rm before}} \approx \frac{5\mathcal{M}^2 - 1}{4} \,. \tag{9.14}$$

Adopting a reasonable value of $\nu_{\rm brk}^{\rm before} = 50$ MHz for 1 Gyr old fossil radio plasma (e.g., Enßlin & Gopal-Krishna 2001), we would need a $\mathcal{M} > 8$ shock to push $\nu_{\rm brk}^{\rm after}$ above 4 GHz. For more realistic Mach numbers of $\mathcal{M} \lesssim 4$ we should thus observe steep and curved radio spectra. This contradicts the flat spectral indices of $\alpha = -0.6$ we find and the straight power-law integrated radio spectrum.

Only in the unlikely scenario that the plasma is about 0.1 Gyr old, before it is compressed by the shock, the break frequency could be pushed up to a few GHz. We also note that to produce a spectral index gradient a high mass load is required, which would allow the shock wave to successively compress the radio plasma. In the case of a high mass load due to undetectable

cool gas, a shock forms and the adiabatic gains are restricted due to the limited compression factor of such a shock wave (Enßlin & Gopal-Krishna 2001).

9.7.3 Magnetic field

The RM for the west part of the main relic (B1) deviates from the foreground RM, determined from compact sources in the field around the cluster. This suggests that the west part of the relic is located deeper into the ICM, also consistent with the higher amount of depolarization found for that part of the relic. A constant magnetic field of 1 μGauss, $n_e = 1 \times 10^{-4}$ cm^{-3} and a path length 500 kpc, will give a Faraday depth of about 40 rad m^{-2}. The observed difference of about 60 rad m^{-2}, compared to the galactic foreground value, suggests a relatively high magnetic field ($B \gtrsim 1$ μGauss). Also because the magnetic field topology is likely more complex, i.e., the magnetic field could have reversals along the line of sight.

We estimate the magnetic field at the front of relic B1 by assuming minimum energy densities in the relics (e.g., Govoni & Feretti 2004) and using the same procedure as described in van Weeren et al. (2009b). We take $k = 100$, i.e, the ratio of energy in relativistic protons to that in electrons, 250 kpc for the depth (d) along the line of sight, a spectral index of -0.6, and a surface brightness of 0.205 mJy arcsec^{-2} at 610 MHz. We use low and high energy cutoffs ($\gamma_{\rm min}$ and $\gamma_{\rm max}$, with $\gamma_{\rm min} \ll \gamma_{\rm max}$) instead of low and high frequency cutoffs (Beck & Krause 2005; Brunetti et al. 1997), giving the so-called “revised” equipartition magnetic strength ($B'_{\rm eq}$). For $\gamma_{\rm min} = 100$ this gives $B'_{\rm eq} = 9.2$ μGauss. If we take $\gamma_{\rm min} = 5000$ we get $B'_{\rm eq} = 7.4$ μGauss. The revised equipartition magnetic field strength scales with $(1 + k)^{1/(3-\alpha)}$.

The polarization and equipartition results indicate a relatively high magnetic field strength. These relatively high values have also been found for other relics by Finoguenov et al. (2010); van Weeren et al. (2010) using limits on the IC X-ray emission or modeling the relic’s brightness profile.

9.8 Conclusions

We presented detailed GMRT and WSRT radio observations of a newly discovered cluster of galaxies at $z = 0.225$. We find the cluster to host three radio relics and also a giant ~ 2 Mpc radio halo. The radio power follows the $L_{\rm X}$–$P_{1.4\rm GHz}$ correlation for giant radio halos. The extended X-ray emission and complex diffuse radio emission indicate we are witnessing an ongoing cluster merger event.

The WSRT observations reveal that the front of the relic is highly polarized, with a polarization fraction of up to $\sim 60\%$ at 4.9 GHz. At lower frequencies (in the L-band), the polarization fraction drops considerably, as has been seen for other well studies relics, e.g., in A2256 (Brentjens 2008) and A2255 (Pizzo et al. 2011). The observed depolarization and Faraday depth suggest that the west part of the main relic is located deeper into the ICM of the cluster. Using equipartition argument we find a high magnetic field strength of about 7–9 μGauss for the bright relic.

For the radio halo we find a spectral index of $\alpha = -1.15 \pm 0.06$. The spectrum for the bright radio relic is a power-law between 74 MHz and 4.9 GHz with $\alpha = -1.10 \pm 0.02$. If this relic traces a shock, where particles are accelerated by the DSA mechanism, then the injection spectral index of -0.6 would imply a Mach number of 4.5. The spectral index steepens systematically across

the width of the relic from about -0.6 to ~ -2. For the bright western part of the relic we can trace the spectral steepening to $\alpha < -2.5$. The radio spectrum at the front of the relic has a power-law shape with $\alpha = -0.6$ to -0.7, while the amounts of spectral curvature increases gradually towards the back of the relic.

We analyzed the radio spectra making use of color-color and shift diagrams (Katz-Stone et al. 1993; Katz-Stone & Rudnick 1994) and divided the relic into an eastern and western part. Both parts were further divided into smaller regions based on the spectral index map in Fig. 9.9 (left panel). We found that the individual radio spectra in each region could all be lined up. This implies the existence of a single global electron energy distribtuion. The shifts needed to align up the individual spectra, indicate that spectral ageing is the dominant factor explaining the changes in the spectra from one region to another. Changes in the magnetic field, total number of electrons, or adiabatic expansion/compression do not seem to be important.

In addition, we find evidence for mixing of radio emission with different amounts of spectral ageing within the beam. The amount of mixing increases away from the front of the relic. A so-called KGJP model (see Sect. 9.5.1), which can be thought of as a mix of spectra with different ages, describes the global spectral shape for the east part of the relic. For the west part of the relic, in particular the region with the steepest spectral index, we find a small deviation from this shape, possibly because the amount of mixing increases here.

The effects of spectral curvature are suppressed by mixing and this pushes the radio spectra closer towards power-law shapes. This means that if a spectral index gradient is seen, but no spectral curvature (or only very little), this does not necessarily imply that the spectral index gradient is not related to spectral ageing.

We conclude that the color-color and shift diagrams provide a powerful tool to constrain physical conditions that shape the radio spectra. In the future we plan (i) to expand the color-color analyses to smaller regions, by obtaining higher resolution maps, (ii) increase the frequency range to < 150 MHz or > 3 GHz, and (iii) apply the technique to other radio relics and halos.

For the origin of the relativistic electrons (in the bright relic), the results favor a scenario where particles are accelerated or re-accelerated in a shock. Surprising and somewhat puzzling is the high Mach number of 4.5, shocks with these Mach numbers in cluster are rare. A crucial test would be the to measure the Mach number directly from the jump conditions and compare this with $\alpha_{\rm inj}$. Deep X-ray observations of this cluster will also be needed to constrain the merger scenario and determine the dynamical state of the cluster.

Acknowledgements. We thank the staff of the GMRT who have made these observations possible. The GMRT is run by the National Centre for Radio Astrophysics of the Tata Institute of Fundamental Research. The Westerbork Synthesis Radio Telescope is operated by ASTRON (Netherlands Institute for Radio Astronomy) with support from the Netherlands Foundation for Scientific Research (NWO). The National Radio Astronomy Observatory is a facility of the National Science Foundation operated under cooperative agreement by Associated Universities, Inc. The William Herschel Telescope are operated on the island of La Palma by the Isaac Newton Group in the Spanish Observatorio del Roque de los Muchachos of the Instituto de Astrofísica de Canarias.

This publication makes use of data products from the Two Micron All Sky Survey, which is a joint project of the University of Massachusetts and the Infrared Processing and Analysis Center/California Institute of Technology, funded by the National Aeronautics and Space Administration and the National Science Foundation.

RJvW acknowledges funding from the Royal Netherlands Academy of Arts and Sciences. MB and MH acknowledges support by the research group FOR 1254 funded by the Deutsche Forschungsgemeinschaft.

LR acknowledges support from the U.S. National Science Foundation, under grant AST0908668 to the University of Minnesota. RJvW would like to thank C. Pfrommer for discussions and G. Heald for his explanation of the `RM-CLEAN` algorithm.

CHAPTER 10

Using double radio relics to constrain galaxy cluster mergers: A model of double radio relics in CIZA J2242.8+5301

Abstract. Galaxy clusters grow by mergers with other clusters and galaxy groups. These mergers create shock waves within the intracluster medium (ICM) that can accelerate particles to extreme energies. In the presence of magnetic fields, relativistic electrons form large regions emitting synchrotron radiation, so-called radio relics. Behind the shock front, synchrotron and inverse Compton (IC) losses cause the radio spectral index to steepen away from the shock front. In a binary cluster merger, two shock waves are generated which move diametrically outwards along the merger axis. Two radio relics can then form on both sides of the cluster center. An example of such a cluster is CIZA J2242.8+5301, where very clear spectral steepening in the downstream region is observed. The main relic has a total extent of 1700 kpc, while its width is only 55 kpc. Together with the high observed polarization fraction, this implies the relic is seen very close to edge-on which makes it easier to constrain the merger geometry. Here we present hydrodynamical simulations of idealized binary cluster mergers with the aim of constraining the merger scenario for this cluster. From our simulations, we find that CIZA J2242.8+5301 is probably undergoing a merger in the plane of the sky (less then 10° from edge-on) with a mass ratio ($M_1 : M_2$) of about 2 : 1, and an impact parameter $\lesssim$ 400 kpc. We find that the core passage of the clusters happened about 1 Gyr ago. We conclude that double relics relics can set constraints on the mass ratios, impact parameters, timescales, and viewing geometry of binary cluster mergers, which is particularly useful when detailed X-ray observations are not available. In addition, the presence of large radio relics can be used to constrain the degree of clumping in the outskirts of the ICM, which is important to constrain the baryon fraction, density and entropy profiles, around the virial radius and beyond. We find that the amplitude of density fluctuations, with sizes of $\lesssim$ 200 kpc, in the relic in CIZA J2242.8+5301 is not larger than 30%.

R. J. van Weeren, M. Brüggen, H. J. A. Röttgering and M. Hoeft
Monthly Notices of the Royal Astronomical Society, 2011, in press

10.1 Introduction

Radio relics are diffuse, steep-spectrum radio sources found in merging galaxy clusters. They have been divided into three groups (Kempner et al. 2004): radio gischt, radio phoenix and AGN relics. Here we will only be concerned with so-called *radio gischt* relics, these are elongated arc-like radio sources with sizes of up to 2 Mpc (e.g., Ensslin et al. 1998). They are mostly found in the outskirts of galaxy clusters. Recent observations have given support to the hypothesis that they trace shock fronts in which particles are accelerated via the diffusive shock acceleration mechanism (DSA; Krymskii 1977; Axford et al. 1977; Bell 1978a,b; Blandford & Ostriker 1978; Drury 1983; Blandford & Eichler 1987; Jones & Ellison 1991; Malkov & O'C Drury 2001).

A particularly interesting "class" of radio gischt are the so-called double-relics. In this case two relics are diametrically located on both sides of the cluster center (e.g., Bonafede et al. 2009b; van Weeren et al. 2009b; Venturi et al. 2007; Bagchi et al. 2006; Röttgering et al. 1997; van Weeren et al. 2010; Brown et al. 2011; van Weeren et al. 2011c; Bagchi et al. 2011). These double relics are very rare, with only about ten known so far. However, most of them were found in the last few years suggesting that more of them await discovery, especially with future deep radio surveys. Large cosmological simulations that include radio emission from shocks, also indicate that double radio relics are more common (e.g., Skillman et al. 2011; Battaglia et al. 2009; Hoeft et al. 2008).

Double radio relics are thought to trace outward moving shock waves from a binary cluster merger, which develop after core passage of the two subclusters. In the DSA scenario, synchrotron and IC losses cool the particles at the back of the shock front. If the relics are seen roughly edge-on this creates a radio spectral index gradient towards the cluster center. The line connecting the two relics should represent the (projected) merger axis of the system. Thus, double relics in principle can be used to set constraints on the merger timescale, mass ratio, impact parameter and viewing angle.

An example of a cluster hosting a double radio relic is CIZA J2242.8+5301 (van Weeren et al. 2010). The cluster is located at $z = 0.1921$ and has an X-ray luminosity of 6.8×10^{44} ergs^{-1}, between 0.1 and 2.4 keV (Kocevski et al. 2007). With this X-ray luminosity the total mass of the cluster is roughly 5.5×10^{14}M$_\odot$ (Pratt et al. 2009). In van Weeren et al. (2010) we presented Westerbork Synthesis Radio Telescope (WSRT) and Metrewave Radio Telescope (GMRT) observations of this cluster that showed the presence of an impressive double relic system. In the north of the cluster, a large radio relic is found with a total extent of 1700 kpc (we did not include the patch of emission at RA $22^{\rm h}\ 42^{\rm m}\ 20^{\rm s}$, Dec $+53^\circ\ 08'\ 45''$). To the south of the cluster center a second fainter relic is found with an extent of 1450 kpc. The relics are located along the major axis of the elongated X-ray emission from the ICM, while the relics themselves are orientated perpendicular to this axis. This configuration is expected for a "clean" (i.e., a merger event without much substructure) binary merger event in which shock waves are propagating diametrically outwards to the north and south. Within the shock particles are proposed to be accelerated by DSA. The relics are separated by a distance of 2.8 Mpc. The northern relic is strongly polarized at 4.9 GHz, with a polarisation fraction of $\sim 50\%$. The polarization magnetic field vectors (corrected for the effect of Faraday rotation) are parallel to the major axis of the relic. The magnetic fields are thus mainly orientated within the plane of the shock wave and the relic must be seen close to edge-on (Ensslin et al. 1998). We also observe clear steepening of the radio spectrum (with the spectral index changing from $-0.6 \sim -0.8$ to more than -2.0 between

0.61 and 2.3 GHz) in the direction of the cluster center, across the width of the relic. Between the two relics additional diffuse emission is found, which is also seen in a deep 150 MHz GMRT image (van Weeren et al. 2011d).

However, there are still quite a few puzzles that surround radio relics, such as:

- Which processes accelerate electrons so efficiently at relatively low Mach number ($M \sim 2-4$) shocks?
- What produces the magnetic fields inside relics?
- Why do some relics have very sharp edges while others appear very fuzzy?
- Under which conditions do relics form? When do we see single and when double relics?

Many of these questions touch physical processes that are poorly understood, such as diffusive shock acceleration and magnetogenesis in collisionless shocks, and relate to regions of the cosmos of which we know very little. At the same time, outskirts of galaxy clusters have attracted considerable interest for cosmology as they are governed primarily by simple gas physics and gravity and much less by complicated processes such as radiative cooling, star formation and AGN feedback. However, information about the periphery of galaxy clusters is scarce. Recent X-ray observations with Suzaku have measured surface brightness profiles out to the virial radius for a number of nearby clusters (Bautz et al. 2009; George et al. 2009; Reiprich et al. 2009; Hoshino et al. 2010; Simionescu et al. 2011). The results indicate significant deviations from extrapolated profiles of the gas mass fraction which are explained by an increased clumpiness of the ICM that occurs on scales of several 100 kpc or smaller. As the cluster outskirts are difficult to access via X-ray observations owing to the low surface brightness at large cluster-centric radii, important information may be derived from radio relics which illuminate the outskirts of merging galaxy clusters.

In this paper we will describe simulations with the aim of reconstructing the merger event of the cluster CIZA J2242.8+5301. In particular we will focus on the mass ratio and impact parameter of the merger and how they can be constrained from the observations and simulations. We further attempt to infer properties of the ICM at distances beyond the virial radius from the observed features of the radio relics, such as the morphology of the emission.

In Sect. 10.2 we will shortly discuss previous work on idealized models of cluster mergers, and in Sect. 10.3 we describe the method and adopted initial conditions. This is followed the results in Sects. 10.4 and 10.5. We end with a discussion and summary in Sects. 10.6 and 10.7.

10.2 Overview: Simulations of galaxy cluster mergers

Numerical simulations of idealized binary galaxy cluster mergers were performed by Roettiger et al. (1993); Schindler & Mueller (1993); Burns et al. (1994b); Pearce et al. (1994); Roettiger et al. (1997); Ricker (1998); Roettiger & Flores (2000); Ricker & Sarazin (2001).

Roettiger et al. (1993) simulated a head-on merger with a mass ratio of 8. The clusters were modeled as King-spheres. They used a hybrid Hydro/N-body code, simulating the hydrodynamical component with the ZEUS-3D code on a nonuniform grid, and the N-body component with the Hernquist treecode (Hernquist 1987). Their simulation showed the development of a single shock that reached a Mach number ($\mathcal{M}$) of more than 4. In addition the core of the main

cluster was heated to 3×10^8 K. The simulated X-ray surface brightness was double peaked and elongated parallel to the merger axis. Burns et al. (1994b) simulated the collision between the Coma cluster and the NGC 4839 galaxy group using the same code as described by Roettiger et al. (1993).

Schindler & Mueller (1993) simulated collisions of clusters using a uniform grid-PPM (piecewise-parabolic method) code for the gas dynamics, while an N-body code was used for the collisionless component consisting of dark matter and galaxies. They showed the development of outward propagating shock waves generated during the collisions between subclusters.

None of the works mentioned above included the baryonic contribution to the gravitational potential. Head-on equal mass collisions between clusters were simulated by Pearce et al. (1994) using smoothed-particle hydrodynamics (SPH), including both baryons and dark matter. Roettiger et al. (1997) used a PPM/particle-mesh code to simulate a collision intended to resemble the cluster Abell 754. Roettiger et al. (1999b) presented the first three-dimensional numerical magnetohydrodynamical (MHD) simulations of the magnetic field evolution in merging clusters of galaxies, which they subsequently applied to model the double radio relics in Abell 3367 (Roettiger et al. 1999a). They concluded that the radio structures arise from a slightly off-axis merger that occurred nearly in the plane of the sky approximately 1 Gyr ago, with the subcluster having a total mass of 20% of the primary cluster. Roettiger & Flores (2000) also modeled the X-ray substructure seen in Abell 3266 as an off-axis merger with a mass ratio of 2.5 : 1.

Ricker (1998) simulated off-center collisions of equal mass clusters using a PPM code and an isolated multigrid potential solver. They simulated off-center collisions with 0, 5, and 10 times the cluster core radius and studied how the virialisation time, X-ray luminosity, and structure of the merger depended on the impact parameter of the collision. They found that the increase in X-ray luminosity due to the merger depends on the impact parameter of the collision. Ritchie & Thomas (2002) also reported that mergers can lead to large increases in bolometric X-ray luminosities and emission-weighted temperatures. Cool cores are completely disrupted by equal mass head-on mergers, while for mergers with mass ratios of 8 : 1 the cooling flow restarts within a few Gyr. For mergers with impact parameters of 500 kpc the cool-core is not disrupted. Ricker & Sarazin (2001) investigated cluster collisions, varying both the mass ratio and impact parameters. They found that merger events created large-scale turbulent motions with eddy sizes up to several hundred kiloparsecs.

FLASH (Fryxell et al. 2000) high-resolution N-body/hydrodynamics simulations have been carried out by Zu Hone et al. (2009) to model the cluster Cl 0024+17, a proposed merger of two clusters, with the interaction occurring along our line of sight. Also, gas sloshing initiated by mergers with subclusters, and the effects of mergers on the entropy of the ICM were investigated by ZuHone et al. (2010); ZuHone (2011). Various simulations of cluster merger were also presented by Takizawa (1999, 2000); Takizawa & Naito (2000); Takizawa (2008). In Takizawa (2008) N-body + magnetohydrodynamical simulations were performed from which is was found that cluster mergers cause various characteristic magnetic field structures. The magnetic field component perpendicular to the collision axis is amplified by the merger which results in a cool region wrapped by field lines. McCarthy et al. (2007) focussed on the generation of entropy during cluster mergers and Akahori & Yoshikawa (2010) investigated how the ionization equilibrium state is affected by cluster mergers. They report that the ICM significantly departs from the ionization equilibrium state at the location of shocks.

Poole et al. (2006) carried out a suite of SPH simulations of merger of clusters whose initial conditions resembled relaxed cool core clusters. They investigated the efficacy of (i) centroid

variance, (ii) power ratios, and (iii) X-ray surface brightness/projected mass displacement to quantify the degree to which observed clusters are disturbed. From this it was found that the centroid variance gives the best measure of the state of clusters and how far they are from virial and hydrostatic equilibrium.

Cluster mergers can decouple the baryonic matter component from the dark matter (DM) which causes and offset between the gravitational center (measured from lensing) and X-ray center of the cluster. This was first observed for the "Bullet cluster" (1E0657−56, Clowe et al. 2006). Springel & Farrar (2007) presented hydrodynamical models of galaxy cluster mergers to reproduce the dynamical state and mass models (from gravitational lensing) of the "Bullet" cluster (1E0657−56). They showed that the size of the spatial offset between the baryonic peak and mass is quite sensitive to the structural details of the merging systems. This offset was earlier also found in numerical models by Takizawa (2006). Mastropietro & Burkert (2008) presented detailed N-body/SPH simulations of the system. They found that the X-ray morphology is best simulated with a mass ratio of 6 : 1 and an impact parameter of 150 kpc.

10.3 Numerical method

We used the FLASH 3.2 framework (Fryxell et al. 2000) for the simulations which includes standard hydrodynamics and gravity. We did not include the effects of radiative cooling, as this is not very relevant for the spatial and temporal time scales considered here. Furthermore, the hydrogen number density was assumed to be related to the electron number density as $n_{\rm H} = 0.6 n_{\rm e}$. We chose outflow boundary conditions. We simulated a box with a size of $5 \times 5 \times 5$ Mpc. A maximum of 6 refinement levels are allowed, resulting in a maximum resolution of 3.25 kpc. The minimum refinement level was set to 3 giving a resolution of 26 kpc. The simulations were run at this relatively low-resolution in order to study a larger range of merger parameters.

For the gravitational potential of each subcluster we assume hydrostatic equilibrium and spherical symmetry,

$$\frac{d\phi}{dr} = \frac{k_{\rm B}}{\mu m_{\rm H}} \left[\frac{T(r)}{\rho(r)} \frac{d\rho(r)}{d\log r} + \frac{dT(r)}{d\log r} \right] , \tag{10.1}$$

where $T(r)$ and $\rho(r)$ are the radial density and temperature profiles, $m_{\rm H}$ the hydrogen mass, and μ the mean molecular weight (we adopt $\mu = 0.6$). We move the center of the gravitational potential of the merging subcluster around the fixed potential of the main cluster, ignoring the interactions between the dark matter.

10.3.1 Radio emission from shocks

We use passive tracer particles in the simulations to model the radio emission. At the start of the simulation the particles are distributed proportional to the density throughout the complete computation volume. The advantage is that in this way each passive tracer particle represent roughly the same amount of mass which simplifies the normalization of the radio emission, as the contribution from every particle can be simply added up. For each tracer particle, 5 million in total, we record the position, velocity, density and temperature as a function of time, writing the results to disk every 30×10^6 yr. In order to create synthetic radio maps, we locate all particles that have passed through the shock waves in the simulation by looking at the variation of the temperature as function of time for each tracer particle. We define a particle to have

passed through a shock if the temperature between two successive outputs spaced 30×10^6 yr apart increases by more than a factor of 1.5 (no radio emission is generated below this number). For each particle that passes through the shock we then compute the Mach number ($\mathcal{M}$, using Rankine-Hugoniot jump conditions and adiabatic index $\gamma = 5/3$ (Landau & Lifshitz 1959), compression ratio, entropy ratio, and the time since it has passed through the shock. With these parameters we compute the synchrotron emission at a given frequency ν using the JP model (Jaffe & Perola 1973), taking into account the spectral ageing due to synchrotron and IC losses. We apply eq. 5 and 6 from Komissarov & Gubanov (1994) and use $t_0 = 0$, see also Kardashev (1962); Pacholczyk (1970).

The amount of synchrotron emission for each tracer particle is recorded. A radio map is then simply computed by integrating the radio emission from each tracer particle in the computational volume along a chosen line of sight.

We take $B_{\rm CMB} = 4.6\ \mu$Gauss the equivalent magnetic field strength of the CMB at $z = 0.1921$. To compute the radio emission the magnetic field is needed. Since we do not include magnetic fields in our simulation we adopt constant values for the magnetic field B. The spectra are then normalized using the method described by Hoeft & Brüggen (2007), which takes into account the efficiency of acceleration as function of Mach number. We start with a spectrum of suprathermal electrons with a power-law distribution $n(E) \propto E^{-s}$, with E the energy. The index s, with $s = 1-2\alpha_{\rm inj}$, and $\alpha_{\rm inj}$ the injection radio spectral index, depends only on the compression ratio (or Mach number), r, of the shock front:

$$s = \frac{r+2}{r-1} \tag{10.2}$$

and (e.g., Giacintucci et al. 2008)

$$\alpha_{\rm inj} = \frac{1}{2} - \frac{\mathcal{M}^2+1}{\mathcal{M}^2-1}\,. \tag{10.3}$$

We assume that a small fraction $\xi_{\rm e}$ of the thermal energy goes into the acceleration of electrons (Keshet et al. 2004). Furthermore, we take into account that the electrons can only be accelerated to a finite maximum energy ($E_{\rm max}$) (Keshet et al. 2003). The electron spectrum with a smoothed high-energy cut-off is then given by

$$\frac{{\rm d}n_{\rm e}}{{\rm d}E} = \begin{cases} n_{\rm e}\, C_{\rm spec}\, \frac{1}{m_{\rm e}c^2}\, \tilde{e}^{-s} \left\{1 - \frac{\tilde{e}}{\tilde{e}_{\rm max}}\right\}^{s-2} & : \quad \tilde{e} < \tilde{e}_{\rm max} \\ 0 & : \quad \text{elsewhere} \end{cases}, \tag{10.4}$$

where $\tilde{e} = E/m_{\rm e}c^2$. The normalization constant $C_{\rm spec}$ gives the fraction of electrons at $E = m_{\rm e}c^2$.

Following Hoeft & Brüggen (2007), we assume that the thermal Maxwell-Boltzmann distribution goes over continuously into the power-law spectrum of the suprathermal electrons. Hoeft & Brüggen (2007) show that the normalization of the electron spectrum is given by

$$C_{\rm spec} = \xi_e \frac{u_{\rm d}}{c^2} \frac{m_{\rm p}}{m_{\rm e}}\, \frac{(q-1)}{q} \frac{1}{I_{\rm spec}}, \tag{10.5}$$

where $u_{\rm d}$ is the downstream velocity, q the entropy ratio ($S_{\rm d}/S_{\rm u}$) across the shock, and

$$I_{\rm spec} = \int_{\tilde{e}_{\rm min}}^{\infty} {\rm d}\tilde{e}\ \tilde{e}^{1-s} \left\{1 - \frac{\tilde{e}}{\tilde{e}_{\rm max}}\right\}^{s-2}. \tag{10.6}$$

The minimum energy, $\tilde{e}_{\rm min} = E_{\rm min}/m_{\rm e}c^2$, is the energy above which electrons are considered to be suprathermal. This results is an implicit equation for $E_{\rm min}$ that has to be solved simultaneously with the normalization of the spectrum. We directly apply the code from Hoeft & Brüggen for this.

10.3.2 Initial conditions

For the initial conditions we start with two spherically symmetric (sub)clusters with masses M_1 and M_2 separated by a distance d. Subscript 1 always refers to the more massive cluster (i.e., $M_1 > M_2$). The density profiles of both subclusters are described by single β-models (Cavaliere & Fusco-Femiano 1976)

$$\rho(r) = \rho_0 \left[1 + \left(\frac{r}{r_{\rm c}}\right)^2\right]^{-\frac{3\beta}{2}} , \tag{10.7}$$

where ρ_0 the central density, $r_{\rm c}$ the core radius. We decided to fix β to $2/3$ (e.g., Böhringer et al. 2000) and $\rho_0 = 2 \times 10^{-26}$ g cm^{-3} (0.02 particles per cm^3) for both subclusters. This value for ρ_0 is roughly the average of the values found by Croston et al. (2008) for a sample of 31 clusters. They found that the central densities did not show any clear trend with the overall mass and temperature of the clusters.

We used the $M - T$ scaling relation from Mantz et al. (2010) to get the global average temperature from the cluster's mass.

$$T_{\rm avg} = 10^{0.88+0.48\log_{10}(M/10^{14}{\rm M}_\odot)}\ [{\rm keV}] \ . \tag{10.8}$$

For the radial temperature distribution we use a polytropic profile (e.g., Pratt & Arnaud 2002)

$$T(r) = T_{\rm avg}\tau\rho(r)^{\gamma_{\rm T}-1} \tag{10.9}$$

with $\tau = 1.1$ and $\gamma_{\rm T} = 1.2$ and $T_{\rm avg}$ given by Eq. 10.8. In addition we allow for a temperature drop in the center of the cluster to simulate a relaxed cool core cluster (e.g., Fabian et al. 1991; Peterson & Fabian 2006). The temperature decline is the central region is given by (Allen et al. 2001; Vikhlinin et al. 2006)

$$T_{\rm cool}(r) = \frac{x + T_{\rm min}/T_{\rm avg}}{x+1} \ , \ x = \left(\frac{r}{r_{\rm cool}}\right)^{a_{\rm cool}} , \tag{10.10}$$

where $T_{\rm min}/T_{\rm avg}$ is the relative temperature drop in the center, $r_{\rm cool}$ the radius of the cool core, and $a_{\rm cool}$ controls de rate of the temperature decrease. The final temperature model is given by

$$T_{\rm full}(r) = T(r)T_{\rm cool}(r) \ . \tag{10.11}$$

For the merger scenario we follow Sarazin (2002), where two subclusters merge at time $t_{\rm merge}$ (the age of the Universe at the time of the merger). The two clusters have a large initial separation, d_0. The value of d_0 does not strongly affect the merger because the infall velocity approaches free-fall from infinity. If we assume that the clusters dominate the mass in the region of the Universe they occupy

$$d_0 \approx 4.5 \left(\frac{M_1 + M_2}{10^{15}{\rm M}_\odot}\right)^{1/3} \left(\frac{t_{\rm merge}}{10^{10}\ {\rm yr}}\right)^{2/3} [{\rm Mpc}] \ . \tag{10.12}$$

For CIZA J2242.8+5301 ($z = 0.1921$) $t_{\rm merge}$ is 11.0 Gyr.

To speed up the simulations the centers of the two subclusters are placed at a distance $d = 2$ Mpc from each other. This we define as $t = 0$. The relative velocity between the clusters at that starting point is given by Sarazin (2002) as

$$v \approx 2930 \left(\frac{M_1 + M_2}{10^{15} \mathrm{M}_\odot} \frac{1 - \frac{d}{d_0}}{1 - \left(\frac{b}{d_0}\right)^2} \right)^{1/2} \left(\frac{d}{1\ \mathrm{Mpc}} \right)^{-1/2} \ [\mathrm{km\ s^{-1}}], \tag{10.13}$$

where b is the impact parameter of the collision. Using the starting location, initial velocities and masses of the subclusters we move the center of the gravitational potential of the merging subcluster (M_2) around the fixed potential of the "main" cluster (M_1), ignoring the interactions between the dark matter and treating the clusters as point masses. This fixes the subcluster's orbit around the main cluster. The point $(x, y, z) = (0, 0, 0)$ is defined by the center of mass of the system. The gravitational acceleration of the gas was then computed using Eq. 10.1.

To reconstruct the merger that gave rise to the double radio relic CIZA J2242.8+5301, we varied the mass ratio and impact parameter in the simulation. In the post-processing (to create the radio maps) we also varied the viewing angle. The total mass of the two (sub)clusters ($M_1 + M_2$) was kept constant to $5.5 \times 10^{14} \mathrm{M}_\odot$. The values for $r_{\rm c}$ are fixed by the total mass of the system and the required mass ratio (these are reported in Table 10.1). In Sect. 10.6 we will discuss the effect on the simulations if we take different values for β and $r_{\rm c}$. For the default runs we chose $T_{\rm min}/T_{\rm avg} = 1$, i.e., no temperature drop in the cluster center. In Sect. 10.4.1.5 we discuss the effect of including a central cool core to the most massive subcluster. For all runs we place the merger axis along the y-axis with the least massive cluster located at positive y-value and the initial velocity (given by Eq. 10.13 being in negative y-direction).

10.4 Results

The names and parameters for the different FLASH runs are given in Table 10.1. We start with a description of the basic hydrodynamical quantities (the density, temperature, and the velocity field) from the simulations. We will discuss the results for a merger with a mass ratio of 2 : 1 and zero impact parameter (R21b0; see Fig. 10.1), and for a merger with the same mass ratio but with an impact parameter of 4 ($4r_{\rm c,1}$; R21b4), see Fig. 10.2.

The R21b0 merger starts with the subcluster approaching the main cluster. Two shocks, with $\mathcal{M} \sim 1.15$ at $t = 600$ Myr, develop as the cores approach each other. After core passage, at $t = 1.25$ Gyr, a pair of stronger symmetrical shock waves form that travel diametrically outwards in front of the two subclusters. The shock waves increase in size as the time advances, although their Mach numbers decrease. At $t = 1.95$ Gyr the maximum Mach numbers are about 3.1 and 2.3 for the top and bottom shock waves, respectively. At $t = 2.28$ Gyr the two shock are separated by 2.8 Mpc, as is the case for the double relics in CIZA J2242.8+5301. The Mach numbers at this time have decreased to about 2.7 and 2.2, for the top and bottom relics, respectively. Thus, the most massive cluster with the largest core radius develops the largest (and slightly stronger) shock wave in front of it after core passage. The velocity field at $t = 2.3$ Gyr is shown in Fig. 10.3 (left panel).

Mergers with different mass ratios, ranging between 1 to 5, show a similar picture. The size and strength of the shock waves depend on the mass ratio (which in turn determines the core radii of the subclusters). In collisions with a larger mass ratio the shock waves in front of the less massive subcluster reduces in relative size and strength.

A 2 : 1 merger with an impact parameter of $b = 4r_{c,1}$ (R21b4) develops two asymmetric spiral-like shock waves, and again the two shocks have different sizes depending on the mass ratio used. The amount of asymmetry deepens on the impact parameter. The Mach numbers across these asymmetric shocks decrease more slowly on the left side of the merger axis. At $t = 2.1$ Gyr the maximum Mach number is about 2.9 and 2.2 for the top and bottom shock waves, respectively. This decreases to about 2.7 and 2.1 at $t = 2.4$ Gyr when the two shocks are separated by 2.8 Mpc. The velocity field at $t = 2.4$ Gyr is shown in Fig. 10.3 (right panel).

10.4.1 Radio maps

In this section we present the simulated radio maps for a range of mass ratios, impact parameters, viewing angles and radial density/temperature profiles, and compare them to the observed WSRT radio map at 1382 MHz. To create the radio maps, we integrated the radio emission from each tracer particle that passed through the shock along the line of sight. All radio maps are normalized to the peak flux in the simulated map and are smoothed with a 2-dimensional Gaussian of 50×40 kpc to match the resolution of the WSRT image. This smoothing is also needed as the radio emission is computed using a discrete number of particles with insufficient sampling to create images at the resolution of the hydro-grid. For making the radio maps, we assumed a constant magnetic field strength of $B = 5.0\,\mu$Gauss, see van Weeren et al. (2010).

It takes about 1.0 Gyr for the two relics to be separated by 2.8 Mpc after core passage. This number varies very little for mass ratios between 1.5:1 and 3:1. For impact parameters $b > 0$ kpc the time since cores passage only increases slightly to about 1.1 Gr for $b = 5r_{c,1}$ (e.g., Fig. 10.3). Therefore, the time since core passage does not depend much on the adopted initial conditions such as the mass ratio and impact parameter. However, the time since core passage will also depend on the adopted total mass of the system and on the temperature profile, since this affects the sound speed. Detailed X-ray observations would be helpful here to better constrain the total mass and measure the temperature profile.

10.4.1.1 Mass ratio

We varied the mass ratios for the collisions between 1 : 1 and 3 : 1. The mass ratio (which also set the core radii) affects the size of the two outwards moving shock waves after core passage. The resulting radio maps for mergers with four different mass ratios are displayed in Fig. 10.4 and the largest linear extent of the relics are listed in Table 10.2. The radio maps display a double relic system, with the front of the two relics tracing the shock waves. Towards the cluster center and the left/right edges of the relics, the surface brightness decreases. The size of the shock waves (the $\mathcal{M} \gtrsim 2$ part) directly reflects the extent of the relics in the radio maps.

We compare the synthetic radio maps to the observed 1382 MHz WSRT map. The observed and synthetic maps are aligned by eye to the bright northern relic in CIZA J2242.8+5301, by simple translation and rotation. With a visual comparison and the taking into account the sizes listed in Table. 10.2, we find the best match between the observed and simulated radio maps for a mass ratio around 2 : 1 to 1.5 : 1 For more equal mass ratios the bottom relic increases to a size that is larger than the observed size. The opposite happens for larger mass ratios. When we compare the simulated radio images with the temperature map in Fig. 10.3 (left panel) we note that the relic emission does not trace the full extent of the shock waves. This is a consequence of the non-linear relation between the Mach number and normalization of the radio spectrum,

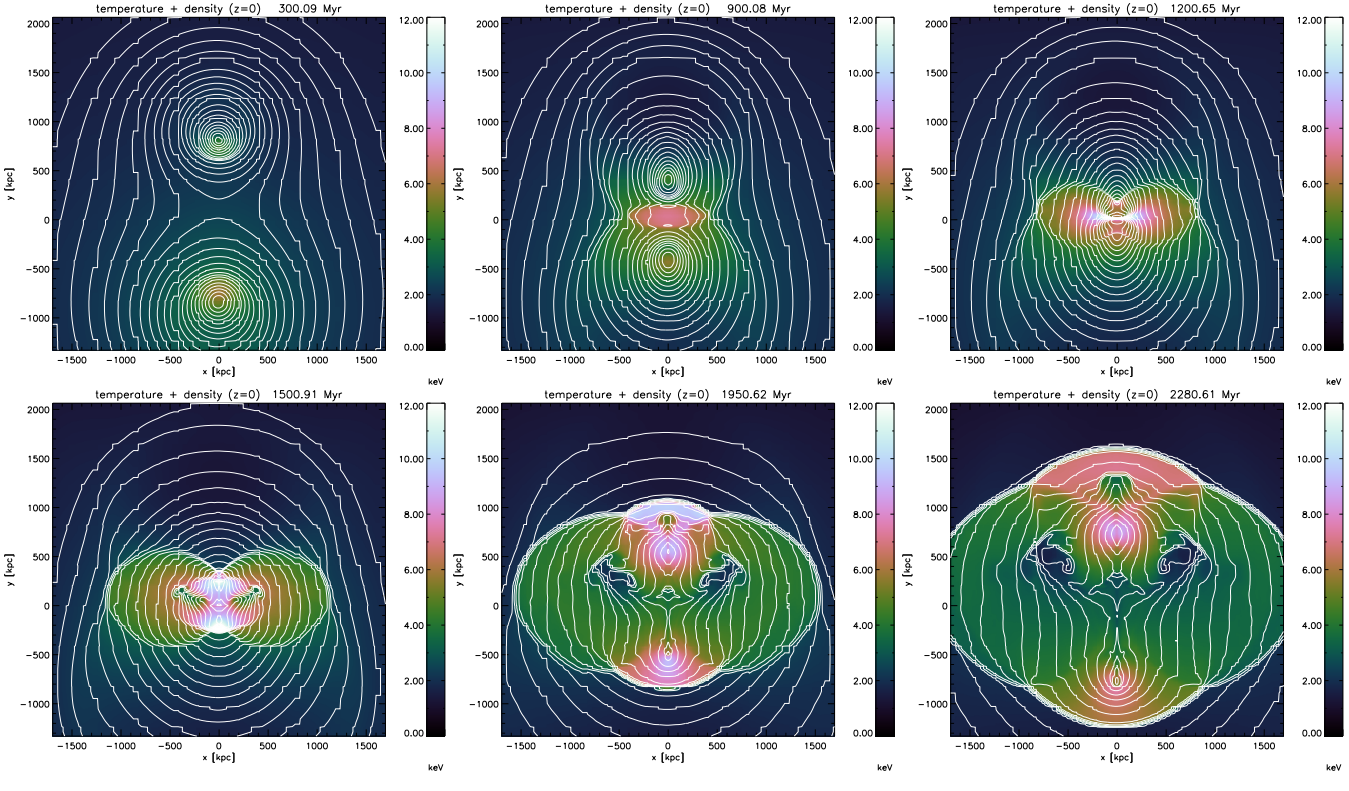

Figure 10.1: Temperature and density evolution for a 2:1 merger with zero impact parameter. The images display the temperature at a slice $z = 0$, while the white contours follow the density. The density contours are drawn at levels of $\log_{10}(\rho([\mathrm{g\ cm^{-3}}]) = [-27.9, -27.8, -27.7, \ldots]$.

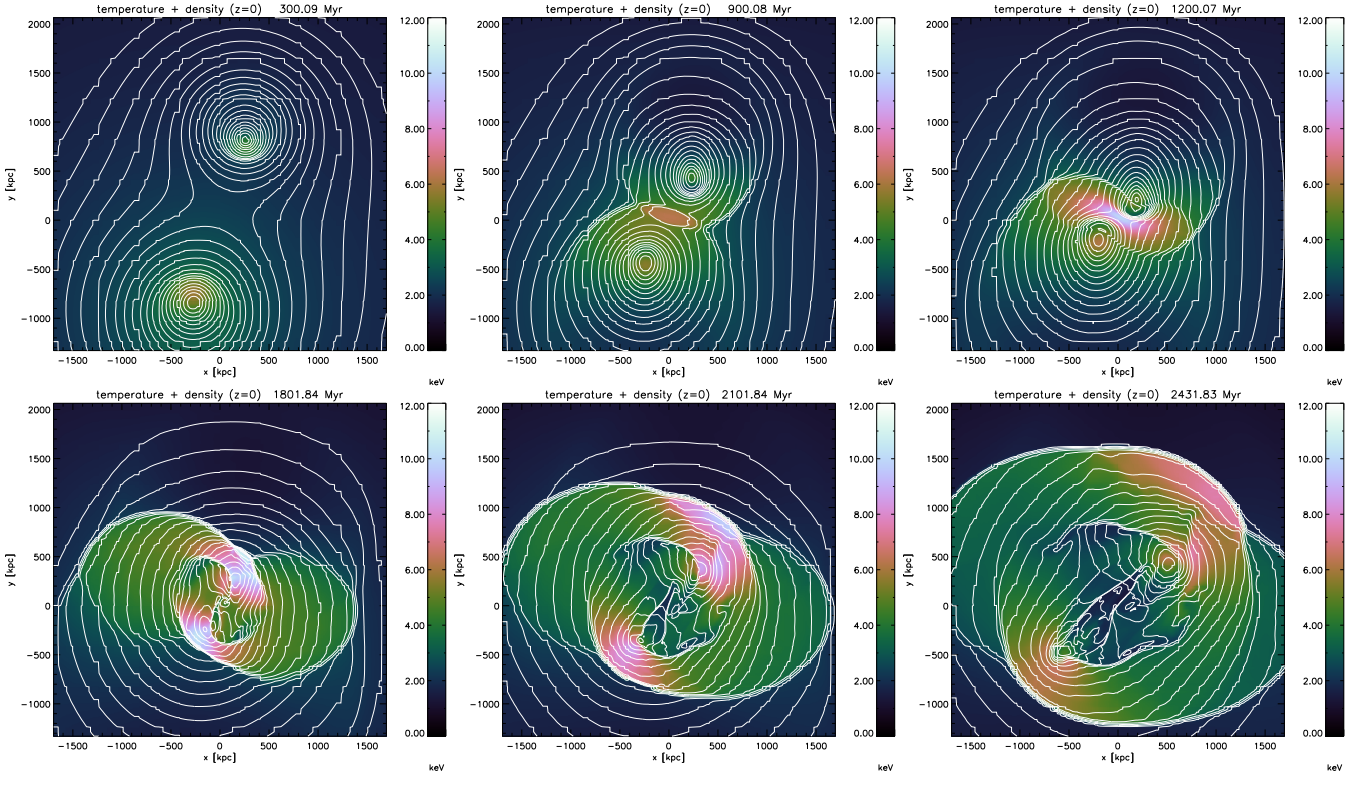

Figure 10.2: Temperature and density evolution for a 2:1 merger with an impact parameter $b = 4r_{c,1}$. The images display the temperature at a slice $z = 0$, while the white contours follow the density. The density contours are drawn at levels of $\log_{10}(\rho([\mathrm{g\ cm^{-3}}]) = [-27.9, -27.8, -27.7, \ldots]$.

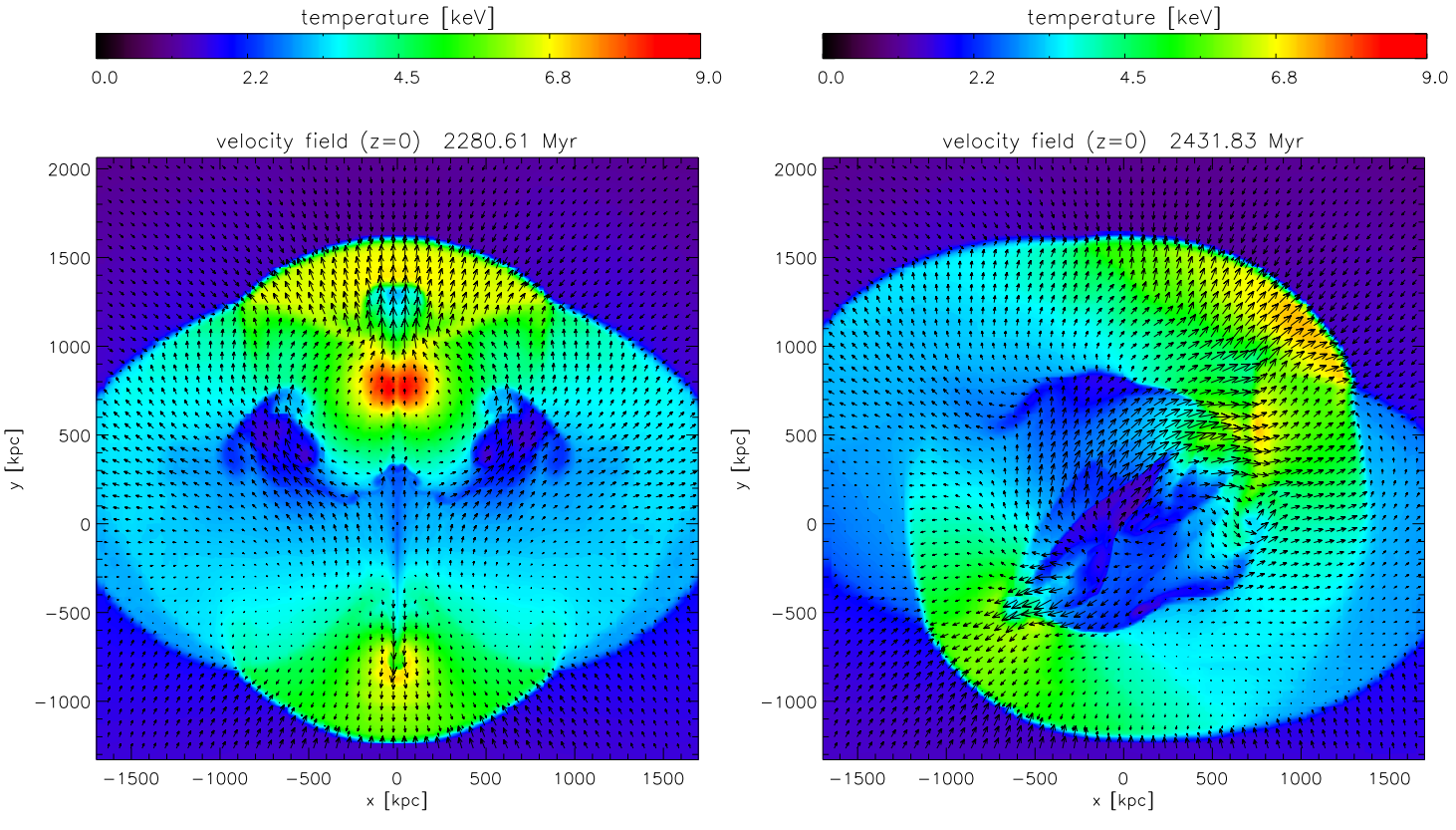

Figure 10.3: Velocity field for a 2:1 merger with impact parameters $b = 0$ kpc (left) and $b = 4r_{c,1}$ (right) for the slice $z = 0$. The two snapshots were chosen such that the center of the two shock waves have a linear separation of 2.8 Mpc. The images display the temperature distribution. The maximum absolute velocity is ~ 1400 km s^{-1}.

Table 10.1: List of simulations with their defining parameters

run	mass ratio[a] $M_1 : M_2$	impact parameter (b) kpc	$r_{c,1}$, $r_{c,2}$ kpc, kpc	$T_{avg,1}$, $T_{avg,2}$ keV, keV	v_y[c] km s^{-1}	comment
R11b0	1:1	0	115, 115	4.1, 4.1	–937	
R1.51b0	1.5:1	0	126, 101	4.5, 3.7	–927	
R21b0	1:1	0	134, 90	4.7, 3.3	–922	
R2.51b0	2.5:1	0	139, 84	4.8, 3.1	–926	
R31b0	3:1	0	145, 80	5.0, 3.0	–944	
R21b0.5	2:1	$1r_{c,1}$ = 67 kpc	134, 90	4.7, 3.3	–922	
R21b1	2:1	$1r_{c,1}$ = 134 kpc	134, 90	4.7, 3.3	–921	
R21b2	2:1	$2r_{c,1}$ = 268 kpc	134, 90	4.7, 3.3	–916	
R21b3	2:1	$3r_{c,1}$ = 402 kpc	134, 90	4.7, 3.3	–908	
R21b4	2:1	$4r_{c,1}$ = 536 kpc	134, 90	4.7, 3.3	–897	
R21b5	2:1	$5r_{c,1}$ = 670 kpc	134, 90	4.7, 3.3	–883	
R21b0β0.5	2:1	0	82.6, 90	4.7, 3.3	–922	$\beta_1 = 0.5$
R21b0β0.75	2:1	0	162.5, 90	4.7, 3.3	–922	$\beta_1 = 0.75$
R21b0cc	2:1	0	134, 90	4.7, 3.3	–922	cool core[b] for cluster 1
R21b0ss (A=0.2, λ = 100 kpc)	2:1	0	134, 90	4.7, 3.3	–922	substructure
R21b0ss (A=0.3, λ = 75 kpc)	2:1	0	134, 90	4.7, 3.3	–922	substructure
R21b0ss (A=0.3, λ = 150 kpc)	2:1	0	134, 90	4.7, 3.3	–922	substructure
R21b0ss (A=0.3, λ = 200 kpc)	2:1	0	134, 90	4.7, 3.3	–922	substructure
R21b0ss (0.4, 200 kpc)	2:1	0	134, 90	4.7, 3.3	–922	substructure

[a] subscript 1 refers to the most massive subcluster, $M_1 + M_2 = 5.5 \times 10^{14}$ M$_\odot$
[b] $T_{min,1}/T_{avg,1} = 0.3$, $r_{cool,1} = 50$ kpc and , $a_{cool,1} = 2$
[c] starting velocity in y-direction for the least massive cluster 2 (Eq.10.13)

Table 10.2: Relic sizes

	top relic	bottom relic
CIZA J2242.8+5301	1700	1450
run R1.51b0	1730	1570
run R21b0	1670	1220
run R2.51b0	1680	930
run R31b0	1690	660

discussed in Sect. 10.3.1. Below $\mathcal{M} \sim 2$ there is no observable radio emission generated. Another reason for the gradual disappearance of the radio emission at the right/left edges of the relics is that the amount of projected shock surface along the line of sight decreases.

10.4.1.2 Impact parameter

Taking the 2 : 1 merger event, we varied the impact parameter, see Fig. 10.4. As discussed in the beginning of Sect. 10.4, two asymmetric shock waves develop, breaking the cylinder symmetry (or reflection symmetry in the resulting image) around the merger axis. The variation in Mach number across the shock front and the amount of projected shock surface along the line of sight cause the radio emission to fade away more slowly on one side of the radio relics. Integrated brightness profiles for the top relic across the y-axis are shown in Fig. 10.5 (top panel). The total extent of the relic decreases by about 10% from $b = 0$ kpc to $b = 5r_{c,1}$.

The CIZA J2242.8+5301 relics are more or less symmetrically located along the proposed merger axis, although the brightness profile at the east end of the northern relic is not well determined because of a bright compact radio source at this location. To obtain a better match with the observed radio map, we reflected the map along the y-axis, i.e., placing the off-axis merger point on the other side (this is equivalent of changing the impact parameter from b to $-b$). The simulated profiles all peak around $x = 0$ kpc, while the observed profile does not. From these profiles it is therefore difficult to constrain the impact parameter. However, by looking at Fig. 10.4 we find that $b \lesssim 3r_{c,1}$ is required to obtain a reasonable match. For larger impact parameters the curvature of top shock does not match the observed one (i.e., this can be seen on the right side of the top relic in the R21b4 panel from Fig. 10.4).

10.4.1.3 Viewing angle

We varied the viewing angle (i) by rotating our computational box around the x-axis before projecting it along the line of sight. The extent of the emission towards the cluster center increases by about a factor of three from $i = 5°$ to $i = 30°$, see Fig. 10.4. Radial profiles of the brightness distribution are shown in Fig. 10.5 (middle panel). The outer edge of the northern relic in CIZA J2242.8+5301 is very pronounced and the brightness of the radio emission drops also quickly towards the cluster center, therefore the relic is likely seen close to edge on, roughly under an angle $\lesssim 10$ deg. In all cases, the simulated brightness profiles do not reproduce the very quick drop towards the cluster center as it is observed for the northern relic. The southern relic is more diffuse and extended in CIZA J2242.8+5301, as is the case in our simulated maps.

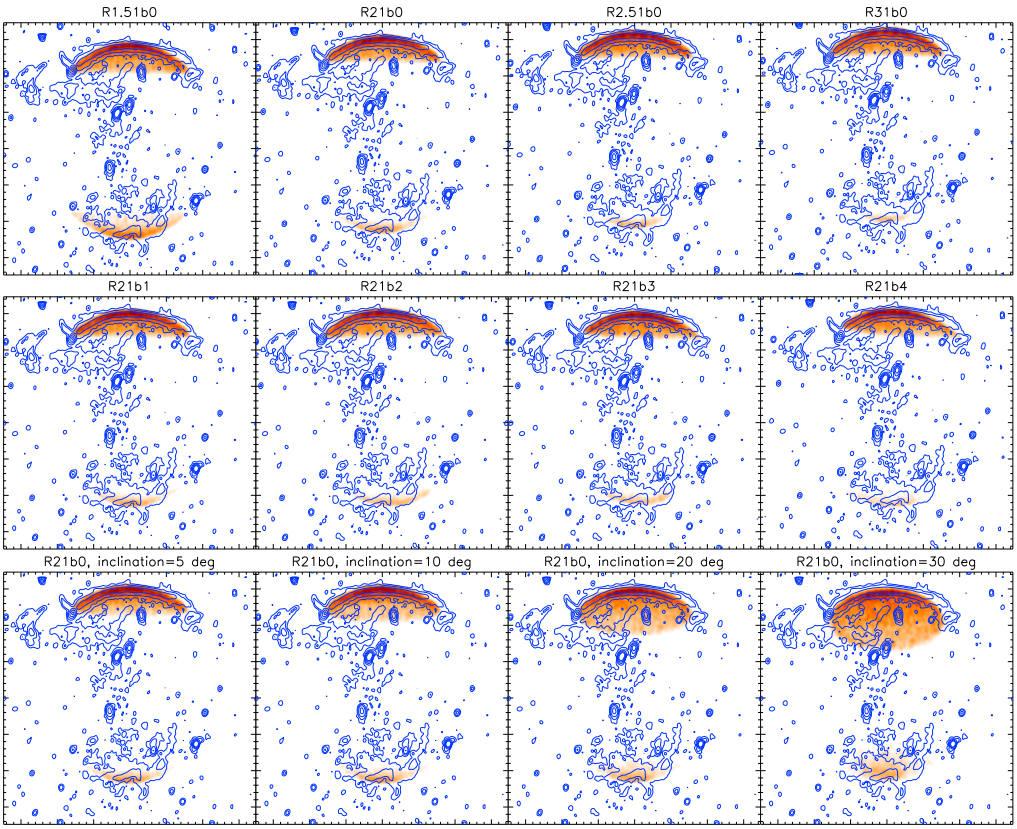

Figure 10.4: Simulated radio emission for cluster mergers with different mass ratios (top row), impact parameters (middle row) and viewing angles (bottom row). The radio maps to the hydrodynamical snapshot where the two shock are separated by 2.8 Mpc. The images span 3.4×3.4 Mpc. WSRT 1382 MHz contours from CIZA J2242.8+5301 are overlaid on the synthetic radio images. Contours are spaced by factors of four in brightness.

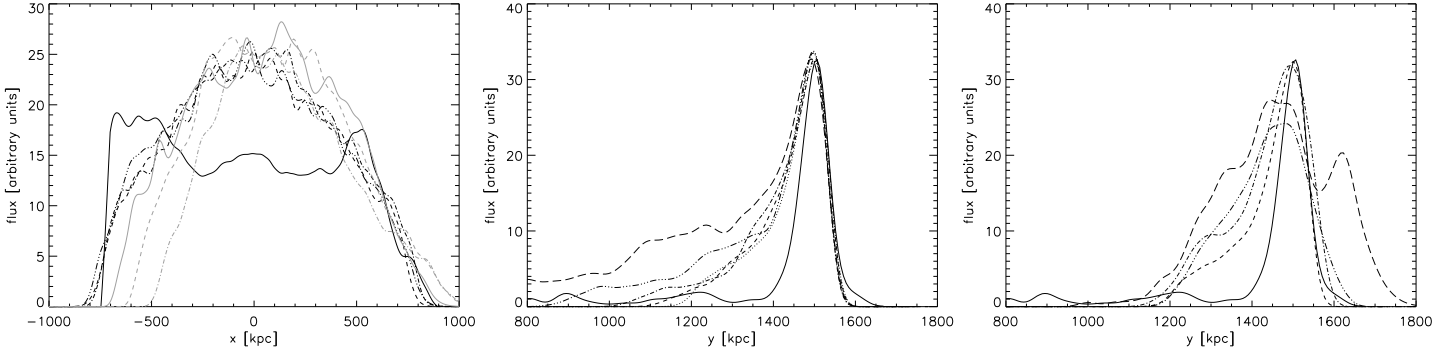

Figure 10.5: Left: integrated brightness profiles across the y-axis for the top relic. Black line displays the observed profile for the northern relic in CIZA J2242.8+5301. Black dashed line: $b = 0$ kpc, black dash-dotted line: $b = 1r_c$, black dashed-triple-dotted line: $b = 2r_c$, grey solid line: $b = 3r_c$, grey dashed line: $b = 4r_c$, grey dash-dotted line: $b = 5r_c$. Middle: integrated brightness profiles across the x-axis from $|x| < 100$ kpc for the top relic for relics seen under different viewing angles. Solid line displays the observed profile for the northern relic in CIZA J2242.8+5301, dotted line : $i = 0°$, dashed line: $i = 5°$, dash-dotted line: $i = 10°$, dash-triple-dotted line: $i = 20°$, long dashed line: $i = 30°$. Right: integrated brightness profiles across the x-axis from $|x| < 100$ kpc for simulations including substructure. Solid line displays the observed profile for the northern relic in CIZA J2242.8+5301, dashed line: no substructure, dash-dotted line: $A = 0.2$, $\lambda = 100$ kpc, dash-triple-dotted line: $A = 0.3$, $\lambda = 150$ kpc, long dashed line: $A = 0.4$, $\lambda = 200$ kpc.

10.4.1.4 β-model

One of the parameters which could influence the size of the radio relics is the core radius used in our β-profile (Eq. 10.7). Because the total mass is fixed in our simulations the core radius is set by the β parameter in Eq. 10.7. We changed β from the default value of $2/3$ to 0.5 and 0.75 for the most massive cluster to investigate the effect this has on the produced radio maps. For $\beta = 0.5$, the core radius decreases from 134 kpc to about 83 kpc, while for $\beta = 0.75$ the core radius increases to 163 kpc. We run the simulations with these different core radii and β values for the standard R21b0 merger scenario. The resulting radio maps are displayed in Fig. 10.6.

The change in $r_{\mathrm{c},1}$ has a direct influence on the size of the resulting shock waves and radio relics formed. For $r_{\mathrm{c},1} = 83$ kpc, the northern and southern relics are almost a factor of 2 smaller in size. For $r_{\mathrm{c},1} = 163$ kpc, the relics have a slightly larger size and are similar to the R1.51b0 merger (see Fig. 10.4). This implies that our best fitting mass ratio found in Sect. 10.4.1.1 depend on the adopted core radii. In particular if the most massive cluster has a larger core radius this mimics a merger with a smaller mass ratio (e.g., 1.5 : 1), see Fig. 10.4. By increasing the core radius of the less massive subcluster the size of the smaller southern relic can be increased, to some extent mimicking a 2.5 : 1 merger. Taking different core radii, the range of matching mass ratios for CIZA J2242.8+5301 is therefore larger and lies roughly between 1.5 : 1 and 2.5 : 1 .

10.4.1.5 Cool core

In massive relaxed galaxy clusters the ICM temperature decreases strongly towards the center. To investigate the effect of such a cool core, we add a central cool core to the most massive subcluster using Eq. 10.10. We take typical value of $T_{\mathrm{min}}/T_{\mathrm{avg}} = 0.3$, $r_{\mathrm{cool}} = 50$ kpc and $r_{\mathrm{cool}} = 2$ (e.g., Vikhlinin et al. 2006) and use the standard R21b0 merger scenario. We find that the addition of a central cool core does not influence the size and shape of the resulting radio relics. The resulting radio map looks almost identical to the default R21b0 merger map, see Fig. 10.4.

10.4.2 Spectral index

We computed a spectral index map between 610 and 1382 MHz for the R21b0 merger, again taking a constant magnetic strength of 5 μGauss, see Fig. 10.7. We find that the spectral index in front of the two relics is ~ -1.1, while the spectral index steepens quickly to ~ -2 in the direction of the cluster center. After the initial spectral steepening to $\alpha \sim -2$, the spectral index remains constant. The radio emission in this region comes from (i) aged radio plasma with a steep spectrum in the post-shock region and (ii) projected radio emission from the front of the shock wave with a flatter spectral index of ~ -1.

The observed spectral index in front of the northern CIZA J2242.8+5301 relic is flatter, with $\alpha \sim -0.6$ or -0.7, than in our simulated spectral index map. The observed spectral index corresponds to a $\mathcal{M} = 4.6$ shock. In the our R21b0 merger, we find a Mach number of about 2.7–2.4 for the upper shock wave. This translates into $\alpha_{\mathrm{inj}} = -0.8$ to -0.9. However, in the simulated map α is steeper by about 0.3 units at the front of the relic. This difference is caused by the limited spatial resolution (~ 50 kpc) of our synthetic radio map: radio emission directly at the front of the shock with $\alpha_{\mathrm{inj}} \approx -0.85$ is always mixed with some emission from particles that have already have undergone some synchrotron losses. For CIZA J2242.8+5301 this implies

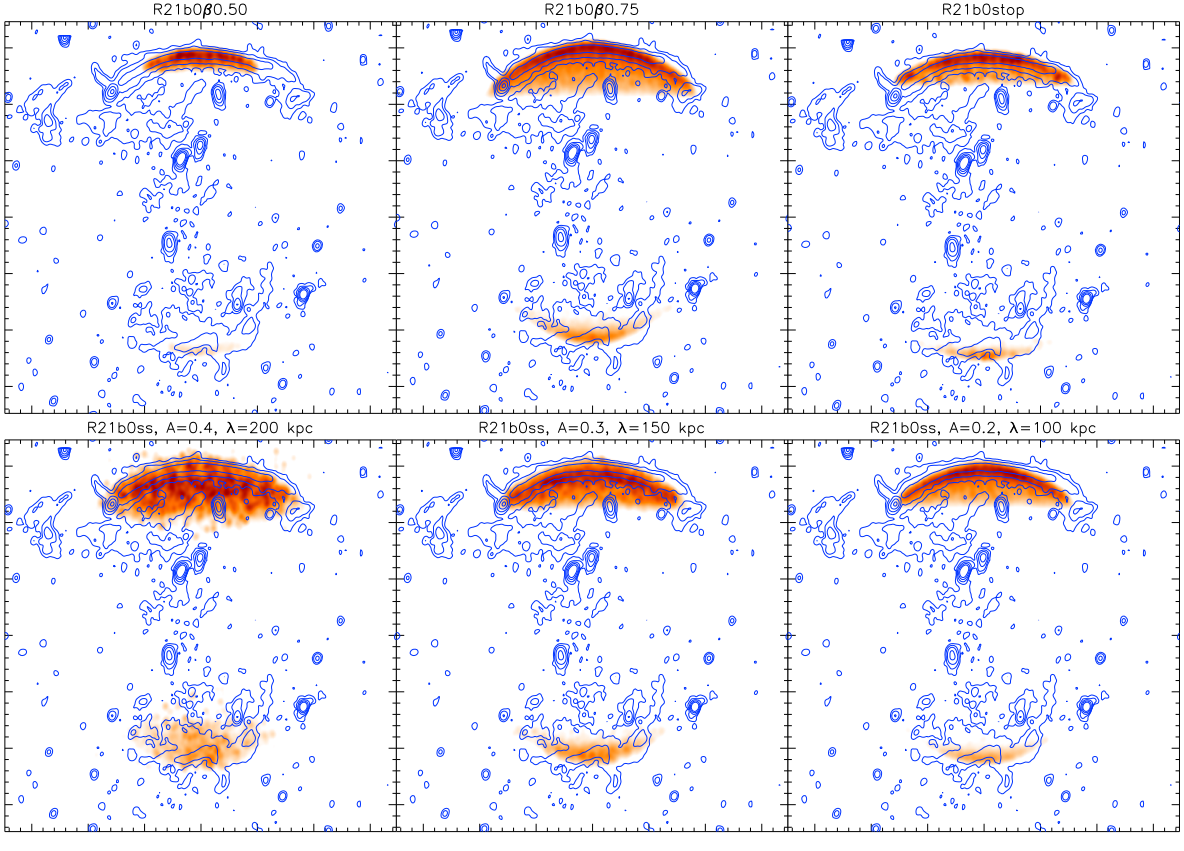

Figure 10.6: Top row: Simulated radio emission for R21b0 cluster merger with different values of β_1 and $r_{c,1}$ and for a R21b0 cluster merger with the two halos sticking at core passage, which represents the extreme case of infinite tidal friction. Bottom row: Simulated radio emission for a R21b0 cluster mergers with substructure. Contours are the same as in Fig. 10.4. The images span 3.4×3.4 Mpc.

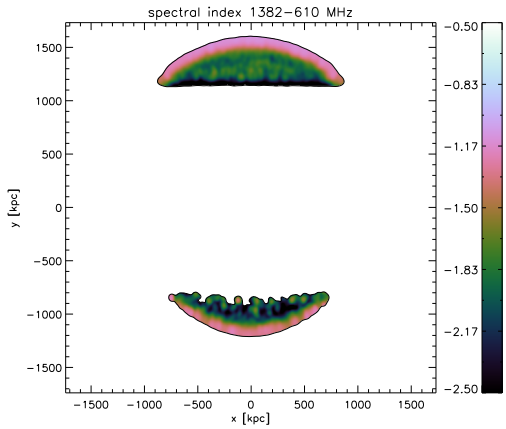

Figure 10.7: Simulated spectral index map between 610 and 1382 MHz for the R21b0 merger. The small scale spectral index variations seen in the post-shock region are due to the finite number of particles used to compute the radio map.

that the true injection spectral index is probably even flatter than −0.6, if the shock front has a similar shape as in our simulations.

10.5 Substructure & clumping

Real mergers are more complex than in our idealized simulations. Hence, the detailed properties, such as the shapes or brightness profiles of radio relics, do not necessarily match with the observations. In particular the presence of less massive substructures and galaxy filaments extending from the large scale cosmic web will modify the shock morphologies and locations (e.g., Paul et al. 2011). Indeed, there are additional smaller relics located in CIZA J2242.8+5301 that points towards a more complex merger event. These more complex relics are also seen in simulations which include large-scale structure formation with radio emission from shocks (e.g., Pfrommer et al. 2008; Hoeft et al. 2008; Battaglia et al. 2009). Although we cannot easily embed our simulation into a large-scale cosmological environment, we investigate the effect of small scale ($\lesssim$ 200 kpc) substructures/clumps. Matter falling onto clusters is expected to be clumpy in nature and the clumps have typical dimensions of galaxies or small galaxy-groups (Roncarelli et al. 2006). If the gas in the cluster's outskirts is clumpy, and this is not taken into account, it can lead to an overestimation of the baryon fraction and affect the derived entropy and pressure profiles (e.g., Simionescu et al. 2011). The presence of well-defined radio relics with sharp outer rims can be used to constrain the amount of clumping in the ICM at large distances ($\gtrsim$ 1 Mpc) from the cluster center.

We modified our initial density and temperature profiles by adding sinusoidal density fluctuations throughout the computational volume. The two parameters which control this are the relative amplitude (A) and wavelength (λ) of these density fluctuations. These sinusoidal waves were inserted parallel to the x, y and z-axes. To keep the pressure unchanged, we also included temperature fluctuations that are inversely proportional to the density fluctuations, see Fig. 10.8

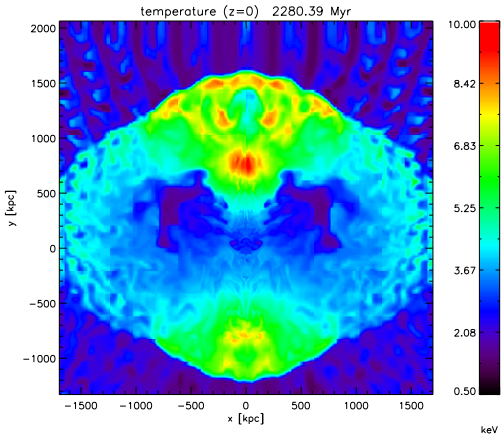

Figure 10.8: Left: Temperature distribution at the slice $z = 0$ for the R21b0ss (A=0.4, $\lambda = 200$ kpc) merger.

for an example. We carried out several runs changing the amplitude and wavelength of the fluctuations. Radio images from runs with $A = 0.2, 0.3, 0.4$ and $\lambda = 100, 150, 200$ kpc, respectively, are shown in Fig. 10.6. Brightness profiles along the y-axis are displayed in Fig. 10.5 (bottom panel).

The resulting radio relics are similar in shape to the canonical R21b0 merger map, but the relics are wider and display brightness fluctuations in the radio emission. The effect of this substructure is that the outer boundary of the relics is less well defined. For relics observed close to edge-on, projection effects average out some of the variations in the strength of the radio emission. The northern relic in CIZA J2242.8+5301 has a smooth appearance and well-defined outer rim. This probably implies that few clumps are present this location in the ICM. We find that the radio maps with $A \gtrsim 0.3$ do not provide a good match to the observed northern relic in CIZA J2242.8+5301. There is little difference between runs with $A = 0.3$ and $\lambda = 75, 150, 200$ kpc. We can therefore put upper limits on the amplitude of density fluctuations of roughly 30%, for substructures with scales of $\lesssim 200$ kpc, at the location of the northern relic. This means that clumping appears to be much less than that inferred from Suzaku observations of Perseus with $\sqrt{< n_e^2 > / < n_e >^2} \sim 3 - 4$ near the virial radius (e.g., Simionescu et al. 2011). The reason for this could be that the shock waves in CIZA J2242.8+5301 are expanding into a region sufficiently far from filaments such that it is largely free from infalling substructure.

A more realistic representation of density clumps could probably be used to put tighter constraints on the amount of substructure. This is beyond the scope of this paper and we leave this for future work.

10.6 Discussion

10.6.1 Effect of dark matter dynamics

Clearly, a gross simplification of our setup is the treatment of the gravity in the form of rigid potentials that move on set trajectories without interacting. In reality, the dark matter particles of the progenitor halos will interact in the course of the merger to form a new halo. In the course of this, the potential changes mainly due to two effects: i) dynamic friction and ii) tidal shocking. The first one is the most important effect. After core passage, it will cause the halos to slow with respect to each other until they turn around on their orbits. As the merger shock waves are running out of the cluster faster than the speeds of the halos with respect to each other, this will not change the results dramatically. To test the magnitude of this effect, we ran a simulation where we made the two halos stick at core passage, which represents the extreme case of infinite tidal friction. The result is shown in Fig. 10.6. The relics are now somewhat narrower (about 10% for the top relic) but apart from that there are not many changes in the radio map even though the temperature and density are quite different in the center. The main change are the lower Mach numbers (which drop from 2.7 to 2.2, and from 2.2 to 1.9 for the top and bottom relics compared to the default R21b0 merger), but since this affects both for the top and bottom shocks the end result is not too different from the default R21b0 map. Finally, we ignore the effect of tidal shocking, which leads to heating of the central DM orbits of the cluster and leads to a puffing up of the potential. This will affect the cluster potential within the core radius but will leave the regions where the shocks are located largely unaffected. For a proper simulation of this effect, one would need to resort to a simulation with a dynamic DM component.

10.6.2 Relic width and brightness profiles

One of the most intriguing properties of the northern relic in CIZA J2242.8+5301 is its very narrow width and rather uniform luminosity along its extent. From our simulated radio map we find the brightest part of the top relic to be $\sim 20\%$ wider than the observed width. In Sect. 10.6.1 we found a smaller width by including infinite tidal friction. This affects the shock downstream velocity, which determines how far the the synchrotron emitting electrons are carried away from the shock front (e.g., Markevitch et al. 2005). The relic's width is linearly proportional to the downstream shock velocity. In case of infinite tidal friction the simulated radio relic is only $\sim 10\%$ wider compared to the observed width. In addition, the width depends on the adopted magnetic field strength, but increasing B to 7 μGauss decreases the width only by a few percent. This implies that projection effects and the finite resolution of our simulations play and important role in determining the width.

For the southern relic, the emission fades slowly towards the east and west ends. The reason why this does not happen for the top relic in the simulation is because of the quick drop in the Mach number at $|x| > 850$ kpc, see Fig. 10.3 (left panel). However, for the CIZA J2242.8+5301 northern relic the integrated brightness profile across the y-axis (Fig 10.5, top panel) drops much quicker and is flatter than in the simulations. The reason for this is unclear, it could be caused by variations in the magnetic field strength, Mach number, or because the shock surface is more complex. The Mach number found from the injection spectral index is higher than that in the simulations (4.6 versus 2.7 for the northern relic), this difference is puzzling. It could indicate that our temperature profiles are not correct or that Eq. 10.3, which links $\alpha_{\rm inj}$ and $\mathcal{M}$, is not

directly applicable. X-ray observations are crucial here to directly determine the Mach number from the temperature jump.

10.6.3 Origin of single radio relics

Another interesting outcome of our simulations concerns the existence of single radio relics, e.g., the relic in A521 (Giacintucci et al. 2008). In binary cluster mergers, two shocks should be generated and hence one expects the majority of relics to come in pairs. In the simulations with mass ratios $\gtrsim 3$ very little radio emission is generated by the shock wave in front of the less massive subcluster. The Mach number of these shocks is quite low ($\mathcal{M} \lesssim 2$) and the shock surfaces are small, which results in very little observable radio emission. Based on the simulations, one would thus expect most double relics to be located in merging systems with small mass ratios, while single should be found in mergers with larger mass ratios.

10.6.4 A quantitative metric for the goodness of fit

We did not define a quantitative metric for the goodness of fit between the simulated and observed radio images. This paper is meant to be illustrative of the potential of the method and in this work we chose to apply it only to the relics in CIZA J2242.8+5301. We also note that the position, shape, and surface brightness distribution of relics are influenced by the cluster environment (e.g., connected galaxy filaments) which affect the derived merger parameters. However, for future work when constraining merger parameters for larger numbers of double relics systems, it is important to develop a metric for the goodness of fit. We discuss here a possible approach and address some of the issues involved.

A first step should be the removal (or masking) of point sources and extended radio galaxies. In addition, one may have to subtract the emission from a radio halo in the cluster center. Removing extended radio galaxies and a radio halo is not entirely trivial as the spatial scales of these structures can be comparable to that of relics. However, this should still be feasible as double radio relics are relatively bright and their morphology is quite different from radio halos or radio galaxies.

For constraining the merger parameters there are two aspects that can be considered: (i) the spatial information of the location of the relics and (ii) the brightness distribution. We ignore information about the spectral and polarization properties because this complicates matters and this information is not available for all double relics. Due to the uncertainties in the magnetic field strength the brightness of the emission is probably not a very good criteria for a quantitative metric. It is also not entirely clear under what conditions relics precisely form, i.e, in the case of Abell 2146 two shocks are found in a Chandra X-ray image, but no bright radio relics are detected (Russell et al. 2010, 2011).

Radio relics, especially their outer edges, should directly trace the location of the merger shock waves and thus provide most of the constraints for the merger scenario. This is also what we mainly used in our qualitative comparison for the relics in CIZA J2242.8+5301. The viewing geometry is mostly constrained from the downstream extent of the relics. In the light of what we discussed above, we propose a two-dimensional spatial cross-correlation. This should be repeated for every possible rotation angle for a given image from the simulations. The height of the peak in the cross-correlation then gives a quantitative metric for the goodness of fit for a single simulated image. Image scaling should not be considered here as this relates to the

absolute sizes and distances of the relics which evolve over time, and the time since core passage is one of the parameters we wish to constrain. The process can then be repeated for different merger parameters (mass ratios and impact parameters), snapshots in time and viewing angles to find the best fit. Because the brightness distribution is uncertain, we propose to apply a fixed cut in the radio flux (a few times the noise level in the observed radio image), and put all pixels values to either 1 (emission) or 0 (no emission). This is done also for the simulated images. The overall normalization of the simulated radio emission can be fixed by normalizing to the total flux in the observed image. Instead of a cross-correlation, one could also consider a simple image subtraction (after x, y-shifting and rotation) followed by taking the sum of the absolute difference. It may be worth giving the outer edges of the relics a somewhat large weight in the process, for example by setting these to a higher value (e.g., 2), some experimentation will be needed here. Applications of these cross-correlations shall be reserved for future work.

10.7 Summary

We have presented simulated radio maps of idealized binary cluster mergers, varying the mass ratios, impact parameters, viewing angles and density/temperature profiles. The radio emission in these simulations is produced by relativistic electrons which are accelerated via the DSA mechanism in the shock waves created by the merger event.

We have used these simulated radio maps to constrain the merger scenario for the cluster CIZA J2242.8+5301, which hosts a Mpc scale double radio relic. We find that a merger with a mass ratio between 1.5 : 1 and 2.5 : 1 provides the best match to the observed radio emission in this cluster. The main uncertainty in the derived mass ratio comes from the unknown core radii of the clusters before the merger. The viewing angle is mostly constrained by the extent of the top relic towards the cluster center, additional substructure/clumps also increase the relic's extent in the downstream region. Since the observed extent is only 55 kpc this implies that the relic is seen close to edge-on (i.e., $i \lesssim 10°$). The impact parameter is difficult to constrain as the observed brightness profile along the x-axis is not reproduced for any our merger scenarios. Only for $b \gtrsim 3r_{c,1} \approx 400$ kpc we find that the curvature of the simulated relics do not match with the observations. From our simulations we find that the time since core passage does not depend much on the adopted initial conditions. We therefore constrain this number to 1.0 Gyr, although it also depends on the adopted total mass of the system and temperature profile.

One of the main uncertainties for comparing the simulated radio emission with observations, in particular the brightness profiles, is the structure and strength of the magnetic field. Especially the brightness profile of the main relic along the relic's length is not well reproduced by our simulations. Little is known about the magnetic field strength at distances larger than 1 Mpc from the cluster center. Using equipartition arguments magnetic fields strengths of the order of $\sim 1\ \mu$G have been derived (e.g., Govoni & Feretti 2004). Upper limits on the IC emission from radio relics indicate magnetic fields of a few μG (e.g., Nakazawa et al. 2009; Finoguenov et al. 2010). Faraday rotation measures give similar results (e.g., Bonafede et al. 2010). However, the spatial variations of the magnetic field strength at these distances from the cluster center are unknown. In addition, several smaller relics are found in the cluster which are not present in our simulations. These relics are probably caused by additional substructures which are not included in our initial conditions.

We find that radio relics can be used to put constraints of the amount of clumping or sub-

structure in the ICM at large distances (about 1 to 2 Mpc) from the cluster center, under the assumption that relics are tracers of shocks. The sharp outer boundary of the northern relic in CIZA J2242.8+5301 implies density fluctuations with an amplitude $\lesssim$ 30% of the average density (the size of fluctuations being $\sim$ 200 kpc).

The simulations also indicate that most double relics should be located in merging system with mass ratios between 1 : 1 and 1 : 3, while single radio relics from in clusters that undergo less energetic mergers with larger mass ratios.

We conclude that double radio relics can be used to constrain cluster merger events, which is especially useful when detailed X-ray observations are not available. Relics are often located at large distances from the cluster center, where the density is so low that even deep X-ray observations cannot be used to probe the physical conditions there (e.g., to measure the temperature jump). In addition, relics can be located in lower-mass systems where the thermal X-ray emission is not detected in the ROSAT All Sky Survey, for example (Voges et al. 1999). Some examples of possible radio relics in poor systems without a X-ray counterparts have been reported by Brown & Rudnick (2009); van Weeren et al. (2009c, 2011e).

One important parameter is the strength and structure of the magnetic field at the location of the radio relics. MHD simulations of cluster mergers will be needed to study the variations and strength of the magnetic field at large distances from the cluster center, and investigate the effect this has on the derived merger parameters from radio maps.

Acknowledgements. We would like to thank the referee Shea Brown for his comments and useful suggestions. RJvW acknowledges funding from the Royal Netherlands Academy of Arts and Sciences. MB and MH acknowledge support by the research group FOR 1254 funded by the Deutsche Forschungsgemeinschaft. We gratefully acknowledge the use of the supercomputers JUROPA at the John von Neumann Institute for Computing in Juelich. The software used in this work was in part developed by the DOE-supported ASC / Alliance Center for Astrophysical Thermonuclear Flashes at the University of Chicago.

CHAPTER 11

The discovery of diffuse steep spectrum sources in Abell 2256

Abstract. Hierarchical galaxy formation models indicate that during their lifetime galaxy clusters undergo several mergers. An example of such a merging cluster is Abell 2256. Here we report on the discovery of three diffuse radio sources in the periphery of Abell 2256, using the Giant Metrewave Radio Telescope (GMRT). The aim of the observations was to search for diffuse ultra-steep spectrum radio sources within the galaxy cluster Abell 2256. We have carried out GMRT 325 MHz radio continuum observations of Abell 2256. V, R and I band images of the cluster were taken with the 4.2m William Herschel Telescope (WHT). We have discovered three diffuse elongated radio sources located about 1 Mpc from the cluster center. Two are located to the west of the cluster center, and one to the southeast. The sources have a measured physical extent of 170, 140 and 240 kpc, respectively. The two western sources are also visible in deep low-resolution 115 – 165 MHz Westerbork Synthesis Radio Telescope (WSRT) images, although they are blended into a single source. For the combined emission of the blended source we find an extreme spectral index (α) of -2.05 ± 0.14 between 140 and 351 MHz. The extremely steep spectral index suggests these two sources are most likely the result of adiabatic compression of fossil radio plasma due to merger shocks. For the source to the southeast, we find that $\alpha < -1.45$ between 1369 and 325 MHz. We did not find any clear optical counterparts to the radio sources in the WHT images. The discovery of the steep spectrum sources implies the existence of a population of faint diffuse radio sources in (merging) clusters with such steep spectra that they have gone unnoticed in higher frequency ($\gtrsim$ 1 GHz) observations. Simply considering the timescales related to the AGN activity, synchrotron losses, and the presence of shocks, we find that most massive clusters should possess similar sources. An exciting possibility therefore is that such sources will determine the general appearance of clusters in low-frequency high resolution radio maps as will be produced by for example LOFAR or LWA.

R. J. van Weeren, H. T. Intema, J. B. R. Oonk, H. J. A. Röttgering, and T. E. Clarke
Astronomy & Astrophysics, **508**, 1269, 2009

11.1 Introduction

Models of large-scale structure (LSS) formation show that nearly all galaxy clusters grow via mergers of smaller clusters and sub-structures. These mergers can create shocks and turbulence within the intra cluster medium (ICM) that are likely to amplify magnetic fields and accelerate relativistic particles. In the presence of magnetic fields, these particles will emit synchrotron radiation, observable at radio frequencies (see the review by Ferrari et al. 2008, and references therein). Giant peripheral radio relics are thought to be tracers of the shock waves generated by cluster mergers (Ensslin et al. 1998; Miniati et al. 2000). At the location of the shock front particles are accelerated via diffusive shock acceleration (DSA) by the Fermi-I process (e.g., Drury 1983; Blandford & Eichler 1987; Jones & Ellison 1991; Malkov & O'C Drury 2001). Shock waves generated by cluster mergers can also compress fossil radio plasma from previous episodes of AGN activity and produce radio relics (Enßlin & Gopal-Krishna 2001; Enßlin & Brüggen 2002). Proposed examples of these radio relics, also called radio *phoenices*, are the sources found by Slee et al. (2001). These sources have a steep spectral index[1] ($\alpha \lesssim -1.5$) and filamentary morphologies. The steep spectral indices are the result of synchrotron and inverse Compton (IC) losses.

Abell 2256 is a massive cluster located at a redshift of 0.0581 (Struble & Rood 1999). Extensive observations from X-ray to radio wavelengths have shown that the cluster is presently undergoing a merger with a smaller sub-structure. These X-ray observations revealed significant sub-structure within the cluster. The most prominent feature are two separate X-ray peaks (Briel et al. 1991; Briel & Henry 1994; Sun et al. 2002) providing strong evidence that Abell 2256 is indeed undergoing a merger. At radio wavelengths, the cluster shows a very complex morphology. The cluster is known to host a bright peripheral radio relic, a radio halo, a number of complex relatively compact filamentary sources, and several "head-tail" sources (Bridle & Fomalont 1976; Bridle et al. 1979; Röttgering et al. 1994; Miller et al. 2003; Clarke & Ensslin 2006; Brentjens 2008).

Here we present deep 325 MHz radio continuum observations of Abell 2256 with the GMRT, complemented by WSRT 115 – 165 MHz observations and optical WHT imaging. In this paper we focus on the discovery of three diffuse sources in the cluster periphery. A detailed comparison of the other sources in the cluster has been presented by Intema (2009). The layout of this paper is as follows. In Sect. 11.2 we give an overview of the observations and data reduction. In Sect. 11.3 we present the radio and optical maps. We end with a discussion and conclusions in Sects. 11.4 and 11.5. Throughout this paper we assume a ΛCDM cosmology with $H_0 = 73$ km s^{-1} Mpc^{-1}, $\Omega_m = 0.27$, and $\Omega_\Lambda = 0.73$. At the distance of Abell 2256 $1''$ corresponds to 1.08 kpc (Wright 2006).

11.2 Observations & data reduction

Abell 2256 was observed with the GMRT at a frequency of 325 MHz. The observations recorded both LL and RR polarizations in two sub-bands (IFs) with a total bandwidth of 32 MHz, and 128 frequency channels per IF. The observations were carried out on May 25 & 26, 2008. The absolute flux scale was set according to the Perley & Taylor (1999) extension of the Baars et al. (1977) scale using the calibrators 3C48, 3C147, and 3C286. The total on-source time

[1] $F_\nu \propto \nu^\alpha$, with α the spectral index

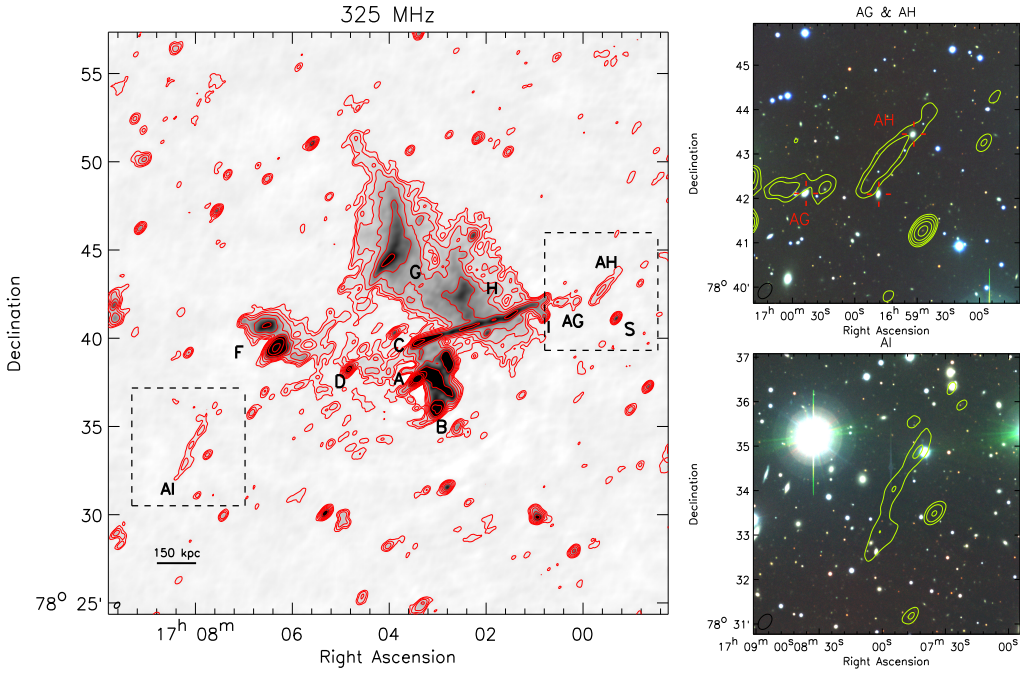

Figure 11.1: Left: Radio map at 325 MHz with a restoring beam size of $23.9'' \times 15.9''$, indicated in the bottom left corner. The red contours are drawn at levels of $[1, 2, 4, 8, \ldots] \times 3\sigma_{\rm rms}$ μJy beam^{-1}. Various sources are labeled with capital letters. Right: Optical images around AG+AH (top right panel) and AI (bottom right panel) composed out of V (blue), R (green), and I (red) band images.

for Abell 2256 was about 9.5 hours. The data were reduced using the NRAO Astronomical Image Processing System (AIPS). The data was corrected for the instrumental bandpass and complex gain solutions were determined using the calibrators and applied to our target source. The sidelobes from six bright sources affected our target source in the center of the field. We removed these six sources using the "peeling"-method (e.g., Noordam 2004). We used the polyhedron imaging method (Perley 1989; Cornwell & Perley 1992) to reduce the effects of non-coplanar baselines. The final primary beam corrected image was made using robust weighting set to 0.5 (Briggs 1995), yielding a synthesized beam of $23.9'' \times 15.9''$. The rms noise in this image was 119 μJy beam^{-1}.

A2256 was observed with the WSRT in 8 IFs, each IF having 2.5 MHz bandwidth and 128 channels, placed between 115 and 165 MHz. The total integration time was 6×12 hours using six different configurations (with four moveable antennas) to suppress grating lobes. Each 12 hour observation and IF were calibrated separately, correcting for the bandpass and slow gain variations (using 3C48 and 3C295). The data was further self-calibrated using three rounds of phase and one round of amplitude and phase selfcalibration. The data for the six configurations were then combined per IF and imaged separately. The noise in the images ranged between 5.0 – 14.6 mJy beam^{-1}, and the resolution varied from 175″ at 115 MHz to 130″ at 165 MHz. For more details on the reduction see Intema (2009).

Optical V, R and I band images were taken at the location of our newly discovered sources with the 4.2m WHT telescope (PFIP CCD camera) on April 19, 2009. The seeing during the observations was about 1.5″, the total exposure time was 600 s per band. The images were reduced with IRAF (Tody 1986, 1993) using the *mscred* package (Valdes 1998). All images were flat fielded and bias-corrected. The I band image was fringe corrected. Zero-points were determined using various observations of standard stars taken during the night. The final images have a depth (SNR of 4 for point sources) of approximately 23.9, 24.2, 22.8 magnitude (Vega) in the V, R and I band, respectively.

11.3 Results

We adopt the radio source labeling from Bridle & Fomalont (1976) and Röttgering et al. (1994). The 325 MHz GMRT image (Fig. 11.1) clearly shows the presence of the known AGN related sources (A, B, C, and I), the bright peripheral relic (the combined emission from G and H) and the complex source F. The radio halo is only partly visible around source D since the shortest baselines were severely affected by RFI and had to be flagged. In this paper we focus on three new diffuse sources discovered in the maps, which we label source AG, AH, and AI, see Fig. 11.1. AG and AH are neighboring sources (about 1′) to the west of the cluster center and have an extent of 130″ and 160″, respectively. Source AI is located on the SE side of the cluster and has an extent of 220″. The integrated 325 MHz fluxes are 7 ± 1, 12 ± 1, and 11 ± 1 mJy for sources AG, AH and AI, respectively (by summing the flux within a region half an arcminute outside the 3σ contours). Sources AG and AH are also seen in the 351 MHz image presented by Brentjens (2008). However, due to the lower resolution of this image, the diffuse nature of the sources is not apparent. Source AI is also seen in the same image, but only the southern brighter part is visible. The northern half of AI is too faint to be visible in this map. At a redshift of 0.0581 the sources have a physical extent of 140 (AG), 170 (AH) and 240 kpc (AI). They are located at a projected distance of about one Mpc from the cluster center.

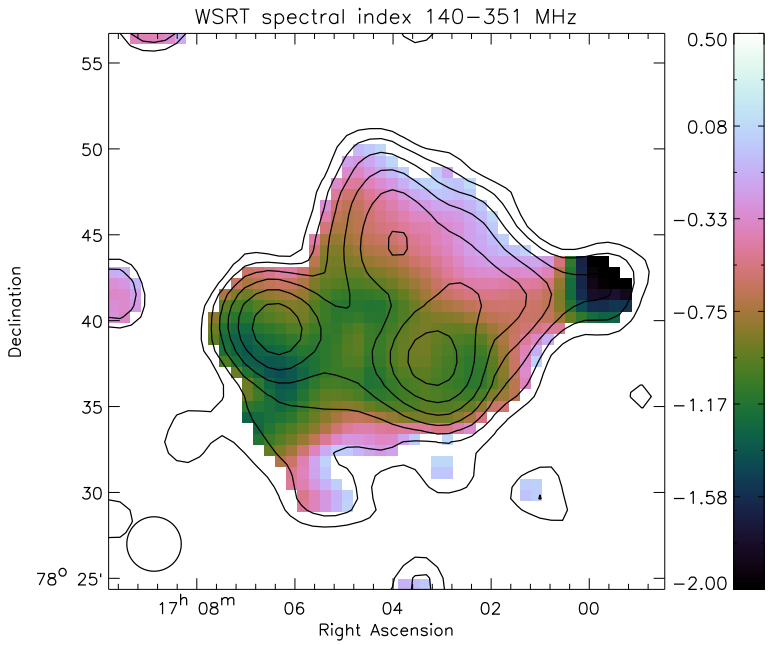

Figure 11.2: WSRT spectral index map between 140 and 351 MHz. Total intensity contours at 140 MHz are shown at levels of [1, 2, 4, 8, 16, 32, ...] ×18 mJy beam^{-1}. The total intensity map is a linear combination of six IFs between 115 and 165 MHz. The 351 MHz image was taken from Brentjens (2008).

Optical images at the position of the radio sources are also shown in Fig 11.1. At a redshift of 0.0581 any cluster member capable of hosting an AGN should be visible in our optical images. We cannot unambiguously identify an optical counterpart for sources AH and AI. The western part of source AG may be identified with a background galaxy, (most likely) located behind the cluster. However, no radio source at this location is found in 1.4 GHz Very Large Array (VLA) images (Clarke & Ensslin 2006), indicating the source must have a steep spectrum.

11.3.1 Spectral indices

Sources AG+AH are detected in each individual WSRT band. Source AI is probably detected ($\sim 3\sigma$) in a deep low-resolution (175″) WSRT 140 MHz continuum image, a combination of images from six IFs convolved to 175″ resolution, see Fig. 11.2 (the images of two IFs affected by strong RFI have been left out). By fitting a single spectral index through the 6 individual IFs, it was found that the spectral index around AG+AH was steeper by about -1.5 units than that of the main relic to the east. A better spectral index map was created using the 351 MHz image from Brentjens (Fig. 2 convolved to a resolution of 175″). The spectral index of AG+AH in this map is -2.05 ± 0.14.

Sources AG, AH and AI are not detected in deep 1369, 1413, 1513, and 1703 MHz VLA C-array (L-band) observations from Clarke & Ensslin (2006), which have noise levels of 34, 40, 40, and 43 μJy beam^{-1}, respectively. This implies a steep spectrum for these sources and rules

out an identification as a radio-loud AGN within the cluster (which have a typical spectral index of −0.7). We combined these four L-band images to create a deeper image, using the 1369 MHz image as a reference. The images were all convolved to a beam size of 16″ × 16″. The images were scaled to a common flux scale by adopting different spectral indices ranging between −0.5 and −3.0, but we did not detect the diffuse sources in any of these combined maps. Using a spectral index scaling of −1.0 resulted in a noise level about a factor 0.7 lower compared to the 1369 MHz image. We have taken this image to derive an upper limit on the spectral index between 1369 and 325 MHz. The local rms noise level near AI in the combined L-band image is 58 μJy beam^{-1}. AI covers an area of 61 beams (using the same area over which we measured the integrated flux as reported in Sect. 11.3). Assuming that the noise scales $\propto \sqrt{N_{\rm beams}}$, with $N_{\rm beams}$ the number of beams, this gives an upper limit for the 1369 MHz flux of 1.36 mJy, using a signal to noise ratio of (SNR) of 3 for a detection. Combined with the 325 MHz flux this implies that $\alpha < -1.45$ for AI (between 325 and 1369 MHz). We do a combined analysis for sources AG and AH as they are not separable in the spectral index map. The rms noise level near AG+AH is 40 μJy beam^{-1}. The sources cover an area of 92 beams, which gives an upper limit of 1.15 mJy for the 1369 MHz flux, implying that $\alpha < -1.95$ (between 325 and 1369 MHz). This is consistent with the spectral index of -2.05 ± 0.14 between 140 and 351 MHz.

11.4 Discussion

Three different origins have been proposed for the presence of radio relics in clusters: (i) in-situ acceleration by the DSA mechanism, (ii) adiabatic compression of fossil radio plasma (producing radio *phoenices*), and (iii) *AGN relics*. The first mechanism is thought to be responsible for the presence of giant Mpc-size radio relics in the periphery of clusters, as is the case for the well known bright relic in A2256. In the second case a passing shock wave in the ICM adiabatically compresses fossil radio plasma, producing a radio phoenix. The morphologies of such sources can be filamentary or toroidal (Enßlin & Brüggen 2002). This radio plasma is proposed to originate from a previous episode of AGN activity. After the electrons have lost most of their energy they become invisible as “radio ghosts”. At the passage of a shock wave they are revived (their brightness increases) and they become visible again with very steep radio spectra. The size of these sources is in general limited to a few hundred kpc as the time to compress larger ghosts would remove most of the energetic electrons responsible for the radio emission by radiative energy losses (Clarke & Ensslin 2006). Radio plasma which originated from a previous episode of AGN activity can remain visible as a steep-spectrum AGN relic. These sources are generally fainter than radio phoenices of the same age, as no compression of radio plasma has taken place (Enßlin & Gopal-Krishna 2001; Enßlin & Brüggen 2002). These AGN relics do not require shocks from cluster mergers.

The two radio sources to the west of the cluster center are probably radio phoenices or AGN relics, as they have steep radio spectra, relatively small sizes, are not clearly identified with galaxies, and diffuse in nature. Since the cluster is undergoing a merger, and the sources do not show a symmetric double lobe structure (like some of the AGN relics found by Dwarakanath & Kale (2009)), these sources are more likely to be radio phoenices than AGN relics. Spectral modeling as carried out by e.g., Intema (2009) and Dwarakanath & Kale (2009) can be used to separate between these two scenarios. At present we do not have enough flux measurements for our sources available to carry out such an analysis. Source AI is located at the edge of the radio

halo, this source could be a radio phoenix or a faint radio relic tracing a shock front.

Since the plasma from both radio phoenices and AGN relics should originate from AGN, we have searched for any nearby galaxies that could have harbored an AGN. These galaxies are marked with red crosses in Fig. 11.1. Sources AG and AH are located at the end of head-tail source C. It could be that the radio plasma originated from this tail. Other galaxies located in the cluster are also present in the neighborhood: 2MASX J17002352+7842076 ($z = 0.058834$, Berrington et al. 2002), is located at the position of AG. For AH we find two possible galaxies, Abell 2256:[BLC2002] 0056 ($z = 0.056518$) to the north, and 2MASX J16594813+7842055 ($z = 0.055357$) to the south. However, none of these are classified as a giant ellipticals which are more likely to have been active. A typical maximum age for a radio phoenix is 10^8 yr (Enßlin & Gopal-Krishna 2001). Using the velocity dispersion of 1269 km s^{-1} (Miller et al. 2003) for A2256, the displacement radius would be around 130 kpc ($\sim 2'$). This radius could be several times larger if the radio plasma is older, or if the host galaxy has a higher peculiar velocity. Within the range of several hundreds of kpc many cluster members are found, we therefore cannot identify the sources of the radio plasma.

There are about 50 elliptical galaxies within the cluster which can host an AGN, 15 of which are observed to be radio-loud (Miller et al. 2003; Berrington et al. 2002). This radio-loud fraction is consistent with the results from Best et al. (2005) for the general population of massive galaxies. Enßlin & Gopal-Krishna (2001) showed that the fossil radio plasma in radio ghosts needs to be revived within 10^8 to 10^9 yr to become a radio phoenix, depending on the synchrotron losses. Here we adopt the more conservative value of 10^8 yr. The number of radio phoenices in a cluster ($N_{\rm phoenix}$) is the product of the number of inactive AGNs in a cluster, that produced radio ghosts less than 10^8 yr old ($N_{\rm ghost}$), and the fraction of them being compressed ($f_{\rm compressed}$) by (merger) shocks waves: $N_{\rm phoenix} = N_{\rm ghost} \times f_{\rm compressed}$. To estimate $N_{\rm ghost}$ one needs to know which fraction of elliptical galaxies in a cluster goes through phases of AGN activity and their duty cycle. These numbers are not well constrained, but we know that the fraction of active AGN is at least $15/50 = 0.3$ in the case of A2256. Estimates for the duty cycle of AGN are around 10^8 yrs (e.g., Bîrzan et al. 2004; Pope et al. 2006; Shabala et al. 2008), but these estimates vary by an order of magnitude and are only for cD galaxies in the center of cool core clusters. Although it is difficult to estimate the number of radio phoenices in a cluster, the fact that there are several radio phoenices in A2256 makes it likely that other merging clusters have radio ghosts, which have been revived by merger shock waves and are visible as radio phoenices.

11.5 Conclusions

We have presented GMRT 325 MHz radio observations of the cluster Abell 2256. Our radio maps reveal the presence of three diffuse sources located in the periphery of the cluster. The sources have a steep spectrum. For the combined emission from AG and AH we find $\alpha = -2.05 \pm 0.14$ between 140 and 351 MHz. For AI we set an upper limit of $\alpha < -1.45$ between 325 and 1369 MHz. Optical images do not reveal any obvious counterparts. Source AI could be a faint radio relic tracing a shock front in the ICM or a radio phoenix. Detailed spectral index modeling and/or deep X-ray observations (searching for shock fronts within the ICM) could be used to separate between these scenarios. Sources AG & AH are most likely radio phoenices, fossil radio plasma from a previous episode of AGN activity that has been compressed by merger

shock waves. Although, we cannot exclude the possibility that the sources are AGN relics. In this case the sources might be related to the long head-tail source C within the cluster.

Most massive merging clusters should possess similar sources, considering the timescales related to AGN activity, the number of active AGN in clusters, the presence of shocks, and synchrotron and IC losses. These sources are very faint at high-frequencies ($\gtrsim$ 1 GHz) so they have gone previously unnoticed. Since the radio spectra of these sources are steep, they will probably determine the observed appearance of clusters in low-frequency radio maps as will be produced for example by LOFAR (Röttgering et al. 2006) or the Long Wavelength Array (LWA; Kassim & Erickson 2008).

Acknowledgements. We would like to thank Michiel Brentjens for providing the 351 MHz WSRT map. We thank the staff of the GMRT who have made these observations possible. GMRT is run by the National Centre for Radio Astrophysics of the Tata Institute of Fundamental Research. The Westerbork Synthesis Radio Telescope is operated by the ASTRON (Netherlands Institute for Radio Astronomy) with support from the Netherlands Foundation for Scientific Research (NWO). The William Herschel Telescope is operated on the island of La Palma by the Isaac Newton Group in the Spanish Observatorio del Roque de los Muchachos of the Instituto de Astrofsica de Canarias. Basic research in radio astronomy at the NRL is supported by 6.1 Base funding. RJvW acknowledges funding from the Royal Netherlands Academy of Arts and Sciences.

CHAPTER 12

LOFAR Abell 2256 observations between 18 and 67 MHz

Abstract.

Abell 2256 is one of the best known examples of a galaxy cluster hosting large-scale diffuse radio emission that is unrelated to individual galaxies. It contains both a giant radio halo and a relic as well as number of head-tail sources and smaller diffuse steep-spectrum radio sources. The origin of radio halos and relics is still being debated, but over the last years it has become clear that the presence of these radio sources is closely related to galaxy cluster merger events. Here we present the first LOFAR Low-band antenna (LBA) observations of Abell 2256 between 18 and 67 MHz. To our knowledge, the images made at 20, 30 and 63 MHz are the deepest ever obtained at frequencies below 100 MHz. Both the radio halo and the giant relic are clearly detected in the LBA image at 63 MHz, and the diffuse radio emission remains visible at frequencies as low as 20 MHz. The observations confirm the presence of a previously claimed ultra-steep spectrum source to the west of the cluster center with a spectral index of -2.3 ± 0.4 between 63 and 153 MHz. The steep spectrum suggests that this source is an old part of the head-tail radio source C in the cluster. For the radio relic we find an integrated spectral index of -0.81 ± 0.03, after removing the flux contribution from the other sources. This flat integrated spectral index could indicate that in the observed frequency range the electron cooling time is longer than the age of the relic. If shocks are assumed to be responsible for relic formation, this would imply that the relic traces a shock that only recently formed (within the last ~ 0.1 Gyr). In the radio halo region we find indications of low-frequency spectral steepening.

R. J. van Weeren et al., on behalf of the LOFAR collaboration

to be submitted

12.1 Introduction

Radio halos and relics are diffuse radio sources, unrelated to individual galaxies, found in disturbed galaxy clusters (see the reviews by Feretti 2005; Ferrari et al. 2008, and references therein). These sources are rare – only several dozen examples have been previously identified. The presence of diffuse radio emission indicates magnetic fields and relativistic particles in the intracluster medium (ICM) that are (re)accelerated in-situ, due to the limited lifetime of the synchrotron emitting electrons (Jaffe 1977). The origin of this diffuse emission is presently still being debated and is crucial for understanding the non-thermal component in the ICM and particle acceleration mechanisms.

Over the last decade it has become clear that the diffuse radio emission in galaxy clusters is often related to galaxy cluster merger events (e.g., Cassano et al. 2010b; van Weeren et al. 2010). It is also predicted in the framework of the concordant cosmological model that galaxy clusters grow as a result of the mergers of smaller clusters and sub-structures creating turbulence and shocks (e.g., Markevitch et al. 2002; Vazza et al. 2006; Russell et al. 2010) in their ICM.

Diffuse sources in merging clusters have commonly been classified as radio *relics* and *halos*. In this context, elongated filamentary sources have generally been called relics. Relics are usually further subdivided into three classes (see also Kempner et al. 2004). (1) *Radio Gischt* are large extended arc-like sources mostly found in the outskirts of galaxy clusters. They are often highly polarized at frequencies $\gtrsim$ 1 GHz (20% or more). It has been proposed that they directly trace shock waves (Ensslin et al. 1998; Miniati et al. 2001), in which particles are accelerated by the diffusive shock acceleration mechanism (DSA; Blandford & Ostriker 1978; Drury 1983; Blandford & Eichler 1987; Jones & Ellison 1991; Malkov & O'C Drury 2001) in a first-order Fermi process. A related scenario is that of shock re-acceleration of pre-accelerated electrons in the ICM, which may be a more efficient mechanism in weak shocks (e.g., Markevitch et al. 2005; Giacintucci et al. 2008; Kang & Ryu 2011) and might be needed because the efficiency with which collisionless shocks can accelerate particles is unknown, and might not be enough (e.g., Macario et al. 2011) to produce the observed radio brightness. The pre-accelerated electrons could for example originate from the radio galaxies in clusters. (2) *Radio phoenices* are most likely related to fossil radio plasma from previous episodes of AGN activity adiabatically compressed by merger shock waves, boosting the radio emission (Enßlin & Gopal-Krishna 2001; Enßlin & Brüggen 2002). (3) *AGN relics* trace old (uncompressed) radio plasma from previous episodes of AGN activity. The radio spectra of both radio phoenices and AGN relics are expected to be steep ($\alpha \lesssim -1.5$, $F_\nu \propto \nu^\alpha$, where α is the spectral index) and curved due to synchrotron and Inverse Compton (IC) losses.

Radio halos are extended sources with sizes of about a Mpc. They are typically unpolarized and their radio emission roughly follows the thermal X-ray emission from the ICM. Two classes of models have been put forward to explain the origin of these halos. In the first model the energetic electrons are the secondary products of proton-proton collisions (e.g., Dennison 1980; Blasi & Colafrancesco 1999; Dolag & Enßlin 2000; Enßlin et al. 2011). In the second model the electrons are re-accelerated in-situ through a second order Fermi mechanism by magneto-hydrodynamical (MHD) turbulence (e.g., Brunetti et al. 2001; Petrosian 2001) The existence of ultra-steep spectrum radio halos (USSRH, $\alpha \lesssim -1.5$, Brunetti et al. 2008; Macario et al. 2010; Dallacasa et al. 2009) does not support a secondary origin for the electrons as it requires an unrealistic amount of energy in the relativistic protons (Brunetti 2004).

Abell 2256 is a nearby, $z = 0.0581$ (Struble & Rood 1999), cluster that contains a giant

radio halo, relic and a large number of tailed radio galaxies. The relic has a large integrated flux, compared to other relics, of about 0.5 Jy at 1.4 GHz. The large angular extent of the diffuse emission and its large integrated flux make it a prime target for low-frequency observations which typically suffer from low spatial resolution and sensitivity, compared to observations at high frequencies ($\gtrsim$ 1 GHz).

The cluster hosts a handful of head-tail radio sources as well as several smaller diffuse radio sources not directly related to individual galaxies (Bridle & Fomalont 1976; Bridle et al. 1979; Röttgering et al. 1994; Miller et al. 2003; Clarke & Ensslin 2006; Brentjens 2008; Intema 2009; van Weeren et al. 2009a; Kale & Dwarakanath 2010). X-ray and optical observations provide strong evidence that A2256 is undergoing a merger event between a main cluster ($T_{\rm ICM} \sim$ 7–8 keV), a major sub-structure ($T_{\rm ICM} \sim 4.5$ keV) and, possibly, a third infalling group (Briel et al. 1991; Briel & Henry 1994; Sun et al. 2002; Berrington et al. 2002; Miller et al. 2003). The cluster has an X-ray luminosity of $L_{\rm X,\ 0.1-2.4\ keV} = 3.7 \times 10^{44}$ erg s^{-1} (Ebeling et al. 1998).

At wavelengths larger than 1 m, the diffuse radio emission in A2256 has been studied with the GMRT at 150 MHz (Intema 2009; Kale & Dwarakanath 2010), and with the WSRT between 115 and 165 MHz (van Weeren et al. 2009a; Intema 2009). The VLSS 74 MHz image (Cohen et al. 2007) shows a hint of diffuse emission, and the 8C and 6C survey images (Hales et al. 1995; Masson & Mayer 1978) have too low resolution to properly separate the flux contributions from the discrete sources. The observations by Intema (2009) and van Weeren et al. (2009a) showed the presence of three previously unknown diffuse sources with steep radio spectra ($\alpha \lesssim -1.5$). These steep radio spectra suggest that these sources trace old radio plasma from previous episodes of AGN activity in the cluster.

In this paper we present the first LOFAR observations of Abell 2256, focussing on the frequency range around 63 MHz. The layout of this paper is as follows: In Sect. 12.2 we give an overview of the observations and the data reduction. In Sect. 12.2.1 we present the results, including the radio images and a spectral index map. We conclude with a discussion and the results presented in Sects. 2.6 and 2.7, respectively. Throughout this paper we assume a ΛCDM cosmology with $H_0 = 71$ km s^{-1} Mpc^{-1}, $\Omega_{\rm m} = 0.3$, and $\Omega_\Lambda = 0.7$.

12.2 Observations & data reduction

Abell 2256 was observed with LOFAR on July 15, 2011, with the LBA system for 10 hrs, mostly during night-time. Complete frequency coverage between 18 and 67 MHz was obtained, although there were a few gaps at frequencies where usually strong radio frequency interference (RFI) is present. All four linear correlation products were recorded. The observed frequency range was divided into 244 sub-bands (IFs), each having a bandwidth of 0.1953 MHz. Each sub-band was subdivided into 64 frequency channels. The integration time was 1 s. The so-called LBA_OUTER configuration was used for the LBA stations. In this mode 48 (of 96) LBA antennas are used, located mostly in the outer part of the antenna fields/stations (which have diameters of about 80 m). This increases the sidelobe levels for the station beams but reduces the field of view (FOV) with respect to other station antenna configurations.

In total 25 stations (8 remote and 17 core) were used for the A2256 observation. The longest baseline, between stations RS208 and RS509, is about 80 km and the shortest baselines corresponds to $\sim$ 90 m. The uv-coverage is shown in Fig. 12.1. The FOV (FWHM of the primary beam) is about 4.6° and 9.2° at 60 and 30 MHz, respectively. It should be noted though that

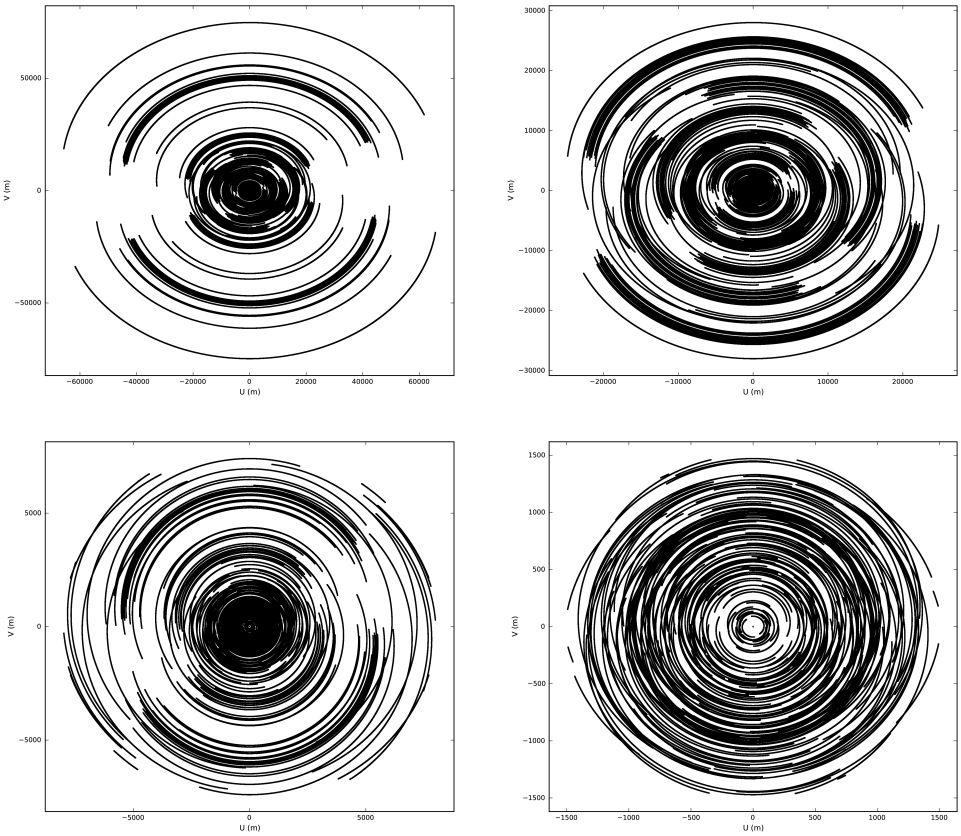

Figure 12.1: UV-coverage of the observations. The outer UV-coverage is shown in the top left frame, the next frames progressively zoom inwards. The relatively broad bandwidth fills the uv-plane radially (not shown in the figures).

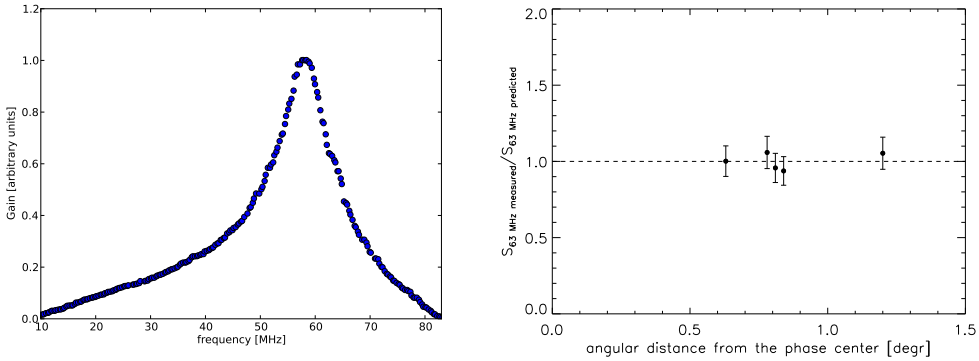

Figure 12.2: Left: LBA global bandpass. The bandpass peaks at about 58 MHz. Right: Measured LOFAR fluxes and predicted fluxes for 5 bright sources in the A2256 field. For all these sources 8C, VLSS, 7C, WENSS, and NVSS fluxes were available. We used second order polynomial fits in $\log(S) - \log(\nu)$ space to compute the predicted 63 MHz fluxes. An overall scaling factor of 1.23 was applied to the LOFAR fluxes. The error bars display the adopted 10% uncertainty in the flux scale.

the stations beams are complex-valued, time and direction dependent, and slightly differ from station to station.

As a first step, the RFI was flagged with the AOFlagger (Offringa et al. 2010) using default settings, and the first and last two channels at the edge of each sub-band were removed. The amount of RFI flagged was typically only few percent or less above 30 MHz. The amount of RFI increases strongly below $\sim$ 28 MHz. Between 30% and 70% had to be flagged below this frequency for most sub-bands, with at least some of this attributable to short-wave radio transmissions. The RFI situation was somewhat better after midnight. After flagging, the data were averaged in time to 5 s.

For this A2256 observation, the bright radio sources Cas A, Cyg A and Vir A (the so-called "A-team sources") were located 34, 42, and 74° away from the phase center, respectively. These sources have integrated flux densities of about 17764, 17205, and 2085 Jy at 74 MHz, respectively. Therefore the attenuated signals from Cas A and Cyg A are still much stronger (more than a factor of 10) than the signal from the sources in the primary FOV. Their amplitudes are strongly modulated as they move in and out of the station beam sidelobes. For the first 2.5 hr of the observations Vir A also affects the observed visibilities, until the source sets below the horizon. At frequencies $\lesssim$ 35 MHz, 3C 390.3 (located 4.7° from the phase center) is sufficiently bright, 145 ± 14 Jy at 38 MHz (Hales et al. 1995), that it needs to be treated separately as described below.

The first calibration step consisted of the removal of the three "A-team" sources. Below 35 MHz, 3C 390.3 was also included in the calibration model. For the models of the A-team sources and 3C 390.3 we used the clean component models at 74 MHz from VLA A-array[1] observations (Kassim et al. 2007) with resolution of 25″. For all calibration steps we used the BlackBoard Selfcal (BBS) software (e.g., Heald et al. 2010). Full polarization direction

[1]http://lwa.nrl.navy.mil/tutorial/

dependent complex gain solutions were obtained for the three A-team sources (and 3C 390.3 below 35 MHz) independently per sub-band. Vir A was only included in the calibration model for the first 2.5 hr. In general, high-quality solutions were obtained for Cas A and Cyg A, while the solutions for Vir A and 3C 390.3 were noisier due to their lower apparent fluxes. The A-team sources were then subtracted ("peeled") with the estimated gain solutions. 3C390.3 was not subtracted as it is in the main FOV below 35 MHz and used in subsequent calibration steps. After removal of the A-team sources from the visibility data we performed another round of flagging with the AOFlagger and averaged the data to 4 channels and 10 sec per sub-band, to decrease the size of the dataset whilst mitigating bandwidth and time smearing effects in the central FOV.

The responses of the LBA antennas depends on the observed frequency (see Fig. 12.2). The LBA response was obtained from observations of Cyg A. Observations carried out over the course of several months show that the bandpass response is stable at the few precent level or better. We divided out this sensitivity pattern to avoid the need to obtain amplitude calibration solutions for each individual sub-band. The reason behind this is that the signal to noise ratio (SNR) per sub-band is not sufficient to obtain good gain solutions due to the limited effective bandwidth of 0.183 MHz. By combining several sub-bands this limitation can be overcome. However, a problem at low frequencies is that the ionospheric phase distortions are frequency dependent, and this effect increases towards lower frequencies. At about 60 MHz this means that if this effect is not included only about 1 MHz bandwidth can be used for calibration, depending on the ionospheric conditions (e.g., eq. 4 from Intema et al. 2009). To obtain high-quality solutions more bandwidth is required. This can be accomplished by solving for the differential total electron content: TEC. This adds a frequency dependent phase term (TEC/ν). During the calibration we therefore solve for a single polarization dependent complex gain factor (to set the amplitudes and capture other instrumental effects such as clock drift) and polarization independent TEC value per station and time-slot (10 s). We used 20 sub-bands around 20 MHz, 20 around 30 MHz, and 30 around 63 MHz for this "global calibration" including TEC solving. Due to computational limitations we concentrated our efforts on these three frequency ranges.

We calibrated the data against a 74 MHz 80″ VLSS model of the field around A2256 (covering $15^\circ \times 15^\circ$), assuming that all sources are unpolarized, which is a reasonable assumption at these low frequencies. We used an overall flux scaling with a spectral index of -0.8 to get a first order approximation of the flux-scale. For computing the model visibilities we included the complex beam attenuation of each station beam.

12.2.1 Primary beam correction, absolute flux-scale and self-calibration

We applied the calibration solutions and corrected the data for the each station's beam response in the phase center. Note that it is only possible to correct for the stations beam response in a single direction. For the other directions (within the main FOV) this correction is only a first order approximation. The entire FOV (to an attenuation factor of 0.15 compared to the beam center) was then imaged and cleaned with Casapy with w-projection (Cornwell et al. 2005, 2008), 768 w-planes in total. Ideally, to create flux corrected wide-field images, the time-variable direction dependent effects need to be taken into account (e.g., Bhatnagar et al. 2008). This functionality is still under development. We made images with "briggs" weighting (Briggs 1995) with robust=-0.1, a compromise between resolution and sensitivity to emission at larger spatial scales. We combined groups of sub-bands around 63, 30 and 20 MHz for multi-frequency

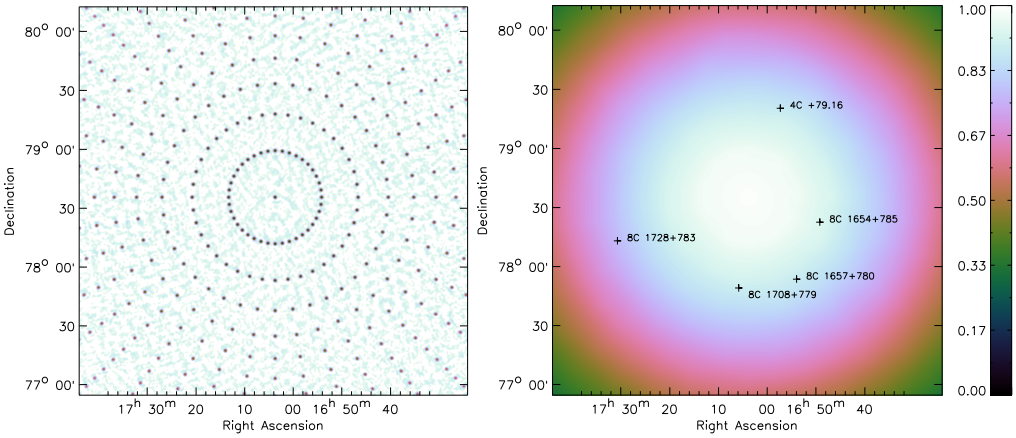

Figure 12.3: Left: Simulated point sources of 1 Jy in the A2256 field at 63 MHz. Right: Effective primary beam attenuation of the A2256 observations at 63 MHz, fitting a surface to the integrated fluxes of the sources in the left panel. Sources which were used to obtain the flux-scale are marked.

synthesis imaging, producing three broadband images.

To obtain the correct relative flux scale over the field we simulated a dense grid of 1 Jy point sources in the A2256 field including the LOFAR station beam. This grid is illustrated in Fig. 12.3. With this we could track the effective beam attenuation as a function of position in the FOV. This simulated dataset (with the same frequency setup and uv-coverage as the observed data) was then imaged the same way as the observed A2256 data. We extracted the integrated fluxes for these simulated point sources using the `PyBDSM` source detection software[2]. A 2D surface was fitted to these extracted source fluxes using the `griddata` module from the python matplotlib, which employs a Delaunay triangulation[3]. This triangulated surface gives the effective sensitivity as function of position in the A2256 field and can be used to create a primary beam corrected image. We used the flux-corrected image to obtain an updated sky model (again with `PyBDSM`) for a subsequent round of self-calibration (the calibration strategy remaining unchanged).

The final images (robust=−0.1) have noise levels of 10, 43, 250 mJy beam^{-1} at 60, 30 and 20 MHz respectively. A lower resolution, robust=0.5 weighting, image at 63 MHz has a noise of 25 mJy beam^{-1}. See Table 12.1 for a summary of the resolution, bandwidth and sensitivity of the images. Thermal noise is expected to be around 2.5 mJy beam^{-1} at 63 MHz and 8 mJy beam^{-1} at 30 MHz.

The presence of residual ionospheric phase errors after calibration lead to a wider point source width. We measure a point source width that is about 20″ larger than the synthesized beamwidth at 63 MHz. This effect has also been seen for 74 MHz VLA observations (e.g., Cohen et al. 2007). At lower frequencies this worsens to 70″ and 180″ at 30 and 20 MHz, respectively. In this case the unresolved sources are elongated, distorted, and partly broken up into smaller components. Because of this reason, we only use the 63 MHz maps for quantitative

[2]see the LOFAR Imaging Cookbook at http://www.astron.nl/radio-observatory/lofar/lofar-imaging-cookbook
[3]http://matplotlib.sourceforge.net

Table 12.1: LOFAR LBA images

central frequency MHz	image bandwidth MHz	$\sigma_{\rm rms}$ mJy beam^{-1}	synthesized beam arcsec
63 (robust -0.1)	5.5	10	22×26
63 (robust 0.5)	5.5	25	52×62
30 (robust -0.1)	3.7	43	58×69
20 (robust -0.1)	3.7	250	108×116

analysis in this paper, while the 30 and 20 MHz maps are used for qualitative analysis until a more complete ionospheric correction is made.

To obtain and check the overall flux scale we measured the integrated fluxes for five bright sources in the FOV: 4C +79.16 , 8C 1654+785, 8C 1657+780, 8C 1708+779, and 8C 1728+783 (see Fig. 12.3). For these sources we collected flux measurements from the 1.4 GHz NVSS (Condon et al. 1998), 325 MHz WENSS (Rengelink et al. 1997), 151 MHz 7C (Hales et al. 2007), 74 MHz VLSS (Cohen et al. 2007) and 38 MHz 8C (Hales et al. 1995) surveys. We fitted second order polynomials to these flux measurements in $\log(S) - \log(\nu)$ space and compared the LOFAR flux measurements at 63 MHz against the predicted fluxes from the polynomial fits. The median of correction factors was used to tie the LOFAR images to an absolute flux-scale. The correction factor we found was modest, being 1.23 at 63 MHz. The spread in the individual correction factors is about 7%, see Fig 12.2 (right panel).

From this we adopt a conservative error in the LOFAR flux scale of 10% compared to these surveys.

12.2.2 Radio images

The 63 MHz images are displayed in Fig. 12.4 and the 20 and 30 MHz images in Fig. 12.5. We labelled some of the known sources in the cluster following the scheme from Bridle & Fomalont (1976); Röttgering et al. (1994); van Weeren et al. (2009a). The LOFAR 63 MHz image reveals some of the well-known tailed radio sources (A, B, F), the main relic (G and H), and part of the radio halo. A hint of the long and straight head-tail source C is also visible.

The main radio relic and halo are somewhat better visible in the lower resolution 63 MHz image (Fig. 12.4, right panel). Interestingly, the LOFAR image also reveals source AG+AH. This source has only been recently discovered (van Weeren et al. 2009a) and is not visible in the deep VLA L-band observations from the VLA (Clarke & Ensslin 2006), implying a steep spectral index. We do not detect the steep spectrum source AI, but this was expected since the integrated flux of this source is about a factor of two lower than AG+AH at 325 MHz. The 30 MHz image reveals source F and the combined emission from A and B. The relic is also detected. At 20 MHz the ionospheric phase distortions are quite severe, causing the relic to partly blend with sources F and the A+B complex.

An overlay of the 63 MHz image with a VLA L-band image is shown in Fig. 12.6 (right panel). For this we combined 1369, 1413, 1513, and 1703 MHz VLA C-array images from Clarke & Ensslin (2006). These images were convolved to a common resolution of $16'' \times 16''$ and combined adopting a flux scaling according to a spectral index, $\alpha = -1$. It is interesting

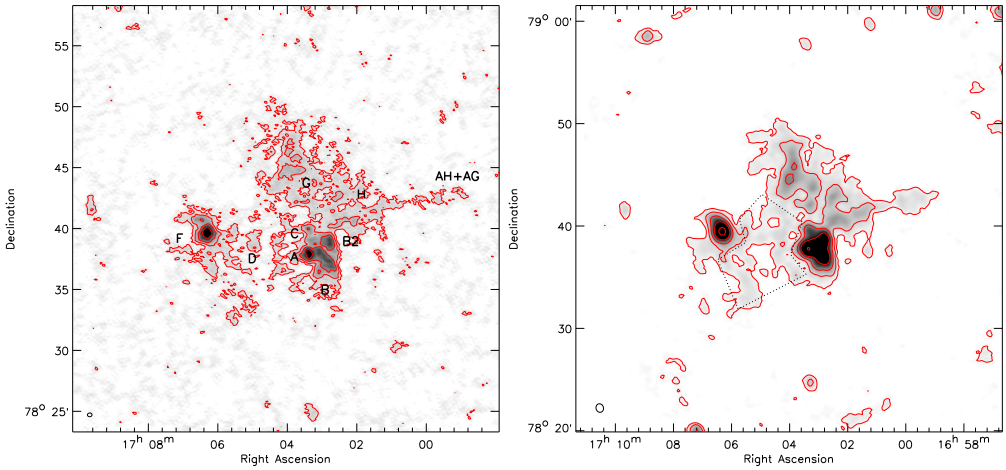

Figure 12.4: A2256 61-67 MHz images. Left: High-resolution, 22″ × 26″, image made with robust=-0.1 weighting. Contour levels are drawn at $[1, 2, 4, \ldots] \times 3\ \sigma_{\rm rms}$. Right: Low-resolution image, 52″ × 62″, image made with robust=0.5 weighting. The area for the halo spectral index measurement is indicated by the dotted lines. Contours are drawn as in the left panel.

to note the differences between the L-band and LBA images around the A+B complex. The VLA image peaks in brightness at the "heads" of the head-tail sources, while the LOFAR image mainly shows the "tails". The steep spectrum B2 region, noticed by Intema (2009), also clearly stands out. A Chandra X-ray overlay is shown in Fig. 12.7.

12.2.3 Spectral index map and integrated fluxes

We made a spectral index map between 63 and 351 MHz, making use of the WSRT 351 MHz map from Brentjens (2008). We made a LOFAR image with uniform weighting of the visibilities and applying a Gaussian taper in the uv-plane to approximately match up the WSRT resolution of 67″ ×67″. To increase the SNR per beam for the diffuse emission we convolved both images to 100″ resolution, pixels below $3\sigma_{\rm rms}$ were blanked. The LOFAR-WSRT spectral index map is shown in Fig. 12.6 (left panel).

The spectral index map reveals that the relic has a relatively flat spectral index of about −0.8 with variations of 0.3 in α across the structure. For the parts of the radio halo where the spectral index can be measured we find α to be in the range −1.0 to −1.7. For source F the spectral index is around −1.0. For the combined emission from AH and AG we find a steep spectral index between −2.2 to −1.7.

We extracted the integrated fluxes for sources in the cluster from the 63 MHz image, see Table 12.2. The integrated fluxes of the radio halo and relic (source G+H) are difficult to measure as they are partly blended with some of the complex head-tail radio sources in the cluster. To estimate their flux contribution we used both the high and low resolution images (Fig. 12.4). From the high resolution image we measured the fluxes for source F, and the combined emission from A and B (A+B). Head-tail source C contributes a significant amount of flux to the relic

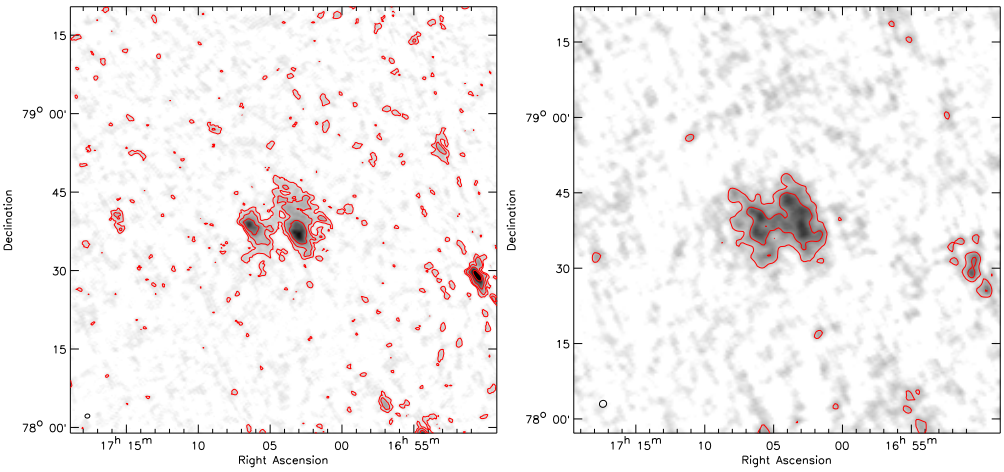

Figure 12.5: A2256 30 and 20 MHz images. Left: 28–32 MHz image with a resolution, 58″×69″. Contour levels are drawn at $[1, 2, 4, \ldots] \times 3\ \sigma_{\rm rms}$. Right: 18–22 MHz image with a resolution of 108″ × 116″. Contours are drawn as in the left panel. Both images were made with robust=0.1 weighting. The bright compact source to the west around RA 17^h51^m is 8C 1654+785.

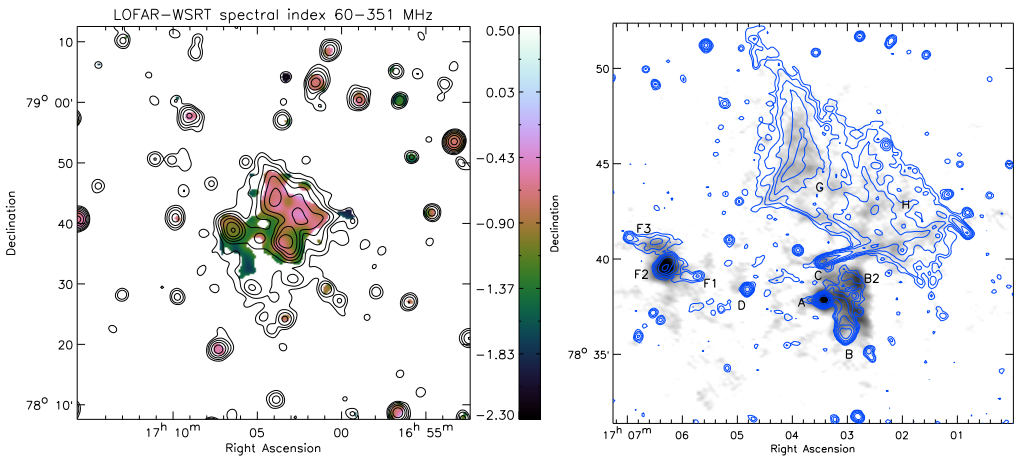

Figure 12.6: Left: LOFAR LBA - WSRT spectral index map between 63 and 351 MHz. Total intensity contours at 351 MHz are shown at levels of $[1, 2, 4, 8, \ldots] \times 1.0$ mJy beam^{-1}. The 351 MHz image comes from Brentjens (2008). Right: LOFAR LBA 63 MHz image overlaid with VLA L-band C-array contours. The contour levels are drawn at $[1, 2, 4, 8, \ldots] \times 90\ \mu$Jy beam^{-1}.

Table 12.2: 63 MHz source fluxes

Source	$S_{63\mathrm{MHz}}$ Jy	α_{63}^{153}
A+B	5.1 ± 0.6	−1.1 ± 0.2
F	2.8 ± 0.3	−1.2 ± 0.2
AG + AH	0.75 ± 0.10	−2.3 ± 0.4
relic (G + H)	5.6 ± 0.8	−0.81 ± 0.03[a]
halo	6.6 ± 1.3	−1.3 ± 0.1[b]

[a] from a polynomial fit in $\log(S) - \log(\nu)$ space, see Fig. 12.8 (left panel)
[b] between 63 and 351 MHz, α taken from Fig. 12.8 (right panel)

emission, as judged from the GMRT 153 MHz image from Intema (2009). In the 63 MHz image the source blends with the radio relic, making it impossible to obtain a reliable flux estimate. Using the 153 MHz GMRT image (giving a flux of 0.48 ± 0.05 Jy) and the reported 327 MHz VLA flux (0.247 ± 0.020 Jy, Röttgering et al. 1994) we find $\alpha = -0.87 \pm 0.17$ for source C. Extrapolating this to 63 MHz, we estimate a flux of 1.05 Jy. To measure the relic flux we summed the flux over the same region as indicated in fig. 10 by Brentjens (2008). After subtracting the flux contribution for source C we obtain a relic flux of 5.6 Jy, with an estimated uncertainty of 15%. A power-law fit through the relic flux measurements at 1369 (Clarke & Ensslin 2006), 351 (Brentjens 2008), 153 (Intema 2009), and 63 MHz gives a spectral index of -0.81 ± 0.03, see Fig. 12.8. For the radio halo we find a flux of 6.6 ± 1.3 Jy from Fig. 12.4 (right panel), integrating over the entire halo area as defined by the 351 MHz image.

12.3 Discussion

The results on the radio spectra for source F, AG+AH, and the radio halo and relic are discussed in the following subsections.

12.3.1 Source F

Source F is known for its complex Z-shape morphology (see Fig. 12.6) and steep radio spectrum (e.g., Bridle et al. 1979). The source is composed out of three smaller structures: F1, F2 and F3. The brightest component F2 has a toroidal filamentary shape (Röttgering et al. 1994; Miller et al. 2003; Intema 2009). F3 has been classified as a head-tail radio source associated with galaxy 122 (Fabricant et al. 1989). No optical counterparts have been found for F1 and F2, and their origin is still being debated. Bridle et al. (1979) suggested that all three components are the tail of galaxy 122, this scenario is also discussed by Brentjens (2008). In another scenario F2 could be the compressed fossil radio plasma from previous episodes of AGN activity (Enßlin & Gopal-Krishna 2001; Enßlin & Brüggen 2002), in this case the fossil plasma could also have originated from galaxy 122. This agrees with the observed toroidal shape (Enßlin & Brüggen 2002).

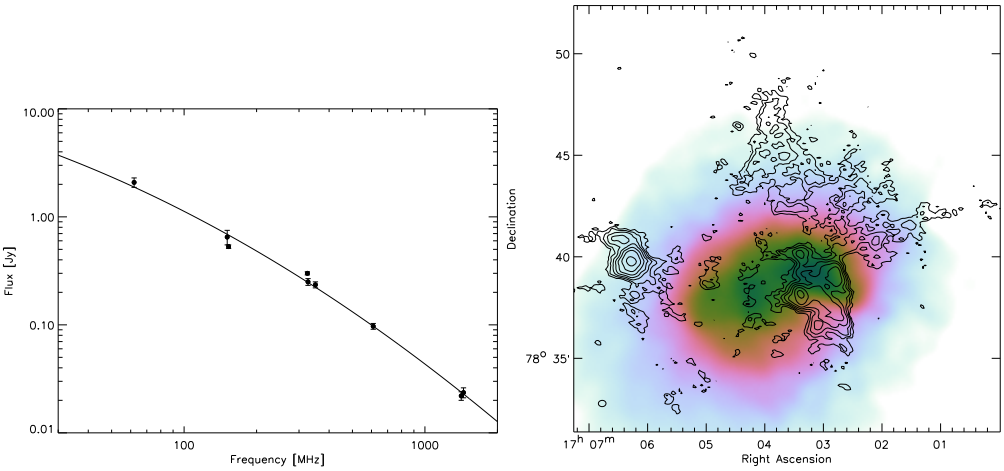

Figure 12.7: Left: Radio spectrum of F2. The fluxes were taken from the Brentjens (2008). Solid line is a second order polynomial fit through the flux measurements in $\log(S) - \log(\nu)$ space. During the fitting procedure we assumed 10% uncertainty in the flux measurements because flux measurement are not all consistent within their 1σ reported error. This prevents the fit to be forced to go through a few measurements with small reported uncertainties. Right: Chandra 0.5–7 keV ACIS-I/S co-added image smoothed by a variable-width Gaussian, fig. 1 from Sun et al. (2002). LOFAR 63 MHz contours from the high-resolution image are overlaid at levels of $[1, 2, 4, 8, \ldots] \times 3.5\ \sigma_{\rm rms}$.

We collected flux measurements for F2 from the literature (see Brentjens 2008), these are plotted in Fig. 12.7. The spectrum for F2 is clearly curved with the spectral index flattening towards lower frequencies. From the fit, see caption Fig. 12.7, we find a spectral index of -0.95 between 63 and 153 MHz. Between 150 and 350 MHz Kale & Dwarakanath (2010) reported $\alpha = -1.10 \pm 0.05$ (but no flux measurements were reported for F2). We however find a spectral index of -1.34 between 150 and 350 MHz using the polynomial fit. The reason for the difference is unclear, but it should be noted that the measurements from the literature are not consistent within their reported uncertainties. Between 610 and 1400 MHz we obtain $\alpha = -1.67$, much steeper than at low-frequencies. Brentjens (2008) estimated a possible break frequency to be located at 26 MHz, assuming a constant magnetic field of 7.3 μG and an ageing time of 0.2 Gyr. The 63 MHz flux measurement indicates the spectrum continues to flatten. However, high-resolution measurements below 60 MHz are needed to determine the possible underlying ("zero ageing") power-law component. The origin of source F2 remains unclear, although it is likely the source is somehow related to the fossil radio plasma from previous phases of AGN activity given its brightness and steep radio spectrum.

12.3.2 Source AG+AH

The combined emission from source AG+AH is detected in the LOFAR 63 MHz image. With the non-detection of these sources in the deep L-band image from Clarke & Ensslin (2006), van Weeren et al. (2009a) determined that $\alpha < -1.95$ between 325 and 1369 MHz. Between 140 and

351 MHz, using WSRT observations, the spectral index is -2.05 ± 0.14 at a resolution of 175″ (at this resolution the flux of this feature partly blends with the relic emission). With the 153 MHz image from Intema (2009) we find a flux of 95 ± 10 mJy for the combined emission from AG+AH. From the GMRT 325 MHz image we reported a flux of 19 ± 2 mJy (van Weeren et al. 2009a). This gives a spectral index of -2.1 ± 0.2 between these two frequencies, in agreement with the earlier reported result of -2.05 ± 0.14. The LOFAR flux is 0.75 ± 0.10 Jy for this source. This results in a spectral index of -2.3 ± 0.4 between 63 and 153 MHz. At low-frequencies the spectrum thus remains steep, although the uncertainty in the spectral index is too large to rule out a spectral turnover.

We consider the possibility that this emission is related to the head-tail source C. Following Miley (1980); Brentjens (2008) for a constant magnetic field and no adiabatic losses the radiative lifetime/spectral age (τ) is given as

$$\tau = \frac{2.6 \times 10^{10} \sqrt{B}}{\left(B^2 + B_{\rm CMB}^2\right)(1+z)\nu_{\rm brk}} \ \ [{\rm yr}] \,, \tag{12.1}$$

where B is the magnetic field strength in μG, $B_{\rm CMB}\,[\mu{\rm G}] = 3.25(1+{\rm z})^2$ the equivalent magnetic field strength of the microwave background and $\nu_{\rm brk}$ the break frequency in MHz. The LOFAR 63 MHz flux measurement indicates that $\nu_{\rm brk}$ is located $\lesssim 50$ MHz as the spectrum is still very steep between 63 and 153 MHz. The magnetic field is difficult to estimate as the spectral shape is poorly constrained. With a reasonable value of 10 μG we obtain a spectral age of 0.1 Gyr. This increases to 0.2 Gyr for $B = 5\,\mu$G. In all cases we assumed $\nu_{\rm brk} = 50$ MHz. Röttgering et al. (1994) estimated a velocity (v) of ~ 2000 km s^{-1} for the head-tail source. Then the separation between the "head" and AG+AH would be $v \times \tau = 200$ kpc, for $B = 10\,\mu$G. AG+AH is located about 800 kpc (projected distance) from the head of C. A lower magnetic field strength of $B = 3.0\,\mu$G would give a distance of 600 kpc. It is also possible that the break frequency is located at a lower frequency. If the radio plasma from the tail (the AG+AH part) is compressed by the merger shock wave, the radiative age of the source could be older (about 0.5 Gyr or more, e.g., Dwarakanath & Kale 2009; Kale & Dwarakanath 2011). This makes it easier to explain the distance of (at least) 800 kpc. Given all the uncertainties, source AG+AH could indeed be an old part of the tail of source C.

12.3.3 Radio relic and halo

Giant radio relics are proposed to trace particles (re)accelerated at shocks via the DSA mechanism. In the linear test particle regime, the injection spectral index is related to the Mach number ($\mathcal{M}$) of the shock (e.g., Blandford & Eichler 1987)

$$\alpha_{\rm inj} = \frac{1}{2} - \frac{\mathcal{M}^2 + 1}{\mathcal{M}^2 - 1} \,. \tag{12.2}$$

If the properties of the shock remain unchanged and the age of the shock is larger than the electron cooling time, the integrated radio spectrum will be a power-law, with a spectral index about 0.5 units steeper than $\alpha_{\rm inj}$ (Miniati 2002). The radio spectrum of the relic has a power-law shape over the observed frequency range, with a spectral index of -0.81 ± 0.03. This would imply $\alpha_{\rm inj} \sim -0.3$ for a simple shock model. The flattest possible spectral index is -0.5 from DSA, suggesting that the relic recently brightened or just formed. In this case no equilibrium

has yet been reached between the electron cooling and injection within the observed frequency range below 1369 MHz. Another possibility is that the area over which we integrate the flux does not include all of the relic emission. It could be that some of this steep-spectrum emission is blended with that of the radio halo. Finally, the flat radio spectrum could also imply that DSA is not fully understood or that the radio emitting electrons do not originate from the DSA mechanism. If the relic traces a recently formed shock, then spectral steepening is expected at high-frequencies. Clarke & Ensslin (2006) indeed reported a steeper spectral index of −1.2 between 1369 and 1703 MHz for the relic.

For a typical magnetic field strength of 2 μG for the relic (Clarke & Ensslin 2006) and $\nu_{\rm brk}$ = 1400 MHz, the spectral age is about 0.05 Gyr. Berrington et al. (2002) proposed that A2256 is undergoing a triple merger event. One between a subcluster and the primary cluster and one between the primary cluster and subcluster (or the primary cluster only) with a smaller galaxy group. The relative velocity between the subcluster and primary cluster is estimated to be $\sim$ 2000 km s^{-1} and they are near the time of the first close passage of the subcluster and primary cluster centers. The group is infalling from the north. The "primary cluster–subcluster" merger has a mass ratio of about 3 and the "primary cluster (+subcluster)–group" merger event has a mass ratio of about 10. Miller et al. (2003) argued that the "primary cluster–galaxy group" merger is responsible for the radio relic and that the merger event is viewed 0.3 Gyr after the core passage. From the radio spectra alone it is not possible to disentangle the merger scenario, but usually the strongest shocks form after core passage and the flat integrated radio spectrum implies that the relic only recently formed, $\lesssim$ 0.1 Gyr or so. The relic in A2256 is thus probably seen at a relatively early stage, just after core passage, compared to some of the double radio relic clusters (e.g., Röttgering et al. 1997; Bagchi et al. 2006; Bonafede et al. 2009b; van Weeren et al. 2011c). Further flux measurements above 2 GHz are needed to better constrain the high-frequency end of the spectrum and confirm the radio spectrum steepens here.

No shock has been found so far in X-ray observations. Although, given the large extent of the relic in both the NS and EW directions we are probably not viewing the relic close to edge-on, making it more difficult to detect a shock. For an edge-on shock/relic one would expect a much larger ratio between the largest physical extent and the relic width (e.g., van Weeren et al. 2010). Because of the large size of the relic it is unlikely we are seeing fossil radio plasma compressed by a shock wave since radiative energy losses during the time it takes to compress a several hundred kiloparsec sized radio ghost would remove most of the electrons responsible for the observable radio emission Clarke & Ensslin (2006). In addition, we would expect steep curved radio spectra due to synchrotron and IC losses.

The spectral index of the radio halo was measured by summing the flux in the region around source D, see Fig. 12.4 (right panel). In this region the halo is detected at the 1–3σ level per beam in the LOFAR 63 MHz image. The flux was measured from the 63 MHz image used for the spectral index map. We sumed the flux over the same region in the 351 MHz WSRT and 1369 MHz VLA D-array (Clarke & Ensslin 2006) images. The resulting radio spectrum is shown in Fig. 12.8. The 63–351 MHz spectral index is -1.3 ± 0.1 and the 351–1369 MHz spectral index is -1.1 ± 0.1. In the image made with robust 0.5 weighting (Fig. 12.4) we measure a halo flux that is a factor of 1.5 higher than in the uniform weighted tapered image from the spectral index map (summing the flux over the same region). With this higher flux the 63–351 MHz spectral index would be about −1.5. Therefore the low-frequency spectral index is probably steeper than the high-frequency one. This low-frequency steepening was also reported by Kale & Dwarakanath (2010) and is consistent with a combination of spectra from (at least)

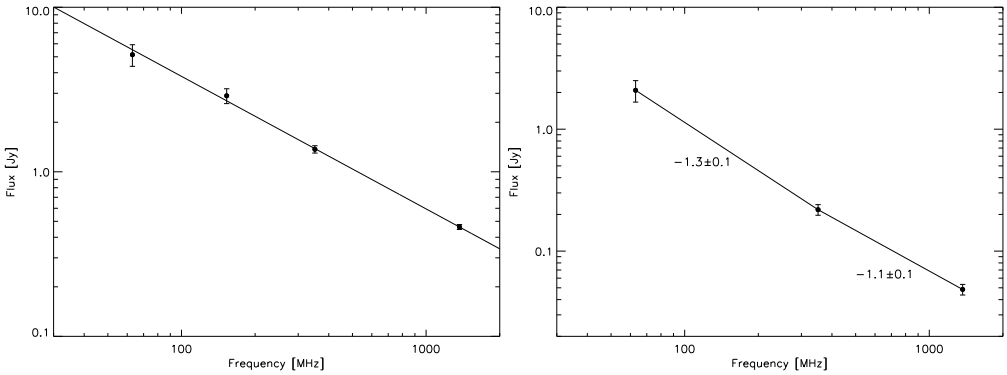

Figure 12.8: Left: Radio spectrum of the relic. Flux measurements from Clarke & Ensslin (2006), Brentjens (2008), and Intema (2009) were included. Solid line is a power-law fit to the flux measurements. Right: Radio halo spectrum from flux measurements summed over the region indicated in Fig. 12.4.

two populations of relativistic electrons.

Three different possibilities to explain this would be: (1) a model where protons and their secondaries live in a turbulent medium and get re-accelerated. The re-acceleration time scale here is very long (about 1 Gyr), meaning that most of the signal at higher frequencies is dominated by the process of injection of secondaries (with a flatter spectrum), while at lower frequencies turbulent re-acceleration boosts the radio emission (Brunetti & Lazarian 2011), (2) a model where there is a halo with a steep turbulent re-acceleration spectrum, while some projected emission from the relic (in the northern part) is superimposed on the halo emission. In this case the 1369 MHz flux is dominated by the tail of the relic emission downstream that is projected onto the halo, or (3) an "inhomogeneous" turbulent re-acceleration model, in this case the turbulence is not homogeneous over the emitting volume which leads to a distribution of different spectral components.

With only three data points it is not possible to distinguish between these models, but with future (LOFAR) observations it will be possible to much better determine the low-frequency spectrum. This opens new theoretical questions and it would be interesting to determine if low-frequency spectral steepening is unique to Abell 2256 or whether it also occurs for other radio halos.

12.4 Conclusions

We have presented LOFAR LBA observations between 67 and 18 MHz of the cluster Abell 2256. We focussed mainly on the 63 MHz map as at lower frequencies ionospheric phase distortions were severe. At 63 MHz we detect both the radio halo and main radio relic. The integrated spectral index we find for the relic is consistent with being a power-law with $\alpha = -0.81 \pm 0.03$. The integrated radio spectrum of the relic is quite flat, which could mean that the relic has only recently been formed, within the last ~ 0.1 Gyr. For the radio halo there are indications of a low-frequency spectral steepening, this was previously also reported by Kale & Dwarakanath (2010).

Additional flux measurements are needed to better determine the low-frequency spectrum of the halo and the origin of the convex spectrum.

We detected a recently found steep spectrum source to the west of the cluster center, located roughly at the end of the head-tail source C. For this source we find an extremely steep spectral index of -2.3 ± 0.4 between 63 and 153 MHz. This steep spectrum source could be an older part of the tail of source C. For source F2 we find the spectral index flattens to -0.95 between 63 and 153 MHz. The origin of the source remains unclear.

In the future we plan to extend our investigation to lower frequencies. For this, ionospheric calibration schemes will be important to retain enough spatial resolution to separate the contribution from the various complex sources in the cluster.

Acknowledgements. LOFAR, the Low Frequency Array designed and constructed by ASTRON, has facilities in several countries, that are owned by various parties (each with their own funding sources), and that are collectively operated by the International LOFAR Telescope (ILT) foundation under a joint scientific policy. We thank Michiel Brentjens and Ming Sun for providing the 351 MHz WSRT and Chandra X-ray image, respectively. RJvW acknowledges funding from the Royal Netherlands Academy of Arts and Sciences.

Bibliography

Abazajian, K. N., Adelman-McCarthy, J. K., Agüeros, M. A., et al. 2009, ApJS, 182, 543

Abell, G. O., Corwin, Jr., H. G., & Olowin, R. P. 1989, ApJS, 70, 1

Aguerri, J. A. L., Sánchez-Janssen, R., & Muñoz-Tuñón, C. 2007, A&A, 471, 17

Akahori, T. & Yoshikawa, K. 2010, PASJ, 62, 335

Allen, S. W., Schmidt, R. W., & Fabian, A. C. 2001, MNRAS, 328, L37

Andernach, H., Feretti, L., & Giovannini, G. 1984, A&A, 133, 252

Andrei, A. H., Souchay, J., Zacharias, N., et al. 2009, A&A, 505, 385

Athreya, R. 2009, ApJ, 696, 885

Axford, W. I., Leer, E., & Skadron, G. 1977, in International Cosmic Ray Conference, Vol. 11, International Cosmic Ray Conference, 132–+

Baars, J. W. M., Genzel, R., Pauliny-Toth, I. I. K., & Witzel, A. 1977, A&A, 61, 99

Bacchi, M., Feretti, L., Giovannini, G., & Govoni, F. 2003, A&A, 400, 465

Bade, N., Engels, D., Voges, W., et al. 1998, A&AS, 127, 145

Bagchi, J., Durret, F., Neto, G. B. L., & Paul, S. 2006, Science, 314, 791

Bagchi, J., Enßlin, T. A., Miniati, F., et al. 2002, New Astronomy, 7, 249

Bagchi, J., Jacob, J., Gopal-Krishna, et al. 2009, MNRAS, 399, 601

Bagchi, J., Sirothia, S. K., Werner, N., et al. 2011, ApJ, 736, L8+

Barrena, R., Boschin, W., Girardi, M., & Spolaor, M. 2007, A&A, 467, 37

Battaglia, N., Pfrommer, C., Sievers, J. L., Bond, J. R., & Enßlin, T. A. 2009, MNRAS, 393, 1073

Baum, S. A., Zirbel, E. L., & O'Dea, C. P. 1995, ApJ, 451, 88

Bautz, M. W., Miller, E. D., Sanders, J. S., et al. 2009, PASJ, 61, 1117

Beasley, A. J., Gordon, D., Peck, A. B., et al. 2002, ApJS, 141, 13

Beck, R. & Krause, M. 2005, Astronomische Nachrichten, 326, 414

Becker, R. H., Helfand, D. J., White, R. L., Gregg, M. D., & Laurent-Muehleisen, S. A. 2003, VizieR Online Data Catalog, 8071, 0

Becker, R. H., White, R. L., & Helfand, D. J. 1995, ApJ, 450, 559

Bell, A. R. 1978a, MNRAS, 182, 147

Bell, A. R. 1978b, MNRAS, 182, 443

Berrington, R. C., Lugger, P. M., & Cohn, H. N. 2002, AJ, 123, 2261

Bertin, E. & Arnouts, S. 1996, A&AS, 117, 393

Best, P. N., Kauffmann, G., Heckman, T. M., et al. 2005, MNRAS, 362, 25

Bhatnagar, S., Cornwell, T. J., Golap, K., & Uson, J. M. 2008, A&A, 487, 419

Bîrzan, L., Rafferty, D. A., McNamara, B. R., Wise, M. W., & Nulsen, P. E. J. 2004, ApJ, 607, 800

Blandford, R. & Eichler, D. 1987, Phys. Rep., 154, 1

Blandford, R. D. & Ostriker, J. P. 1978, ApJ, 221, L29

Blasi, P. & Colafrancesco, S. 1999, Astroparticle Physics, 12, 169

Böhringer, H., Schuecker, P., Guzzo, L., et al. 2004, A&A, 425, 367

Böhringer, H., Voges, W., Huchra, J. P., et al. 2000, ApJS, 129, 435

Bonafede, A., Feretti, L., Giovannini, G., et al. 2009a, A&A, 503, 707

Bonafede, A., Feretti, L., Murgia, M., et al. 2010, A&A, 513, A30+

Bonafede, A., Giovannini, G., Feretti, L., Govoni, F., & Murgia, M. 2009b, A&A, 494, 429

Bonafede, A., Govoni, F., Feretti, L., et al. 2011, A&A, 530, A24+

Bondi, M., Ciliegi, P., Venturi, T., et al. 2007, A&A, 463, 519

Brentjens, M. A. 2007, PhD thesis, Rijksuniversiteit Groningen, The Netherlands

Brentjens, M. A. 2008, A&A, 489, 69

Brentjens, M. A. & de Bruyn, A. G. 2005, A&A, 441, 1217

Bridle, A. H. & Fomalont, E. B. 1976, A&A, 52, 107

Bridle, A. H., Fomalont, E. B., Miley, G. K., & Valentijn, E. A. 1979, A&A, 80, 201

Briel, U. G. & Henry, J. P. 1994, Nature, 372, 439

Briel, U. G., Henry, J. P., Schwarz, R. A., et al. 1991, A&A, 246, L10

Briggs, D. S. 1995, PhD thesis, New Mexico Institute of Mining Technology, Socorro, New Mexico, USA

Brown, S., Duesterhoeft, J., & Rudnick, L. 2011, ApJ, 727, L25+

Brown, S. & Rudnick, L. 2009, AJ, 137, 3158

Brown, S. & Rudnick, L. 2011, MNRAS, 412, 2

Brüggen, M., Bykov, A., Ryu, D., & Röttgering, H. 2011, Space Sci. Rev., 138

Brunetti, G. 2004, Journal of Korean Astronomical Society, 37, 493

Brunetti, G., Cassano, R., Dolag, K., & Setti, G. 2009, A&A, 507, 661

Brunetti, G., Giacintucci, S., Cassano, R., et al. 2008, Nature, 455, 944

Brunetti, G. & Lazarian, A. 2011, MNRAS, 410, 127

Brunetti, G., Setti, G., & Comastri, A. 1997, A&A, 325, 898

Brunetti, G., Setti, G., Feretti, L., & Giovannini, G. 2001, MNRAS, 320, 365

Brunetti, G., Venturi, T., Dallacasa, D., et al. 2007, ApJ, 670, L5

Buote, D. A. 2001, ApJ, 553, L15

Burn, B. J. 1966, MNRAS, 133, 67

Burns, J. O., Rhee, G., Owen, F. N., & Pinkney, J. 1994a, ApJ, 423, 94

Burns, J. O., Roettiger, K., Ledlow, M., & Klypin, A. 1994b, ApJ, 427, L87

Burns, J. O., Sulkanen, M. E., Gisler, G. R., & Perley, R. A. 1992, ApJ, 388, L49

Byram, E. T., Chubb, T. A., & Friedman, H. 1966, Science, 152, 66

Carilli, C. L., Perley, R. A., Dreher, J. W., & Leahy, J. P. 1991, ApJ, 383, 554

Cassano, R. 2010, A&A, 517, A10+

Cassano, R. & Brunetti, G. 2005, MNRAS, 357, 1313

Cassano, R., Brunetti, G., Röttgering, H. J. A., & Brüggen, M. 2010a, A&A, 509, A68+

Cassano, R., Brunetti, G., & Setti, G. 2006, MNRAS, 369, 1577

Cassano, R., Brunetti, G., Setti, G., Govoni, F., & Dolag, K. 2007, MNRAS, 378, 1565

Cassano, R., Brunetti, G., Venturi, T., et al. 2008, A&A, 480, 687

Cassano, R., Ettori, S., Giacintucci, S., et al. 2010b, ApJ, 721, L82

Cavagnolo, K. W., Donahue, M., Voit, G. M., & Sun, M. 2009, ApJS, 182, 12

Cavaliere, A. & Fusco-Femiano, R. 1976, A&A, 49, 137

Cen, R. & Ostriker, J. P. 1999, ApJ, 514, 1

Chandra, P., Ray, A., & Bhatnagar, S. 2004, ApJ, 612, 974

Clarke, T. E. & Ensslin, T. A. 2006, AJ, 131, 2900

Clarke, T. E., Kronberg, P. P., & Böhringer, H. 2001, ApJ, 547, L111

Clowe, D., Bradač, M., Gonzalez, A. H., et al. 2006, ApJ, 648, L109

Cohen, A. S., Lane, W. M., Cotton, W. D., et al. 2007, AJ, 134, 1245

Condon, J. J., Anderson, M. L., & Helou, G. 1991, ApJ, 376, 95

Condon, J. J., Cotton, W. D., Greisen, E. W., et al. 1998, AJ, 115, 1693

Cornwell, T., Braun, R., & Briggs, D. S. 1999, in Astronomical Society of the Pacific Conference Series, Vol. 180, Synthesis Imaging in Radio Astronomy II, ed. G. B. Taylor, C. L. Carilli, & R. A. Perley, 151–+

Cornwell, T. J. 2008, IEEE Journal of Selected Topics in Signal Processing, vol. 2, issue 5, pp. 793-801, 2, 793

Cornwell, T. J., Golap, K., & Bhatnagar, S. 2005, in Astronomical Society of the Pacific Conference Series, Vol. 347, Astronomical Data Analysis Software and Systems XIV, ed. P. Shopbell, M. Britton, & R. Ebert, 86–+

Cornwell, T. J., Golap, K., & Bhatnagar, S. 2008, IEEE Journal of Selected Topics in Signal Processing, vol. 2, issue 5, pp. 647-657, 2, 647

Cornwell, T. J. & Perley, R. A. 1992, A&A, 261, 353

Cotton, W. D. 1999, in Astronomical Society of the Pacific Conference Series, Vol. 180, Synthesis Imaging in Radio Astronomy II, ed. G. B. Taylor, C. L. Carilli, & R. A. Perley, 357–+

Cotton, W. D. 2008, PASP, 120, 439

Cotton, W. D., Condon, J. J., Perley, R. A., et al. 2004, in Presented at the Society of Photo-Optical Instrumentation Engineers (SPIE) Conference, Vol. 5489, Society of Photo-Optical Instrumentation Engineers (SPIE) Conference Series, ed. J. M. Oschmann, Jr., 180–189

Crawford, C. S., Edge, A. C., Fabian, A. C., et al. 1995, MNRAS, 274, 75

Croston, J. H., Pratt, G. W., Böhringer, H., et al. 2008, A&A, 487, 431

Dallacasa, D., Brunetti, G., Giacintucci, S., et al. 2009, ApJ, 699, 1288

De Breuck, C., Tang, Y., de Bruyn, A. G., Röttgering, H., & van Breugel, W. 2002a, A&A, 394, 59

De Breuck, C., van Breugel, W., Röttgering, H. J. A., & Miley, G. 2000, A&AS, 143, 303

De Breuck, C., van Breugel, W., Stanford, S. A., et al. 2002b, AJ, 123, 637

de Bruyn, A. G. & Brentjens, M. A. 2005, A&A, 441, 931

de Vries, N., Snellen, I. A. G., Schilizzi, R. T., Lehnert, M. D., & Bremer, M. N. 2007, A&A, 464, 879

Dennison, B. 1980, ApJ, 239, L93

Dolag, K., Bykov, A. M., & Diaferio, A. 2008, Space Science Reviews, 134, 311

Dolag, K. & Enßlin, T. A. 2000, A&A, 362, 151

Dolag, K., Vogt, C., & Enßlin, T. A. 2005, MNRAS, 358, 726

Donnert, J., Dolag, K., Brunetti, G., Cassano, R., & Bonafede, A. 2010a, MNRAS, 401, 47

Donnert, J., Dolag, K., Cassano, R., & Brunetti, G. 2010b, MNRAS, 407, 1565

Douglas, J. N., Bash, F. N., Bozyan, F. A., Torrence, G. W., & Wolfe, C. 1996, AJ, 111, 1945

Drury, L. O. 1983, Reports on Progress in Physics, 46, 973

Dwarakanath, K. S. & Kale, R. 2009, ApJ, 698, L163

Ebeling, H., Barrett, E., & Donovan, D. 2004, ApJ, 609, L49

Ebeling, H., Barrett, E., Donovan, D., et al. 2007, ApJ, 661, L33

Ebeling, H., Edge, A. C., Bohringer, H., et al. 1998, MNRAS, 301, 881

Ebeling, H., Edge, A. C., & Henry, J. P. 2001, ApJ, 553, 668

Ebeling, H., Mullis, C. R., & Tully, R. B. 2002, ApJ, 580, 774

Ebeling, H., White, D. A., & Rangarajan, F. V. N. 2006, MNRAS, 368, 65

Edge, A. C., Ebeling, H., Bremer, M., et al. 2003, MNRAS, 339, 913

Enßlin, T., Pfrommer, C., Miniati, F., & Subramanian, K. 2011, A&A, 527, A99+

Ensslin, T. A., Biermann, P. L., Klein, U., & Kohle, S. 1998, A&A, 332, 395

Enßlin, T. A. & Brüggen, M. 2002, MNRAS, 331, 1011

Enßlin, T. A. & Gopal-Krishna. 2001, A&A, 366, 26

Enßlin, T. A. & Röttgering, H. 2002, A&A, 396, 83

Fabian, A. C., Nulsen, P. E. J., & Canizares, C. R. 1991, A&A Rev., 2, 191

Fabian, A. C., Sanders, J. S., Taylor, G. B., et al. 2006, MNRAS, 366, 417

Fabricant, D. G., Kent, S. M., & Kurtz, M. J. 1989, ApJ, 336, 77

Fanaroff, B. L. & Riley, J. M. 1974, MNRAS, 167, 31P

Farnsworth, D., Rudnick, L., & Brown, S. 2011, AJ, 141, 191

Feretti, L. 2005, Advances in Space Research, 36, 729

Feretti, L., Bacchi, M., Slee, O. B., et al. 2006, MNRAS, 368, 544

Feretti, L., Fusco-Femiano, R., Giovannini, G., & Govoni, F. 2001, A&A, 373, 106

Feretti, L. & Giovannini, G. 1996, in IAU Symposium, Vol. 175, Extragalactic Radio Sources, ed. R. D. Ekers, C. Fanti, & L. Padrielli, 333–+

Feretti, L., Orrù, E., Brunetti, G., et al. 2004, A&A, 423, 111

Feretti, L., Schuecker, P., Böhringer, H., Govoni, F., & Giovannini, G. 2005, A&A, 444, 157

Ferrari, C., Govoni, F., Schindler, S., Bykov, A. M., & Rephaeli, Y. 2008, Space Science Reviews, 134, 93

Finoguenov, A., Sarazin, C. L., Nakazawa, K., Wik, D. R., & Clarke, T. E. 2010, ApJ, 715, 1143

Fryxell, B., Olson, K., Ricker, P., et al. 2000, ApJS, 131, 273

Fujita, Y., Takizawa, M., & Sarazin, C. L. 2003, ApJ, 584, 190

Garn, T., Green, D. A., Hales, S. E. G., Riley, J. M., & Alexander, P. 2007, MNRAS, 376, 1251

George, M. R., Fabian, A. C., Sanders, J. S., Young, A. J., & Russell, H. R. 2009, MNRAS, 395, 657

Giacintucci, S., Venturi, T., Macario, G., et al. 2008, A&A, 486, 347

Giovannini, G., Bonafede, A., Feretti, L., Govoni, F., & Murgia, M. 2010, A&A, 511, L5+

Giovannini, G., Bonafede, A., Feretti, L., et al. 2009, A&A, 507, 1257

Giovannini, G., Feretti, L., , T., Kim, K.-T., & Kronberg, P. P. 1993, ApJ, 406, 399

Giovannini, G. & Feretti, L. 2000, New Astronomy, 5, 335

Giovannini, G., Feretti, L., Girardi, M., et al. 2011, A&A, 530, L5+

Giovannini, G., Feretti, L., & Stanghellini, C. 1991, A&A, 252, 528

Giovannini, G., Tordi, M., & Feretti, L. 1999, New Astronomy, 4, 141

Girardi, M., Boschin, W., & Barrena, R. 2006, A&A, 455, 45

Gitti, M., Brunetti, G., Feretti, L., & Setti, G. 2004, A&A, 417, 1

Gitti, M., Brunetti, G., & Setti, G. 2002, A&A, 386, 456

Gitti, M., Ferrari, C., Domainko, W., Feretti, L., & Schindler, S. 2007, A&A, 470, L25

Goldshmidt, O. & Rephaeli, Y. 1994, ApJ, 431, 586

Gopal-Krishna, Kulkarni, V. K., Bagchi, J., & Melnick, J. 2002, in IAU Symposium, Vol. 199, The Universe at Low Radio Frequencies, ed. A. Pramesh Rao, G. Swarup, & Gopal-Krishna, 159–+

Govoni, F. & Feretti, L. 2004, International Journal of Modern Physics D, 13, 1549

Govoni, F., Feretti, L., Giovannini, G., et al. 2001, A&A, 376, 803

Govoni, F., Markevitch, M., Vikhlinin, A., et al. 2004, ApJ, 605, 695

Govoni, F., Murgia, M., Feretti, L., et al. 2005, A&A, 430, L5

Govoni, F., Murgia, M., Feretti, L., et al. 2006, A&A, 460, 425

Govoni, F., Murgia, M., Markevitch, M., et al. 2009, A&A, 499, 371

Green, D. A. 2011, Bulletin of the Astronomical Society of India, 39, 289

Green, D. A. & Joncas, G. 1994, A&AS, 104, 481

Gursky, H., Kellogg, E., Murray, S., et al. 1971, ApJ, 167, L81+

Hales, S. E. G., Riley, J. M., Waldram, E. M., Warner, P. J., & Baldwin, J. E. 2007, MNRAS, 382, 1639

Hales, S. E. G., Waldram, E. M., Rees, N., & Warner, P. J. 1995, MNRAS, 274, 447

Harris, D. E., Forman, W., Gioa, I. M., et al. 1996, VizieR Online Data Catalog, 9013, 0

Haynes, M. P., Giovanelli, R., Herter, T., et al. 1997, AJ, 113, 1197

Heald, G., Braun, R., & Edmonds, R. 2009, A&A, 503, 409

Heald, G., McKean, J., Pizzo, R., et al. 2010, in ISKAF2010 Science Meeting

Hernquist, L. 1987, ApJS, 64, 715

Higgs, L. A. 1989, JRASC, 83, 105

Hoeft, M. & Brüggen, M. 2007, MNRAS, 375, 77

Hoeft, M., Brüggen, M., Yepes, G., Gottlöber, S., & Schwope, A. 2008, MNRAS, 391, 1511

Högbom, J. A. 1974, A&AS, 15, 417

Hoshino, A., Henry, J. P., Sato, K., et al. 2010, PASJ, 62, 371

Inoue, S., Sigl, G., Miniati, F., & et al. 2008, in International Cosmic Ray Conference, Vol. 4, International Cosmic Ray Conference, 555–558

Intema, H. T. 2009, PhD thesis, Leiden University, The Netherlands

Intema, H. T., van der Tol, S., Cotton, W. D., et al. 2009, A&A, 501, 1185

Jackson, N., Battye, R. A., Browne, I. W. A., et al. 2007, MNRAS, 376, 371

Jaffe, W. J. 1977, ApJ, 212, 1

Jaffe, W. J. & Perola, G. C. 1973, A&A, 26, 423

Jaffe, W. J., Valentijn, E. A., & Perola, G. C. 1976, A&A, 49, 179

Jeltema, T. E. & Profumo, S. 2011, ApJ, 728, 53

Joncas, G. & Higgs, L. A. 1990, A&AS, 82, 113

Jones, F. C. & Ellison, D. C. 1991, Space Science Reviews, 58, 259

Kale, R. & Dwarakanath, K. S. 2010, ApJ, 718, 939

Kale, R. & Dwarakanath, K. S. 2011, ArXiv e-prints

Kang, H. & Ryu, D. 2011, ApJ, 734, 18

Kang, H., Ryu, D., & Jones, T. W. 1996, ApJ, 456, 422

Kardashev, N. S. 1962, Soviet Astronomy, 6, 317

Kassim, N. E. & Erickson, W. C. 2008, in Astronomical Society of the Pacific Conference

Series, Vol. 395, Frontiers of Astrophysics: A Celebration of NRAO's 50th Anniversary, ed. A. H. Bridle, J. J. Condon, & G. C. Hunt, 368–+

Kassim, N. E., Lazio, T. J. W., Erickson, W. C., et al. 2007, ApJS, 172, 686

Katgert, P., Mazure, A., Perea, J., et al. 1996, A&A, 310, 8

Katz-Stone, D. M. & Rudnick, L. 1994, ApJ, 426, 116

Katz-Stone, D. M., Rudnick, L., & Anderson, M. C. 1993, ApJ, 407, 549

Kempner, J. C., Blanton, E. L., Clarke, T. E., et al. 2004, in The Riddle of Cooling Flows in Galaxies and Clusters of galaxies, ed. T. Reiprich, J. Kempner, & N. Soker, 335–+

Kempner, J. C. & Sarazin, C. L. 2001, ApJ, 548, 639

Kempner, J. C., Sarazin, C. L., & Markevitch, M. 2003, ApJ, 593, 291

Kennicutt, Jr., R. C. 1998, ApJ, 498, 541

Keshet, U. 2010, ArXiv e-prints

Keshet, U. & Loeb, A. 2010, ApJ, 722, 737

Keshet, U., Waxman, E., & Loeb, A. 2004, ApJ, 617, 281

Keshet, U., Waxman, E., Loeb, A., Springel, V., & Hernquist, L. 2003, ApJ, 585, 128

Kim, K.-T. 1999, Journal of Korean Astronomical Society, 32, 75

Kocevski, D. D., Ebeling, H., Mullis, C. R., & Tully, R. B. 2007, ApJ, 662, 224

Koester, B. P., McKay, T. A., Annis, J., et al. 2007, ApJ, 660, 239

Komatsu, E., Smith, K. M., Dunkley, J., et al. 2011, ApJS, 192, 18

Komissarov, S. S. & Gubanov, A. G. 1994, A&A, 285, 27

Konar, C., Jamrozy, M., Saikia, D. J., & Machalski, J. 2008, MNRAS, 383, 525

Kovac, J. M., Leitch, E. M., Pryke, C., et al. 2002, Nature, 420, 772

Kronberg, P. P., Kothes, R., Salter, C. J., & Perillat, P. 2007, ApJ, 659, 267

Krymskii, G. F. 1977, Akademiia Nauk SSSR Doklady, 234, 1306

Landau, L. D. & Lifshitz, E. M. 1959, Fluid mechanics, ed. Landau, L. D. & Lifshitz, E. M.

Liang, H., Hunstead, R. W., Birkinshaw, M., & Andreani, P. 2000, ApJ, 544, 686

Loeb, A. & Waxman, E. 2000, Nature, 405, 156

Lonsdale, C. J. & Helou, G. 1985, Cataloged galaxies and quasars observed in the IRAS survey (Pasadena: Jet Propulsion Laboratory (JPL), 1985)

Ma, C., Ebeling, H., & Barrett, E. 2009, ApJ, 693, L56

Ma, C.-J., Ebeling, H., Donovan, D., & Barrett, E. 2008, ApJ, 684, 160

Macario, G., Markevitch, M., Giacintucci, S., et al. 2011, ApJ, 728, 82

Macario, G., Venturi, T., Brunetti, G., et al. 2010, A&A, 517, A43+

Machalski, J., Kozieł-Wierzbowska, D., Jamrozy, M., & Saikia, D. J. 2008, ApJ, 679, 149

Malkov, M. A. & O'C Drury, L. 2001, Reports on Progress in Physics, 64, 429

Mantz, A., Allen, S. W., Ebeling, H., Rapetti, D., & Drlica-Wagner, A. 2010, MNRAS, 406, 1773

Marecki, A., Falcke, H., Niezgoda, J., Garrington, S. T., & Patnaik, A. R. 1999, A&AS, 135,

273

Marini, F., Bardelli, S., Zucca, E., et al. 2004, MNRAS, 353, 1219

Markevitch, M. 1998, ApJ, 504, 27

Markevitch, M. 2006, in ESA Special Publication, Vol. 604, The X-ray Universe 2005, ed. A. Wilson, 723–+

Markevitch, M., Gonzalez, A. H., David, L., et al. 2002, ApJ, 567, L27

Markevitch, M., Govoni, F., Brunetti, G., & Jerius, D. 2005, ApJ, 627, 733

Masson, C. R. & Mayer, C. J. 1978, MNRAS, 185, 607

Mastropietro, C. & Burkert, A. 2008, MNRAS, 389, 967

Mather, J. C., Cheng, E. S., Cottingham, D. A., et al. 1994, ApJ, 420, 439

Mather, J. C., Cheng, E. S., Eplee, Jr., R. E., et al. 1990, ApJ, 354, L37

Maughan, B. J., Jones, C., Forman, W., & Van Speybroeck, L. 2008, ApJS, 174, 117

Mazure, A., Katgert, P., den Hartog, R., et al. 1996, A&A, 310, 31

McCarthy, I. G., Bower, R. G., Balogh, M. L., et al. 2007, MNRAS, 376, 497

Miley, G. 1980, ARA&A, 18, 165

Miley, G. & De Breuck, C. 2008, A&A Rev., 15, 67

Miley, G. K. 1973, A&A, 26, 413

Miller, N. A., Owen, F. N., & Hill, J. M. 2003, AJ, 125, 2393

Miniati, F. 2002, MNRAS, 337, 199

Miniati, F. 2003, MNRAS, 342, 1009

Miniati, F., Jones, T. W., Kang, H., & Ryu, D. 2001, ApJ, 562, 233

Miniati, F., Koushiappas, S. M., & Di Matteo, T. 2007, ApJ, 667, L1

Miniati, F., Ryu, D., Kang, H., et al. 2000, ApJ, 542, 608

Miyauchi-Isobe, N. & Maehara, H. 2002, Publications of the National Astronomical Observatory of Japan, 6, 107

Moshir, M. & et al. 1990, in IRAS Faint Source Catalogue, version 2.0 (1990), 0–+

Murgia, M., Fanti, C., Fanti, R., et al. 2002, New Astronomy Review, 46, 307

Murgia, M., Govoni, F., Markevitch, M., et al. 2009, A&A, 499, 679

Nakazawa, K., Sarazin, C. L., Kawaharada, M., et al. 2009, PASJ, 61, 339

Nicastro, F., Mathur, S., Elvis, M., et al. 2005, Nature, 433, 495

Nilson, P. 1973, Nova Acta Regiae Soc. Sci. Upsaliensis Ser. V, 0

Noordam, J. E. 2004, in Society of Photo-Optical Instrumentation Engineers (SPIE) Conference Series, Vol. 5489, Society of Photo-Optical Instrumentation Engineers (SPIE) Conference Series, ed. J. M. Oschmann, Jr., 817–825

Norman, C. A., Melrose, D. B., & Achterberg, A. 1995, ApJ, 454, 60

Nuza, S. E., Hoeft, M., van Weeren, R. J., Gottlöber, S., & Yepes, G. 2011, MNRAS, to be submitted

Oegerle, W. R. & Hill, J. M. 2001, AJ, 122, 2858

Offringa, A. R., de Bruyn, A. G., Biehl, M., et al. 2010, MNRAS, 405, 155

Orrú, E., Murgia, M., Feretti, L., et al. 2007, A&A, 467, 943

Owen, F. N. & Ledlow, M. J. 1994, in Astronomical Society of the Pacific Conference Series, Vol. 54, The Physics of Active Galaxies, ed. G. V. Bicknell, M. A. Dopita, & P. J. Quinn, 319–+

Owen, F. N. & White, R. A. 1991, MNRAS, 249, 164

Pacholczyk, A. G. 1970, Radio astrophysics. Nonthermal processes in galactic and extragalactic sources (Series of Books in Astronomy and Astrophysics, San Francisco: Freeman, 1970)

Parma, P., Murgia, M., de Ruiter, H. R., et al. 2007, A&A, 470, 875

Patnaik, A. R., Browne, I. W. A., Wilkinson, P. N., & Wrobel, J. M. 1992, MNRAS, 254, 655

Paturel, G., Petit, C., Prugniel, P., et al. 2003, A&A, 412, 45

Paul, S., Iapichino, L., Miniati, F., Bagchi, J., & Mannheim, K. 2011, ApJ, 726, 17

Peacock, J. A., Cole, S., Norberg, P., et al. 2001, Nature, 410, 169

Pearce, F. R., Thomas, P. A., & Couchman, H. M. P. 1994, MNRAS, 268, 953

Perley, R. A. 1989, in Astronomical Society of the Pacific Conference Series, Vol. 6, Synthesis Imaging in Radio Astronomy, ed. R. A. Perley, F. R. Schwab, & A. H. Bridle, 259–+

Perley, R. T. & Taylor, G. B. 1999, VLA Calibrator Manual, Tech. rep., NRAO

Peterson, J. R. & Fabian, A. C. 2006, Phys. Rep., 427, 1

Petrosian, V. 2001, ApJ, 557, 560

Pfrommer, C. 2008, MNRAS, 385, 1242

Pfrommer, C. & Enßlin, T. A. 2004, MNRAS, 352, 76

Pfrommer, C., Enßlin, T. A., & Springel, V. 2008, MNRAS, 385, 1211

Pfrommer, C., Springel, V., Enßlin, T. A., & Jubelgas, M. 2006, MNRAS, 367, 113

Pizzo, R. F. 2010, PhD thesis, Rijksuniversiteit Groningen, The Netherlands

Pizzo, R. F. & de Bruyn, A. G. 2009, A&A, 507, 639

Pizzo, R. F., de Bruyn, A. G., Bernardi, G., & Brentjens, M. A. 2011, A&A, 525, A104+

Poole, G. B., Fardal, M. A., Babul, A., et al. 2006, MNRAS, 373, 881

Pope, E. C. D., Pavlovski, G., Kaiser, C. R., & Fangohr, H. 2006, MNRAS, 367, 1121

Popesso, P., Böhringer, H., Brinkmann, J., Voges, W., & York, D. G. 2004, A&A, 423, 449

Pratt, G. W. & Arnaud, M. 2002, A&A, 394, 375

Pratt, G. W., Croston, J. H., Arnaud, M., & Böhringer, H. 2009, A&A, 498, 361

Raychaudhury, S., Temple, R. F., & et al. 2009, in preparation

Rees, N. 1990, MNRAS, 244, 233

Reid, A. D., Hunstead, R. W., Lemonon, L., & Pierre, M. M. 1999, MNRAS, 302, 571

Reiprich, T. H., Hudson, D. S., Zhang, Y.-Y., et al. 2009, A&A, 501, 899

Rengelink, R. B., Tang, Y., de Bruyn, A. G., et al. 1997, A&AS, 124, 259

Ricker, P. M. 1998, ApJ, 496, 670

Ricker, P. M. & Sarazin, C. L. 2001, ApJ, 561, 621

Riess, A. G., Filippenko, A. V., Challis, P., et al. 1998, AJ, 116, 1009

Rines, K. & Diaferio, A. 2006, AJ, 132, 1275

Ritchie, B. W. & Thomas, P. A. 2002, MNRAS, 329, 675

Roettiger, K., Burns, J., & Loken, C. 1993, ApJ, 407, L53

Roettiger, K., Burns, J. O., & Stone, J. M. 1999a, ApJ, 518, 603

Roettiger, K. & Flores, R. 2000, ApJ, 538, 92

Roettiger, K., Loken, C., & Burns, J. O. 1997, ApJS, 109, 307

Roettiger, K., Stone, J. M., & Burns, J. O. 1999b, ApJ, 518, 594

Roncarelli, M., Ettori, S., Dolag, K., et al. 2006, MNRAS, 373, 1339

Röttgering, H., Snellen, I., Miley, G., et al. 1994, ApJ, 436, 654

Röttgering, H. J. A., Braun, R., Barthel, P. D., et al. 2006, in Cosmology, galaxy formation and astroparticle physics on the pathway to the SKA, Oxford

Röttgering, H. J. A., Wieringa, M. H., Hunstead, R. W., & Ekers, R. D. 1997, MNRAS, 290, 577

Roy, J., Gupta, Y., Pen, U., et al. 2010, Experimental Astronomy, 28, 25

Rudnick, L. 2001, in Astronomical Society of the Pacific Conference Series, Vol. 250, Particles and Fields in Radio Galaxies Conference, ed. R. A. Laing & K. M. Blundell, 372–+

Rudnick, L. & Katz-Stone, D. 1996, Powerful diagnostics of Cygnus A's relativistic electrons, ed. Carilli, C. L. & Harris, D. E., 158–+

Rudnick, L. & Lemmerman, J. A. 2009, ApJ, 697, 1341

Russell, H. R., Sanders, J. S., Fabian, A. C., et al. 2010, MNRAS, 406, 1721

Russell, H. R., van Weeren, R. J., Edge, A. C., et al. 2011, MNRAS, 417, L1

Ruzmaikin, A. A. & Sokoloff, D. D. 1979, A&A, 78, 1

Ryu, D., Kang, H., Hallman, E., & Jones, T. W. 2003, ApJ, 593, 599

Saito, M., Ohtani, H., Asonuma, A., et al. 1990, PASJ, 42, 603

Sarazin, C. L. 1999, ApJ, 520, 529

Sarazin, C. L. 2002, in Astrophysics and Space Science Library, Vol. 272, Merging Processes in Galaxy Clusters, ed. L. Feretti, I. M. Gioia, & G. Giovannini, 1–38

Schindler, S. & Mueller, E. 1993, A&A, 272, 137

Schlegel, D. J., Finkbeiner, D. P., & Davis, M. 1998, ApJ, 500, 525

Schwab, F. R. 1984, AJ, 89, 1076

Shabala, S. S., Ash, S., Alexander, P., & Riley, J. M. 2008, MNRAS, 388, 625

Shan, H., Qin, B., Fort, B., et al. 2010, MNRAS, 406, 1134

Shen, S., Kauffmann, G., von der Linden, A., White, S. D. M., & Best, P. N. 2008, MNRAS, 389, 1074

Sijbring, D. & de Bruyn, A. G. 1998, A&A, 331, 901

Simionescu, A., Allen, S. W., Mantz, A., et al. 2011, Science, 331, 1576

Skillman, S. W., Hallman, E. J., O'Shea, B. W., et al. 2011, ApJ, 735, 96

Skillman, S. W., O'Shea, B. W., Hallman, E. J., Burns, J. O., & Norman, M. L. 2008, ApJ, 689, 1063

Skrutskie, M. F., Cutri, R. M., Stiening, R., et al. 2003, VizieR Online Data Catalog, 7233, 0

Skrutskie, M. F., Cutri, R. M., Stiening, R., et al. 2006, AJ, 131, 1163

Slee, O. B., Roy, A. L., Murgia, M., Andernach, H., & Ehle, M. 2001, AJ, 122, 1172

Slinglend, K., Batuski, D., Miller, C., et al. 1998, ApJS, 115, 1

Small, T. A., Ma, C., Sargent, W. L. W., & Hamilton, D. 1998, ApJ, 492, 45

Smoot, G. F., Bennett, C. L., Kogut, A., et al. 1992, ApJ, 396, L1

Snellen, I. A. G., Bremer, M. N., Schilizzi, R. T., Miley, G. K., & van Ojik, R. 1996, MNRAS, 279, 1294

Sokoloff, D. D., Bykov, A. A., Shukurov, A., et al. 1998, MNRAS, 299, 189

Solomon, P. M., Downes, D., Radford, S. J. E., & Barrett, J. W. 1997, ApJ, 478, 144

Springel, V. & Farrar, G. R. 2007, MNRAS, 380, 911

Springel, V., Frenk, C. S., & White, S. D. M. 2006, Nature, 440, 1137

Springob, C. M., Haynes, M. P., Giovanelli, R., & Kent, B. R. 2005, ApJS, 160, 149

Struble, M. F. & Rood, H. J. 1999, ApJS, 125, 35

Subrahmanyan, R., Beasley, A. J., Goss, W. M., Golap, K., & Hunstead, R. W. 2003, AJ, 125, 1095

Sun, M., Murray, S. S., Markevitch, M., & Vikhlinin, A. 2002, ApJ, 565, 867

Takizawa, M. 1999, ApJ, 520, 514

Takizawa, M. 2000, ApJ, 532, 183

Takizawa, M. 2006, PASJ, 58, 925

Takizawa, M. 2008, ApJ, 687, 951

Takizawa, M. & Naito, T. 2000, ApJ, 535, 586

Taylor, A. R., Stil, J. M., & Sunstrum, C. 2009, ApJ, 702, 1230

Thierbach, M., Klein, U., & Wielebinski, R. 2003, A&A, 397, 53

Thompson, T. A., Quataert, E., Waxman, E., Murray, N., & Martin, C. L. 2006, ApJ, 645, 186

Tody, D. 1986, in Presented at the Society of Photo-Optical Instrumentation Engineers (SPIE) Conference, Vol. 627, Society of Photo-Optical Instrumentation Engineers (SPIE) Conference Series, ed. D. L. Crawford, 733–+

Tody, D. 1993, in Astronomical Society of the Pacific Conference Series, Vol. 52, Astronomical Data Analysis Software and Systems II, ed. R. J. Hanisch, R. J. V. Brissenden, & J. Barnes, 173–+

Tribble, P. C. 1991, MNRAS, 250, 726

Vacca, V., Murgia, M., Govoni, F., et al. 2010, A&A, 514, A71+

Valdes, F. G. 1998, in Astronomical Society of the Pacific Conference Series, Vol. 145, Astronomical Data Analysis Software and Systems VII, ed. R. Albrecht, R. N. Hook, & H. A. Bushouse, 53–+

Vallee, J. P. 1980, A&A, 86, 251

Valtchanov, I., Murphy, T., Pierre, M., Hunstead, R., & Lémonon, L. 2002, A&A, 392, 795

van Weeren, R. J., Brüggen, M., Röttgering, H. J. A., & Hoeft, M. 2011a, ArXiv e-prints

van Weeren, R. J., Brüggen, M., Röttgering, H. J. A., et al. 2011b, A&A, 533, A35+

van Weeren, R. J., Hoeft, M., Röttgering, H. J. A., et al. 2011c, A&A, 528, A38+

van Weeren, R. J., Intema, H. T., Oonk, J. B. R., Röttgering, H. J. A., & Clarke, T. E. 2009a, A&A, 508, 1269

van Weeren, R. J., Intema, H. T., Röttgering, H. J. A., Brüggen, M., & Hoeft, M. 2011d, Mem. Soc. Astron. Italiana, 82, 569

van Weeren, R. J., Röttgering, H. J. A., Bagchi, J., et al. 2009b, A&A, 506, 1083

van Weeren, R. J., Röttgering, H. J. A., & Brüggen, M. 2011e, A&A, 527, A114+

van Weeren, R. J., Röttgering, H. J. A., Brüggen, M., & Cohen, A. 2009c, A&A, 508, 75

van Weeren, R. J., Röttgering, H. J. A., Brüggen, M., & Cohen, A. 2009d, A&A, 505, 991

van Weeren, R. J., Röttgering, H. J. A., Brüggen, M., & Hoeft, M. 2010, Science, 330, 347

Vazza, F., Brunetti, G., & Gheller, C. 2009, MNRAS, 395, 1333

Vazza, F., Brunetti, G., Gheller, C., & Brunino, R. 2010, New Astronomy, 15, 695

Vazza, F., Tormen, G., Cassano, R., Brunetti, G., & Dolag, K. 2006, MNRAS, 369, L14

Venturi, T., Giacintucci, G., Dallacasa, D., et al. 2011, MNRAS, L251+

Venturi, T., Giacintucci, S., Brunetti, G., et al. 2007, A&A, 463, 937

Venturi, T., Giacintucci, S., Dallacasa, D., et al. 2008, A&A, 484, 327

Vikhlinin, A., Kravtsov, A., Forman, W., et al. 2006, ApJ, 640, 691

Vink, J. & Laming, J. M. 2003, ApJ, 584, 758

Voges, W., Aschenbach, B., Boller, T., et al. 2000, IAU Circ., 7432, 1

Voges, W., Aschenbach, B., Boller, T., et al. 1999, A&A, 349, 389

Vogt, C., Dolag, K., & Enßlin, T. A. 2005, MNRAS, 358, 732

Waldram, E. M., Yates, J. A., Riley, J. M., & Warner, P. J. 1996, MNRAS, 282, 779

Wardle, J. F. C. & Kronberg, P. P. 1974, ApJ, 194, 249

Weinberger, R., Saurer, W., & Seeberger, R. 1995, A&AS, 110, 269

White, D. A. 2000, MNRAS, 312, 663

White, R. L., Becker, R. H., Helfand, D. J., & Gregg, M. D. 1997, ApJ, 475, 479

Willott, C. J., Rawlings, S., Jarvis, M. J., & Blundell, K. M. 2003, MNRAS, 339, 173

Willson, M. A. G. 1970, MNRAS, 151, 1

Windhorst, R. A., Fomalont, E. B., Partridge, R. B., & Lowenthal, J. D. 1993, ApJ, 405, 498

Wright, E. L. 2006, PASP, 118, 1711

Zanichelli, A., Vigotti, M., Scaramella, R., Grueff, G., & Vettolani, G. 2001, A&A, 379, 21

Zeldovich, Y. B. & Sunyaev, R. A. 1969, Ap&SS, 4, 301

Zhang, X., Zheng, Y., Chen, H., et al. 1997, A&AS, 121, 59

Zu Hone, J. A., Ricker, P. M., Lamb, D. Q., & Karen Yang, H.-Y. 2009, ApJ, 699, 1004

ZuHone, J. A. 2011, ApJ, 728, 54

ZuHone, J. A., Markevitch, M., & Johnson, R. E. 2010, ApJ, 717, 908

Nederlandse samenvatting

In dit proefschrift worden radiowaarnemingen en computer simulaties van samensmeltende clusters van sterrenstelsels besproken. Om dit beter te begrijpen wordt eerst uitgelegd wat clusters van sterrenstelsels zijn en hoe we denken dat deze ontstaan. Daarna wordt toegelicht hoe we de radiostraling, afkomstig van samensmeltende clusters, kunnen waarnemen met radiotelescopen. Ten slotte wordt het onderzoek dat in dit proefschrift beschreven is kort samengevat per hoofdstuk.

Clusters van sterrenstelsels

Alle sterren die we met het blote oog 's nachts kunnen zien behoren tot ons eigen sterrenstelsel de Melkweg. De meeste van deze sterren bevinden zich relatief dichtbij de Aarde. De Melkweg bevat echter veel meer sterren dan zichtbaar met het blote oog, wel een paar honderd miljard. Daarnaast bevat de Melkweg ook stof en gas. De Melkweg is niet het enige sterrenstelsel in het heelal. Er zijn tenminste 100 miljard sterrenstelsels en waarschijnlijk nog veel meer sterrenstelsels die elk weer uit miljarden sterren bestaan. Sterrenstelsels bevinden zich vaak in groepen. Onze Melkweg behoort tot de Lokale Groep die enkele tientallen leden bevat. Er zijn echter veel grotere groepen van sterrenstelsels, die noemen we clusters van sterrenstelsels. De sterrenstelsels in groepen en clusters worden bij elkaar gehouden door de zwaartekracht. Clusters van sterrenstelsels nemen een bijzondere plaats in als grootste door de zwaartekracht gebonden structuren in het heelal.

De dichtstbijzijnde cluster is de Virgo Cluster op een afstand van 54 miljoen lichtjaar. Dit betekent dat het licht, reizend met een snelheid van $300,000$ km/s, er 54 miljoen jaar over doet om de Aarde te bereiken. We kijken dus 54 miljoen jaar terug in de tijd voor deze cluster. De meeste clusters staan veel verder weg, op afstanden van enkele miljarden lichtjaren.

Zichtbaar licht is een vorm van elektromagnetische straling net zoals radio, infrarode, ultraviolette, Röntgen en gammastraling. Het enige verschil tussen deze verschillende vormen van straling is de golflengte. Ultraviolet, Röntgen en gammastraling hebben kortere golflengtes dan zichtbaar licht. De meeste straling met kortere golflengtes en ook infrarode straling wordt tegengehouden door de atmosfeer. Radiostraling daarentegen dringt grotendeels ongehinderd door de atmosfeer heen, net zoals zichtbaar licht.

De sterrenstelsels in clusters worden bestudeerd in zichtbaar licht, maar astronomen kijken ook naar clusters op andere golflengtes. Op deze manier kan veel meer kennis worden verkregen

over de processen die zich hier afspelen. Behalve in de sterrenstelsels is er ook gas aanwezig tussen de sterrenstelsels in clusters. De massa van dit gas is zelfs veel groter dan de massa van de sterrenstelsels. Het gas in clusters is zeer ijl en heet, met een temperatuur van rond de 10 miljoen graden of hoger. Dit hete gas straalt voornamelijk Röntgenstraling uit en we kunnen dit waarnemen met Röntgen-satellieten. Clusters bevatten ook kleinere hoeveelheden koeler gas dat voornamelijk op infrarode golflengtes wordt bestudeerd.

Hoe ontstaan clusters van sterrenstelsels?

Eén van de belangrijkste vragen die sterrenkundigen proberen te beantwoorden is hoe sterren, sterrenstelsels, en clusters van sterrenstelsels zich hebben gevormd na de Big Bang, 13.7 miljard jaar geleden. Vlak na de Big Bang bestond het heelal namelijk alleen uit heet gas. Het idee is dat het gas begon samen te klonteren toen de temperatuur genoeg gedaald was, onder invloed van de zwaartekracht. Hierbij ontstonden de eerste sterren en sterrenstelsels. Uiteindelijk toen het heelal ongeveer de helft van zijn huidige leeftijd bereikt had begonnen sterrenstelsels zich te groeperen in clusters. Clusters van sterrenstelsels zijn dus relatief jong ten opzichte van de eerste sterren en sterrenstelsels. Clusters vormen zich door samensmeltingen van kleinere clusters en groepen, dit groeiproces vindt nog steeds plaats in het huidige heelal.

Tijdens de samensmeltingen en botsingen tussen clusters gebeurt er vrij weinig met de individuele sterren en sterrenstelsels. Ze bewegen meestal gewoon langs elkaar heen. Het hete gas in de groepen en clusters botst echter op elkaar en hierbij worden schokgolven in het gas gevormd. Hierdoor wordt het hete gas nog verder verhit. Deze schokgolven kunnen we zien met Röntgen-satellieten. Al met al duurt een samensmelting wel een miljard jaar lang, zodat we slechts moment opnames van deze gebeurtenissen te zien krijgen. Toch kan dit proces bestudeerd worden, door naar verschillende samensmeltingen te kijken die zich elk in verschillende stadia bevinden.

Radiostraling van clusters

In 1970 werd een belangrijke ontdekking gedaan in de Coma Cluster. Behalve Röntgenstraling bleek het gas in de cluster ook diffuse radiostraling uit te zenden. Daarna werden ook in sommige andere clusters van deze diffuse radiobronnen gevonden. Alle clusters die diffuse radiobronnen hebben zijn aan het samensmelten tot grotere clusters. Het gas in deze clusters is dan ook heter dan in clusters die zich in rust bevinden. De diffuse radiostraling is onder te verdelen in twee groepen. Er zijn radio *halo's* die zich centraal in de cluster bevinden en radio *relics* die verder van het centrum staan. De halo's laten over het algemeen weinig structuur zien, terwijl de relics vaak langgerekt zijn en onregelmatige verschillen in helderheid vertonen. De radiostraling die wordt waargenomen is van het type *synchrotron-straling*. Een specifieke eigenschap van de synchrotron-straling van halo's en relics is dat deze sterk in helderheid toeneemt met langere golflengtes. Synchrotron-straling komt vrij wanneer geladen deeltjes rondom magnetische veldlijnen cirkelen met snelheden dichtbij de lichtsnelheid. Om deze straling te produceren zijn dus hoog-energetische deeltjes nodig en een magnetisch veld. Astronomen willen graag weten waar deze deeltjes en magnetische velden vandaan komen. De deeltjes kunnen alleen deze extreme energieën bereiken als ze versneld worden, net zoals in een deeltjesversneller op aarde.

Clusters zijn niet de enige objecten in het heelal die radiostraling uitzenden. Sommige sterrenstelsels, met een zwart gat in het centrum, zenden zeer heldere synchrotron-straling uit. Daarnaast zijn er nog veel meer radiobronnen, zoals de Zon, planeten, sterren, restanten van sterren en gas in sterrenstelsels die allen radiostraling uitzenden. Deze straling is soms van een ander type dan synchrotron-straling.

Radiotelescopen

Radiotelescopen kunnen tegenwoordig gedetailleerde afbeeldingen maken van de radiobronnen in clusters. Een radiotelescoop bestaat gewoonlijk uit een grote schotel om de straling te bundelen. De resolutie, de mate waarin kleine details kunnen worden onderscheden, wordt bepaald door de diameter van de schotel. De gevoeligheid voor de radiostraling wordt bepaald door de oppervlakte van de schotel. De grootste beweegbare schotel heeft een diameter van iets meer dan 100 meter. Er is zelfs een schotel van 300 meter maar deze kan niet bewegen. Omdat radiotelescopen waarnemen op veel langere golflengtes dan zichtbaar licht is de resolutie erg beperkt, zelfs voor schotels van 100 meter. Dit komt doordat de resolutie omgekeerd evenredig schaalt met de golflengte van de straling. Omdat clusters erg ver weg staan is een resolutie die overeenkomt met een schotel van tenminste enkele kilometers nodig om clusters in detail te kunnen bestuderen. Het is onmogelijk en te duur om zulke grote schotels te bouwen. Door gebruik te maken van radio-interferometrie kunnen we dit probleem echter omzeilen.

Radio-interferometrie

Radio-interferometrie is een techniek waarbij de opgevangen signalen van meerdere radioschotels worden gecombineerd, hiermee kun je een veel grotere telescoop nabootsen. In plaats van de diameter van de individuele schotels bepaalt nu de grootste afstand tussen de schotels de resolutie en de totale oppervlakte van alle schotels bepaalt de gevoeligheid. Dus hoe meer signalen van schotels gecombineerd worden des te beter.

De drie belangrijkste radio-interferometrie telescopen zijn de Westerbork Synthesis Radio Telescope (WSRT) in Drenthe, bestaande uit 14 schotels van elk 25 meter. De grootste afstand tussen de schotels bedraagt 2.7 km. De Amerikaanse Very Large Array (VLA) bestaat uit 27 schotels van 25 meter over een maximale afstand van 30 km. De Indiase Giant Metrewave Radio Telescope (GMRT) heeft 30 schotels van 45 meter, ook verspreid over een gebied van 30 km. De telescopen verschillen onderling in de golflengtes die ze kunnen ontvangen. De GMRT is vooral gevoelig voor straling met lange golflengtes, dit is een voordeel omdat de relics en halo's vooral helder zijn bij deze lange golflengtes.

Een nadeel van de lange golflengtes is het feit dat de resolutie van een telescoop afneemt met de golflengte. Ook is er op langere golflengtes vaak meer storing door radiostraling afkomstig van bijvoorbeeld mobiele telefoons en radio stations. Een nog lastiger probleem is dat een laag van de atmosfeer van de Aarde (de ionosfeer) de radiostraling iets kan afbuigen. Deze afbuiging neemt toe met de golflengte en dat kan resulteren in onscherpe beelden. De Low Frequency Array (LOFAR) is een nieuwe radiotelescoop die voor het grootste gedeelte zich in Nederland bevindt en is gebouwd door ASTRON. Deze is specifiek ontworpen voor het doen van waarnemingen op de langste golflengtes. In plaats van schotels bestaat LOFAR uit vele honderden kleine antennes die elektronisch worden gekoppeld tot stations. LOFAR heeft stations over een

gebied van 100 km in Nederland. Daarnaast zijn er ook stations in Duitsland, Engeland, Frankrijk en Zweden. De grootste afstanden tussen deze stations zijn meer dan 1000 km. Het grote aantal stations, meer dan 40, en de enorme afstanden betekent een enorme doorbraak in gevoeligheid en resolutie. Dit alles maakt LOFAR tot de meeste krachtige radiotelescoop ter wereld. Naast clusters zullen vele andere bronnen in detail bestudeerd kunnen worden.

Dit proefschrift

In dit proefschrift wordt de radiostraling van samensmeltende clusters van sterrenstelsel bestudeerd. De belangrijkste vragen zijn: Waar komen de hoog-energetische deeltjes vandaan die de radiostraling uitzenden? Hoe worden deze deeltjes versneld? Hoe is het magnetisch veld in clusters ontstaan en wat zijn de eigenschappen van dit magnetisch veld? Het beantwoorden van de bovenstaande vragen is van belang om het vormingsproces van clusters beter te begrijpen. Naast radiowaarnemingen wordt er in dit proefschrift ook gebruik gemaakt van waarnemingen van Röntgen-satellieten en optische telescopen. Tevens zijn numerieke simulaties op krachtige computers gedaan om deze samensmeltingen van clusters beter te begrijpen. Een van de problemen voor het bestuderen van samensmeltende clusters is dat er maar weinig (enkele tientallen) clusters bekend zijn met radio halo's en relics. Een ander doel is dus om meer halo's and relics te vinden om zo de gezamenlijke eigenschappen van de clusters te kunnen bestuderen en te vergelijken.

In **Hoofdstuk 2** en **3** worden GMRT, WSRT en VLA waarnemingen beschreven van 26 potentiële nieuwe halo's en relics. Deze bronnen waren gevonden in oudere radiokaarten en vielen op doordat hun helderheid sterk toenam op langere golflengtes. Het blijkt dat inderdaad enkele van deze bronnen nieuwe relics en halo's zijn. De bronnen zijn verder bestudeerd met vervolgwaarnemingen op verschillende golflengtes. Door deze gegevens te combineren met al bekende radio relics zijn correlaties gevonden tussen verschillende eigenschappen van de bronnen, zoals hun grootte en de mate waarin de intensiteit toeneemt met de golflengte. In **Hoofdstuk 4** wordt ook een zoektocht naar nieuwe halo's en relics ondernomen. Dit resulteert in de ontdekking van zes nieuwe relics en twee halo's. Het blijkt dat deze halo's en relics allemaal te vinden zijn in samensmeltende clusters, zoals verwacht. We vinden ook dat de kans om een relic te vinden toeneemt naarmate de cluster meer massa heeft. Een van deze nieuw halo's wordt in meer detail bestudeerd in **Hoofdstuk 5**. Deze halo is de meeste verre en helderste die tot nu toe gevonden is. De halo bevindt zich in de massieve cluster MACS J0717.5+3745, welke een complexe samensmelting ondergaat van ten minste drie clusters.

In **Hoofdstuk 6** and **7** wordt de ontdekking van relics in de clusters ZwCl 2341.1+0000 en ZwCl 0008.8+5215 beschreven. Het bijzondere is dat beide clusters twee relics hebben die symmetrisch liggen aan weerszijden van het centrum van de clusters. Deze soort relics worden "dubbel relics" genoemd en zijn zeer zeldzaam. Er zijn er maar enkelen van bekend. De radio, Röntgen en optische waarnemingen van deze clusters laten zien dat deze bezig zijn samen te smelten. De dubbel relics bevinden zich op de positie van de verwachte schokgolven. Er zijn aanwijzingen gevonden dat de deeltjes die de radiostraling uitzenden versneld worden in de schokgolven van de botsingen.

In **Hoofdstuk 8** worden GMRT, WSRT en VLA waarnemingen besproken van de cluster genaamd CIZA J2242.8+5301. Deze waarnemingen laten een enorm grote relic zien. Via een

ingenieuze techniek wordt voor het eerst een precieze meting van het magnetisch veld gedaan in de cluster. Tevens is het effect van de beweging van de schokgolf waargenomen via de radiostraling. De waarnemingen van deze cluster geven het beste bewijs tot nu toe dat deeltjes inderdaad in schokgolven van clusters versneld worden tot extreme energieën.

In **Hoofdstuk 9** wordt een gedetailleerde analyse gedaan van een nieuwe cluster met een complexe radio relic en halo. Verschillende technieken om de radiostraling in detail te bestuderen worden hier ontwikkeld. Hiermee kan nieuwe informatie over het magnetisch veld en de specifieke deeltjes versnellingsmechanismen worden verkregen.

In **Hoofdstuk 10** worden simulaties van de samensmeltende clusters gepresenteerd. Door de simulaties te vergelijken met de radiokaarten is het mogelijk te reconstrueren hoe de samensmeltingen zijn verlopen. Deze techniek is toegepast op de cluster beschreven in **Hoofdstuk 8**. In dit specifieke geval vinden we dat de waarnemingen verklaard kunnen worden door een botsing tussen twee clusters met een massaverhouding van 2 staat tot 1. Ook zijn de simulaties gebruikt om de eigenschappen van het gas te onderzoeken op grote afstanden van het centrum van de cluster. Op grote afstand van het centrum van clusters is het gas zo ijl dat het nauwelijks waarneembaar is met Röntgenstraling.

GMRT en WSRT waarnemingen van de cluster Abell 2256 worden beschreven in **Hoofdstuk 11**. Een aantal nieuwe zwakke diffuse radio bronnen worden gedetecteerd. De helderheid van de bronnen neemt sterk toe met de golflengte, waardoor deze bronnen op langere golflengtes veel duidelijker zichtbaar zouden moeten zijn. Ten slotte wordt in **Hoofdstuk 12** de eerste LOFAR waarneming van de cluster Abell 2256 gepresenteerd. Deze waarneming laat voor het eerst de relic and halo zien op lange golflengtes. Zoals verwacht is ook een van de diffuse radiobronnen, beschreven in **Hoofdstuk 11**, zichtbaar op de LOFAR kaarten.

Curriculum vitae

Ik ben geboren op 22 augustus 1980 te De Bilt. Op mijn 13de verhuisde ik met mijn ouders en twee zussen naar Rotterdam. Mijn fascinatie voor sterrenkunde begon waarschijnlijk toen mijn vader een kleine telescoop kocht waarmee nog net wat kraters op de Maan te zien waren. Later bouwde ik een 15 cm Newton telescoop op Dobson montering waar veel meer mee was te zien, zelfs in het lichtvervuilde Rotterdam. Tegelijkertijd begon ik ook steeds meer boeken over sterrenkunde te lezen en kreeg ik een lidmaatschap op het maandblad over sterrenkunde Zenit.

In 2000 haalde ik mijn VWO diploma op het Montessori Lyceum Rotterdam. Na een paar maanden geld verdienen ben ik gaan backpacken in Australië, Nieuw-Zeeland en Thailand en besloot ik mij in te schrijven voor de studie sterrenkunde aan de Universiteit Leiden. Tijdens de doctoraalfase van mijn studie heb ik gewerkt aan radio waarnemingen van de cluster van sterrenstelsels Abell 2256, onder leiding van Prof. Huub Röttgering. Deze waarnemingen waren gedaan met nieuwe lage frequentie ontvangers op de Westerbork Synthesis Radio Telescope (WSRT), ter voorbereiding op het LOFAR project.

Na het vierde jaar van mijn studie besloot ik een jaar te gaan werken op een school in Thailand. Hier heb ik zowel wis -en natuurkunde les gegeven op een middelbare school. Het jaar daarop ben ik weer verder gegaan met de studie sterrenkunde. Voor mijn afstudeeronderzoek heb ik de chemische evolutie tijdens de vorming van protoplanetaire schijven bestudeerd met behulp van computersimulaties, onder leiding van Dr. Michiel Hogerheijde. Dit resulteerde uiteindelijk in een eerste en tweede auteurs publicatie in een vaktijdschrift. Ook kreeg ik de mogelijkheid waarnemingen te verrichten met de Giant Metrewave Radio Telescope (GMRT) in India. In het 5de studiejaar heb ik als student assistent gewerkt aan het maken van kalibratie modellen voor de nieuwe LOFAR radiotelescoop. Ik studeerde (cum Laude) af op 28 augustus 2007.

In september 2007 begon ik aan mijn promotie-onderzoek, met KNAW financiering van Prof. George Miley en financiële ondersteuning van de Sterrewacht. Het plan was om te werken aan de eerste waarnemingen van de LOFAR radiotelescoop die in aanbouw was in het noorden van Nederland en omliggende landen. Omdat de bouw van LOFAR langzamer ging dan verwacht, ben ik mijn onderzoek gestart met waarnemingen van al bestaande grote radio telescopen. Voor mijn onderzoek heb ik de radiostraling van botsende clusters van sterrenstelsels bestudeerd met de GMRT, WSRT, en Very Large Array. Voor de GMRT waarnemingen ben ik meerdere malen naar India geweest. Tevens heb ik waarnemingen verricht met de Isaac Newton Telescope en William Herschel Telescope (twee keer) op La Palma (Spanje). Ook heb ik waargenomen

met de APEX telescoop (Chile) en op Kreta (wat geen succes was door de storm die er op de berg woedde). De laatste twee jaar van mijn promotietijd heb ik vele malen ASTRON bezocht om te werken aan de eerste LOFAR observaties. De resultaten van dit promotie-onderzoek, en ook de eerste LOFAR waarnemingen, kunt u in dit proefschrift vinden.

Tijdens mijn promotie periode heb ik deelgenomen aan de MCCT-SKADS training school in Bologna, de NOVA herfstschool en een conferentie in Hamburg. Ik heb twee persberichten uitgebracht en heb gewerkt aan de eerste hoge-resolutie LOFAR beelden van 3C 61.1 en Abell 2256 welke gebruikt zijn voor de LOFAR openingsceremonie. Ik werd genomineerd voor 'de ontdekker van het jaar' in 2010. Tijdens mijn promotie periode heb ik drie maal geassisteerd bij het vak Astronomische Waarneemtechnieken onder leiding van Rudolf le Poole, Dr. Bernard Brandl, en Prof. Walter Jaffe. In september 2010 heb ik een werkbezoek gebracht aan de Jacobs Universiteit in Bremen om met Prof. Marcus Brüggen te werken aan simulaties van botsende clusters van sterrenstelsels. Ik heb mijn onderzoek gepresenteerd op conferenties in Bangalore (India), Rio de Janeiro (Brazilië) en Nice (Frankrijk) en op verscheidene workshops/conferenties in Nederland. Ook heb ik mijn werk gepresenteerd op het National Centre for Radio Astrophysics in Pune (India, twee keer), Cambridge, Edinburgh IfA, Harvard CfA, NASA Goddard, Naval Research Laboratory (Washington), National Radio Astronomy Observatory (Charlottesville, Virginia), UC Berkeley (San Francisco) en ASTRON. Na mijn promotie zal ik mijn onderzoek voortzetten als postdoc.

Nawoord / Acknowledgements

Zonder de hulp van anderen was dit proefschrift er niet geweest. De laatste pagina's van dit proefschrift wil ik daarom graag gebruiken om enkele mensen te noemen die een bijdrage hebben geleverd aan de totstandkoming van dit proefschrift.

David, Erik, Aart en Tycho, bedankt voor alle support op het gebied van software en computers. Mede dankzij jullie hoefde ik me hier geen zorgen over te maken en was altijd de laatste versie van een software pakket beschikbaar. Tycho nog bedankt voor de tip: een kapotte harddisk omdraaien kan inderdaad een maand van je promotie schelen. Kirsten, Evelijn, Jeanne, Liesbeth en Anita bedankt voor de secretariële ondersteuning.

Tijdens mijn onderzoek heb ik dankbaar gebruik gemaakt van de financiële steun van de Koninklijke Nederlandse Akademie van Wetenschappen, de Sterrewacht Leiden, de Nederlandse Onderzoeksschool voor Astronomie, het Leids Kerkhoven-Bosscha Fonds, en het Leidse Sterrewacht Fonds.

Special thanks to the people and former members of the Leiden radio-group: David, Niruj, Laura, Bas and Huib. Niruj, thanks for adding some spices to our meetings. Huib en Bas, ik heb altijd veel van onze discussies over kalibratie van radio data opgestoken. David thanks for all your support and fixing things so quickly. I would also like to mention a few people at ASTRON, George, John and especially Roberto, for organizing all the LOFAR "busy days" and "weeks". Manu, Francesco, Annalisa, Roberto, Cyril, and other busy weekers, it was good not to struggle alone with the LOFAR data. Teun and Ashish, your support during the summer holiday was very welcome, even more so because you allowed me to brake the computing cluster a few times. Joris, Sven, and Ger thanks for all your efforts, BBS really has become a powerful calibration software package for radio data, and without it there would be no LOFAR chapter in this thesis.

Raymond, Ernst, Maarten, kamergenoot Babs, en anderen, bedankt voor de welkome afleiding en (te) lange koffiepauzes.

Ten slotte wil ik graag mijn familie, ouders, zussen en Fon noemen. Zonder jullie was het natuurlijk allemaal niet mogelijk geweest.